MEASUREMENT-BASED INVESTIGATIONS OF RADIO WAVE PROPAGATION: AN EXPOSÉ ON BUILDING CORNER DIFFRACTION

A Thesis
Presented to
The Academic Faculty

by

Ryan J. Pirkl

In Partial Fulfillment
of the Requirements for the Degree
Doctor of Philosophy in the
School of Electrical and Computer Engineering

Georgia Institute of Technology
May 2010

MEASUREMENT-BASED INVESTIGATIONS OF RADIO WAVE PROPAGATION: AN EXPOSÉ ON BUILDING CORNER DIFFRACTION

Approved by:

Professor Gregory D. Durgin, Advisor
School of Electrical and Computer Engineering
Georgia Institute of Technology

Professor Andrew F. Peterson
School of Electrical and Computer Engineering
Georgia Institute of Technology

Professor Glenn S. Smith
School of Electrical and Computer Engineering
Georgia Institute of Technology

Professor Paul G. Steffes
School of Electrical and Computer Engineering
Georgia Institute of Technology

Dr. Kate A. Remley
Electronics Engineer
National Institute of Standards and Technology

Date Approved: 11 January 2010

For Kelly

ACKNOWLEDGEMENTS

This work was made possible by a National Science Foundation Graduate Research Fellowship. Many thanks to the public officials out there who continue to support investing in science education and scientific research.

This research would have been impossible without the guidance, wisdom, and support of my advisor, Prof. Gregory Durgin. A wellspring of patience and goodwill, I could always rely on him to cheer me on through ups and downs. My sincere thanks for all of the so-called "pep rallies".

A round of thanks also goes out to my committee members, Prof. Andrew F. Peterson, Dr. Kate A. Remley, Prof. Glenn S. Smith, and Prof. Paul G. Steffes for their helpful comments, suggestions, and constructive criticism. I'm also grateful to Prof. Aaron Lanterman for generously allowing me to use his oscilloscope for my measurements.

The measurements presented in this dissertation would not have been possible without the patience and cooperation of the in-band spectrum license holders. Thanks to Ed Fowler, Michael P. Goggin, David Shively, and Robert V. Vitanza of AT&T; Christy Burrow and David Don of SpectromCo; Eric Hagerson, Kathleen Ham, and Dan Wilson of T-Mobile; and Sonya Dutton and David Mason of Verizon Wireless.

A special shout out to past and present members of the Propagation Group for making grad school a great experience. A special word of thanks to Chris Durkin, Josh Griffin, Azhar Hasan, Lorne Liechty, Albert Lu, and Matt Trotter for always being there to celebrate on the good days and commisserate on the bad. Also, thanks to Jet Zhu for giving me his awesome desk by the window and for establishing the

precedent that returning lab alumni should always bring snacks, and to my Opportunity Research Scholars: Seema Bhandari, Santiago Hässig, and Rodrigo Quinteros Soria for their hard work, dedication, and overall awesomeness.

I'm also deeply indebted to my friends down in Auckland, New Zealand for putting me up and putting up with me for three months. Special thanks to Profs. Micheal J. Neve and Kevin W. Sowerby and their families for looking after me, the "Betsy" crew for the many adventures, and Andrew C. M. Austin for his in invaluable FDTD data.

Finally, a most humble word of thanks to my mother and father, Shirley and Dennis Pirkl, to whom I owe much if not everything that I have achieved.

TABLE OF CONTENTS

LIST OF TABLES

LIST OF FIGURES

LIST OF SYMBOLS OR ABBREVIATIONS

General Notation:

$\|(\cdot)\|$	L-2 norm of $(\cdot)$
$\langle(\cdot)\rangle$	Ensemble average of $(\cdot)$
$\mathrm{Re}(\cdot)$	Real part of $(\cdot)$
$\mathrm{Im}(\cdot)$	Imaginary part of $(\cdot)$
$\tilde{(\cdot)}$	Approximation to $(\cdot)$
$\hat{\mathbf{x}}$	Unit norm of vector $\mathbf{x}$
$\mathbf{r} = (\rho, \phi)$	Observation position
$\mathbf{r}' = (\rho', \phi')$	Source position
θ	Angle of reflection with respect to normal
β	Direction of propagation
λ	Wavelength
k	Wavenumber
$\mathbf{k} = (k_x, k_y)$	Wavevector
t	Time
τ	Delay
f	Baseband frequency
f_0	Carrier frequency

Diffraction:

Φ	Wedge interior angle
n	Normalized wedge exterior angle
$\perp$	Perpendicular polarization
$\parallel$	Parallel polarization

E_0	Source excitation phasor
$C^i(\phi, \phi')$	ISB pattern function for UTD impedance wedge diffraction coefficient
$C^r(\phi, \phi')$	RSB pattern function for UTD impedance wedge diffraction coefficient
$D^{\perp\!\!\!\parallel}_{\mathrm{GTD}}(\phi, \phi')$	GTD's PEC wedge diffraction coefficient
$D^{\perp\!\!\!\parallel}_{\mathrm{PEC}}(\phi, \phi')$	UTD's PEC wedge diffraction coefficient
$D^{\perp\!\!\!\parallel}_{\mathrm{UTD}}(\phi, \phi')$	UTD impedance wedge diffraction coefficient
$D^{\perp\!\!\!\parallel}_0(\beta)$	General purpose UTD-style diffraction function
$\Gamma^{\perp\!\!\!\parallel}(\theta)$	Reflection coefficient
$E^i(\mathbf{r})$	GO's incident electric field
$E^r(\mathbf{r})$	GO's reflected electric field
$E^d(\mathbf{r})$	GTD/UTD's diffracted electric field
$E^t(\mathbf{r})$	GTD/UTD's total electric field
$E^{i,\perp}_{\mathrm{PEC}}(\mathbf{r})$	GO's incident electric field for $\perp$-incidence on a PEC wedge
$E^{r,\perp}_{\mathrm{PEC}}(\mathbf{r})$	GO's reflected electric field for $\perp$-incidence on a PEC wedge
$E^{d,\perp}_{\mathrm{PEC}}(\mathbf{r})$	GTD/UTD's diffracted electric field for $\perp$-incidence on a PEC wedge
$E^{t,\perp}_{\mathrm{PEC}}(\mathbf{r})$	GTD/UTD's total electric field for $\perp$-incidence on a PEC wedge

Wireless Channel:

$h(f, \mathbf{r})$	Complex baseband wireless channel
$H(\tau; \mathbf{r})$	Complex baseband channel impulse response
$H(\mathbf{k}; f)$	Complex banseband plane wave spectrum
$H(\tau, \mathbf{k})$	Complex banseband channel transfer function
$C_h(\cdot)$	Wireless channel autocorrelation with respect to $(\cdot)$
$\varrho_h(\cdot)$	Wireless channel unit autocovariance with respect to $(\cdot)$
$S_h(\cdot)$	Wireless channel power spectrum with respect to $(\cdot)$

$p(\phi)$	Power angle spectrum
$p(\tau, \phi)$	Power delay-angle spectrum

Measurements:

Δ_s	Spatial sampling period
d	Separation distance between concentric contours
D	Diameter of smallest circle circumscribing the field reconstruction region
$\lambda_{\max}$	Measurement bandwidth's largest free-space wavelength
$\lambda_{\min}$	Measurement bandwidth's smallest free-space wavelength
f_c	PN chip rate

Material Properties:

Z_s	Surface impedance
η	Intrisic impedance
$\theta_{\parallel}^{\perp}$	Normalized impedance angle
μ	Permeability
ϵ	Permittivity
η_0	Free-space intrisic impedance
μ_0	Free-space permeability
ϵ_0	Free-space permittivity
μ_R	Complex relative permeability
ϵ_R	Complex relative permittivity

Abbreviations and Acronymns:

0-face	Wedge face corresponding to 0 radians
n-face	Wedge face corresponding to $n\pi$ radians
2-D	2-dimensional

3-D	3-dimensional
AoA	Angle-of-arrival
BPF	Band-pass filter
CWE	Cylindrical wave expansion
DSP	Digital signal processing
FDTD	Finite-difference time-domain
GO	Geometrical optics
GTD	Geometrical theory of diffraction
I/Q	Inphase/quadrature
IF	Intermediate frequency
Imp.	Impedance
ISB	Reflection shadow boundary
LPF	Low-pass filter
PEC	Perfectly electrically conducting
PN	Pseudo-random binary noise
PRBS	Pseudo-random binary sequence
RF	Radio frequency
RMS	Root-mean-square
RSB	Reflection shadow boundary
Rx	Receiver
SIMO	Single-input multiple-output
Tx	Transmitter
UTD	Uniform geometrical theory of diffraction
UWB	Ultra-wideband
VNA	Vector network analyzer

SUMMARY

Predicting performance metrics for the next-generation of multi-mode and multi-antenna wireless communication systems demands site-specific knowledge of the wireless channels underlying radio wave propagation mechanisms. This thesis describes the first measurement system capable of characterizing individual propagation mechanisms in situ. The measurement system merges a high-resolution spatio-temporal wireless channel sounder with a new field reconstruction technique to provide complete knowledge of the wireless channels impulse response throughout a 2-dimensional region. This wealth of data may be combined with space-time filtering techniques to isolate and characterize individual propagation mechanisms. The utility of the spatio-temporal measurement system is demonstrated through a measurement-based investigation of diffraction around building corners. These measurements are combined with space-time filtering techniques and a new linear wedge diffraction model to extract the first semi-empirical diffraction coefficient. Specific contributions of this thesis are:

- The first ultra-wideband single-input multiple-output (SIMO) channel sounder based upon the sliding correlator architecture.
- A quasi 2-dimensional field reconstruction technique based upon a conjoint cylindrical wave expansion of coherent perimeter measurements.
- A wireless channel "filming" technique that records the time-domain evolution of the wireless channel throughout a 2-dimensional region.
- High-resolution measurements of the space-time wireless channel near a right-angled brick building corner.

- The application of space-time filtering techniques to isolate the edge diffraction problem from the overall wireless channel.
- An approximate uniform geometrical theory of diffraction (UTD)-style linear model describing diffraction by an impedance wedge.
- The first-ever semi-empirical diffraction coefficient extracted from in situ measurement data.

This thesis paves the way for several new avenues of research. The comprehensive measurement data provided by channel "filming" will enable researchers to develop and implement powerful space-time filtering techniques that facilitate measurement-based investigations of radio wave propagation. The measurement procedure described in this thesis may be adapted to extract realistic reflection and rough-surface scattering coefficients. Finally, exhaustive measurements of individual propagation mechanisms will enable the first semi-empirical propagation model that integrates empirical descriptions of propagation mechanisms into a UTD-style mechanistic framework.

CHAPTER I

INTRODUCTION

Chapter Summary: This chapter introduces a semi-empirical radio wave propagation model based upon in situ measurements of individual propagation mechanisms. A review of recent propagation mechanism measurements reveals the need for more effective techniques capable of characterizing edge diffraction. This is followed by a review of the GTD's diffraction coefficient and a brief summary of this document's organizanization.

Analytical and empirical models represent two contrasting yet complementary paradigms in radio wave propagation. Analytical models based on exact or approximate solutions to Maxwell's equations provide insight into the physical mechanisms underlying radio wave propagation. However, these solutions are only applicable to simplistic real-world scenarios and thus tend to show poor agreement with measurement data from complex environments. Empirical models, on the other hand, are based on exhaustive measurement data and thus tend to be very accurate, particularly for path loss prediction. However, because empirical models are based on statistical analyses, they offer extremely limited information as to the actual mechanisms contributing to the observed field, particularly when generalized to configurations and environments beyond those in which the measurements were conducted. The challenge is to combine analytical and empirical models so as to offer insight into the contributing propagation mechanisms while also providing accurate prediction capabilities in both a large- and small-scale sense.

1.1 Small-Scale Radio Wave Propagation Models

The small-scale form of this problem has been addressed extensively; all more or less building upon the ideas by Clarke, who showed that the narrowband fading distributions formulated from empirical measurements were rooted in and could be derived from a physical model of the incident radio waves [19]. Turin extended this principle to broadband radio wave propagation and developed an analytical model for small-scale spatio-temporal fading [111]. Physically, the time- and angle-of-arrival of radio waves at the receiver depends on the geometry and electromagnetic composition of the environment. Therefore, in principle, an accurate small-scale model requires knowledge of the large-scale propagation mechanisms. Given that these are by definition small-scale models, such a requirement is hardly practical. The solution has been to reformulate these small-scale propagation models as stochastic processes and determine the probability density function of random variables from measurement data [105, 91]. Measurement data from different environment archetypes provide a means for specializing the small-scale propagation models to different propagation scenarios [84, 30, 22, 120, 15, 11, 59]. This approach has been extremely successful and has led to the development of various channel simulators for evaluating the performance and reliability of next-generation communications systems [92].

1.2 Large-Scale Radio Wave Propagation Models

In contrast to the small-scale radio wave propagation models, large-scale models have had limited success in merging the deterministic formulations of analytical models with empirical data. Reasons for this are manifold and vary over the course of history (cf. [55]), though the physical and mathematical complexities of large-scale radio wave propagation problems have played a reoccurring role [117, 52, 20]. Before Keller introduced his geometrical theory of diffraction (GTD) in 1962 [54], analytical solutions could only be formulated for very basic, canonical propagation problems.

Notable among these are the knife-edge diffraction solution and Sommerfeld's solution to radiation over an imperfectly electrically conducting ground plane, both of which have been used extensively with and without modification for many practical problems [14]. Furthermore, until recently, there was little need to know the actual mechanisms underlying radio wave propagation. On the large-scale, wireless communication engineers have primarily been concerned with path loss, which can be efficiently and accurately computed from empirical models like the Okumura-Hata model [44] or the COST-231 model [114, 48]. Provided some minimum average received power and carefully designed hardware to compensate for small-scale fading, wireless communication systems have proven reliable despite being planned and deployed with minimal deterministic knowledge.

1.2.1 Changing Demands

Path loss models are sufficient if one is only interested in guaranteeing that a system work at some minimum performance level. However, if for example one desires to predict data throughput throughout a basestation's coverage area, path loss models alone are inadequate and site-specific propagation models become crucial [3]. Additionally, the performance of new multiple-input multiple-output (MIMO) communication systems is strongly dependent on, among other factors, the angular distributions of transmitted and received power [33]. Thus, site-specific physics-based propagation models are invaluable for planning and deploying next generation wireless systems.

1.2.2 Toward an Empirical-GTD Propagation Model

The aforementioned GTD and its variants are perhaps the most viable and heavily investigated analytical platform for developing site-specific physics-based propagation models [61, 95, 9]. The utility of the GTD is that it allows the solution to complex electromagnetics problems to be expressed as the sum of contributions due to individual propagation mechanisms. Thereby, the GTD provides a deterministic description

of radio wave propagation in complex environments, which also makes it an excellent candidate for integration with empirical data. Measurements of individual propagation mechanisms could be integrated into the GTD's mechanistic framework to realize a physics-based propagation model offering the physical insight of analytical models and the measurement-based accuracy of empirical models.

Integrating measurement data into the GTD framework would also overcome many of the drawbacks of a purely GTD-based ray-tracer. Most implementations rely on the assumption that everyday objects like walls and corners may be accurately modeled by smooth dielectric slabs and wedges, respectively, with known material parameters [10]. Thereby, analytical models neglect an object's fine structural detail and impose a predetermined behavior onto the scattered fields that may or may not be valid depending on the accuracy of the material parameters and significance of neglected model details. Furthermore, although recent research has integrated ray-tracer and radiosity models to account for surface roughness [6, 110, 72], edge roughness and its effect on edge diffraction have yet to be addressed. Actual measurements of individual propagation mechanisms could provide empirical coefficients that compensate for all of these shortcomings. For example, measurements of diffraction around various building corners could provide an empirical diffraction coefficient for a "typical" building corner that accounts for the actual material properties, structural details, and edge roughness while also enabling researchers to determine if other significant propagation mechanisms are present. The challenge, however, is devising a measurement technique that would allow researchers to isolate and characterize individual mechanisms - preferably in situ.

1.3 Measuring Individual Propagation Mechanisms

The preferred method for measuring propagation mechanisms in general and building corner diffraction in particular involves highly directional antennas or antenna arrays

so as to more heavily weigh field contributions arriving from a small angular sector [16, 58, 93, 106, 42, 88, 24, 26, 28, 27]. This approach has been used in both narrowband and wideband form to measure reflected, transmitted, and diffracted fields. In general, wideband measurement systems are preferrable, because they allow for temporal windowing, which eliminates the ambiguity created by multiple time-harmonic wavefronts incident from the same angular sector. Separating contributions due to specular and diffuse scattering mechanisms is an added challenge for those seeking to develop coefficients directly from the measurement data. The working solution is to base the empirical coefficient on an appropriate analytical model that accounts for diffuse scattering mechanisms such as rough surface scattering [26, 58].

Developing empirical diffraction coefficients for integration into the GTD is somewhat more complicated and remains an unsolved problem. Near the shadow boundaries of geometrical optics (GO), the GO-defined incident and reflected fields exhibit a discontinuity that is exactly canceled by the diffracted field's discontinuity so as to produce a smooth, continuous, and physically realizable total field [56]. Away from the shadow boundaries, these fields' contributions are distinct and lend themselves to a ray-optics represention via Keller's GTD [54]. However, at the so-called *penumbra* regions near the shadow boundaries, the incident, reflected, and diffracted fields of GTD lose their ray-optics interpretation and become impossible to isolate [12]. This is one of the fundamental challenges of characterizing diffracted fields and may explain why researchers have opted to use diffraction measurements to evaluate the accuracy and applicability of GTD coefficients rather than formulate new, empirical diffraction coefficients [29, 21, 4, 8, 85].

1.3.1 In Situ Building Corner Diffraction Measurements

Suprisingly, despite the ubiquity of buildings in propagation environments, there have been only a handful of campaigns aimed specifically at measuring and characterizing

the fields diffracted by real-world building corners [107, 42, 2, 4, 88, 75]. None of these investigations have been comprehensive. In the most extensive measurements, either the receiver was stepped along an angular sector for a single fixed transmitter position or, conversely, the transmitter was stepped along an angular sector for a single fixed receiver position [88, 4, 42, 107, 2]. The majority were narrowband non-coherent measurements that used directional antennas to isolate the diffracted power. Exceptions are [88] and [75], both of which took coherent wideband measurements along a synthetic aperture array and isolated the diffracted power using beamsteering techniques. In addition, all but [4] restricted their measurements to the shadow region. However, [4] used an omnidirectional receive antenna to measure the total field as opposed to just the diffracted field.

1.3.2 Ex Situ Building Corner Diffraction Measurements

To circumvent the hassles of measuring real-world building corner diffraction, researchers at the the University of Birmingham made narrowband measurements of diffraction around model building corners constructed inside of an anechoic chamber [28, 27, 21, 29]. Both a brick and a plasterboard corner were constructed, and directional measurements were carried out both inside and outside the shadow region. To better compare their brick corner measurements to the theoretical solution for a lossy dielectric wedge, the interior of the brick corner was lined with electromagnetic absorber [28]. The plasterboard corner was unmodified so as to approximate a partially transparent resistive wedge. Thus, whereas the plasterboard corner measurements are likely indicative of what may be observed in the real-world, it is unclear if the brick corner measurements are also representative. Furthermore, although the observation angle was swept from 90° to nearly 270°, the incident angle was 5° for all measurements.

1.4 Enabling Measurement-Based Investigations of Radio Wave Propagation

Existing radio wave propagation measurement methodologies rely entirely on the measurement system's space-time resolution to isolate contributing multipath components. This resolution dependence is the fundamental limitation of modern measurement techniques and has pushed researchers to develop increasingly wideband measurement systems with precise array steering capabilities. However, regardless of its temporal and spatial resolution, no measurement system will ever be capable of isolating the field diffracted within the penumbra region surrounding the shadow boundaries. This suggests that, rather than a "bigger, better, and faster" approach to existing measurement techniques, what is needed is a fundamentally different measurement methodology that does not require direct measurement of individual propagation mechanisms.

This thesis presents a revolutionary new approach to radio wave propagation measurements based upon the flexibility afforded by comprehensive total field measurement data. Using an innovative field reconstruction-based spatio-temporal channel sounder, the wideband wireless channel may be measured throughout a 2-D region of space. Careful filtering of the channel sounder's high-resolution data set in both space and time allows individual radio wave propagation mechanisms to be isolated and analyzed. Where applicable, additional space-time processing may be used to isolate and characterize the individual field components of various propagation mechanisms. For more complicated propagation mechanisms such as diffraction, an appropriate linear model may be fit to the filtered measurement data to simultaneously characterize and extract the contributing field components. To demonstrate the viability and utility of this new measurement technique, the measurement system and accompanying data processing tools are used to obtain the first semi-emprical diffraction coefficient describing building corner diffraction.

1.5 The GTD's Diffraction Coefficient

The diffraction coefficient is a key element of this thesis, and understanding both the coefficient and the closely related GTD are important for appreciating certain aspects of the work presented herein. To clarify the role of the diffraction coefficient in the GTD as well as to facilitate later discussion of various diffraction coefficients used to describe building corner diffraction, the following section reviews the geometrical and uniform geometrical theories of diffraction. For completeness, this is a followed by a brief survey of existing non-empirical diffraction coefficients that have been used in attempts to describe building corner diffraction.

1.5.1 The (Uniform) Geometrical Theory of Diffraction

The *diffraction coefficient* is a core component of the GTD, because it provides a description for the magnitude and phase of the rays that emanate from any edge discontinuties. These edge-based rays and their associated diffraction coefficient form the GTD's high-frequency approximation to the diffracted field. Thereby, an empirical or semi-empirical diffraction coefficient may be easily integrated into the GTD's mechanistic framework to realize a measurement-based model of the building corner's diffracted field.

Figure 1 presents the canonical 2-dimensional (2-D) problem of plane wave diffraction by a infinite perfectly electrically conducting (PEC) wedge. The GTD describes the total field, $E^t(\mathbf{r})$, as the sum of contributions from the incident, reflected, and diffracted fields, denoted $E^i(\mathbf{r})$, $E^r(\mathbf{r})$, and $E^d(\mathbf{r})$, respectively.

$$E^t(\mathbf{r}) = E^i(\mathbf{r}) + E^r(\mathbf{r}) + E^d(\mathbf{r}) \tag{1}$$

The incident and reflected fields, $E^i(\mathbf{r})$ and $E^r(\mathbf{r})$, are given by the corresponding geometrical optics solution. The diffracted field, $E^d(\mathbf{r})$, is given by its high-frequency

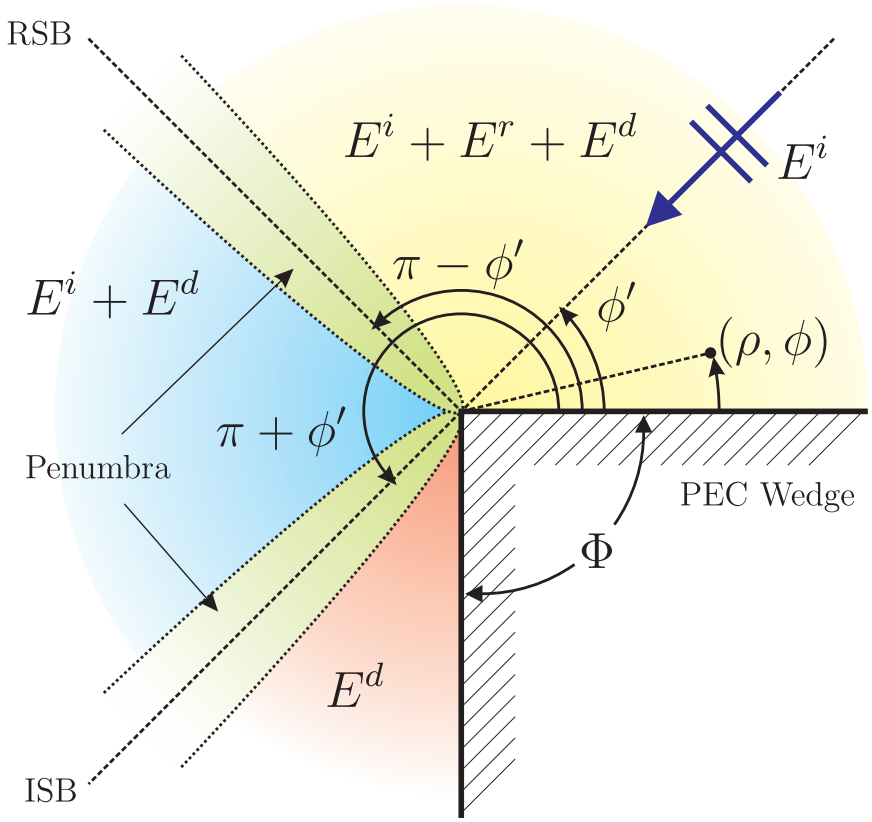

Figure 1: A diagram of the 2-D diffraction problem for a PEC wedge. The total field may be divided into three regions based on the contributions of the GO-defined incident and reflected fields. The UTD's asymptotic diffracted field contributes to the total field in all three regions.

approximation, which may be described by the product of the incident field evaluated at the diffracting edge, $E^i(\mathbf{0})$, an angle- and polarization-dependent diffraction coefficient, $D^{\perp}_{\parallel\,\mathrm{GTD}}(\phi,\phi')$, and an outward propagating cylindrical wave originating at the diffracting edge:

$$E^d(\mathbf{r}) = E^i(\mathbf{0})\frac{e^{-jk_0\rho}}{\sqrt{\rho}}D^{\perp}_{\parallel\,\mathrm{GTD}}(\phi,\phi') \tag{2}$$

where

$$\begin{aligned} D^{\perp}_{\parallel\,\mathrm{GTD}}(\phi,\phi') &= -\frac{e^{-j\frac{\pi}{4}}}{2n\sqrt{2\pi k_0}} \\ &\times\left[\frac{\sin(\pi/n)}{\cos(\pi/n)-\cos([\phi-\phi']/n)} \pm \frac{\sin(\pi/n)}{\cos(\pi/n)-\cos([\phi+\phi']/n)}\right] \end{aligned} \tag{3}$$

In Eqs. (2) and (3), k_0 is the free-space wavenumber of the time-harmonic field, ρ is the distance from the diffracting edge, ϕ' and ϕ are the angles of incidence and observation, respectively, and n describes the wedge angle as given by

$$n = 2 - \Phi/\pi \tag{4}$$

where Φ is the interior wedge angle as shown in Fig. 1. The superscripts in Eq. (3) denote the corresponding diffraction coefficient for an incident electric field that is polarized parallel, $\parallel$, or perpendicular, $\perp$, to the plane of incidence. The polarization determines the appropriate boundary condition for the PEC wedge diffraction problem. For parallel (i.e., horizontal) polarization, the soft (i.e., Neumann) boundary condition is used; for perpendicular (i.e., vertical) polarization, the hard (i.e., Dirichlet) boundary condition is used.

Keller's original diffraction coefficient is restricted to regions away from the penumbra due to the singularity in Eq. (3) at the incident and reflection shadow boundaries (ISB and RSB, respectively) [51]. The UTD introduced by Kouyoumjian and Pathak in 1974 uses an alternative asymptotic approximation to obtain a diffraction

coefficient that is bounded and applicable everywhere [56]. The UTD PEC wedge diffraction coefficient is

$$D_{\mathrm{PEC}}^{\perp\!\!\!\parallel}(\phi,\phi') = -\frac{e^{-j\pi/4}}{2n\sqrt{2\pi k_0}} \left\{ \right. \tag{5}$$

$$\begin{aligned}
&\cot\left(\frac{\pi+[\phi-\phi']}{2n}\right) F[k_0\rho a^+(\phi-\phi',n)] \\
&+\cot\left(\frac{\pi-[\phi-\phi']}{2n}\right) F[k_0\rho a^-(\phi-\phi_0)] \\
&\mp\cot\left(\frac{\pi+[\phi+\phi']}{2n}\right) F[k_0\rho a^+(\phi+\phi')] \\
&\mp\cot\left(\frac{\pi-[\phi+\phi']}{2n}\right) F[k_0\rho a^-(\phi+\phi')] \left. \right\}
\end{aligned} \tag{6}$$

where $F[x]$ is the so-called *transition function* given by

$$F[x] = 2j\sqrt{x}e^{jx}\int_{\sqrt{x}}^{\infty} e^{-j\tau^2}\,d\tau \tag{7}$$

that exactly cancels the singularity of the cotangent function, and

$$a^{\pm}(\beta) = 2\cos^2\left(\frac{2n\pi N^{\pm}-\beta}{2}\right) \tag{8}$$

$$N^{\pm} = \mathrm{round}\left\{\frac{\beta\pm\pi}{2\pi n}\right\} \tag{9}$$

Equation (5) matches the notation used in [56] for the case of plane wave incidence. To facilitate later discussion, we opt to rewrite Eq. (5) in the following form:

$$D_{\mathrm{UTD}}^{\perp\!\!\!\parallel}(\phi,\phi') = -\frac{e^{-j\pi/4}}{2n\sqrt{2\pi k_0}} \Bigg\{ \tag{10}$$

$$\begin{aligned}
&C_1(\phi,\phi')\cot\left(\frac{\pi+[\phi-\phi']}{2n}\right)F[k_0\rho a^+(\phi-\phi',n)] \\
&+C_2(\phi,\phi')\cot\left(\frac{\pi-[\phi-\phi']}{2n}\right)F[k_0\rho a^-(\phi-\phi_0)] \\
&+C_3(\phi,\phi')\cot\left(\frac{\pi+[\phi+\phi']}{2n}\right)F[k_0\rho a^+(\phi+\phi')] \\
&+C_4(\phi,\phi')\cot\left(\frac{\pi-[\phi+\phi']}{2n}\right)F[k_0\rho a^-(\phi+\phi')] \Bigg\}
\end{aligned} \tag{11}$$

Comparing Eqs. (5) and (10), it may be seen that the UTD's PEC wedge diffraction coefficient, $D_{\mathrm{PEC}}^{\perp\!\!\!\parallel}(\phi,\phi')$ is recovered from $D_{\mathrm{UTD}}^{\perp\!\!\!\parallel}(\phi,\phi')$ when $C_1(\phi,\phi') = C_2(\phi,\phi') = 1$ and $C_3(\phi,\phi') = C_4(\phi,\phi') = \mp 1$. For more general wedge compositions, $C_{1-4}(\phi,\phi')$ are angle-dependent pattern functions that shape the contributions from each of the four terms in the diffraction coefficient. Thus, Equation (10) provides a general framework for constructing UTD-style diffraction coefficients for *impenetrable* wedges, whereby any fields refracted into and out of the wedge are negligible.

1.5.2 A Survey of Diffraction Coefficients Applicable to Building Corners

The UTD solution to diffraction by a PEC wedge is a good first-step in describing diffraction by a building corner. A logical improvement is to model the building corner using a solid or, preferrably, a hollow dielectric wedge. Unfortunately, extending the UTD to non-PEC wedges remains a challenging research problem that is compounded by the scarcity of analytical solutions [52, 102]. Aside from the PEC and perfectly absorbing wedges, the impedance wedge is the only other wedge configuration for which an asymptotic UTD-type solution exists [50, 108, 109]. Given the scarcity of analytical formulations, many researchers have attempted to heuristically modify the PEC wedge diffraction coefficient by substituting expressions into the term

coefficients, $C_{1-4}(\phi, \phi')$, in Eq. (10) [17, 62, 74]. Additional heuristic modifications to Eq. (10) have extended the framework to penetrable wedges [89, 90, 8]. Numerical techniques provide an alternative approach that capitalizes on the accuracy and flexibility of computational electromagnetics simulations and could prove especially useful for developing diffraction coefficients for complex geometries [46, 47, 78, 77].

1.6 Thesis Outline

This thesis is organized into six chapters and six appendices. The following succintly summarizes the research contained in each chapter/appendix:

Chapter 1: establishes the research objectives of this thesis. It also reviews current measurement techniques used to investigate diffraction and provides a literature survey of existing diffraction coefficients that have been used to describe diffraction by building corners.

Chapter 2: develops the UTD-style linear model that enables semi-empirical diffraction coefficients to be extracted from total field measurement data.

Chapter 3: describes the field reconstruction-based spatio-temporal channel sounder that enables high resolution measurements of the space-time wireless channel throughout a planar region.

Chapter 4: describes the building corner diffraction measurements.

Chapter 5: describes the mechanism-based space-time filtering technique that was used to isolate the building corner diffraction problem and presents the semi-empirical diffraction coefficients that were extracted from the total field measurement data.

Chapter 6: reviews the contributions of this thesis, discusses possible improvements, and describes future avenues of research enabled by this work.

Appendix A: presents the conjoint cylindrical wave expansion that was used to interpolate perimeter wireless channel measurements throughout a bounded planar region.

Appendix B: provides analytical expressions for the error in the conventional and conjoint cylindrical wave expansion for electromagnetic waves incident upon a circular measurement region at some arbitrary azimuth and elevation angle.

Appendix C: discusses the hardware and software for the custom single-input multiple-output (SIMO) sliding correlator channel sounder that was used in conjunction with the conjoint cylindrical wave expansion to realize the field reconstruction-based spatio-temporal channel sounder.

Appendix D: provides greater detail of the custom pseudo-random noise generators used in the SIMO sliding correlator channel sounder.

Appendix E: provides greater detail of the custom frequency synthesizers used in the SIMO sliding correlator channel sounder.

Appendix F: presents the filtered diffraction measurements as a series of channel impulse response snapshots.

CHAPTER II

UTD-STYLE LINEAR MODEL FOR WEDGE DIFFRACTION

Chapter Summary: This chapter reviews the UTD's solution to diffraction by an impedance wedge. A careful study of this analytical solution is used to formulate a simple UTD-style linear model for diffraction by an impedance wedge. The model is evaluated based on its ability to accurately synthesize impedance wedge diffraction solutions and extract semi-empirical diffraction coefficients from total field data.

The primary difficulty with measuring a building's diffraction coefficient is isolating the contributions of the diffracted field near the incident and reflection shadow boundaries (ISB and RSB, respectively). At these boundaries, the incident and reflected fields are *exactly* aligned with the diffracted field in both time and direction of propagation. This makes it impossible to discriminate each field component's contribution using conventional measurement techniques, regardless of the measurement antenna's directivity or the measurement system's temporal resolution. Thereby, no manner of hardware modifications will ever enable direct measurement of the diffracted field. Thus, rather than *measuring* the diffracted field, we consider the alternative problem of *extracting* the diffracted field from total field measurements by way of an appropriate analytical diffraction model.

The key advantage afforded by an analytical diffraction model is the ability to mathematically decompose the model's total field into its constituent field components. Thus, provided that the model may be fit to the total field measurement data,

a semi-empirical representation of the contributing diffracted field and its corresponding diffraction coefficient may be extracted. The UTD's impedance wedge diffraction solution provides one viable mathematical model that is applicable to a wide range of wedge geometries and compositions. However, fitting the UTD impedance wedge model to total field measurements would require the use of a computationally expensive non-linear least-squares solver to determine the wedge faces' surface impedances that yield the best fit. A more flexible and preferrable diffraction model would enable the use of conventional linear least-squares techniques to rapidly fit the model to the total field measurement data. This motivates the development of a linear model for describing diffraction by an impedance wedge.

The remainder of this chapter is organized as follows. Following a brief review of the impedance wedge diffraction problem, the UTD's high-frequency asymptotic solution is discussed in detail. A careful study of the UTD's impedance wedge diffraction coefficient reveals allowable simplifications for the case of identical impedance wedge faces as well as a list of mandatory characteristics for the pattern functions that weight each of the diffraction coefficient's terms. These observations are used to formulate a simple UTD-style linear diffraction model from the UTD's impedance wedge diffraction solution. A thorough validation of this linear diffraction model examines its accuracy for two practical applications: 1) synthesizing total field solutions to wedge diffraction problems and 2) extracting semi-empirical diffraction coefficients from total field data.

2.1 Impedance Wedge Diffraction Problem

For the 2-D *scalar* transverse magnetic (TM) impedance wedge diffraction problem, the UTD describes the total electric field a summation of three field components: the GO's incident field, $E^i(\mathbf{r})$, the GO's reflected field, $E^r(\mathbf{r})$, and the diffracted field, $E^d(\mathbf{r})$. Thereby

$$E^t(\mathbf{r}) = E^i(\mathbf{r}) + E^r(\mathbf{r}) + E^d(\mathbf{r}) \tag{12}$$

where $E^t(\mathbf{r})$ denotes the total field exterior to the diffracting wedge.

Figure 2 defines the geometry of the generic 2-D impedance wedge diffraction problem as well as illustrates the behavior of the field components. Figure 2(a) and 2(b) depict the polar coordinate system used for the wedge diffraction problem. The "0-face" corresponds to 0 radians, the "n-face" corresponds to $n\pi = 2\pi - \Phi$ radians, and the origin coincides with the diffracting edge. We will denote the location of a transmitting source, $\mathbf{Tx}$, as $\mathbf{r}' = (\rho', \phi')$, the observation point as $\mathbf{r} = (\rho, \phi)$, and require that the source and observation points be exterior to the wedge; that is, $\phi \in (0, n\pi)$ and $\phi' \in (0, n\pi)$.

Fig. 2(a) also identifies the wedge faces with surface impedance, Z_s. Under the first-order impedance boundary condition, the surface impedance relates the tangential components of the electric and magnetic field at the wedge face [99]. That is, along a wedge face

$$\hat{\mathbf{n}} \times \mathbf{E} = Z_s \hat{\mathbf{n}} \times (\hat{\mathbf{n}} \times \mathbf{H}) \tag{13}$$

where $\hat{\mathbf{n}}$, is a unit normal vector indicating wedge face's outward facing direction, and $\mathbf{E}$ and $\mathbf{H}$ designate the vector electric and magnetic fields, respectively. For the related problem of a plane wave incident on a homogenous and isotropic half-space with an intrinsic impedance, η, given by

$$\eta = \sqrt{\frac{\mu}{\epsilon}} = \sqrt{\frac{\mu_R \mu_0}{\epsilon_R \epsilon_0}} = \eta_0 \sqrt{\frac{\mu_R}{\epsilon_R}} \tag{14}$$

where $\mu = \mu_R \mu_0$ and $\epsilon = \epsilon_R \epsilon_0$ are the complex permeability and permittivity of the half-space, respectively, η_0 is the free-space characteristic impedance with associated permeability, μ_0, and permittivity, ϵ_0, and μ_R and ϵ_R denote the medium's complex

relative permeability and permittivity, respectively. The surface impedance describing the boundary condition at the interface is simply $Z_s = \eta$ [99]. The first-order boundary condition along the two faces of an infinite, homogenous, and isotropic wedge is described by the same equality whereby the wedge faces' surface impedances are set equal to the wedge's intrinsice impedance.

Figures 2(b) and 2(c) illustrate where the incident, reflected, and diffracted fields contribute to the total field as well as the incident shadow boundary (ISB) and reflection shadow boundary (RSB) that delineate the discontinuities in the GO's field components. Figure 2(c) provides a graphical representation of $E^t(\mathbf{r})$ defined in Eq. (12) and highlights the ray-like behavior of the individual field components.

Figure 3 breaks the total field presented in Fig. 2(c) into its three field components and identifies their regions of existence. As illustrated in the figures, these regions, denoted $\mathcal{I}$, $\mathcal{R}$, and $\mathcal{D}$, identify where the incident, reflected, and diffracted fields exist, respectively. Outside of these regions, the corresponding fields are zero. We note that, though Fig. 3(b) shows reflection from a single wedge face, reflections from both wedge faces is certainly possible. However, without loss of generality, we only consider reflection from a single face to simplify discussion. Finally, we note that throughout this discussion, it is assumed that the electromagnetic field exhibits a time-harmonic dependence of the form $e^{j2\pi ft}$ for some frequency, f.

2.2 UTD Solution to Impedance Wedge Diffraction

For the 2-D *scalar* field problem, the incident field, $E^i(\mathbf{r})$, is given by

$$E^i(\mathbf{r}) = E_0 g(\mathbf{r}, \mathbf{r}') \text{ for } \mathbf{r} \in \mathcal{I} \tag{15}$$

where $g(\mathbf{r}, \mathbf{r}')$ describes the GO's 2-D point excitation as given by

$$g(\mathbf{r}, \mathbf{r}') = \frac{e^{-jk_0\|\mathbf{r}-\mathbf{r}'\|}}{\sqrt{k_0\|\mathbf{r}-\mathbf{r}'\|}} \tag{16}$$

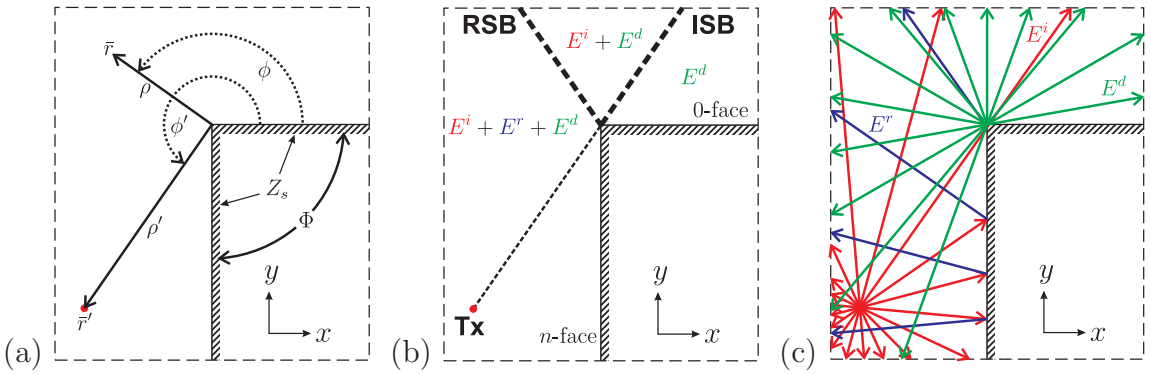

Figure 2: Diagrams of (a) the diffraction geometry's coordinate system, (b) shadow boundaries and wedge face labels, and (c) the ray-like field components contributing to the total field solution.

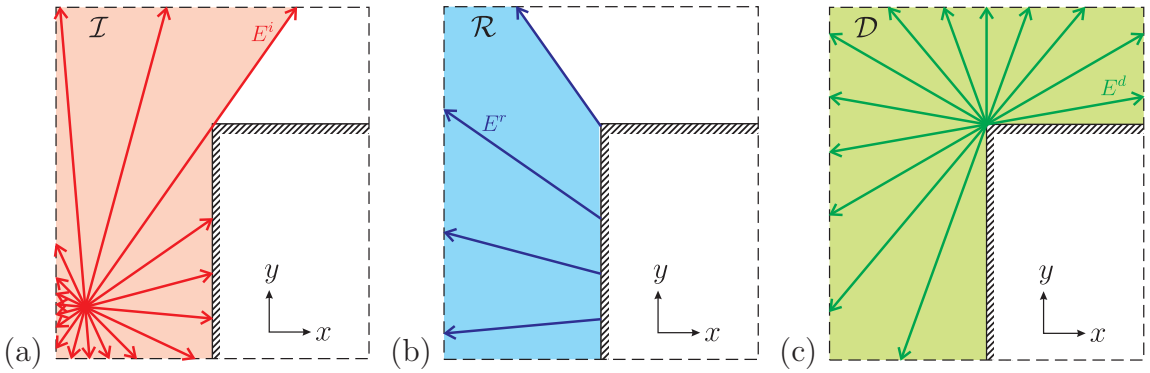

Figure 3: The individual field components contributing to the total field and their corresponding regions of existence: (a) the incident field $E^i(\mathbf{r})$ in $\mathbf{r} \in \mathcal{I}$, (b) the reflected field $E^r(\mathbf{r})$ in $\mathbf{r} \in \mathcal{R}$, and (c) the diffracted field $E^d(\mathbf{r})$ in $\mathbf{r} \in \mathcal{D}$.

where E_0 is the phasor amplitude of the excitation, k_0 is the wavenumber of the time-harmonic field, $\mathbf{r}' = (\rho', \phi')$ is the location of the excitation, and $\mathbf{r} = (\rho, \phi)$ is some observation point exterior to the diffracting wedge. It should be noted that the UTD impedance wedge solution is only applicable for normal incidence with respect to the wedge's diffracting edge.

The reflected field, $E^r(\mathbf{r})$, is given by

$$E^r(\mathbf{r}) = E_0 \Gamma^{\perp}_{\parallel}(\theta) g(\mathbf{r}, \mathbf{r}' - 2[\mathbf{r}' \cdot \hat{\mathbf{n}}]\hat{\mathbf{n}}) \text{ for } \mathbf{r} \in \mathcal{R} \tag{17}$$

where $\hat{\mathbf{n}}$ denotes the outward-facing normal with respect to either wedge face, and $\Gamma^{\perp}_{\parallel}(\theta)$ is the angle- and polarization-dependent reflection coefficient determined from the first-order impedance boundary condition where θ denotes the angle-of-reflection from the wedge face with respect to the unit normal, $\hat{\mathbf{n}}$. For perpendicular polarization, the first-order impedance boundary condition yields a reflection coefficient given by [99]

$$\Gamma^{\perp}(\theta) = -\frac{1 - Z_s/\eta_0 \cos\theta}{1 + Z_s/\eta_0 \cos\theta} \tag{18}$$

For parallel polarization, the reflection coefficient is given by [99]

$$\Gamma^{\parallel}(\theta) = -\frac{1 - \eta_0/Z_s \cos\theta}{1 + \eta_0/Z_s \cos\theta} \tag{19}$$

It should be noted that the reflection coefficients derived using the first-order impedance boundary condition are but approximations to the exact Fresnel reflection coefficients [99].

Equations (18) and (19) may be written as

$$\Gamma^{\perp}_{\parallel}(\theta) = -\frac{1 - \sin\theta^{\perp}_{\parallel} \cos\theta}{1 + \sin\theta^{\perp}_{\parallel} \cos\theta} \tag{20}$$

where

$$\sin\theta^{\perp} = Z_s/\eta_0 \tag{21}$$

$$\sin\theta^{\parallel} = \eta_0/Z_s \tag{22}$$

This alternative notation introduces the *normalized impedance angle*, $\theta^{\perp}_{\parallel}$, which will facilitate later discussion of the UTD's impedance wedge diffraction coefficient.

The diffracted field, $E^d(\mathbf{r})$ in Eq. (12), is given by

$$E^d(\mathbf{r}) = E^i(\mathbf{0})A(\rho)e^{-jk_0\rho}D^{\perp}_{\parallel\,\mathrm{UTD}}(\phi,\phi') \text{ for } \mathbf{r}\in\mathcal{D} \tag{23}$$

where $A(\rho)e^{-jk_0\rho}$ describes the distance-dependent behavior of the diffracted wave with $A(\rho)$ given by

$$A(\rho) = \frac{1}{\sqrt{\rho}} \tag{24}$$

In Eq. (23), $D^{\perp}_{\parallel\,\mathrm{UTD}}(\phi,\phi')$ is the UTD impedance wedge diffraction coefficient given by

$$\begin{aligned} D^{\perp}_{\parallel\,\mathrm{UTD}}(\phi,\phi') = & \\ & C_1(\phi,\phi')D_0^+(\phi-\phi') + C_2(\phi,\phi')D_0^-(\phi-\phi') \\ & +C_3(\phi,\phi')D_0^+(\phi+\phi') + C_4(\phi,\phi')D_0^-(\phi+\phi') \end{aligned} \tag{25}$$

Equation (25) introduces a general purpose UTD-style diffraction function, $D_0^{\pm}(\beta)$, given by

$$D_0^{\pm}(\beta) = -\frac{e^{-j\pi/4}}{2n\sqrt{2\pi k_0}}\cot\left(\frac{\pi-\beta}{2n}\right)F[k_0L(\rho,\rho')a^{\pm}(\beta)] \tag{26}$$

where

$$L(\rho,\rho') = \frac{\rho\rho'}{\rho+\rho'} \tag{27}$$

and $F[x]$ and $a^{\pm}(\beta)$ are UTD-specific functions defined in Eqs. (7) and (8), respectively. Here, we note that though the UTD impedance wedge solution and resulting UTD-style linear model presented in this chapter are for cylindrical wave incidence, they may be adapted to plane or spherical wave incidence by changing the excitation function, $g(\mathbf{r}, \mathbf{r}')$, and appropriately modifying the definitions for $A(\rho)$ and $L(\rho, \rho')$ as discussed in Kouyoumjian and Pathak's original UTD paper [56].

Each of the four angle-dependent pattern functions, $C_{1-4}(\phi, \phi')$, appearing in Eq. (25) compensate for each of the four possible GO field discontinuities at the incident and reflection shadow boundaries:

- $C_1(\phi, \phi')$: 0-face incident shadow boundary
- $C_2(\phi, \phi')$: 0-face reflection shadow boundary
- $C_3(\phi, \phi')$: n-face incident shadow boundary
- $C_4(\phi, \phi')$: n-face reflection shadow boundary

The pattern functions are given by [109]

$$C_1(\phi, \phi') = \Omega(\phi, \phi')A(\phi, -\phi') \tag{28}$$

$$C_2(\phi, \phi') = \Omega(\phi, \phi')A(-\phi, \phi') \tag{29}$$

$$C_3(\phi, \phi') = -\Omega(\phi, \phi')A(\phi, \phi') \tag{30}$$

$$C_4(\phi, \phi') = -\Omega(\phi, \phi')A(-\phi, -\phi') \tag{31}$$

In Eqs. (28)-(31), $\Omega(\phi, \phi')$ is a helper function calculated using

$$\Omega(\phi,\phi') = \frac{M_n\left(\phi,\theta_0^{\perp\!\!\!\parallel},\theta_n^{\perp\!\!\!\parallel},n\right) M_n\left(\phi',\theta_0^{\perp\!\!\!\parallel},\theta_n^{\perp\!\!\!\parallel},n\right)}{4\sin\left(\frac{\phi+\theta_0^{\perp\!\!\!\parallel}}{2n}\right)\sin\left(\frac{n\pi-\phi+\theta_n^{\perp\!\!\!\parallel}}{2n}\right)\sin\left(\frac{\phi'+\theta_0^{\perp\!\!\!\parallel}}{2n}\right)\sin\left(\frac{n\pi-\phi'+\theta_n^{\perp\!\!\!\parallel}}{2n}\right)} \tag{32}$$

where $M_n\left(\phi,\theta_0^{\perp\!\!\!\parallel},\theta_n^{\perp\!\!\!\parallel},n\right)$ is a secondary helper function given by

$$M_n\left(\phi,\theta_0^{\perp\!\!\!\parallel},\theta_n^{\perp\!\!\!\parallel},n\right) = \frac{\psi_n\left(n\pi-\phi-\pi/2-\theta_0^{\perp\!\!\!\parallel}\right)\psi_n\left(\phi-\pi/2-\theta_n^{\perp\!\!\!\parallel}\right)}{\psi_n\left(n\pi-\phi-\pi/2+\theta_0^{\perp\!\!\!\parallel}\right)\psi_n\left(\phi-\pi/2+\theta_n^{\perp\!\!\!\parallel}\right)} \tag{33}$$

and $\psi_n(\alpha)$ is the special Malyuzhinets function [109]. For completeness, we note that the Malyuzhinets function may be expressed in integral form as [122]

$$\psi_n(\alpha) = \exp\left\{-\frac{1}{2}\int_0^\infty \frac{\cosh(\alpha s)-1}{s\cosh(\pi s/2)\sinh(n\pi s)}\,ds\right\} \tag{34}$$

The function $A(\phi,\phi')$ in Eqs. (28)-(31) is given by

$$\begin{aligned} A(\phi,\phi') = & \\ & \left[\cos\left(\frac{\pi-2\theta_0^{\perp\!\!\!\parallel}}{2n}\right)\cos\left(\frac{\pi-2\theta_n^{\perp\!\!\!\parallel}}{2n}\right)-\cos^2\left(\frac{\pi}{2n}\right)\right]-\sin\left(\frac{\phi}{n}\right)\sin\left(\frac{\phi'}{n}\right) \\ & -\frac{1}{2\sin\left(\frac{\pi}{2n}\right)}\left[\sin\left(\frac{\phi}{n}\right)+\sin\left(\frac{\phi'}{n}\right)\right]\left[\cos\left(\frac{\pi-2\theta_0^{\perp\!\!\!\parallel}}{2n}\right)-\cos\left(\frac{\pi-2\theta_n^{\perp\!\!\!\parallel}}{2n}\right)\right] \end{aligned} \tag{35}$$

2.2.1 Simplifications for Identical Impedance Faces

For the special case that the surface impedances of the two wedge faces are identical, $\theta_0^{\perp\!\!\!\parallel} = \theta_n^{\perp\!\!\!\parallel} = \theta^{\perp\!\!\!\parallel}$ and (35) becomes

$$A(\phi,\phi') = \left[\cos^2\left(\frac{\pi-2\theta^{\perp\!\!\!\parallel}}{2n}\right)-\cos^2\left(\frac{\pi}{2n}\right)\right]+\sin\left(\frac{\phi}{n}\right)\sin\left(\frac{\phi'}{n}\right) \tag{36}$$

Thereby, it can be shown that

$$C_1(\phi,\phi') = C_3(\phi,\phi') = C^r(\phi,\phi') \tag{37}$$

$$C_2(\phi,\phi') = C_4(\phi,\phi') = C^r(\phi,\phi') \tag{38}$$

where

$$C^i(\phi,\phi') = \Omega(\phi,\phi')\left\{\left[\cos^2\left(\frac{\pi - 2\theta^{\perp\!\!\!\parallel}}{2n}\right) - \cos^2\left(\frac{\pi}{2n}\right)\right] + \sin\left(\frac{\phi}{n}\right)\sin\left(\frac{\phi'}{n}\right)\right\} \tag{39}$$

$$C^r(\phi,\phi') = \Omega(\phi,\phi')\left\{-\left[\cos^2\left(\frac{\pi - 2\theta^{\perp\!\!\!\parallel}}{2n}\right) - \cos^2\left(\frac{\pi}{2n}\right)\right] + \sin\left(\frac{\phi}{n}\right)\sin\left(\frac{\phi'}{n}\right)\right\} \tag{40}$$

This leads to the following simplified expression for $D^{\perp\!\!\!\parallel}_{\mathrm{UTD}}(\phi,\phi')$:

$$\begin{aligned} D^{\perp\!\!\!\parallel}_{\mathrm{UTD}}(\phi,\phi') = & \\ & C^i(\phi,\phi')\{D_0^+(\phi-\phi') + D_0^+(\phi+\phi')\} \\ & + C^r(\phi,\phi')\{D_0^-(\phi-\phi') + D_0^-(\phi+\phi')\} \end{aligned} \tag{41}$$

In the context of building corner diffraction, it is common for the adjoining walls of a building corner to have the same material composition so as to reduce construction costs and provide a uniform appearance. This suggests that the assumption of identical face impedances is acceptable when modeling a building corner as an impedance wedge. Furthermore, this assumption will allow us to use the simplified diffraction coefficient expression in Eq. (41) in the development of our linear model for wedge diffraction.

2.2.2 Necessary Conditions of Diffraction Coefficient

In [74], Nechayev and Constantinou outlined four key properties of the impedance wedge diffraction coefficient. Here, we show how these properties relate to the angle-dependent pattern functions, $C^i(\phi,\phi')$ and $C^r(\phi,\phi')$, occurring in Equation (41).

2.2.2.1 Total Field Continuity

Exterior to the impedance wedge and away from source singularities, the total field, $E^t(\mathbf{r})$, as defined in Eq. (12) should describe a smooth and continous electric field. Therefore, the diffracted field, $E^d(\mathbf{r})$, must compensate for the discontinuities in the GO's incident and reflected field along the incident and shadow boundaries. Discontinuity compensation is achieved by the product of $D_0^{\pm}(\beta)$ and the pattern functions, $C^i(\phi, \phi')$ and $C^r(\phi, \phi')$, which provide the necessary scaling of the unit discontinuity in $D_0^{\pm}(\beta)$ along the ISB and RSB. This means that $C^i(\phi, \phi')$ must equal unity along the ISB, and $C^r(\phi, \phi')$ must equal the angle-dependent reflection coefficient, $\Gamma^{\perp}_{\parallel}(\theta)$, along the RSB:

- $C^i(\phi, \phi')|_{\text{ISB}} = 1$
- $C^r(\phi, \phi')|_{\text{RSB}} = \Gamma^{\perp}_{\parallel}(\theta)$

Figure 4 illustrates these requirements for $C^i(\phi, \phi')$ and $C^r(\phi, \phi')$. The gray box contains all possible angles of incidence, ϕ', and observation, ϕ, for a wedge whose exterior angle is $n\pi$. The solid red line delineates the ISB where $C^i(\phi, \phi')$ must equal one; the dashed blue line, the RSB where $C^r(\phi, \phi')$ must equal the reflection coefficient, $\Gamma^{\perp}_{\parallel}(\theta)$. Specifically, for reflections off of the 0-face:

$$C^r(\pi/2 + \theta, \pi/2 - \theta) = \Gamma^{\perp}_{\parallel}(\theta) \tag{42}$$

For reflections off of the n-face:

$$C^r([n - 1/2]\pi + \theta, [n - 1/2]\pi - \theta) = \Gamma^{\perp}_{\parallel}(\theta) \tag{43}$$

It should be noted that Figure 4 is to scale for $n = 3/2$. For an arbitrary wedge angle, the midpoints of the upper and lower RSB lines depicted in Fig. 4 are $([n - \frac{1}{2}]\pi, [n - \frac{1}{2}]\pi)$ and $(\frac{\pi}{2}, \frac{\pi}{2})$, respectively as indicated by Eqs. (42) and (43).

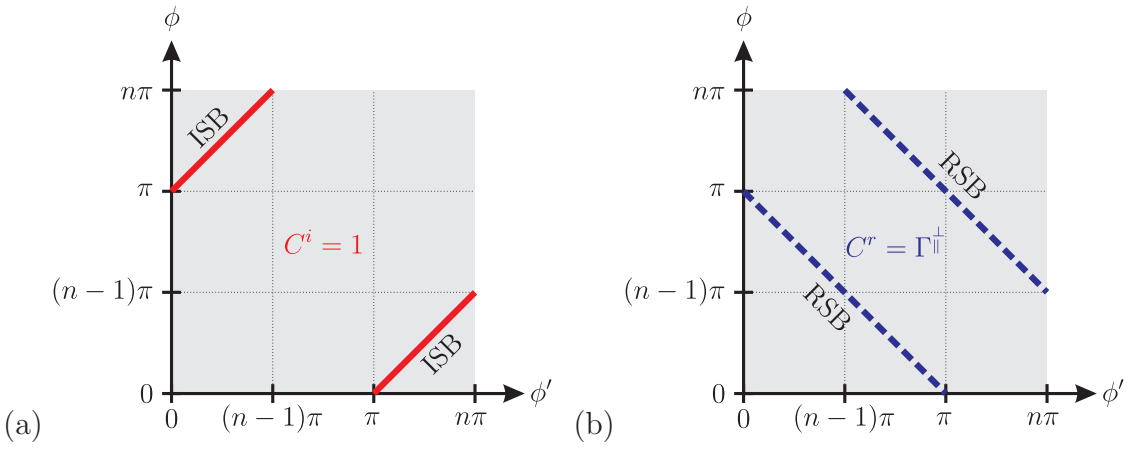

Figure 4: To compensate for the discontinuity in the GO's field, (a) $C^i(\phi, \phi')$ must equal one along the ISB, and (b) $C^r(\phi, \phi')$, must equal the reflection coefficient, $\Gamma^{\perp}_{\parallel}(\theta)$, along the RSB.

2.2.2.2 Boundary Condition for the First-Order Diffraction Coefficient

Excluding the special case of parallel incidence and PEC wedge faces, the first-order impedance wedge diffraction coefficient must vanish along the wedge face:

- $C^i(\phi, \phi') + C^r(\phi, \phi') = 0$ for $\phi, \phi' = \{0, n\pi\}$

2.2.2.3 Reciprocity

The diffracted field must be reciprocal such that interchanging the locations of the source and observation points does not change the result. For the pattern functions, this implies symmetry about the line $\phi = \phi'$:

- $C^i(\phi, \phi') = C^i(\phi', \phi)$
- $C^r(\phi, \phi') = C^r(\phi', \phi)$

2.2.2.4 Symmetry

The coefficient should not depend on which wedge face is defined as the 0- or n-face nor should it depend upon the direction in which ϕ and ϕ' are defined. This implies symmetry about the line $\phi = n\pi - \phi'$:

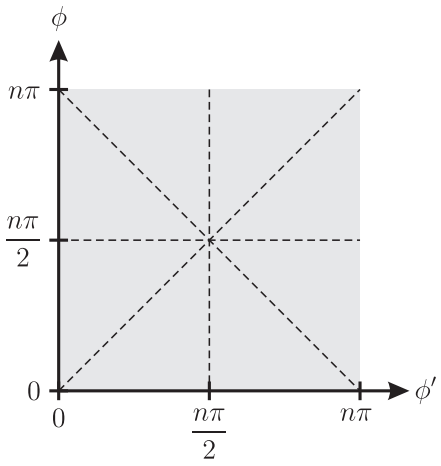

Figure 5: The pattern functions $C^i(\phi, \phi')$ and $C^r(\phi, \phi')$ must exhibit symmetry about $\phi = n\pi/2$, $\phi' = n\pi/2$, $\phi = \phi'$, and $\phi = n\pi - \phi'$.

- $C^i(\phi, \phi') = C^i(n\pi - \phi', n\pi - \phi)$
- $C^r(\phi, \phi') = C^r(n\pi - \phi', n\pi - \phi)$

Additionally, because we are restricting our analysis to wedges with identical impedance faces, the pattern functions must be symmetric about $\phi = n\pi/2$ and $\phi' = n\pi/2$:

- $C^i(\phi, \phi') = C^i(n\pi/2 - \phi, \phi) = C^i(\phi, n\pi/2 - \phi')$
- $C^r(\phi, \phi') = C^r(n\pi/2 - \phi, \phi) = C^r(\phi, n\pi/2 - \phi')$

Figure 5 illustrates the lines of symmetry required by the reciprocity and symmetry relationships. Figure 6 summarizes implications of the field continuity, reciprocity, and symmetry relationships.

2.3 UTD-Style Linear Model for Wedge Diffraction

Starting from the UTD solution to diffraction by an impedance wedge, this section develops the UTD-style linear model for wedge diffraction. Development begins by isolating the material-dependent functions within the impedance wedge diffraction coefficient so as to realize a general purpose UTD-style solution to wedge diffraction. By approximating these nonlinear material-dependent functions with appropriate linear

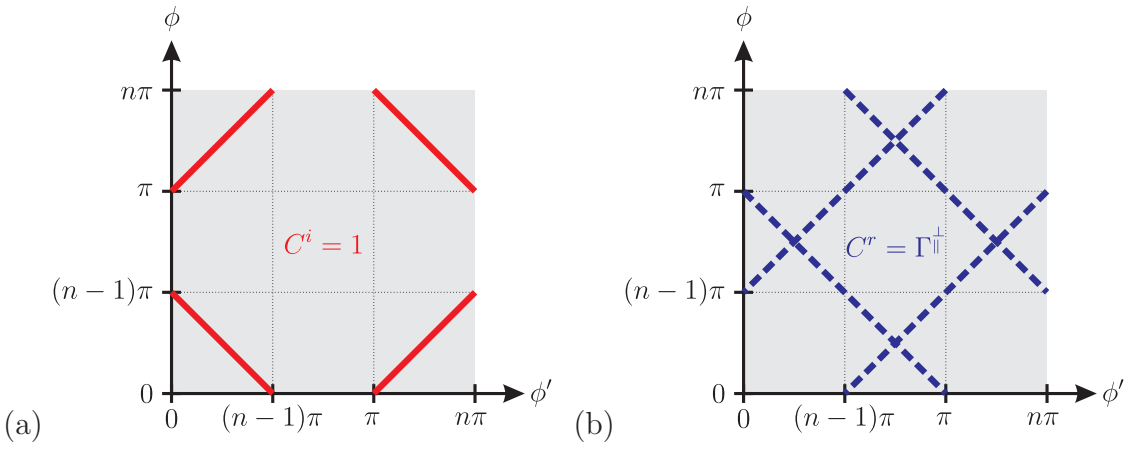

Figure 6: By symmetry, (a) $C^i(\phi, \phi')$ must equal one along th solid red lines, and (b) $C^r(\phi, \phi')$, must equal the reflection coefficient, $\Gamma^{\perp}_{\parallel}(\theta)$, along the dashed blue lines.

equations, the general purpose UTD-style solution to wedge diffraction is transformed into an efficient linear model for wedge diffraction.

2.3.1 A General UTD-Style Diffraction Coefficient

It will prove convenient to express the general UTD wedge diffraction coefficient as a correction to the PEC wedge diffraction coefficient that accounts for the non-PEC impedance faces. Therefore, we rewrite Eq. (41) as

$$\begin{aligned} D^{\perp}_{\parallel\,\mathrm{UTD}}(\phi, \phi') = & \\ & \{D_0^+(\phi - \phi') + D_0^+(\phi + \phi')\} - \{D_0^-(\phi - \phi') + D_0^-(\phi + \phi')\} \\ & + \left[C^i(\phi, \phi') - 1\right] \{D_0^+(\phi - \phi') + D_0^+(\phi + \phi')\} \\ & + \left[C^r(\phi, \phi') + 1\right] \{D_0^-(\phi - \phi') + D_0^-(\phi + \phi')\} \end{aligned} \tag{44}$$

and collect the first two terms, which correspond to the PEC wedge diffraction coefficient for perpendicular incidence, denoted $D^{\perp}_{\mathrm{PEC}}(\phi, \phi')$:

$$D^{\perp}_{\mathrm{PEC}}(\phi, \phi') = \{D_0^+(\phi - \phi') + D_0^+(\phi + \phi')\} - \{D_0^-(\phi - \phi') + D_0^-(\phi + \phi')\} \tag{45}$$

Thereby, Eq. (44) becomes

$$
\begin{aligned}
D_{\mathrm{UTD}}^{\perp_{\parallel}}(\phi,\phi') &= D_{\mathrm{PEC}}^{\perp}(\phi,\phi') \\
&+ \left[C^r(\phi,\phi')+1\right]\left\{D_0^-(\phi-\phi')+D_0^-(\phi+\phi')\right\} \\
&+ \left[C^i(\phi,\phi')-1\right]\left\{D_0^+(\phi-\phi')+D_0^+(\phi+\phi')\right\}
\end{aligned}
\tag{46}
$$

The choice of $D_{\mathrm{PEC}}^{\perp}(\phi,\phi')$ in Eq. (44) rather than $D_{\mathrm{PEC}}^{\parallel}(\phi,\phi')$ becomes clear when we divide Eq. (39) by (40) and solve for $C^r(\phi,\phi')$:

$$
C^r(\phi,\phi') = C^i(\phi,\phi')\frac{\sin\left(\frac{\phi}{n}\right)\sin\left(\frac{\phi'}{n}\right) - \left[\cos^2\left(\frac{\pi-2\theta^{\perp_{\parallel}}}{2n}\right) - \cos^2\left(\frac{\pi}{2n}\right)\right]}{\sin\left(\frac{\phi}{n}\right)\sin\left(\frac{\phi'}{n}\right) + \left[\cos^2\left(\frac{\pi-2\theta^{\perp_{\parallel}}}{2n}\right) - \cos^2\left(\frac{\pi}{2n}\right)\right]}
\tag{47}
$$

Equation (47) enforces the first-order boundary condition for the impedance wedge diffraction coefficient. Along the face of the wedge ($\phi,\phi' = \{0, n\pi\}$), $C^r(\phi,\phi') = -C^i(\phi,\phi')$ provided that $\theta^{\perp_{\parallel}} \neq 0$. For the special case of $\theta^{\perp_{\parallel}} = 0$, which corresponds to parallel incidence on a PEC wedge, $C^r(\phi,\phi') = C^i(\phi,\phi') = 1$ on the wedge faces, and the diffraction coefficient describes a surface wave propagating along the wedge faces. Otherwise, $C^r(\phi,\phi') = -C^i(\phi,\phi') = -1$ along the wedge faces, indicating that no surface wave can propagate along the wedge faces. We therefore consider parallel incidence on a PEC wedge as a special case beyond the scope of our linear diffraction model. This also makes it convenient to use $[C^r(\phi,\phi')+1]$ and thereby, $D_{\mathrm{PEC}}^{\perp_{\parallel}}(\phi,\phi')$ in Eq. (46).

With a few algebraic manipulations and the introduction of a helper function, $\chi(\phi,\phi')$ given by

$$
\chi(\phi,\phi') = \frac{\sin\left(\frac{\phi}{n}\right)\sin\left(\frac{\phi'}{n}\right)}{\left[\cos^2\left(\frac{\pi-2\theta^{\perp_{\parallel}}}{2n}\right) - \cos^2\left(\frac{\pi}{2n}\right)\right] + \sin\left(\frac{\phi}{n}\right)\sin\left(\frac{\phi'}{n}\right)}
\tag{48}
$$

Equation (47) may be alternatively written as

$$C^r(\phi,\phi') = -C^i(\phi,\phi')\left\{1-2\chi(\phi,\phi')\right\} \tag{49}$$

Recalling that $C^i(\phi,\phi')$ must equal one along the ISB (and other lines indicated in Fig. 6(a)), we define a new function $C(\phi,\phi')$ such that

$$C^i(\phi,\phi') - 1 = C(\phi,\phi') \tag{50}$$

Thereby, $C(\phi,\phi')$ is necessarily zero along the ISB. Using Eq. (50), (49) may be rewritten as

$$C^r(\phi,\phi') = -[1+C(\phi,\phi')][1-2\chi(\phi,\phi')] \tag{51}$$

Adding one to both sides yields

$$C^r(\phi,\phi') + 1 = -C(\phi,\phi') + 2\chi(\phi,\phi') + 2C(\phi,\phi')\chi(\phi,\phi') \tag{52}$$

Substituting Eqs. (50) and (52) into (46) yields

$$\begin{aligned} D^{\perp}_{\parallel\,\mathrm{UTD}}(\phi,\phi') &= D^{\perp}_{\mathrm{PEC}}(\phi,\phi') \\ &+C(\phi,\phi')D^{\perp}_{\mathrm{PEC}}(\phi,\phi') \\ &+2\chi(\phi,\phi')\{D_0^-(\phi-\phi') + D_0^-(\phi+\phi')\} \\ &+2C(\phi,\phi')\chi(\phi,\phi')\{D_0^-(\phi-\phi') + D_0^-(\phi+\phi')\} \end{aligned} \tag{53}$$

2.3.2 A General UTD-Style Total Field Solution

We now modify the individual field components in Eq. (12) to be consistent with the general diffraction coefficient given in Eq. (53).

2.3.2.1 Incident Field

None of our analysis affects the GO incident field, $E^i(\mathbf{r})$, described in Eq. (15). Thus, Eq. (15) describes the correct incident field for *any* impedance wedge diffraction problem regardless of the material properties of the wedge. In particular, we note that

$$E^{i,\perp}_{\mathrm{PEC}}(\mathbf{r}) = E^i(\mathbf{r}) \text{ for } \mathbf{r} \in \mathcal{I} \tag{54}$$

where $E^{i,\perp}_{\mathrm{PEC}}(\mathbf{r})$ denotes the incident scalar field for the case of perpendicular polarization and a PEC wedge. Eq. (54) will be used later when we discuss the general total field solution for the impedance wedge.

2.3.2.2 Reflected Field

Equation (53) expresses the diffraction coefficient as the summation of the perpendicular incidence PEC wedge diffraction coefficient plus additive correction terms. Similarly, we rewrite the first-order impedance reflection coefficient, $\Gamma^{\perp}_{\parallel}(\theta)$, as the perpendicular incidence PEC reflection coefficient plus correction terms. Making use of Eq. (52) as well the relationship between $\Gamma^{\perp}_{\parallel}(\theta)$ and $C^r(\phi, \phi')$ described in Eqs. (42) and (43) yields

$$\Gamma^{\perp}_{\parallel}(\theta) = -\left\{1 + C(\theta) - 2\chi(\theta) - 2C(\theta)\chi(\theta)\right\} \tag{55}$$

where the angle of reflection, θ, for $C(\theta)$ and $\chi(\theta)$ may be determined from (42) and (43) for 0-face and n-face reflection, respectively. Combining Eq. (55) with $E^r(\mathbf{r})$ given in Eq. (17) yields

$$E^r(\mathbf{r}) = \left\{1 + C(\theta) - 2\chi(\theta) - 2C(\theta)\chi(\theta)\right\} E^{r,\perp}_{\mathrm{PEC}}(\mathbf{r}) \text{ for } \mathbf{r} \in \mathcal{R} \tag{56}$$

where $E^{r,\perp}_{\mathrm{PEC}}(\mathbf{r})$ describes the GO's reflected field for a perpendicularly polarized incident field and a PEC wedge as given by

$$E^{r,\perp}_{\text{PEC}}(\mathbf{r}) = -E_0 g(\mathbf{r}, \mathbf{r}' - 2[\mathbf{r}' \cdot \hat{\mathbf{n}}]\hat{\mathbf{n}}) \text{ for } \mathbf{r} \in \mathcal{R} \tag{57}$$

for some wedge face normal, $\hat{\mathbf{n}}$. Thus, Eq. (56) describes the reflected field as summation of the perpendicular polarization PEC wedge solution plus additive correction terms that account for the actual reflection coefficient at the faces of the impedance wedge.

2.3.2.3 Diffracted Field

The general diffracted field has a formulation similar to the reflected field. Combining Eqs. (23) and (53) yields

$$\begin{aligned} E^d(\mathbf{r}) = {} & E^{d,\perp}_{\text{PEC}}(\mathbf{r}) \\ & + C(\phi, \phi') E^{d,\perp}_{\text{PEC}}(\mathbf{r}) \\ & + 2\chi(\phi, \phi') E^i(\mathbf{0}) A(\rho) e^{-jk_0\rho} \{D_0^-(\phi - \phi') + D_0^-(\phi + \phi')\} \\ & + 2C(\phi, \phi')\chi(\phi, \phi') E^i(\mathbf{0}) A(\rho) e^{-jk_0\rho} \{D_0^-(\phi - \phi') + D_0^-(\phi + \phi')\} \\ & \text{for } \mathbf{r} \in \mathcal{D} \end{aligned} \tag{58}$$

where $E^{d,\perp}_{\text{PEC}}(\mathbf{r})$ likewise describes the UTD diffracted field due to a perpendicularly polarized incident field and a PEC wedge as given by

$$E^{d,\perp}_{\text{PEC}} = E^{i,\perp}(\mathbf{0}) A(\rho) e^{-jk_0\rho} D^{\perp}_{\text{PEC}}(\phi, \phi') \text{ for } \mathbf{r} \in \mathcal{D} \tag{59}$$

2.3.2.4 Total Field

Combining Eqs. (12), (15), (56), and (58), we find that the general total field solution for the impedance problem may be expressed as

$$
\begin{aligned}
E^t(\mathbf{r}) = {} & E^{t,\perp}_{\mathrm{PEC}}(\mathbf{r}) \\
& + C(\theta) E^{r,\perp}_{\mathrm{PEC}}(\mathbf{r}) + C(\phi,\phi') E^{d,\perp}_{\mathrm{PEC}}(\mathbf{r}) \\
& - 2\chi(\theta) E^{r,\perp}_{\mathrm{PEC}}(\mathbf{r}) \\
& + 2\chi(\phi,\phi') E^i(\mathbf{0}) A(\rho) e^{-jk_0\rho} \{ D_0^-(\phi-\phi') + D_0^-(\phi+\phi', k_0, \rho, n) \} \\
& - 2C(\theta)\chi(\theta) E^{r,\perp}_{\mathrm{PEC}}(\mathbf{r}) \\
& + 2C(\phi,\phi')\chi(\phi,\phi') E^i(\mathbf{0}) A(\rho) e^{-jk_0\rho} \{ D_0^-(\phi-\phi') + D_0^-(\phi+\phi') \}
\end{aligned}
\tag{60}
$$

where $E^{t,\perp}_{\mathrm{PEC}}(\mathbf{r})$ is the UTD's total field solution for a perpendicularly polarized incident field and a PEC wedge:

$$
E^{t,\perp}_{\mathrm{PEC}}(\mathbf{r}) = E^{i,\perp}_{\mathrm{PEC}}(\mathbf{r}) + E^{r,\perp}_{\mathrm{PEC}}(\mathbf{r}) + E^{d,\perp}_{\mathrm{PEC}}(\mathbf{r}) \tag{61}
$$

2.3.3 Approximation to Material-Dependent Functions

There are two unknown functions in Eq. (53): $C(\phi,\phi')$ and $\chi(\phi,\phi')$. Both of these functions depend on the surface impedance of the wedge and are not amenable to further simplification. Therefore, to develop a general linear diffraction model, we approximate $C(\phi,\phi')$ and $\chi(\phi,\phi')$ by two simple functions with unknown coefficients.

2.3.3.1 Approximation to $C(\phi,\phi')$

$C(\phi,\phi')$ must be zero along the lines illustrated in Fig. 6(a) where $C^i(\phi,\phi') = 1$ and exhibit mirror symmetry about the lines indicated in Fig. 5. Thus, a heuristic approximation to $C(\phi,\phi',n)$ is given by

$$
C(\phi,\phi') \approx a_1 \tilde{C}(\phi,\phi') \tag{62}
$$

where a_1 is some to-be-determined complex coefficient and $\tilde{C}(\phi,\phi')$ is the following heuristically determined function:

$$\tilde{C}(\phi,\phi') = \frac{1}{(n\pi)^4}(\phi+\phi'-[n-1]\pi)(\phi+\phi'-[n+1]\pi)(\phi-\phi'+\pi)(\phi-\phi'-\pi) \quad (63)$$

Equation. (62) provides the symmetry and zero crossings required by $C(\phi,\phi')$. The fractional scalar in Eq. (63) normalizes $\tilde{C}(\phi,\phi')$ to unity at $\phi=\phi'=n\pi/2$.

2.3.3.2 Approximation to $\chi(\phi,\phi')$

To facilitate our development of the approximation to $\chi(\phi,\phi')$, we will make two practical assumptions. First, it shall be assumed that the surface impedance, Z_s, of the wedge faces is equal to the wedge's intrinsic impedance, η, as defined in Eq. (14). As previously noted, this is the typical approach to specifying the surface impedances of the wedge faces provided that wedge's material properties are known. The second assumption is that the wedge is nonmagnetic, whereby its relative permeability is $\mu_R = 1$. This is a reasonable assumption for the majority of radio frequency diffraction problems, because at high frequencies the permeability (i.e., magnetic behavior) of conventional magnetic materials like iron tends to be smaller than the material's permittivity (i.e., dielectric behavior) [119, 116].

Examining Eq. (48), it may be seen that the material-dependent function, $\chi(\phi,\phi')$, must also exhibit the mirror symmetries depicted in Fig. 5. Furthermore, $\chi(\phi,\phi')$ has the following asymptotic behavior for small and large magnitudes of the bracketed term in Eq. (48):

$$\chi(\phi,\phi') \sim 1 \text{ for } \left|\cos^2\left(\frac{\pi-2\theta^{\perp}_{\parallel}}{2n}\right)-\cos^2\left(\frac{\pi}{2n}\right)\right| \ll 1 \quad (64)$$

$$\chi(\phi,\phi') \sim \frac{\sin\left(\frac{\phi}{n}\right)\sin\left(\frac{\phi'}{n}\right)}{\cos^2\left(\frac{\pi-2\theta^{\perp}_{\parallel}}{2n}\right)-\cos^2\left(\frac{\pi}{2n}\right)} \text{ for } \left|\cos^2\left(\frac{\pi-2\theta^{\perp}_{\parallel}}{2n}\right)-\cos^2\left(\frac{\pi}{2n}\right)\right| \gg 1 \quad (65)$$

The small magnitude case described by Eq. (64) is applicable when $|\theta^{\perp}_{\parallel}| \ll \frac{\pi}{2n}$, whereas the large magnitude case described by Eq. (65) is applicable when $|\theta^{\perp}_{\parallel}| \gg \frac{\pi}{2n}$. By

examining the normalized impedance angles defined in Eqs. (21) and (22), it may be shown that $|\theta^{\perp}_{\parallel}| \ll \frac{\pi}{2n}$ and $|\theta^{\perp}_{\parallel}| \gg \frac{\pi}{2n}$ correspond to the cases of parallel and perpendicular polarization, respectively, for a wedge with a relative permittivity such that $|\epsilon_R| \gg 1$ (and assuming that $\mu_R = 1$). This suggests that the approximation to $\chi(\phi, \phi')$ should be a polarization-dependent function capable of behaving like Eq. (64) for parallel polarization and Eq. (65) for perpendicular polarization.

However, in our development of the general UTD-style diffraction coefficient, $\theta^{\perp}_{\parallel} = 0$ was excluded, because it was the only case that allowed for a surface wave propagating along the wedge faces. For all other cases $\chi(\phi, \phi') = 0$ along the wedge faces, though as Eq. (64) suggests, if $|\theta^{\perp}_{\parallel}| \ll \frac{\pi}{2n}$ then $\chi(\phi, \phi')$ will rapidly approach unity at small angles relative to the wedge faces. To account for this behavior we opt for the following polarization-dependent heuristic approximation:

$$\chi(\phi, \phi') \approx a_2 \tilde{\chi}^{\perp}_{\parallel}(\phi, \phi') \tag{66}$$

where

$$\tilde{\chi}^{\perp}_{\parallel}(\phi, \phi') = \begin{cases} \sin\left(\frac{\phi}{n}\right)\sin\left(\frac{\phi'}{n}\right) & \text{for} \quad \perp \text{ polarization} \\ \sqrt{\sin\left(\frac{\phi}{n}\right)\sin\left(\frac{\phi'}{n}\right)} & \text{for} \quad \parallel \text{ polarization} \end{cases} \tag{67}$$

The case of perpendicular polarization follows from Eq. (65). Parallel polarization is effectively a modification of the perpendicular polarization case wherein the square-root causes $\tilde{\chi}^{\perp}_{\parallel}(\phi, \phi')$ to more rapidly approach its maximum value for small angles relative to the wedge faces. Like a_1 in Eq. (62), a_2 in Eq. (66) is some to-be-determined complex coefficient.

2.3.4 Diffraction Coefficient Linear Model

Substituting the approximations for $C(\phi, \phi')$ and $\chi(\phi, \phi')$ from (62) and (66) into the diffraction coefficient in Eq. (53) yields the desired angle- and polarization-dependent diffraction coefficient model, denoted $\tilde{D}^{\perp}_{\parallel\,\mathrm{UTD}}(\phi, \phi')$:

$$\begin{aligned}\tilde{D}^{\perp}_{\mathrm{UTD}}(\phi,\phi') &= D^{\perp}_{\mathrm{PEC}}(\phi,\phi') \\ &+a_1\tilde{C}(\phi,\phi')D^{\perp}_{\mathrm{PEC}}(\phi,\phi') \\ &+a_2 2\tilde{\chi}^{\perp}(\phi,\phi')\{D_0^-(\phi-\phi')+D_0^-(\phi+\phi')\} \\ &+a_3 2\tilde{C}(\phi,\phi')\tilde{\chi}^{\perp}(\phi,\phi')\{D_0^-(\phi-\phi')+D_0^-(\phi+\phi')\}\end{aligned} \tag{68}$$

The coefficient a_3 preceeding the fourth term in Eq. (68) arises from the product of $C(\phi,\phi')$ and $\chi(\phi,\phi')$. Nominally $a_3 = a_1 a_2$, though this may be difficult to enforce in practice.

2.3.5 Total Field Linear Model

Substituting the approximations for $C(\phi,\phi')$ and $\chi(\phi,\phi')$ from (62) and (66) into the total field solution in Eq. (60) yields the related model for the total field due to diffraction by an impedance wedge, denoted $\tilde{E}^t(\mathbf{r})$:

$$\begin{aligned}\tilde{E}^t(\mathbf{r}) &= E^{t,\perp}_{\mathrm{PEC}}(\mathbf{r}) \\ &+a_1\left[\,\tilde{C}(\theta)E^{r,\perp}_{\mathrm{PEC}}(\mathbf{r})+\tilde{C}(\phi,\phi',n)E^{d,\perp}_{\mathrm{PEC}}(\mathbf{r})\,\right] \\ &-a_2\left[\,2\tilde{\chi}^{\perp}(\theta)E^{r,\perp}_{\mathrm{PEC}}(\mathbf{r})\right. \\ &\left.+2\tilde{\chi}(\phi,\phi')E^i(\mathbf{0})A(\rho)e^{-jk_0\rho}\{D_0^-(\phi-\phi')+D_0^-(\phi+\phi')\}\,\right] \\ &-a_3\left[\,2\tilde{C}(\theta)\tilde{\chi}^{\perp}(\theta)E^{r,\perp}_{\mathrm{PEC}}(\mathbf{r})\right. \\ &\left.+2\tilde{C}(\phi,\phi')\tilde{\chi}^{\perp}(\phi,\phi')E^i(\mathbf{0})A(\rho)e^{-jk_0\rho}\{D_0^-(\phi-\phi')+D_0^-(\phi+\phi')\}\,\right]\end{aligned} \tag{69}$$

A subtle but important aspect of Eq. (74) is that the corresponding PEC field components $E^{i,\perp}_{\mathrm{PEC}}(\mathbf{r})$, $E^{r,\perp}_{\mathrm{PEC}}(\mathbf{r})$, $E^{d,\perp}_{\mathrm{PEC}}(\mathbf{r})$, and $E^{t,\perp}_{\mathrm{PEC}}(\mathbf{r})$ are implicitly scaled by the source's phasor amplitude, E_0. Thus, unless E_0 is known, there are actually four coefficients in the model. To make this more explicit, we introduce the following *normalized* PEC field components:

$$\hat{E}^{i,\perp}_{\mathrm{PEC}}(\mathbf{r}) = \frac{E^{i,\perp}_{\mathrm{PEC}}(\mathbf{r})}{E_0} \tag{70}$$

$$\hat{E}^{r,\perp}_{\mathrm{PEC}}(\mathbf{r}) = \frac{E^{r,\perp}_{\mathrm{PEC}}(\mathbf{r})}{E_0} \tag{71}$$

$$\hat{E}^{d,\perp}_{\mathrm{PEC}}(\mathbf{r}) = \frac{E^{d,\perp}_{\mathrm{PEC}}(\mathbf{r})}{E_0} \tag{72}$$

$$\hat{E}^{t,\perp}_{\mathrm{PEC}}(\mathbf{r}) = \frac{E^{t,\perp}_{\mathrm{PEC}}(\mathbf{r})}{E_0} \tag{73}$$

Then, Eq. (69) may be written as

$$\begin{aligned}
\tilde{E}^t(\mathbf{r}) &= (E_0)\hat{E}^{t,\perp}_{\mathrm{PEC}}(\mathbf{r}) \\
&+(a_1E_0)\left[\,\tilde{C}(\theta)\hat{E}^{r,\perp}_{\mathrm{PEC}}(\mathbf{r}) + \tilde{C}(\phi,\phi')\hat{E}^{d,\perp}_{\mathrm{PEC}}(\mathbf{r})\,\right] \\
&-(a_2E_0)\left[\,2\tilde{\chi}^{\perp}_{\parallel}(\theta)\hat{E}^{r,\perp}_{\mathrm{PEC}}(\mathbf{r})\right. \\
&\left.+2\tilde{\chi}^{\perp}_{\parallel}(\phi,\phi')\hat{E}^{i}(\mathbf{0})A(\rho)e^{-jk_0\rho}\{D_0^-(\phi-\phi') + D_0^-(\phi+\phi')\}\,\right] \\
&-(a_3E_0)\left[\,2\tilde{C}(\theta)\tilde{\chi}^{\perp}_{\parallel}(\theta)\hat{E}^{r,\perp}_{\mathrm{PEC}}(\mathbf{r})\right. \\
&\left.+2\tilde{C}(\phi,\phi')\tilde{\chi}^{\perp}_{\parallel}(\phi,\phi')\hat{E}^{i}(\mathbf{0})A(\rho)e^{-jk_0\rho}\{D_0^-(\phi-\phi') + D_0^-(\phi+\phi')\}\,\right]
\end{aligned} \tag{74}$$

whereby the four unknown coefficients of the linear model are explicit: E_0, a_1E_0, a_2E_0, and a_3E_0. Once these coefficients are determined, the coefficients for the diffraction coefficient model in Eq. (68) may be found by dividing Eq. (74)'s coefficients by the excitation phasor E_0.

2.3.6 Summary of Linear Model Assumptions

The following lists the assumptions used to develop the linear diffraction model from the UTD's impedance wedge diffraction solution:

1. The wedge faces are characterized by identical surface impedances.

2. No surface wave propagates along either wedge face.

3. $C(\phi, \phi') \propto \tilde{C}(\phi, \phi')$

4. $\chi(\phi, \phi') \propto \tilde{\chi}^{\perp_{\parallel}}(\phi, \phi')$

The first assumption was used to simplify the UTD's impedance wedge solution. The second assumption allowed the UTD impedance wedge solution to be formulated as an additive correction to diffraction of a perpendicularly polarized field by a PEC wedge, though it explicitly excluded the case of a PEC wedge for parallel polarization. The third and fourth assumptions were used to convert the nonlinear impedance wedge diffraction solution into a flexible linear model. The accuracy of the model is strongly dependent upon the validity of the last two assumptions. This will be considered in more detail in the following section.

2.4 Model Validation

There are two applications for the UTD-style linear model that suggest two different validations. In one application, the diffraction coefficient linear model in Eq. (68) might be used as a replacement for the actual UTD impedance wedge diffraction coefficient, which is computationally expensive due to its dependence on the Malyuzhinets function. Provided a database of material-dependent linear model coefficients, a_{1-3}, for the diffraction coefficient linear model, one could rapidly compute approximate diffraction coefficients for ray-tracer-based propagation prediction engines. In this scenario, one is concerned with the accuracy of the approximations in Eq. (63) and (67). In an alternative application, one is interested in fitting the total field linear model described in Eq. (74) to measurements of the electric field in the vicinity of a diffracting wedge. The linear model's coefficients that provide the best fit for the total field could then be used to extract a semi-empirical diffraction coefficient for the diffracting wedge with no *a priori* knowledge of the wedge's internal structure or material properties.

2.4.1 Approximation Accuracy

The model's accuracy was first evaluated by comparing the actual values of the impedance wedge diffraction coefficient's pattern functions, $C^i(\phi,\phi')$ and $C^r(\phi,\phi')$, to those given by the linear model based on a least-squares fit. The coefficients a_{1-3} that yielded the best fit were determined through the following minimization problem:

$$\min\left\{\left|1+a_1\tilde{C}(\phi,\phi')-C^i(\phi,\phi')\right|^2 + \left|-1-a_1\tilde{C}(\phi,\phi')+a_2 2\hat{\chi}^{\perp}(\phi,\phi')+a_3 2\tilde{\chi}^{\perp}(\phi,\phi')\tilde{C}(\phi,\phi')-C^r(\phi,\phi')\right|^2\right\} \tag{75}$$

The resulting coefficients were then used to construct a best-fit to $[C^i(\phi,\phi')-1]$ and $[C^r(\phi,\phi')+1]$ as defined in Eqs. (50 and (52), respectively. The approximation error was calculated in the form of the normalized mean-squared error, denoted $\widehat{\overline{\varepsilon^2}}_{C^rC^i}$, as given by

$$\widehat{\overline{\varepsilon^2}}_{C^rC^i} = \frac{\left\langle\left|a_1\tilde{C}(\phi,\phi')-[C^i(\phi,\phi')-1]\right|^2\right\rangle_{\phi,\phi'}}{\left\langle\left|C^i(\phi,\phi')-1\right|^2\right\rangle_{\phi,\phi'}} + \frac{\left\langle\left|-a_1\tilde{C}(\phi,\phi')+a_2 2\tilde{\chi}^{\perp}(\phi,\phi')+a_3 2\tilde{\chi}^{\perp}(\phi,\phi')\tilde{C}(\phi,\phi')-[C^r(\phi,\phi')+1]\right|^2\right\rangle_{\phi,\phi'}}{\left\langle\left|[C^r(\phi,\phi')+1]\right|^2\right\rangle_{\phi,\phi'}} \tag{76}$$

where $\langle\rangle_{\phi,\phi'}$ denotes the ensemble average taken over all simulated observation and incident angles, ϕ and ϕ', respectively.

The pattern functions $[C^i(\phi,\phi')-1]$ and $[C^r(\phi,\phi')+1]$ were evaluated for various wedge impedances, polarizations, wedge angles n, observation angles ϕ, and incident angles ϕ'. Symmetry of the functions allowed the problem space to be restricted to $\phi\in(0,n\pi/2)$ and $\phi'\in(0,\phi)$. For the simulations, both ϕ and ϕ' were stepped by $\frac{\pi}{180}$ (i.e., 1°) increments through their allowable ranges. Impedance wedges corresponding to $n=\{5/4,3/2,7/8,2\}$ were considered. This corresponds to the practical and relevant wedge interior angles of $\Phi=\{135°,90°,45°,0°\}$. For $n=2$, the exact solution

to the Malyuzhinets function was used; for other values of n, the combined integral and large-argument approximation described in [45] was used. The relative error in [45]'s approximation was shown to be less than 2.4%. The real and imaginary components of the impedance wedge's relative permittivity were varied along a logarithmic scale through $\mathrm{Re}(\epsilon_R) \in [4, 100]$ and $-\mathrm{Im}(\epsilon_R) \in [0.01, 100]$, respectively. One-hundred values were specified for the real and imaginary components, yielding 10,000 unique complex permittivities.

Figure 7 compares the normalized mean-squared error, $\widehat{\overline{\varepsilon^2}}_{C^iC^r}$ as a function of relative permittivity for all eight combinations of polarization and wedge angle. The normalized mean-squared error is presented in decibels as given by $10\log_{10}\left(\widehat{\overline{\varepsilon^2}}_{C^iC^r}\right)$. Figure 7 indicates that the model provides a very good fit for perpendicular incidence. For parallel incidence, the model performs rather poorly. This is more clearly illustrated by Figure 8(a), which presents cumulative distribution functions (CDF) for the normalized mean-squared error at each of the eight wedge angle and polarization combinations. The CDF curves were compiled from the 10,000 simulated complex permittivities.

The errors presented in Figures 7 and 8(a) are for the pattern functions $C^i(\phi, \phi')$ and $C^r(\phi, \phi')$. The error in the corresponding diffraction coefficient will invariably be less due to the shaping provided by the general purpose diffraction function, $D_0^{\pm}(\beta)$ in Eq. (26). For comparison, Figure 8(b) presents CDF curves for the normalized mean-squared error in the resulting diffraction coefficient. The diffraction coefficient's normalized mean-squared error, denoted $\widehat{\overline{\varepsilon^2}}_D$, is given by

$$\widehat{\overline{\varepsilon^2}}_D = \frac{\left\langle \left| \tilde{D}^{\perp\!\!\!\parallel}_{\mathrm{UTD}}(\phi, \phi') - D^{\perp\!\!\!\parallel}_{\mathrm{UTD}}(\phi, \phi') \right|^2 \right\rangle}{\left\langle \left| D^{\perp\!\!\!\parallel}_{\mathrm{UTD}}(\phi, \phi') \right|^2 \right\rangle} \tag{77}$$

where $D^{\perp\!\!\!\parallel}_{\mathrm{UTD}}(\phi, \phi')$ is the UTD impedance wedge diffraction coefficient and $\tilde{D}^{\perp\!\!\!\parallel}_{\mathrm{UTD}}(\phi, \phi')$

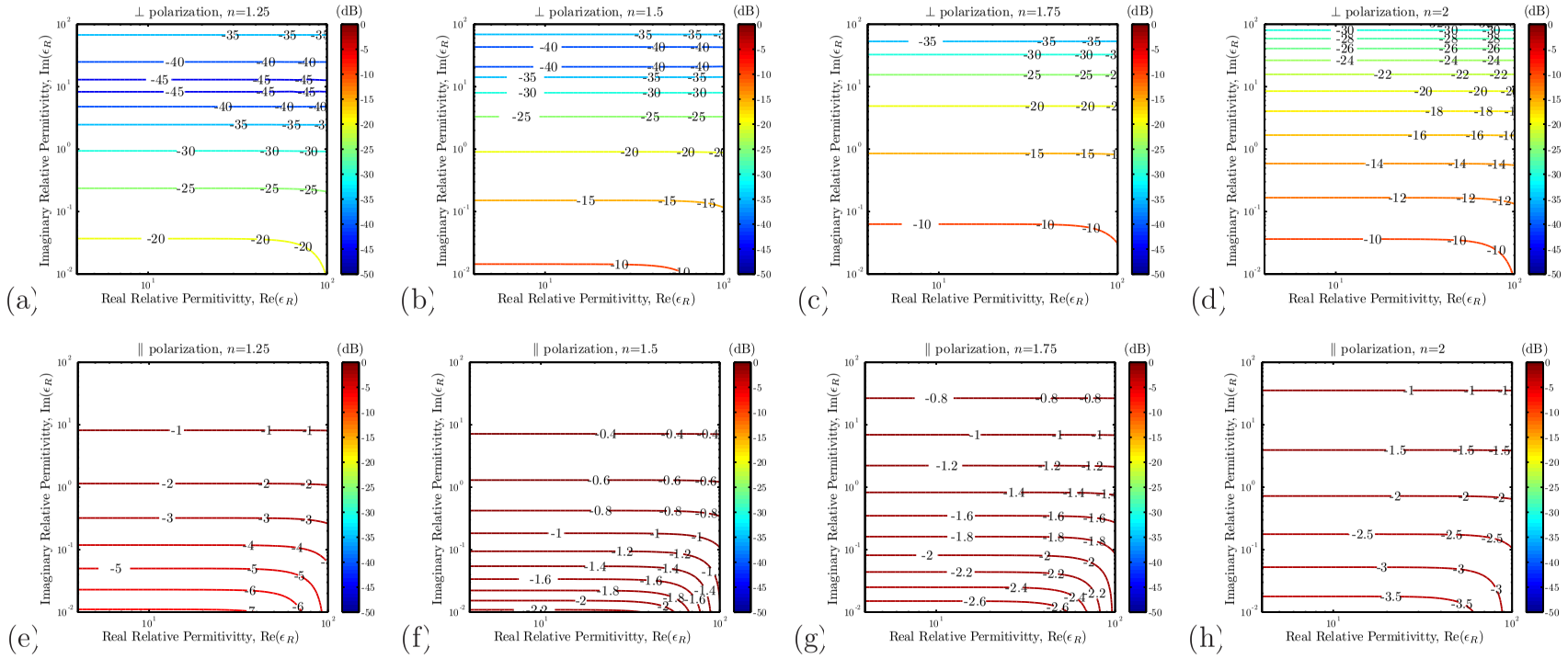

Figure 7: A comparison of the simulated mean-squared error, $\widehat{\overline{\varepsilon^2}}_{C^i C^r}$, as a function of complex relative permittivity, ϵ_R, for eight different combinations of wedge angle and polarization. The linear model's coefficients were determined from a least-squares fit of the pattern functions, $C^i(\phi, \phi')$ and $C^r(\phi, \phi')$: (a) $n = 1.25, \perp$; (b) $n = 1.5, \perp$; (c) $n = 1.75, \perp$; (d) $n = 2, \perp$; (e) $n = 1.25, \parallel$; (f) $n = 1.5, \parallel$; (g) $n = 1.75, \parallel$; (h) $n = 2, \parallel$.

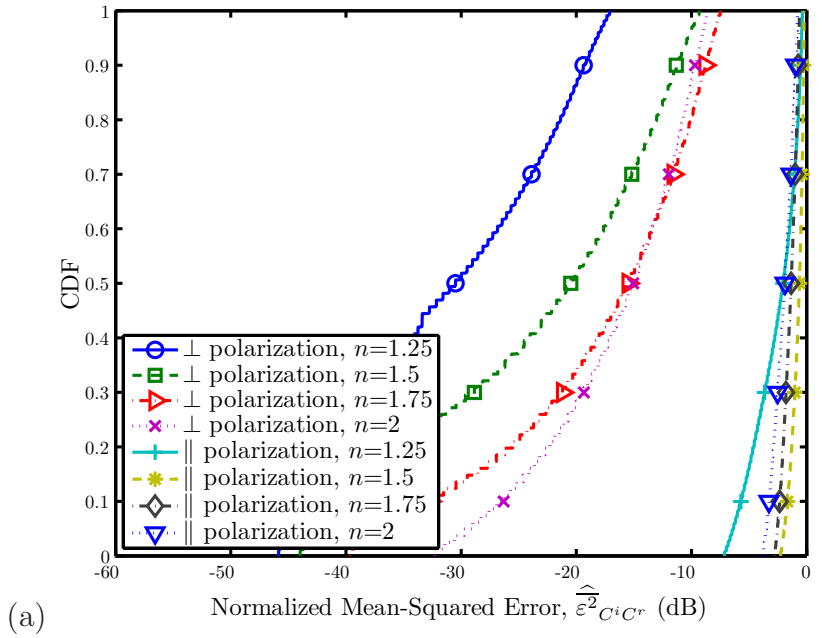

(a)

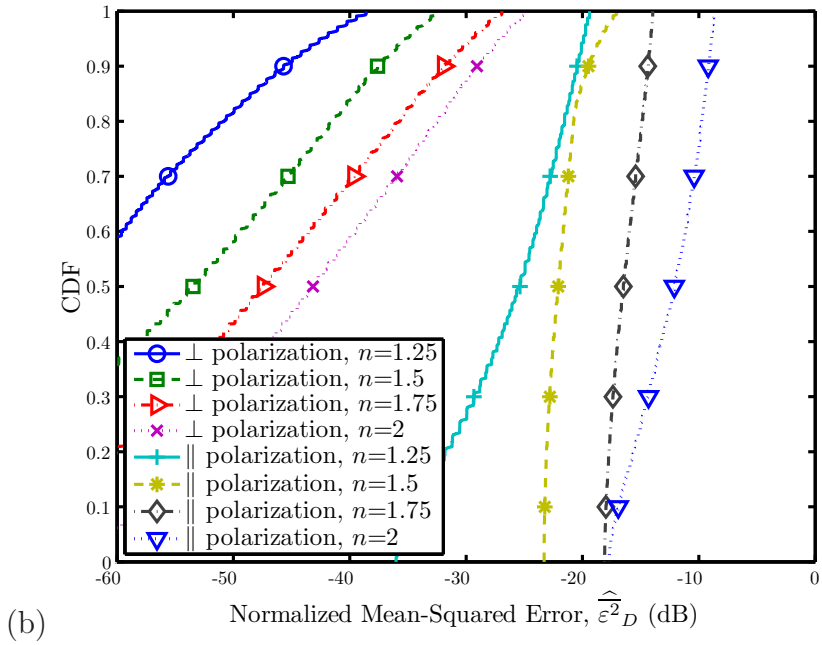

(b)

Figure 8: Cumulative distribution functions (CDF) of the mean-squared error for each of the eight combinations of polarization and wedge angle. The CDF curves were computed from mean-squared errors for a wide range of complex permittivities, ϵ_R, and the model coefficients were determined from a least-squares fit of the pattern functions, $C^i(\phi, \phi')$ and $C^r(\phi, \phi')$: (a) the approximation error, $\widehat{\overline{\varepsilon^2}}_{C^iC^r}$, and (b) the diffraction coefficient error, $\widehat{\overline{\varepsilon^2}}_D$.

is the semi-empirical diffraction coefficient from Eq. (68) with the model coefficients, a_{1-3}, determined from the minimization problem described in Eq. (75). Both the actual and approximate diffraction coefficients were evaluated at a distance of $\rho = 10\lambda$ from the diffracting edge for plane wave incidence at 2.3 GHz.

The poor fit of the model for parallel incidence is attributed to the existence of a Brewster angle at which the wedge faces' reflection coefficient is zero. The approximation to the pattern function, $C^r(\phi, \phi')$, given by Eqs. (51), (62), and (66) is unable to accurately reproduce the resulting null in the magnitude of the diffraction coefficient for all incident angles. This point is illustrated by Fig. 9, which compares the actual and approximate diffraction coefficient for a 90° wedge ($n = 3/2$) with a permittivity of $\epsilon_R = 10 - j0.1$ for various combinations of incident angle, ϕ', and polarization. The model's fit for perpendicular incidence is extremely good, whereas its fit for parallel incidence shows varying degrees of inaccuracy. The accuracy could be improved by adding more terms to the approximation of $C(\phi, \phi')$ and $\chi(\phi, \phi')$ in Eqs. (62) and (66), respectively. However, adding more terms would lead to an increasingly more complicated model, because the total number of model coefficients is given by the product of the number of unknown coefficients in the approximations to $C(\phi, \phi')$ and $\chi(\phi, \phi')$.

The approximate diffraction coefficients in Fig. 9 were generated from the linear diffraction model using the model coefficients, a_{1-3}, determined from a least-squares fit to the pattern functions $C^i(\phi, \phi')$ and $C^r(\phi, \phi')$. Alternatively, the model coefficients may be determined directly from a least-squares fit to the impedance wedge diffraction coefficient via Eq. (68) This approach can provide more accurate diffraction coefficients but is less general because the model's coefficients must be determined from a least-squares fit at a specific frequency. Figure 10 illustrates this improved accuracy for the case of a 90° wedge with a permittivity of $\epsilon_R = 10 - j0.1$. To determine

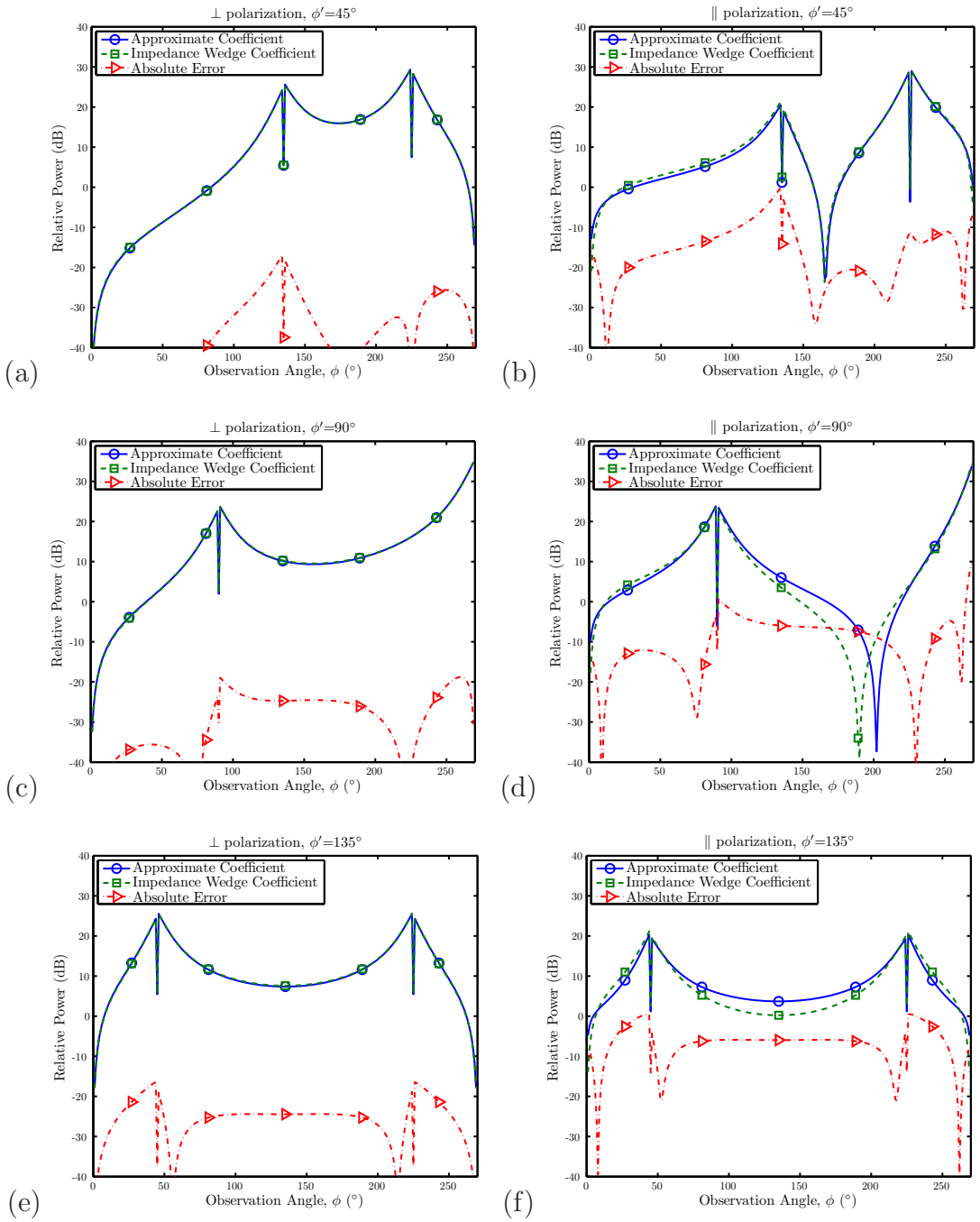

Figure 9: A comparison of the UTD impedance wedge diffraction coefficient, $D^{\perp}_{\parallel\,\mathrm{UTD}}(\phi,\phi')$, and the model's diffraction coefficient, $\tilde{D}^{\perp}_{\parallel\,\mathrm{UTD}}(\phi,\phi')$, for six different combinations of incident angle and polarization where $\epsilon_R = 10 - j0.1$ and $n = 3/2$. The linear model's coefficients were determined from a least-squares fit of the pattern functions, $C^i(\phi,\phi')$ and $C^r(\phi,\phi')$: (a) $\phi' = 45°, \perp$; (b) $\phi' = 45°, \parallel$; (c) $\phi' = 90°, \perp$; (d) $\phi' = 90°, \parallel$; (e) $\phi' = 135°, \perp$; (f) $\phi' = 135°, \parallel$.

the model coefficients, a_{1-3}, the impedance wedge diffraction coefficient and diffraction coefficient model's terms were evaluated at a distance of 10λ from the wedge's diffracting edge at $f = 2.3$ GHz. For wideband applications, the least-squares fitting could be performed across a discrete set of frequencies to yield model coefficients that are applicable across the frequency band. Comparing Figs. 9 and 10, it may be seen that fitting the model directly to the impedance wedge diffraction coefficient improves the accuracy of the resulting diffraction coefficient for parallel incidence. The model still has some difficulty fitting the deep null in the diffraction coefficient for the case of parallel incidence at $\phi' = 90°$.

Finally, we note that previous researchers have attempted to fit a linear model to the pattern functions, $C_{1-4}(\phi, \phi')$ in Eq. (25). In [115] the authors performed a polynomial fit to the magnitude and phase of each of these four pattern functions. Compared to the model presented here, the approach outlined in [115] yields a considerably more complicated model with 19 or more model coefficients depending on the order of the polynomials. Though this may lead to a more accurate and flexible model, it is considerably less efficient and neglects the underlying symmetries and necessary conditions of the diffraction coefficient's pattern functions.

2.4.2 Diffraction Coefficient Extraction

As an alternative validation, we examine the applicability of the linear model to the task of decomposing an observed total field and extracting diffraction coefficients. The UTD total field solution described in Eq. (60) was used to compute the total field, $E^t(\mathbf{r})$, for a range of incidence angles, polarizations, wedge angles, and wedge impedances. The time-harmonic frequency of the electric field was specified to be 2.3 GHz. The total field was computed on a 0.2λ Cartesian grid whose origin coincides with the diffracting edge. The total field data points exterior to the diffracting wedge and within 10λ of the edge were used in conjunction with Eq. (74) to determine

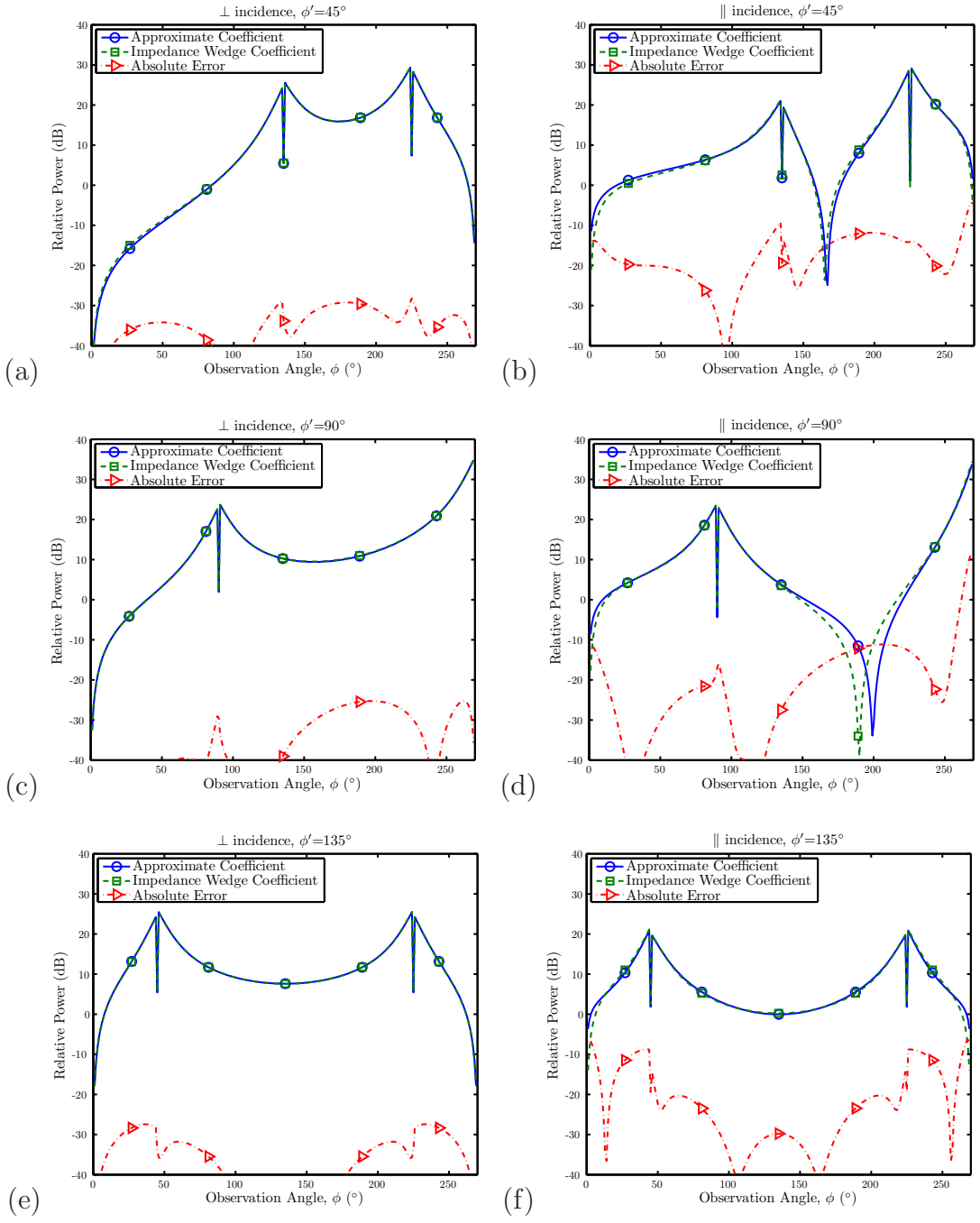

Figure 10: A comparison of the UTD impedance wedge diffraction coefficient, $D^{\perp}_{\parallel\,\mathrm{UTD}}(\phi,\phi')$, and the model's diffraction coefficient, $\tilde{D}^{\perp}_{\parallel\,\mathrm{UTD}}(\phi,\phi')$, for six different combinations of incident angle and polarization where $\epsilon_R = 10 - j0.1$ and $n = 3/2$. The linear model's coefficients were determined from a least-squares fit of $\tilde{D}^{\perp}_{\parallel\,\mathrm{UTD}}(\phi,\phi')$ to $D^{\perp}_{\parallel\,\mathrm{UTD}}(\phi,\phi')$: (a) $\phi = 45°, \perp$; (b) $\phi' = 45°, \parallel$; (c) $\phi' = 90°, \perp$; (d) $\phi' = 90°, \parallel$; (e) $\phi' = 135°, \perp$; (f) $\phi' = 135°, \parallel$.

the amplitude-scaled model coefficients E_0, $E_0 a_1$, $E_0 a_2$, and $E_0 a_3$ that provided the best fit in the least-squares sense. By normalizing these coefficients by E_0, the model coefficients, a_{1-3}, were determined for the diffraction coefficient linear model described in Eq. (68). We note that the total field and diffraction coefficient models, $\tilde{E}^t(\mathbf{r})$ and $\tilde{D}^{\perp}_{\mathrm{UTD}}(\phi, \phi')$, respectively, both require knowledge of the problem geometry by way of the incidence angle, ϕ', the observation angle, ϕ, the polarization of the incident field, and the appropriate wedge angle, n. The models also require knowledge of the time-harmonic field's wavenumber, k_0.

The UTD impedance wedge diffraction coefficient, $D^{\perp}(\phi, \phi')$, and extracted semi-empirical diffraction coefficient, $\tilde{D}^{\perp}_{\mathrm{UTD}}(\phi, \phi')$, derived from the linear diffraction coefficient model were then evaluated at a distance of $\rho = 10\lambda$ from the diffracting edge for plane wave incidence at 2.3 GHz. The incident angle, ϕ', was the same as was used to determine the model coefficients, and the observation angle was $\phi \in (0, n\pi)$ in 1° increments. The semi-empirical diffraction coefficient's normalized mean-squared error, $\widehat{\overline{\varepsilon^2}}_D$, was calculated according to Eq. (77). As before, the real and imaginary components of the impedance wedge's relative permittivity were varied along a logarithmic scale through $\mathrm{Re}(\epsilon_R) \in [4, 100]$ and $-\mathrm{Im}(\epsilon_R) \in [0.01, 100]$, respectively, and both parallel and perpendicular polarizations were considered. The simulated incident angles were $\phi' \in \{45^\circ, 90^\circ, 135^\circ\}$; the wedge angle was 90° ($n = 3/2$).

Figure 11 compares the diffraction coefficient's normalized mean-squared error, $\widehat{\overline{\varepsilon^2}}_D$ as a function of relative permittivity for all six combinations of polarization and incident angle. Again, better accuracy is attained for perpendicular incidence than parallel incidence. This is further illustrated by the CDF curves for the diffraction coefficient's normalized mean-squared error presented in Figure 12. Figure 13 compares the actual and extracted diffraction coefficients for the six combinations of polarization and incident angle. The good agreement between the actual and extracted diffraction coefficients indicates the linear diffraction model may be used to extract

diffraction coefficients from total field measurement data.

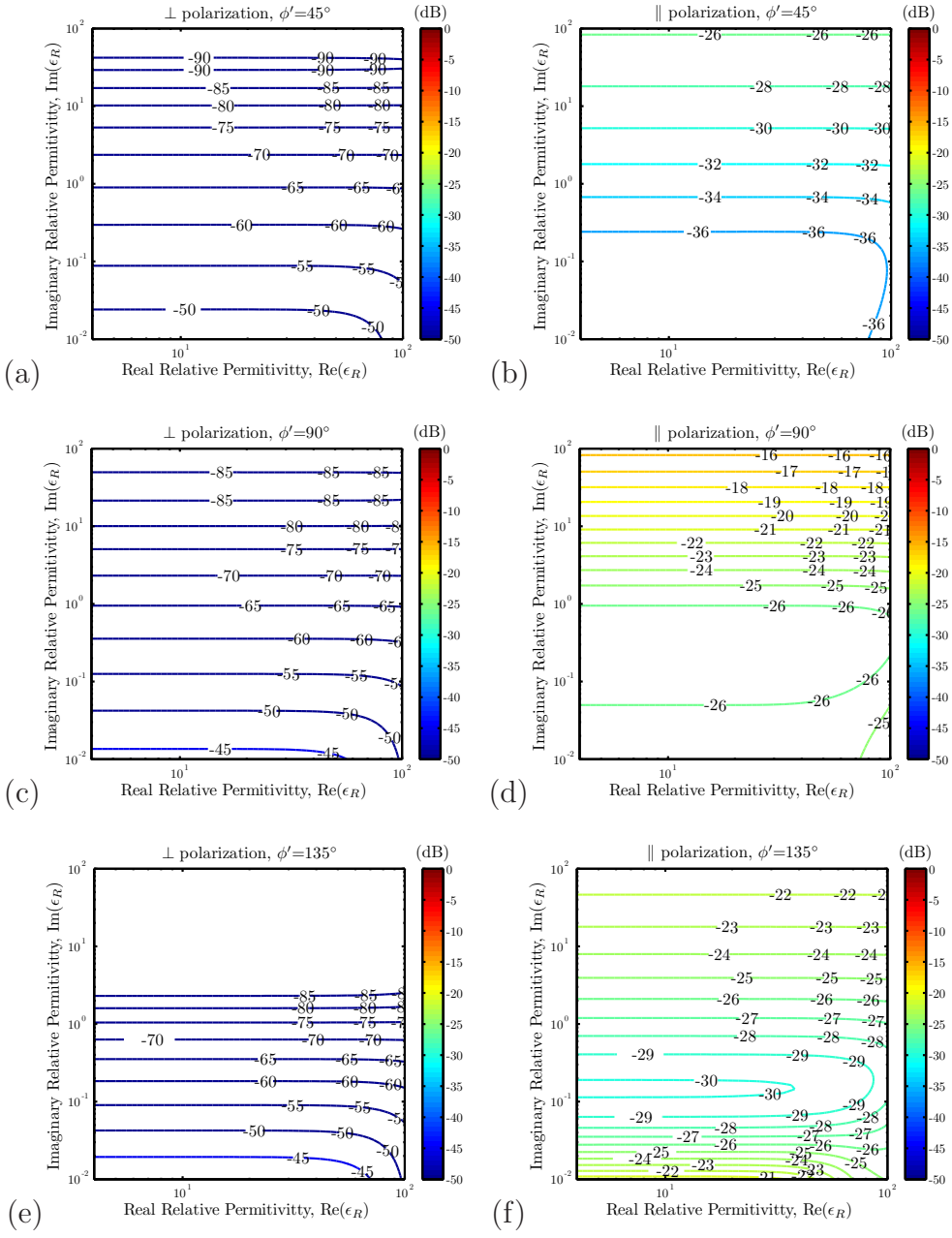

Figure 11: A comparison of the diffraction coefficient's simulated mean-squared error, $\widehat{\overline{\varepsilon^2}}_D$, as a function of complex relative permittivity, ϵ_R, for six different combinations of incident angle and polarization with $n = 3/2$. The linear model's coefficients were determined from a least-squares fit of the UTD impedance wedge solution's total field, $E^t(\mathbf{r})$: (a) $\phi' = 45°, \perp$; (b) $\phi' = 45°, \parallel$; (c) $\phi' = 90°, \perp$; (d) $\phi' = 90°, \parallel$; (e) $\phi' = 135°, \perp$; (f) $\phi' = 135°, \parallel$.

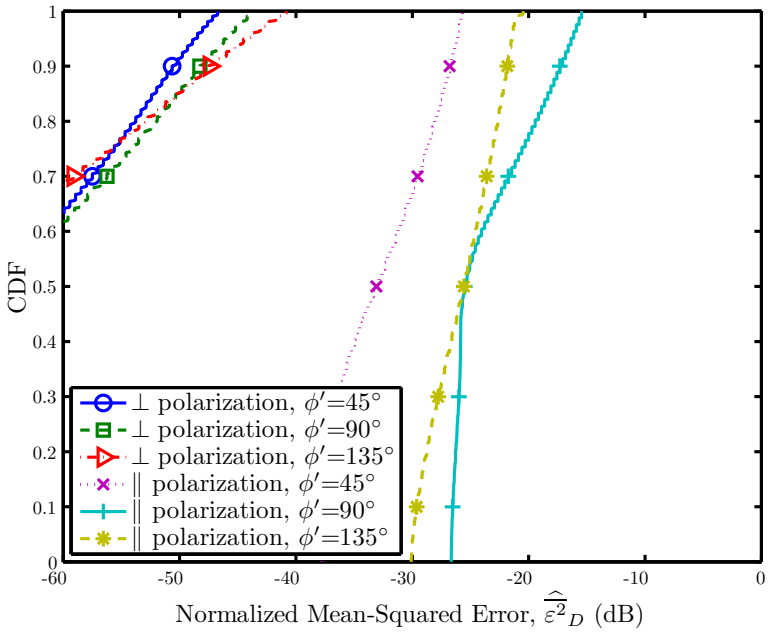

Figure 12: Cumulative distribution functions (CDF) of the diffraction coefficient's mean-squared error for each of the six combinations of incident angle and polarization with $n = 3/2$. The CDF curves were computed from mean-squared errors for a wide range of complex permittivities, ϵ_R, and the model coefficients were determined from a least-squares fit of the UTD impedance wedge solution's total field, $E^t(\mathbf{r})$

.

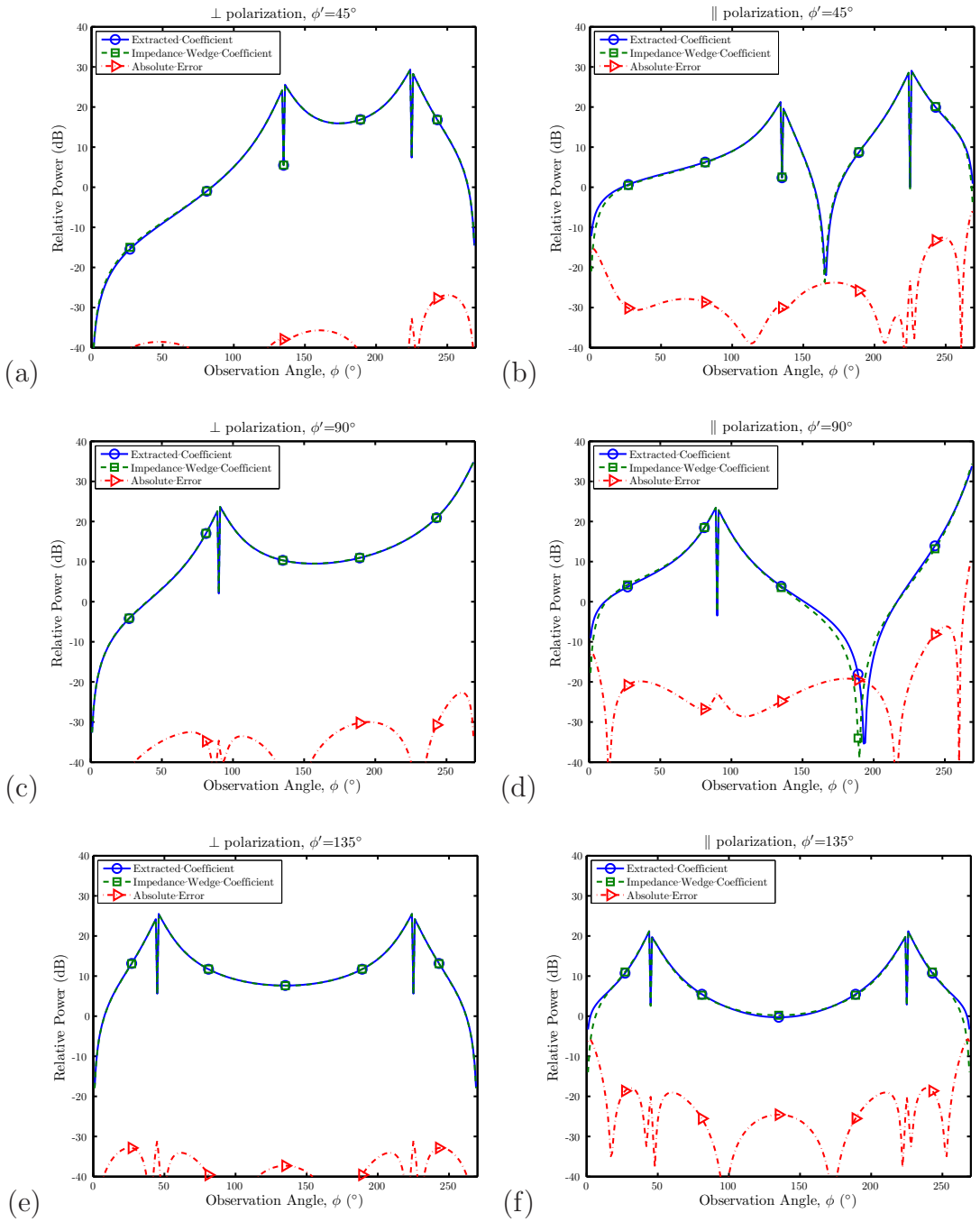

Figure 13: A comparison of the UTD impedance wedge diffraction coefficient, $D^{\perp}_{\parallel}{}_{\mathrm{UTD}}(\phi,\phi')$, and the model's diffraction coefficient, $\tilde{D}^{\perp}_{\parallel}{}_{\mathrm{UTD}}(\phi,\phi')$, for six different combinations of incident angle and polarization where $\epsilon_R = 10 + j0.1$ and $n = 3/2$. The linear model's coefficients were determined from a least-squares fit of the UTD impedance wedge solution's total field, $E^t(\mathbf{r})$: (a) $\phi' = 45°, \perp$; (b) $\phi' = 45°, \parallel$; (c) $\phi' = 90°, \perp$; (d) $\phi' = 90°, \parallel$; (e) $\phi' = 135°, \perp$; (f) $\phi' = 135°, \parallel$.

CHAPTER III

FIELD RECONSTRUCTION-BASED SPATIO-TEMPORAL CHANNEL SOUNDER

Chapter Summary: This chapter presents the spatio-temporal channel sounder and data processing techniques used to measure real-world radio wave propagation mechanisms. Following a brief overview of the measurement system's hardware and accompanying field reconstruction technique, the discussion details how these two components are fused to realize a field reconstruction-based spatio-temporal channel sounder. The chapter concludes by presenting several statistical analyses and filtering techniques enabled by the channel sounder's comprehensive measurement data.

The linear model for wedge diffraction presented in Chapter 2 may be fit to total field diffraction measurements using conventional linear least-squares techniques. However, the underlying assumption for this least-squares fitting is that the *only* fields present are the incident, reflected, and diffracted fields associated with the impedance wedge diffraction problem. For in situ building corner diffraction measurements, the complexity of the propagation environment makes this requirement difficult to enforce. Nearby buildings, trees, and various other objects will scatter additional energy that will interfere with the desired edge diffraction problem.

Conventional measurement techniques use the measurement system's space-time resolution to isolate the desired radio wave propagation problem based upon the angle- and delay-of-arrival [88]. Temporal selectivity is realized by time-gating the

measurement data, whereas angular selectivity is typically realized by steering an antenna array using classic weight-and-sum beamforming techniques. Unlike time-gating, which is effectively a frequency domain filtering technique, array beamsteering reduces the dimensionality of the measurement data, because it collapses a vector of position-dependent received signals down to a single signal. In order to use this resulting signal with the linear diffraction model from Chapter 2, it must be representative of the total field at a particular point in space. Thereby, the array beamforming must be performed in such a way that the incident, reflected, and diffracted fields are summed together without modification to their amplitude and phase while suppressing the undesired field contributions of interfering mechanisms. Furthermore array beamsteering requires far-field measurement data, which restricts where and how the total field measurements may be taken. These complications and limitations make array beamforming unsuitable for isolating an individual radio wave propagation problem's total field.

This chapter introduces an innovative new spatio-temporal wireless channel sounder that enables flexible interference suppression through conventional digital signal processing techniques. The spatio-temporal channel sounder fuses a custom ultra-wideband single-input multiple-output (SIMO) channel sounder with a recently developed quasi 2-D field reconstruction technique to record the evolution of the wireless channel's impulse response throughout a 2-D region of space. Conventional filtering tools may then be applied to the wireless channel in the space (wavevector) and/or frequency (delay) domains so as to isolate the total field corresponding to the desired radio wave propagation problem. Furthermore, unlike conventional beamforming techniques, space-time filtering retains the dimensionality of the measurement data and is applicable to both near- and far-field data.

Discussion begins with a brief overview of the SIMO sliding correlator channel sounder and the quasi 2-D field reconstruction technique based upon the conjoint

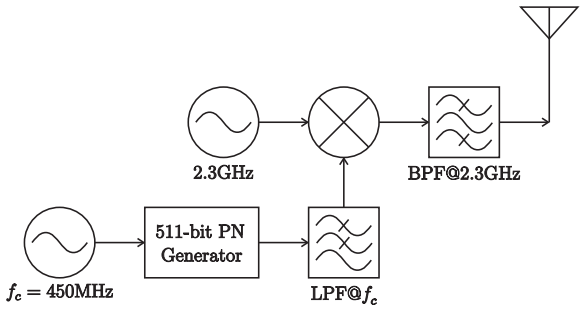

Figure 14: Diagram of the SIMO channel sounder's wideband transmitter.

cylindrical wave expansion. For a detailed discussion of the SIMO sliding correlator channel sounder or the conjoint cylindrical wave expansion, see Appendices C and A, respectively. Following this overview, we discuss how the SIMO channel sounder is combined with the quasi 2-D field reconstruction technique to efficiently perform wideband wireless channel measurements throughout a 2-D region of space. The chapter concludes with a discussion of possible statistical analyses and space-time filtering techniques.

3.1 SIMO Channel Sounder

The measurement system employs the first-ever single-input multiple-output (SIMO) sliding correlator channel sounder to perform phase- and delay-stable measurements of static wireless channels. Figures 14 and 15 illustrate the architecture of the SIMO sliding correlator channel sounder. As depicted in Fig. 14, the system uses a direct conversion transmitter to modulate a $f_0 = 2.3$ GHz RF carrier by pseudo-random noise (PN) chipped at $f_c = 450$ MHz. After band-pass filtering, a wideband antenna radiates the direct sequence spread spectrum signal. The transmitter's UWB-defined -10 dB bandwidth extends from approximately 2.0 GHz up to 2.6 GHz.

Following reception by two wideband antennas, the signal is band-pass filtered and amplified by a low-noise amplifier. A modulated PN is used to synchronously perform the sliding correlation on both received signals as well as downconvert the signals to an intermediate frequency (IF) of 880 MHz. After additional filtering, a pair

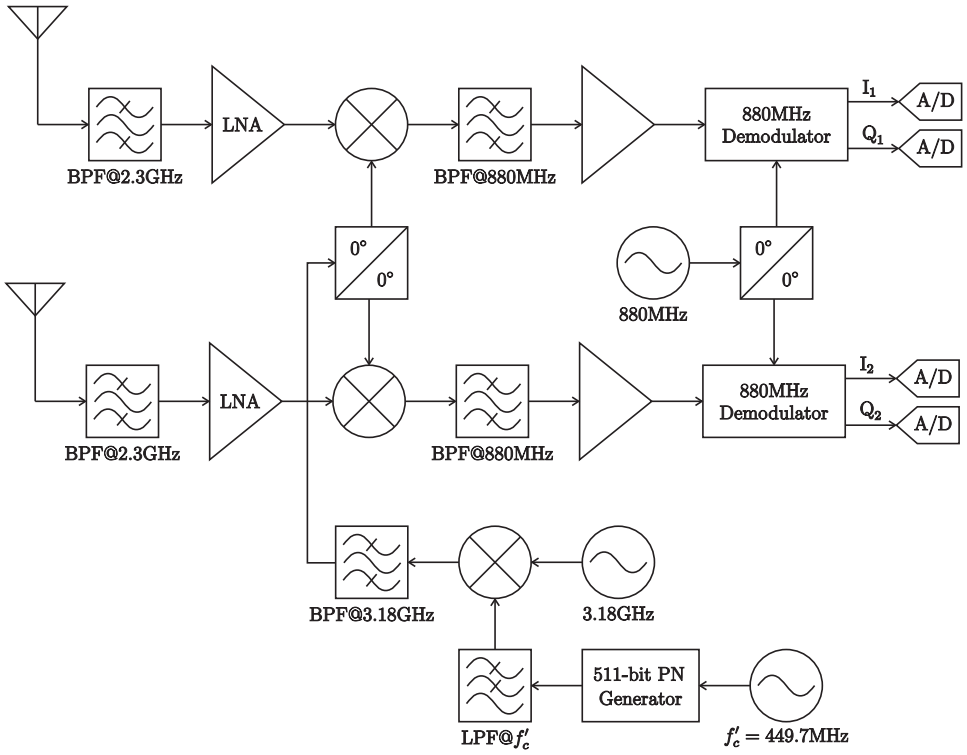

Figure 15: Diagram of the SIMO channel sounder's dual-channel receiver.

of I/Q demodulators downconvert each channel's IF signal to baseband. The signals are then digitized by an oscilloscope and stored on a computer for post-processing. During post-processing, the signals are digitally filtered and calibrated to remove the measurement system's response from the recorded channel impulse responses.

Table 1 summarizes the capabilities of the constructed 2.3 GHz SIMO channel sounder. A complete description of each of these capabilities may be found in Appendix C. Figures 16 and 17 present photos of the channel sounder's transmitter and receiver, respectively. Figure 18 present photos of the three antennas used for field reconstruction-based space-time channel sounding.

3.2 Quasi 2-D Field Reconstruction

From the uniqueness theorem of electromagnetics, it is known that for a source-free, homogeneous, and nominally lossy medium, time-harmonic electric fields within a volume are uniquely determined by the fields tangential to a bounding surface. For

Figure 16: Photo of the spatio-temporal channel sounder's spread spectrum transmitter.

Table 1: SIMO Channel Sounder Capabilities

System Capability	**Realized Performance**
Doppler Resolution, $f_{D,\max}$	391 Hz
Dynamic Range, D_R	34 dB
Temporal Resolution, T_{res}	2.22 ns
Max Multipath Delay, $\tau_{\max}$	1.14 μs
Max Path Length, $d_{\max}$	341 m

Figure 17: Photo of the spatio-temporal channel sounder's dual channel receiver.

(a) 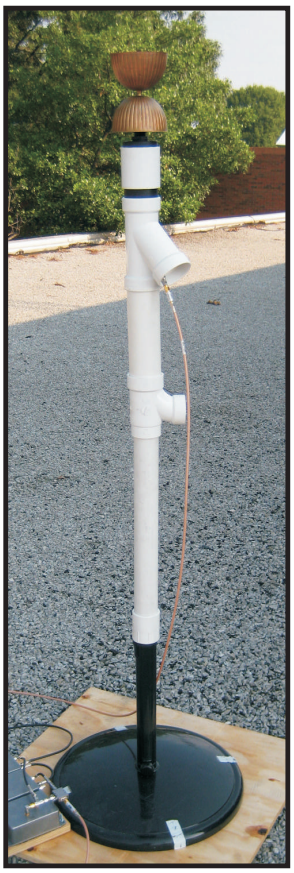 (b)  (c) 

Figure 18: Photos of the antennas used with the spatio-temporal channel sounder: (a) omnidirectional transmit antenna, (b) directional "reference" receive antenna, and (c) omnidirectional "measurement" receive antenna.

strictly 2-dimensional (2-D) fields, this surface collapses to a closed contour about a planar region. Thereby, a set of coherent field measurements along the perimeter of a measurement region will enable an exact reconstruction of the electromagnetic fields in the interior. To actually perform this reconstruction, one may employ any number of techniques ranging from field expansions to finite-element methods to method of moments. Regardless of the specific technique, it is important to note that if only the electric field is measured, *two* $\lambda_0/4$-spaced contour measurements are required so as to suppress the resonant modes of the measurement region's geometry [80].

Strictly speaking, 2-D field reconstruction techniques are only valid for 2-D wireless channels wherein contributing plane waves propagate exactly along the horizon. For many wireless channels, empirical data suggests that the elevation angle-of-arrival (AoA) of incident plane waves tends to cluster tightly about the horizon, thereby producing an *approximately* 2-D wireless channel [53]. However, 2-D field reconstruction techniques rely on *coherent* measurement data. The sensitivity of phase to small variations in distance makes 2-D field reconstruction techniques sensitive to off-the-horizon propagation, particularly when the reconstruction region spans several wavelengths.

To account for plane waves incident at small, nonzero elevation angles, we have developed a conjoint cylindrical wave expansion (CWE) for so-called *quasi 2-D* channels [82]. The conjoint CWE efficiently combines the basis sets of two conventional CWEs with slightly different wavenumbers. Experimental data and analytical results have demonstrated that for typical measurement scenarios, the conjoint CWE produces a more accurate reconstruction than the conventional CWE without requiring additional measurement data [82].

Figure 19 illustrates an example wireless channel reconstruction. A vector network analyzer (VNA) and a pair of bicone-style antennas were used to measure the frequency response of the wireless channel at 2.45 GHz. Figure 19(a) depicts the hallway measurement environment including any large metallic objects in the area. A more

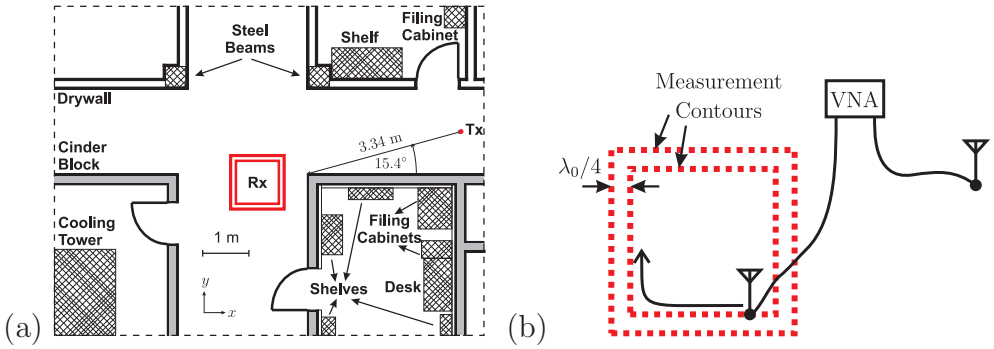

Figure 19: Diagram of the (a) environment and (b) measurement configuration for the wireless channel reconstruction measurements performed with vector network analyzer at 2.45 GHz.

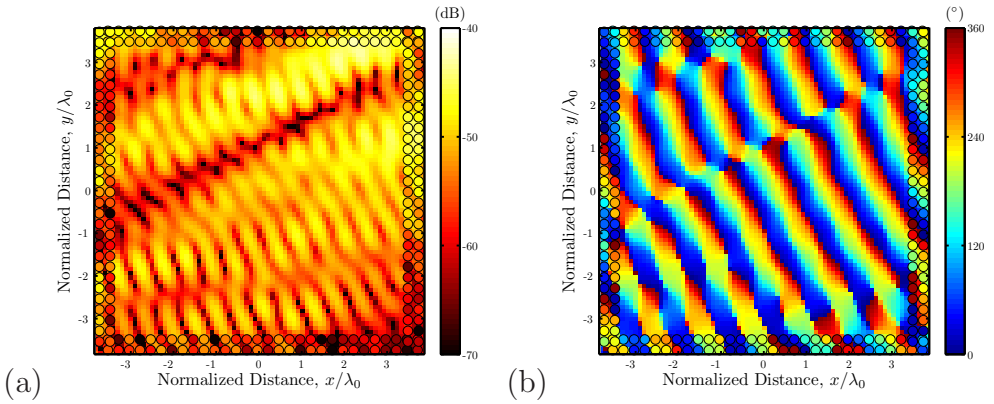

Figure 20: The conjoint cylindrical wave expansion was applied to the 2.45 GHz contour measurements to reconstruct the wireless channel throughout the rectangular region. The circles indicate the measured S_{21} along the pair of concentric rectangular contours. (a) magnitude in dB and (b) phase in degrees.

detailed illustration of the measurement configuration is depicted in Fig. 19(b). S_{21} measurements were taken at quarter-wavelength intervals along the pair of concentric rectangular contours. The conjoint CWE was then used to reconstruct the wireless channel throughout the rectangular measurement region. The magnitude and phase of the resulting reconstructed channel is presented in Fig. 20. Overlayed atop the reconstructed channel are the actual S_{21} measurements from the rectangular contours. It is evident that the magnitude and phase of the measured and reconstructed channel are in excellent agreement.

3.3 Space-Time Channel Measurement Methodology

The SIMO channel sounder provides wideband phase- and delay-stable channel measurements whereas the conjoint CWE provides a means for reconstructing the spatial wireless channel from perimeter measurement data. Thereby, applying the spatial reconstruction technique to the channel sounder's wideband measurement data enables one to accurately capture the space-time channel throughout a 2-D spatial region.

3.3.1 Ideal Measurement Configuration

Conceptually, merging these two technologies is relatively straightforward. Figure 21 illustrates how this might be done. The SIMO channel sounder's transmitter (Tx) is held stationary while one of the channel sounder's receive antennas is moved along each of the concentric rectangular contours bounding the measurement region. Note that the transmitter position must be outside of the measurement region because the conjoint CWE assumes a sourceless reconstruction region. As the one receive antenna is swept along the contours, the other receive antenna is held stationary and provides a reference channel measurement. During post-processing, the reference measurements are used to correct for variations in trigger timing between each measurement. As noted in Appendix C, the SIMO channel sounder's post-processing software yields the discrete frequency response of the measured wireless channel. Working with this discrete frequency response is far more convenient than the time-domain channel impulse response measured directly by the sliding correlator architecture, particularly when the measurement data is to be used in conjunction with a frequency domain field reconstruction technique.

As shown in Figure 21, a common 10 MHz reference signal is used to phase-lock the Tx and Rx oscillators and thereby ensure phase-stable measurements. It is conceivable that the "reference" antenna's measurements could be used to correct for phase deviations between unsynchronized 10 MHz references and thereby circumvent

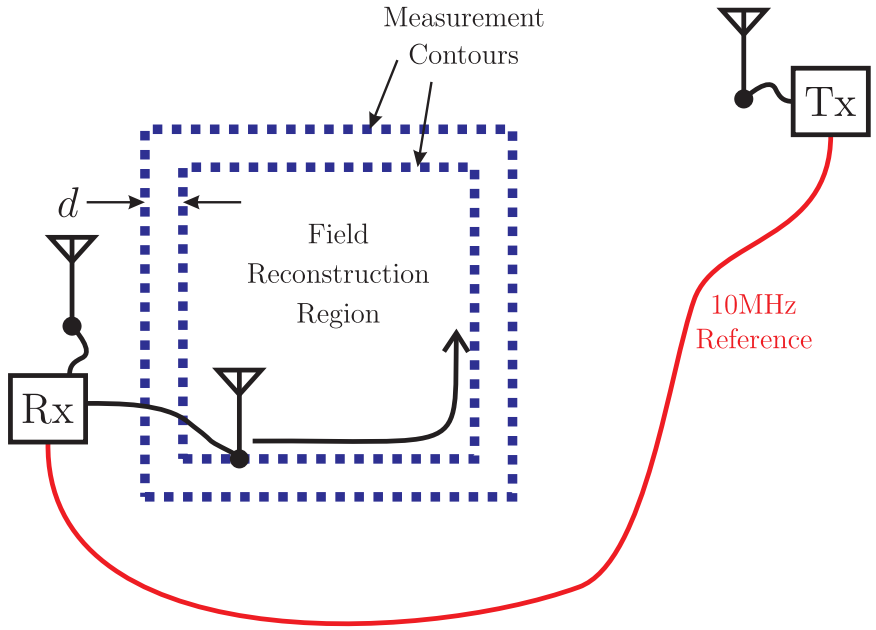

Figure 21: An idealized SIMO channel sounder measurement configuration for reconstructing the space-time wireless channel from perimeter measurements.

the need for a common synchronization cable. This would be particularly advantageous for measurements wherein the Tx-Rx separation distance is large. However, the measurements carried out in this study required Tx-Rx separation distances on the order of meters, so connecting the Tx and Rx with a 10 MHz *sync cable* was considered less troublesome than the additional post-processing required to correct for phase deviations between unsynchronized 10 MHz reference oscillators.

3.3.1.1 Contour Separation Distance

As discussed in [82], and depicted in Fig. 19(b), the nominal separation distance between the two bounding contours is $\lambda_0/4$ for some free-space wavelength, λ_0. Theoretically, an accurate reconstruction may be achieved as long as the contour separation distance, d, depicted in Fig. 21 is such that $d \in (0, \lambda_0/2)$ with $\lambda_0/4$ being the nominal median value [118, 100]. Practically speaking, d should be kept as close as possible to $\lambda_0/4$. For the wideband measurements obtained with the SIMO sliding correlator channel sounder, this requires minimizing the magnitude difference between d and

$\lambda/4$ for all transmitted frequencies. This is achieved provided that

$$\frac{\lambda_{\max}}{4} - d = d - \frac{\lambda_{\min}}{4} \tag{78}$$

where $\lambda_{\max}$ and $\lambda_{\min}$ are the largest and small free-space wavelengths corresponding to the lowest and highest transmitted frequencies, respectively. For a sliding correlator channel sounder operating at center frequency of f_0 with a PN chip rate of f_c, $\lambda_{\min}$ and $\lambda_{\max}$ are given by

$$\lambda_{\min} = \frac{c}{f_0 + f_c} \tag{79}$$

$$\lambda_{\max} = \frac{c}{f_0 - f_c} \tag{80}$$

where c is the propagation velocity in free-space. Substituting (79) and (80) into (78) and simplifying yields

$$d = \frac{c}{4}\left[\frac{f_0}{f_0^2 - f_c^2}\right] \tag{81}$$

Thus, Eq. (81) provides the ideal separation distance between bounding, concentric measurement contours for wideband channel sounders. For the SIMO sliding correlator channel sounder's carrier frequency of $f_0 = 2.3$ GHz and a PN chip rate of $f_c = 450$ MHz, the ideal contour separation distance is $d = 33.9$ mm.

3.3.1.2 Measurement Contour Spatial Sampling Period

The channel measurements along the pair of bounding contours depicted in Fig. 21 will consist of discrete measurements at Δ_s intervals along each contour where Δ_s denotes the *spatial sampling period*. Provided that the measurement region is far from any scatterers such that contributions from inhomogeneous plane waves are negligible, the maximum spatial frequency will be $2\pi/\lambda_{\min}$. For this case the Nyquist-Shannon sampling theorem states that a spatial sampling period $\Delta_s \leq \lambda_{\min}/2$ ensures complete knowledge of the wireless channel at *any* point along either measurement

contour. However, this neglects the effects of measurement noise, which will invariably introduce spatial frequencies greater than $2\pi/\lambda_{\min}$. Therefore, to account for both noise and the possibility of inhomogeneous plane waves due to measurements near scatterers, we opt for a spatial sampling period of $\lambda_{\min}/4$. Using Eq. (79), this leads to a spatial sampling rate, Δ_s, given by

$$\Delta_s = \frac{c}{4(f_0 + f_c)} \tag{82}$$

For the SIMO sliding correlator channel sounder's carrier frequency of $f_0 = 2.3$ GHz and a PN chip rate of $f_c = 450$ MHz, the required spatial sampling rate is $\Delta_s = 27.2$ mm.

3.3.2 Practical Measurement Configuration

As noted, Fig. 21 depicts the ideal measurement configuration, which assumes that an accurate and precise 2-D positioning system is available for realizing the rectangular measurement contours. Unfortunately, this was not the case – the only spatial positioning system on-hand was a Velmex Bislide, a 1-D track-based linear positioner. The Velmex positioner enabled measurements along a line with a maximum displacement of 1.51 m. The following sections discuss how the linear positioner was used to synthesize the rectangular measurement contours.

3.3.2.1 Linear Track Measurements

Figure 22 summarizes how the linear positioner was used to synthesize the required rectangular contours. A set of eight track measurements are made, corresponding to the eight dashed lines in Fig. 22. For each track measurement, the "measurement" receive antenna was stepped along the linear positioner's track at increments corresponding to the spatial sampling period, Δ_s. After completing the linear track measurement, the track was moved to the next position, and the measurement procedure was repeated. Note that throughout this entire measurement process, the

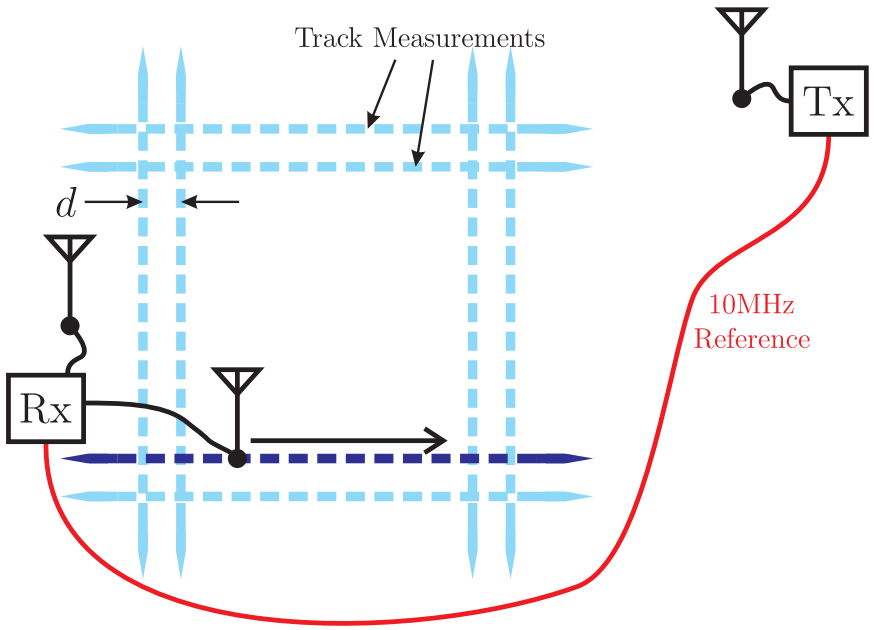

Figure 22: A set of eight linear track measurements were required to synthesize the pair of bounding rectangular contour measurements required for field reconstruction.

receiver's "reference" antenna remained fixed to provide a consistent relative timing reference.

3.3.2.2 Temporal Alignment

For each frequency response recorded by the receiver's "measurement" antenna, a corresponding "reference" frequency response is recorded. This measurement pair forms a single SIMO wireless channel measurement. During post-processing, a linear phase taper is applied to each SIMO frequency response so as to temporally align the corresponding impulse response of *all* of the "reference" measurements. This resolved the timing ambiguity between different SIMO measurements due to the absence of a consistent and reliable measurement acquisition trigger. Thereby, the wireless channel measurements recorded by the receiver's stationary "reference" antenna enabled the channel sounder's delay-stable measurements.

3.3.2.3 Positioning Errors

Electromagnetic field reconstruction techniques are quite sensitive to changes in phase, which also makes them sensitive to errors in the presumed position of the measurements. Thus, to ensure the reconstructed field resembled the true electromagnetic field, it was important to correct any position errors present in the measurement data. Three potential position error sources were identified: 1) the placement of the linear positioner, 2) the levelness of the linear positioner, and 3) the levelness of the "measurement" antenna's mounting pole.

The first error stems from the measurement procedure, which required that the 1-D linear positioner be manually moved to each of the track locations depicted in Fig. 22. The second and third error sources result from the receiver's "measurement" antenna being attached to the linear positioner by way of a long PVC mast. Figure 23 depicts this configuration and identifies the two associated position error sources. From an electromagnetics standpoint, the PVC antenna mast was important for isolating the Velmex BiSlider's aluminum track from the "measurement" antenna and the measured wireless channel. However, as Fig. 23 indicates, the antenna mast also led to large position errors when either the mast or the BiSlider was not perfectly level.

Careful experimental design and execution helped to mitigate these error sources, though the lack of precision measurement and positioning tools made it impossible to eliminate them. Therefore, a position error correction technique was developed and applied during post-processing that enforced the continuity of the wireless channel at the intersection of orthogonal measurement tracks. The following section discusses this position error correction technique.

3.3.2.4 Track Intersection-Based Position Correction

At the intersection of two linear paths traversed by the "measurement" antenna, the observed wireless channel must be the same. Therefore, provided that the positioning

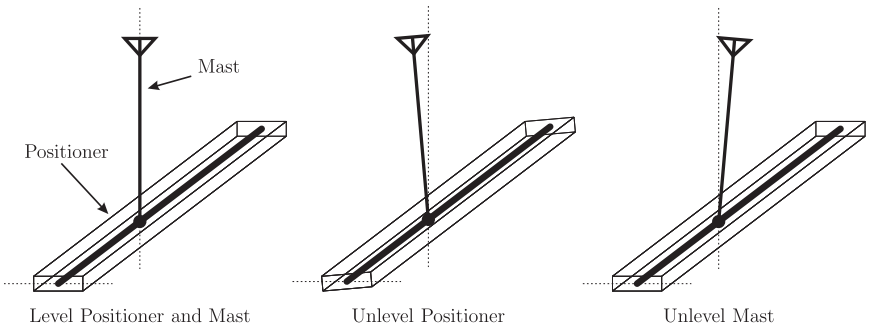

Figure 23: Attaching the receiver's "measurement" antenna to the linear positioner by way of a long mast can lead to additional positioning errors if the linear positioner is not perfectly level or if the mast orientation deviates from vertical.

errors are not large (i.e., $> \lambda_0/4$), it should be possible to correct for the positioning errors by spatially translating each track measurement so as to minimize the difference in the observed channels at the 16 intersections identified in Fig. 24.

This minimization problem was solved using a custom MATLAB function called `shimmy.m`, which relied on MATLAB's `lsqnonlin.m` function to iteratively solve the underlying nonlinear least-squares problem. Spline interpolation was used to interpolate the spatially discrete measurement data to the intersection of any two paths. The target minimization function calculated the difference between the interpolated measurements' discrete frequency response at all 16 intersection points. The resulting error matrix was used in conjunction with `lsqnonlin.m`'s sum-of-squares minimization algorithm to determine the optimal spatial translation for each track's position. Thereby, `shimmy.m` ascertained the positions of the "measurement" antenna's linear paths based on the specified track paths.

In order to accurately interpolate each track measurement to one of the 16 intersections identified in Fig. 24, it was important that the track measurements extend beyond the bounding outer rectangular contour. Specifically, for MATLAB's piecewise cubic spline interpolation, at least three additional measurement points were required to obtain an accurate interpolation. This corresponded to extending the ends of each of the eight track measurement paths $4\Delta_s = \lambda_{\min}$ beyond the outer

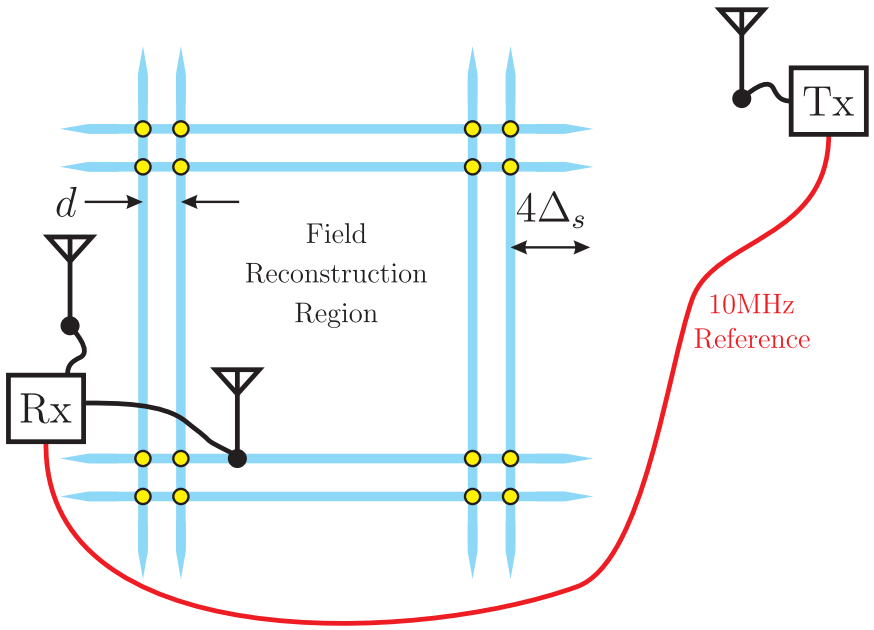

Figure 24: The `shimmy.m` MATLAB function accounted for positioning errors by translating each of the eight linear measurement path so as to minimize the difference in the wireless channels measured along each track at the 16 intersection points.

rectangular contour as illustrated in Fig. 24.

3.3.2.5 Extraction of Measurement Data For Field Reconstruction

Once the positioning errors had been accounted for, the pair of bounding rectangular measurement contours could be extracted from the measurement data. Due to the positioning errors, the actual separation distance between the inner and outer contours was unlikely to be the optimal distance given in Eq. (81) and was invariably different for each side of the rectangle. However, provided that for any side, the separation distance was $d \in (0, \lambda_{\min}/4)$, the conjoint CWE could still be applied to the measurement data.

All of the measurement points lying within the outer bounding contour can and should be used for field reconstruction. In contrast, measurement points exterior to the outer contour should only be used if they lie within the smallest circle circumscribing the reconstruction region as illustrated in Fig. 25. In [82], it is noted that the conjoint CWE's infinite summation of basis functions must be truncated to produce

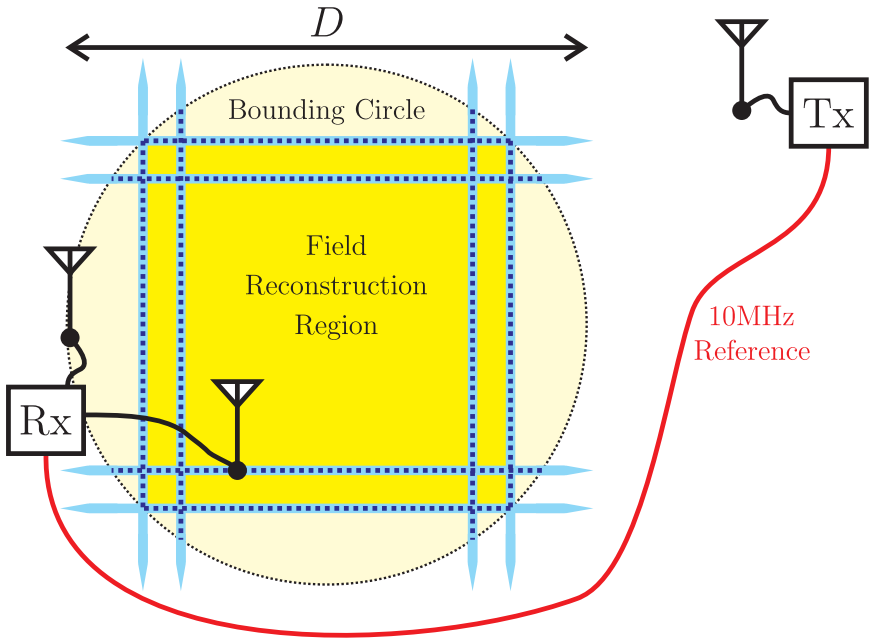

Figure 25: Measurement data lying within the smallest circle of diameter D circumscribing the rectangular reconstruction region may be used with the conjoint CWE to reconstruct the wireless channel.

a nonsingular matrix equation. The truncation point is determined by the distance, D, which corresponds to the diameter of the smallest circle circumscribing the measurement region. If points exterior to the outer bounding contour and outside of the bounding circle are included, these additional measurement points will effectively be outside the range of the truncated basis set. Thus, solving the matrix equation that includes points outside of the bounding circle will lead to a less accurate answer, because only a subset of the basis functions required for an accurate solution are actually being used. In Fig. 25, the dotted lines indicate portions of each linear measurement path that were used to reconstruct the wireless channel within the yellow rectangular region. Note that the included measurements lie within the circle of diameter D that circumscribes the rectangular reconstruction region.

3.3.3 Spatio-Temporal Channel Reconstruction

The SIMO channel sounder directly measures a periodic version of the wireless channel's impulse response. As discussed in Appendix C, during post-processing, this

periodic impulse response is converted to the wireless channel's discrete frequency response via Fourier analysis. Thus, once a subset of measurement data has been selected for inclusion in the field reconstruction, the frequency domain conjoint cylindrical wave expansion may be applied at each of the wireless channel's discrete measurement frequencies to reconstruct the full space-frequency wireless channel. If desired, this space-frequency wireless channel may then be Fourier transformed to realize the wireless channel's impulse response throughout the measurement region. This allows one to actually observe the time-domain evolution of the wireless channel's impulse response analagous to a 2-D finite-difference time-domain (FDTD) simulation and illustrates the "channel filming" capability of this measurement technique.

3.4 Spatio-Temporal Channel Analyses

The complete space-time wireless channel captured by the field reconstruction-based spatio-temporal channel sounder enables a broad range of analyses for characterizing the wireless channel or studying the underlying radio wave propagation. Generally, these analyses fall into two categories: 1) statistical analyses useful for describing the wireless channel as a stochastic process and 2) filtering techniques useful for dissecting and decomposing the wireless channel.

This section will illustrate these analyses using data collected from the indoor channel measurement depicted in Figure 26. An indoor, non-line-of-sight wireless channel was measured using the field reconstruction-based spatio-temporal channel sounder. The blue squares indicate the pair of closed concentric contours bounding the measurement region. The distance from the transmit antenna to the center of the rectangular measurement region was 5.2 m. The distance between the transmit antenna and the receiver's "reference" antenna was 6.2 m. Numerous scatterers were in the environment, as indicated by the dashed boxes in Figure 26. The fill color indicates the approximate height of each scatter: short scatters had a height of less

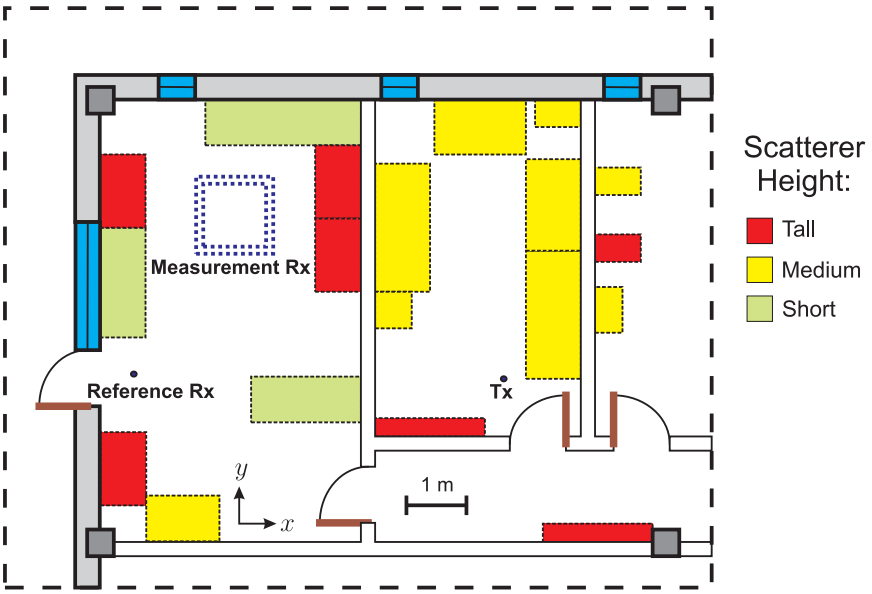

Figure 26: The field reconstruction-based spatio-temporal channel sounder was used to measure the indoor non-line-of-sight wireless channel throughout a rectangular measurement region. The red, orange, and green boxes indicate potential scatterers in the environment. The legend indicates the approximate height of each scatterer.

than 3 ft, medium scatterers had a height between 3 and 5 ft, and tall scatterers had a height greater than 5 ft. Figure 27 presents a series of time-domain wireless channel "snapshots" obtained from the indoor measurement depicted in Figure 26. The "snapshots" reveal the complex dynamics of the indoor spatio-temporal channel.

3.4.1 Preliminaries

Before beginning discussion of the analyses, we briefly review the notation and terminology that will be used throughout this section. Here, the complex-baseband wireless channel refers to the frequency- and 2-D space-dependent function, $h(f, \mathbf{r})$. Physically, $h(f, \mathbf{r})$ may be interpreted as the phasor voltage received by a stationary receive antenna at position $\mathbf{r}$ due to a stationary transmitter broadcasting a continuous tone at frequency $f + f_0$ in an environment that is time-invariant. Implicit in our representation of the complex-baseband wireless channel and related Fourier transforms is a time-dependence of $e^{j2\pi f_0 t}$ for the corresponding real, passband wireless channel, whereby a plane wave propagating in the $\hat{\mathbf{k}}$ direction with wavenumber, k_0, at the

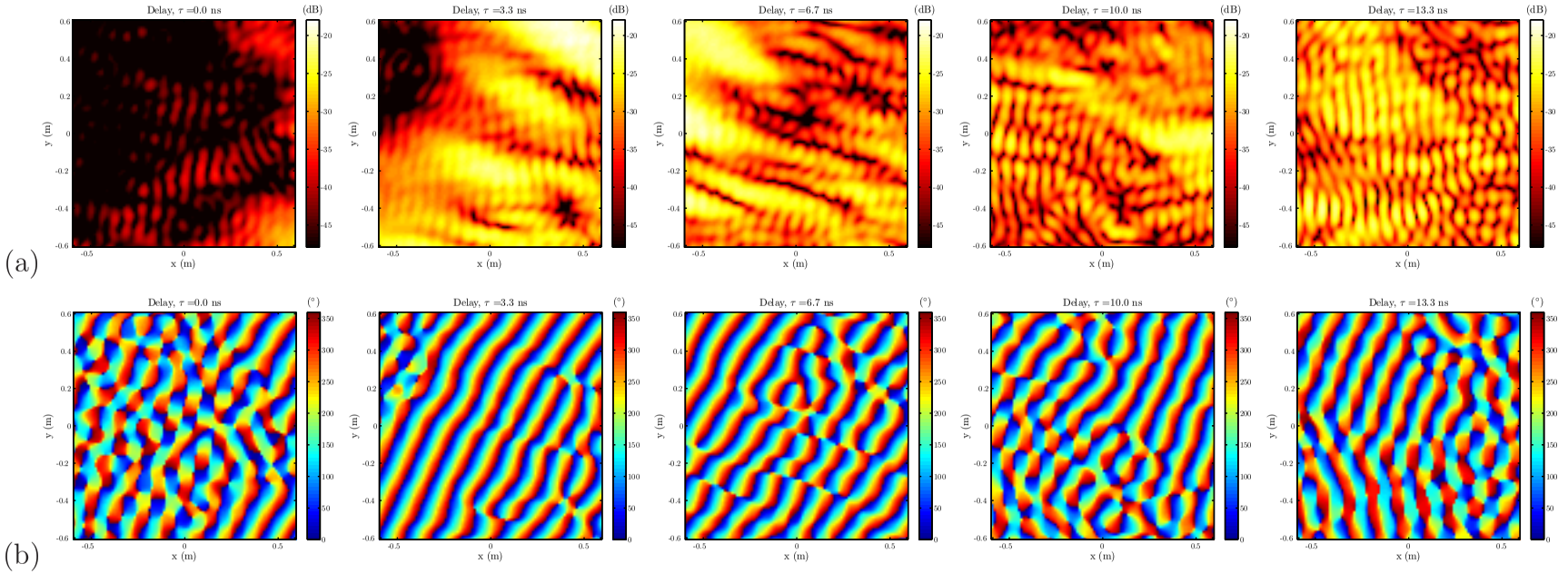

Figure 27: The wireless channel impulse response for the indoor non-line-of-sight wireless channel: (a) magnitude and (b) phase.

carrier frequency, f_0, exhibits a space-time dependence of the form, $e^{j(2\pi f_0 t - k_0 \hat{\mathbf{k}}\cdot\mathbf{r})}$.

The Fourier transform of the wireless channel with respect to frequency, f, is defined as the *channel impulse response* [33]. Mathematically, the channel impulse response, $H(\tau;\mathbf{r})$, is given by

$$H(\tau;\mathbf{r}) = \int h(f,\mathbf{r}) e^{j2\pi f\tau}\, df \tag{83}$$

where τ denotes the *absolute delay* of arriving multipath components with respect to the time at which the channel was excited. The field reconstruction-based spatio-temporal channel sounder records the wireless channel to within some constant phase, which results in an unknown timing offset. Thus, for the measurements presented here, τ, actually represents *excess delay*, which is measured with respect to the first arriving multipath component. Absolute delay and excess delay are related by a constant offset that corresponds to the propagation delay of the first arriving multipath component.

The Fourier transform of the wireless channel with respect to 2-D space, $\mathbf{r}$, is defined as the *plane wave spectrum* [101]. Mathematically, the plane wave spectrum, $H(\mathbf{k};f)$, is given by

$$H(\mathbf{k};f) = \int h(f,\mathbf{r}) e^{j\mathbf{k}\cdot\mathbf{r}}\, d\mathbf{r} \tag{84}$$

where $\mathbf{k}$ is the *wavevector* that indicates spatial frequency in two dimensions. Thereby, the plane wave spectrum describes the 2-D spatial frequency content of the wireless channel.

The Fourier transform of the wireless channel with respect to both frequency, f, and 2-D space, $\mathbf{r}$, is defined as the *channel transfer function*. The mathematical definition for the channel transfer function, $H(\tau,\mathbf{k})$, follows from Eqs. (83) and (84):

$$H(\tau,\mathbf{k}) = \iint h(f,\mathbf{r}) e^{j\mathbf{k}\cdot\mathbf{r}} e^{j2\pi f\tau}\, df\, d\mathbf{r} \tag{85}$$

Finally, we note that the following sections are intended as an overview into potential analysis techniques and are by no means complete. A more thorough discussion of the statistical wireless channel analyses may be found in a variety of sources (cf. [33]). Unfortunately, there is very little documentation on space-time filtering techniques, though the fundamentals may be gleaned from signal processing [13], digital image processing [38], space-time wireless channel theory [33], and classical electromagnetic theory [101].

3.4.2 Envelope Distributions

The envelope probability density function (PDF) describes the distribution of the wireless channel's magnitude. This metric may be used to develop stochastic channel models or to specify fade margins for wireless systems. In practice, it is more convenient to use measurement data to generate empirical cumulative distribution functions (CDF) rather than PDFs. Theoretical CDFs may then be fit to these empirical CDFs to determine the corresponding theoretical PDF that best describes the wireless channel's envelope.

3.4.2.1 Frequency-Dependent envelope CDF

The conventional narrowband envelope CDF describes the distribution of the wireless channel's magnitude for a single frequency. This frequency-dependent envelope CDF is typically compiled from channel measurements taken throughout a region of space. Fig. 28 presents several narrowband CDFs for the indoor wireless channel depicted in Fig. 27. In generating the CDFs, the envelope data at each frequency was normalized by the root-mean-square (RMS) channel envelope. For comparison, Fig. 27 also shows the theoretical envelope CDF for a unit power Rayleigh fading channel. The Rayleigh CDF is given by

$$F_x(x) = 1 - e^{-\frac{x^2}{\sigma^2}} \text{ for } x \geq 0 \tag{86}$$

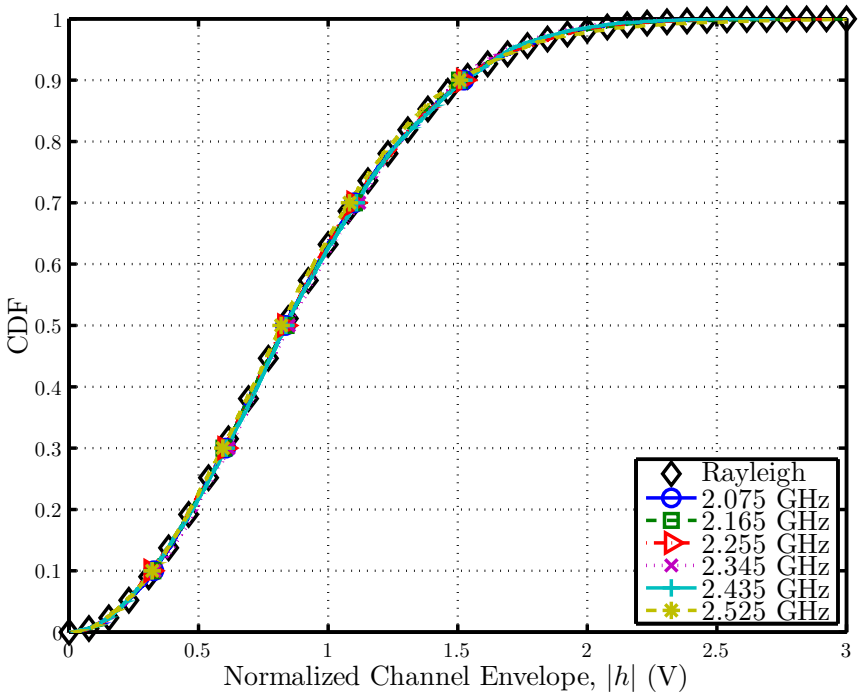

Figure 28: Cumulative distribution functions for the wireless channel's envelope at select frequencies. At each frequency, the data was normalized by the wireless channel's RMS envelope. The diamonds indicate the theoretical envelope CDF for a unit power Rayleigh Channel.

where $\sigma^2 = 1$ for a unit power Rayleigh fading channel. There is consistent agreement in the CDFs for all frequencies, indicating that the wireless channel's narrowband fading distribution follows a Rayleigh distribution.

3.4.2.2 Delay-Dependent Envelope CDF

The large bandwidth of the measurement data also enables the wireless channel's delay-dependent envelope CDF to be constructed. This CDF indicates the distribution of the wireless channel's magnitude as a function of delay and may be determined from the channel impulse response, $H(\tau; \mathbf{r})$. Fig. 29(a) presents a contour map of the delay-dependent envelope CDF for the indoor wireless channel depicted in Fig. 27. The CDF indicates that as the excess delay, τ, increases, the spread of the envelope distribution decreases. This is further evidenced by Fig. 29(b), which shows the maximum-likelihood estimate of the Rayleigh distribution parameter, σ^2, as a

function of delay. Recalling that σ^2 is the average power in a Rayleigh distribution, Fig. 29(b) reveals that the average power in the channel impulse response decreases with increasing delay.

3.4.3 Spatial Analysis

The spatial characteristics of the wireless channel provide information useful for designing wireless systems that exploit the channel's spatial diversity as well as understanding the channel's spatial fading characteristics.

3.4.3.1 2-D Spatial Autocorrelation

The wireless channel's frequency-dependent 2-D spatial autocorrelation, $C_h(\Delta\mathbf{r})$, describes the channel's spatial correlation for some 2-D displacement, $\Delta\mathbf{r}$. The 2-D spatial autocorrelation is given by

$$C_h(\Delta\mathbf{r}) = \left\langle \int h(f,\mathbf{r})h^*(f,\mathbf{r}+\Delta\mathbf{r})\,d\mathbf{r} \right\rangle_f \tag{87}$$

where $\langle\rangle_f$ denotes the ensemble average with respect to frequency, f. In practice it is more useful to consider the channel's 2-D unit autocovariance, $\varrho_h(\Delta\mathbf{r})$. The unit autocovariance is a normalized form of the autocorrelation that facilitates comparisons between channels with different average powers [33]. The unit autocovariance is given by

$$\varrho_h(\Delta\mathbf{r}) = \frac{C_h(\Delta\mathbf{r})}{C_h(\mathbf{0})} \tag{88}$$

Figure 30 presents the 2-D unit autocovariance of the indoor wireless channel shown in Fig. 27. In the evaluation of Eq. (87), the frequency averaging was performed over a 450 MHz band corresponding to $f \in [-225, 225]$ MHz. As was discussed in [83], superimposing an arbitrary array onto the 2-D unit autocovariance allows one to rapidly compute SIMO correlation matrices using actual measurement data.

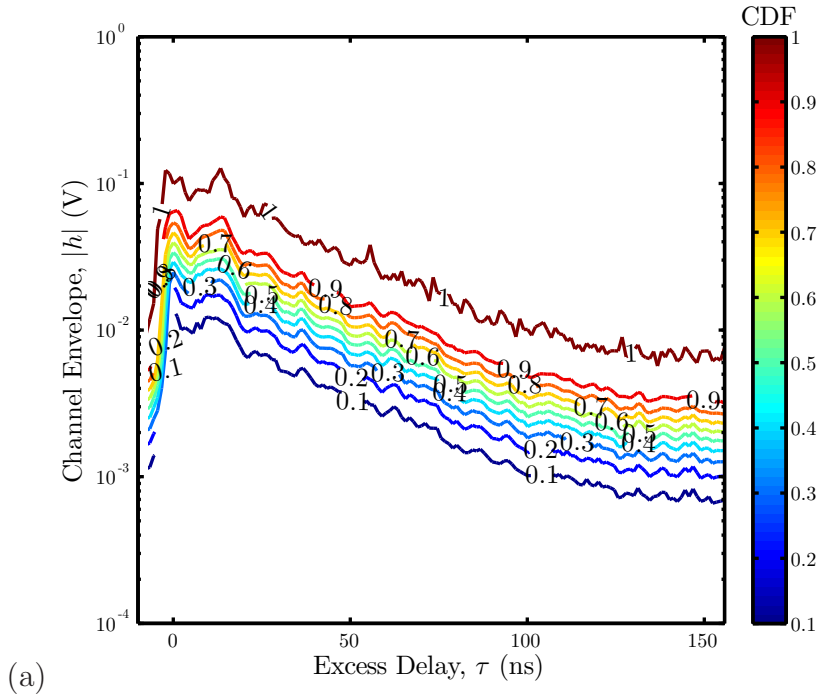

(a)

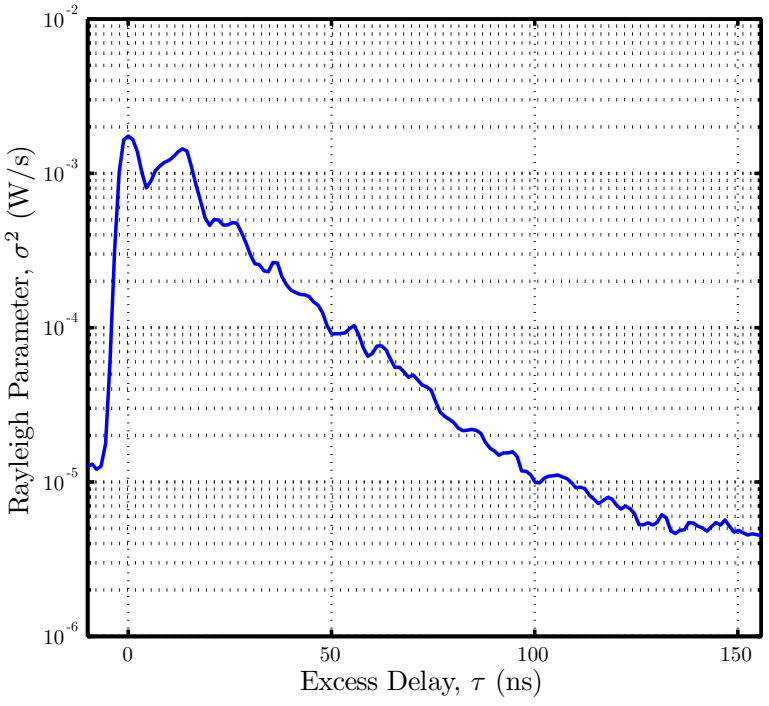

(b)

Figure 29: (a) The cumulative distribution function (CDF) of the wireless channel's envelope with respect to delay, and (b) the maximum-likelihood estimate of the Rayleigh parameter, σ^2, as a function of delay.

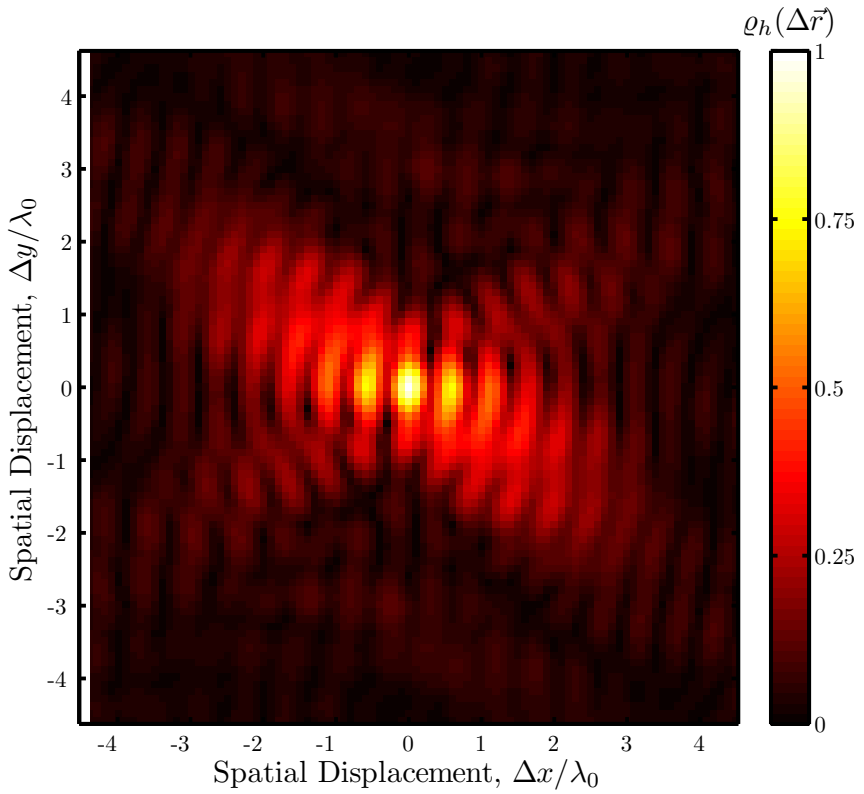

Figure 30: The wireless channel's 2-D spatial autocovariance reveals the average correlation in the wireless channel for some vector spatial displacement, $\Delta\mathbf{r}$.

3.4.3.2 1-D Spatial Autocorrelation

Using the 2-D unit autocovariance given in (88), one may also calculate a general distance-dependent autocovariance function that indicates the spatially-averaged correlation between two observation points separated by a distance, $\Delta\rho$. The one-dimensional spatial autocovariance may be determined by averaging out the angular dependence of the 2-D spatial autocovariance, $\varrho_h(\Delta\mathbf{r})$:

$$\varrho_h(\Delta\rho) = \frac{1}{2\pi}\int_0^{2\pi} \varrho_h(\Delta\mathbf{r})\, d\Delta\phi \tag{89}$$

In Eq. (89), $\Delta\mathbf{r}$ is a two-component vector given by $(\Delta\rho, \Delta\phi)$. Figure 31 presents the distance-dependent autocovariance for the wireless channel presented in Fig. 27. To calculate $\varrho_h(\Delta\rho)$, the 2-D unit autocovariance presented in Fig. 30 was interpolated onto a polar grid and then averaged with respect to angle. Figure 31 shows two different empirical autocovariances corresponding to frequency averaging over bandwidths of 10 MHz and 450 MHz. For comparison, the theoretical autocovariance for a Rayleigh wireless channel as given by [19]

$$\varrho_h(\Delta\rho) = J_0(k_0\Delta\rho) \tag{90}$$

is also presented. In Eq. (90), $J_0(\cdot)$ denotes the zeroth order Bessel function of the first kind, and k_0, is the wavenumber corresponding to the measurement center frequency, $f_0 = 2.3$ GHz. The 10 MHz bandwidth autocovariance shows excellent agreement with the theoretical autocovariance for a narrowband Rayleigh wireless channel. As might be expected, the 450 MHz bandwidth shows good agreement with the theoretical autocovariance for small displacements, $\Delta\rho$, but tends to show a smaller correlation for larger displacements. This improved decorrelation is due to the frequency selectivity of the 450 MHz bandwidth wireless channel.

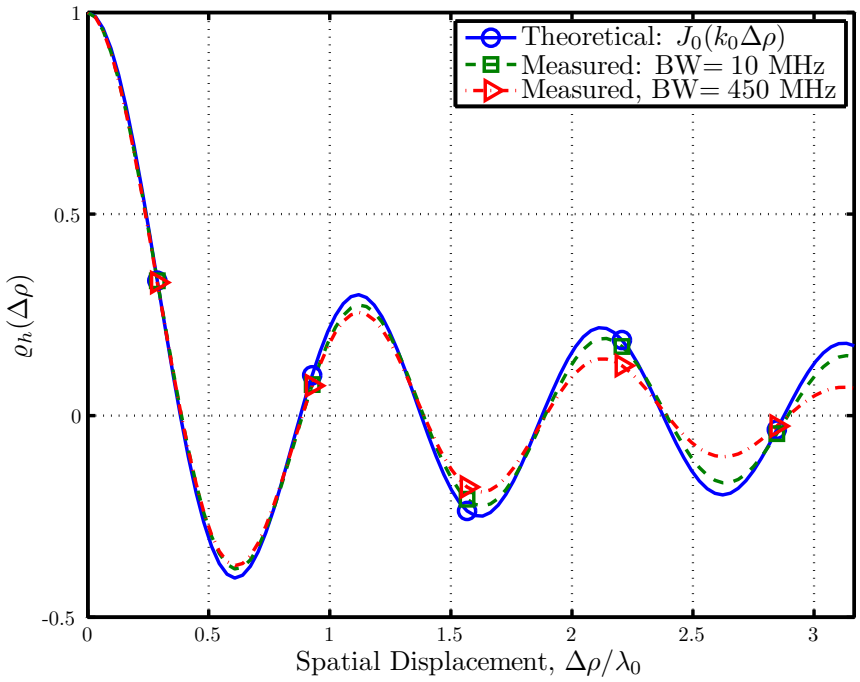

Figure 31: The wireless channel's purely distance-dependent spatial autocovariance. The two empirical autocovariance curves are compared to the theoretical spatial autocovariance for a Rayleigh channel. The spatial correlation obtained from the 450 MHz bandwidth wireless channel shows less correlation than the 10 MHz bandwidth channel for larger displacements, $\Delta\rho$.

3.4.3.3 Wavevector Spectrum

The wireless channel's wavevector spectrum describes the wireless channel's power spectral density for a given 2-D wavevector, $\mathbf{k}$. The wavevector spectrum is particularly useful for studying the plane waves contributing to the wireless channel, because it contains information about both homogeneous and inhomogeneous plane waves. The wavevector spectrum, $S_h(\mathbf{k})$, is given by the 2-D Fourier transform of the wireless channel's 2-D autocorrelation:

$$S_h(\mathbf{k}) = \int C_h(\Delta\mathbf{r}) e^{j\mathbf{k}\cdot\mathbf{r}}\, d\mathbf{r} \tag{91}$$

Figure 32 presents the wavevector spectrum for the indoor wireless channel from Fig. 27. The majority of the power density lies along a circle of radius k_0, indicating that any contributions from inhomogeneous plane waves are negligible.

3.4.3.4 Power Angle Spectrum

Provided that the wireless channel was measured far enough from any scatterers such that the contributing plane waves are homogenous, the 2-dimensional wavevector spectrum, $S_h(\mathbf{k})$, may be mapped to a 1-dimensional power angle spectrum, $p(\phi)$, without loss of information. The power angle spectrum describes how the received power is distributed with respect to azimuth angle-of-arrival, ϕ. This simple physical interpretation makes the power angle spectrum a more convenient analysis tool than the wavevector spectrum, though it should be emphasized that this interpretation breaks down if inhomogeneous plane waves are present. The power angle spectrum is calculated by first integrating the wavevector spectrum with respect to wavenumber, k:

$$S_h(\beta) = \int_0^\infty S_h(\mathbf{k}) k\, dk = \int_0^\infty S_h(k, \beta) k\, dk \tag{92}$$

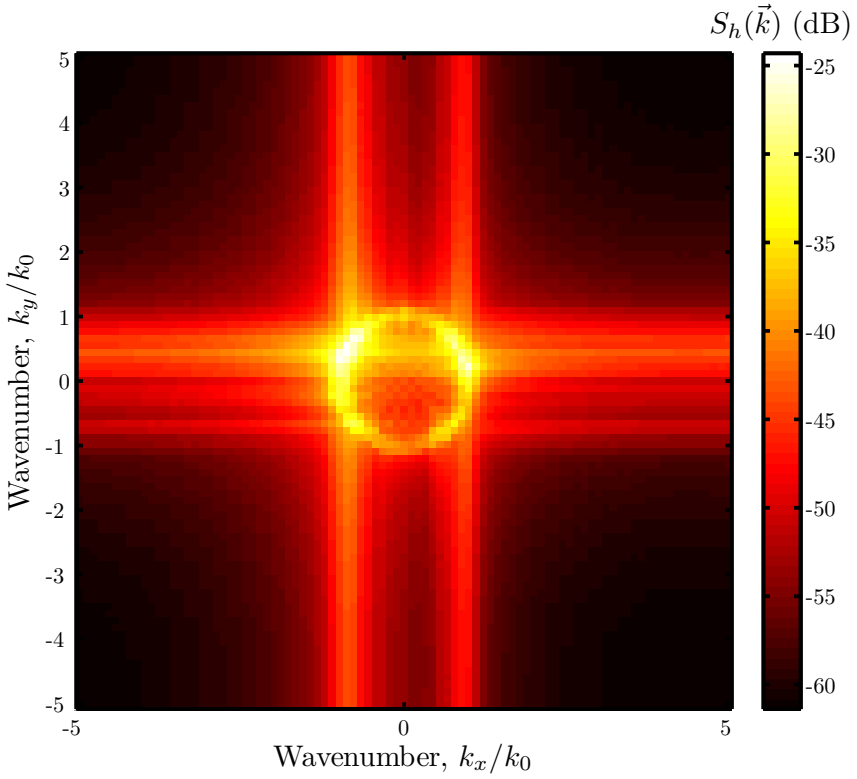

Figure 32: The wavevector spectrum reveals how the power in the wireless channel is distributed with respect to wavevector, **k**. This provides insight into the wireless channel's underlying radio wave propagation.

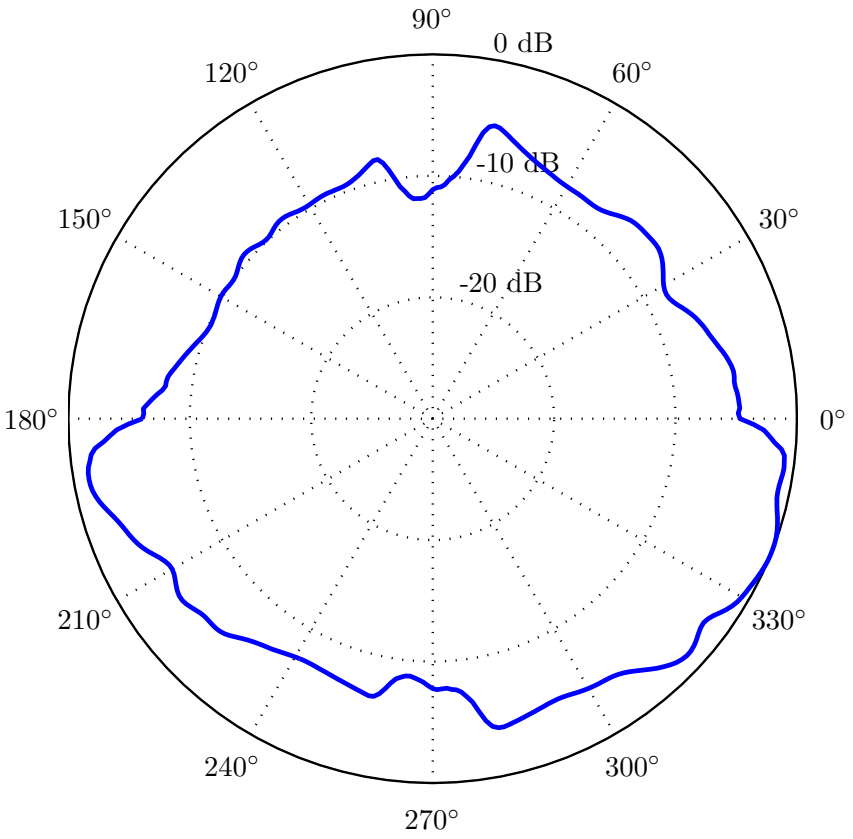

Figure 33: The power angle spectrum reveals how the received power is distributed as a function of incident azimuth angle, ϕ.

In Eq. (92), $\mathbf{k}$ is a two-component vector represented in polar coordinates as (k, β). Whereas the azimuth angle ϕ in the power angle spectrum, $p(\phi)$, indicates the angle-of-arrival of power, β in Eq. (92) indicates the direction of propagation of power. Thus, noting that $\beta = \phi + \pi$, the power angle spectrum, $p(\phi)$, is given by

$$p(\phi) = S_h(\phi + \pi) \tag{93}$$

Figure 33 shows the power angle spectrum for the measured indoor wireless channel.

3.4.4 Frequency Analysis

The frequency characteristics of the wireles channel provide information useful for designing wideband wireless systems that exploit the channel's frequency diversity as well as understanding the channel's frequency-dependent fading characteristics.

3.4.4.1 Frequency Autocorrelation

The wireless channel's frequency autocorrelation, $C_h(\Delta f)$, reveals the wireless channel's frequency selectivity and may be used to determine the channel's coherence bandwidth. The frequency autocorrelation is given by

$$C_h(\Delta f) = \left\langle \int h(f, \mathbf{r}) h^*(f + \Delta f, \mathbf{r})\, df \right\rangle_{\mathbf{r}} \tag{94}$$

where Δf is a relative frequency displacement and $\langle \rangle_{\mathbf{r}}$ denotes the ensemble average with respect to 2-D position, $\mathbf{r}$. As with the spatial autocorrelation, it is more useful in practice to consider the frequency autocovariance, $\varrho_h(\Delta f)$, given by

$$\varrho_h(\Delta f) = \frac{C_h(\Delta f)}{C_h(0)} \tag{95}$$

Figure 34 shows the frequency autocovariance of the measured indoor wireless channel. The wireless channel rapidly decorrelates for frequency displacements on the order of tens of MHz.

3.4.4.2 Delay Spectrum

The wireless channel's delay spectrum describes the wireless channel's power spectral density for a given delay, τ, and is particularly useful for studying the dispersiveness of wideband wireless channels. The delay spectrum, $S_h(\tau)$, is given by the inverse Fourier transform of the wireless channel's frequency autocorrelation:

$$S_h(\tau) = \int C_h(\Delta f) e^{j2\pi\tau f}\, df \tag{96}$$

Figure 35 shows the delay spectrum of the measured indoor wireless channel. It is worth noting that the delay spectrum in Fig. 35 and the plot of the Rayleigh parameter, σ^2, as a function of delay in Fig. 29(b) are nearly identical, because both describe the channel's average power density as a function of delay. However, σ^2, is only applicable because the wireless channel's envelope is Rayleigh distributed with

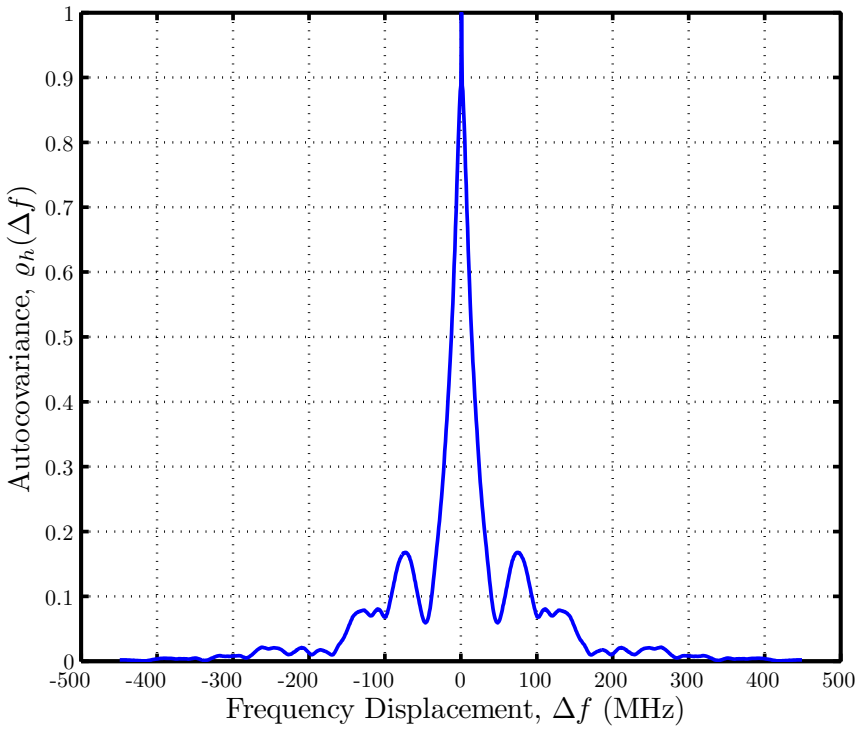

Figure 34: The frequency autocovariance shows the wireless channel's correlation for some frequency displacement, Δf. This reveals the frequency selectivity of the wireless channel.

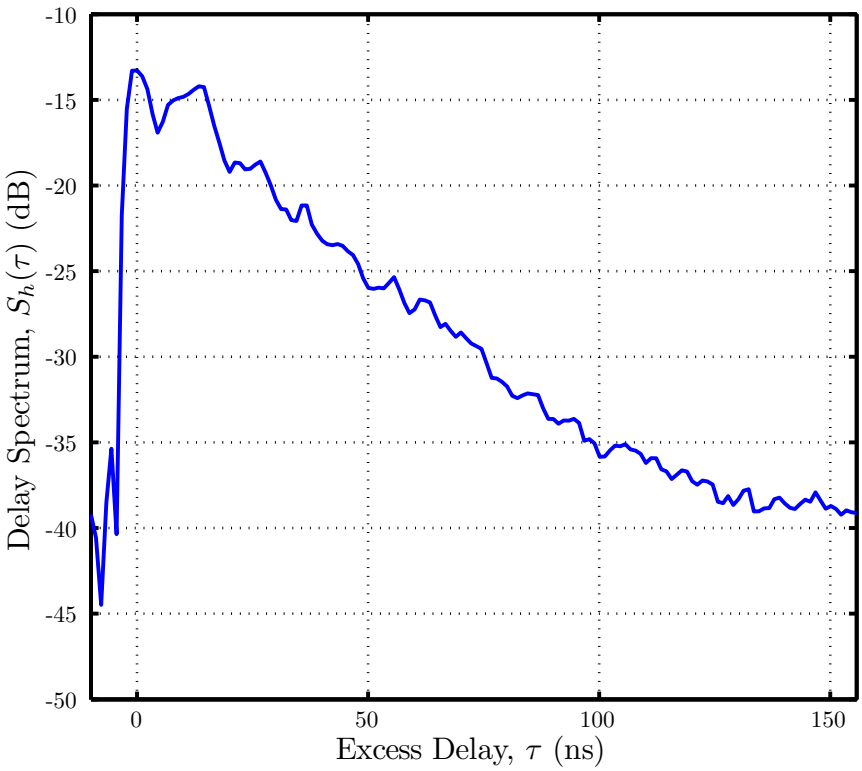

Figure 35: The wireless channel's delay spectrum reveals how the power in wideband channels is distributed across delay, τ.

respect to delay, τ. The delay spectrum, $S_h(\tau)$, is the more generally applicable method of evaluating power density as a function of delay.

3.4.5 Joint Space-Frequency Analysis

The space and frequency dependence of the wireless channel may also be jointly analyzed. For the wireless channel spanning frequency and 2-dimensional space, performing these joint analyses and presenting the resulting data can be challenging due to the size and structure of the data set. However, for many practical applications, the resulting 3-dimensional data set may be transformed into a more amenable and presentable 2-dimensional data set.

3.4.5.1 Space-Frequency Autocorrelation

The full autocorrelation of the wireless channel with respect to frequency and 2-D space is given by

$$C_h(\Delta f, \Delta \mathbf{r}) = \iint h(f, \mathbf{r}) h^*(f + \Delta f, \mathbf{r} + \Delta \mathbf{r})\, d\mathbf{r}\, df \tag{97}$$

wherein the integration is taken with respect to both frequency, f, and 2-D space, $\mathbf{r}$. The full wireless channel autocorrelation provides insight into the channel's correlation for some frequency displacement, Δf, and vector displacement, $\Delta \mathbf{r}$. The single-dependency autocorrelation functions may be recovered from $C_h(\Delta f, \Delta \mathbf{r})$ by setting either of the dependent variables to zero. That is, $C_h(\Delta f, \mathbf{0}) = C_h(\Delta f)$ and $C_h(0, \Delta \mathbf{r}) = C_h(\Delta \mathbf{r})$.

Averaging Eq. 97 with respect to displacement angle, $\Delta\phi$, yields a practical distance-dependent space-frequency autocorrelation, $C_h(\Delta f, \Delta\rho)$, given by

$$C_h(\Delta f, \Delta\rho) = \int_0^{2\pi} C_h(\Delta f, \Delta \mathbf{r})\, d\Delta\phi \tag{98}$$

Normalizing $C_h(\Delta f, \Delta\rho)$ yields the corresponding autocovariance, $\varrho_h(\Delta f, \Delta\rho)$:

$$\varrho_h(\Delta f, \Delta\rho) = \frac{C_h(\Delta f, \Delta\rho)}{C_h(0, 0)} \tag{99}$$

Figure 36 presents the purely distance-dependent space-frequency autocovariance, $\varrho_h(\Delta f, \Delta\rho)$ for the measured indoor wireless channel. As with the the full space-frequency autocorrelation, $\varrho_h(\Delta f, \Delta \mathbf{r})$, the frequency or distance-dependent spatial autocovariance functions may be determined from $\varrho_h(\Delta f, \Delta\rho)$ by setting $\Delta\rho = 0$ or $\Delta f = 0$, respectively. Thus, Fig. 36 reveals the separability of the wireless channel's distance-dependent space-frequency autocovariance whereby $\varrho_h(\Delta f, \Delta\rho) = \varrho_h(\Delta f)\varrho_h(\Delta\rho)$.

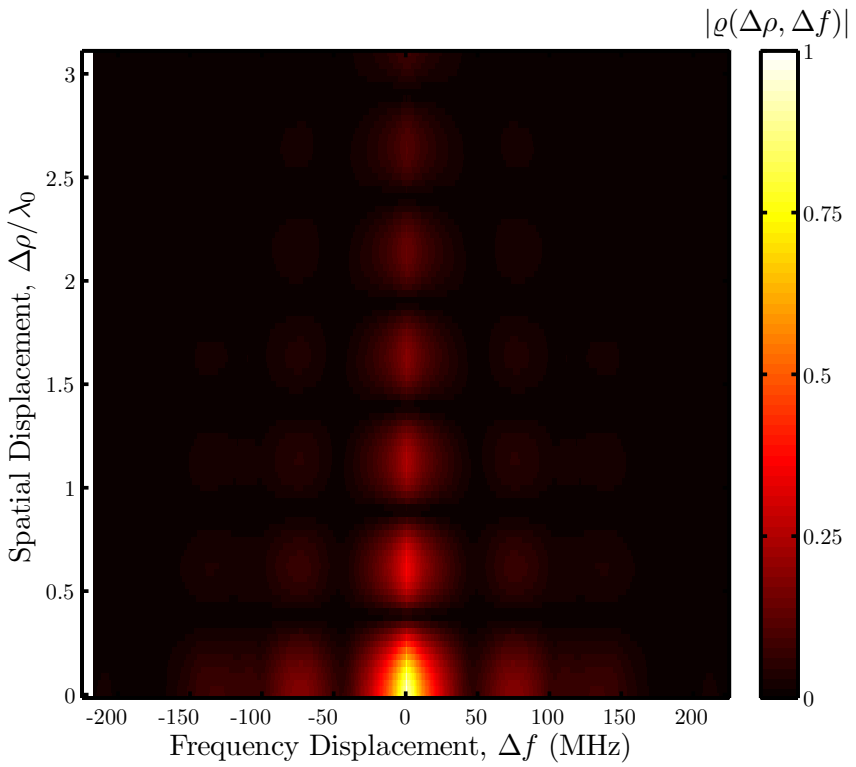

Figure 36: The wireless channel's distance-dependent space-frequency autocovariance describes the wireless channel's correlation with respect to both spatial displacement, $\Delta\rho$, and frequency displacement, Δf.

3.4.5.2 Delay-Wavevector Spectrum

With the full space-frequency autocorrelation, one may compute the wireless channel's delay-wavevector spectrum, $S_h(\tau, \mathbf{k})$, through a Fourier transform of the autocorrelation function with respect to both space, $\Delta\mathbf{r}$, and frequency, Δf:

$$S_h(\tau, \mathbf{k}) = \iint C_h(\Delta f, \Delta\mathbf{r}) e^{j2\pi\tau f} e^{j\mathbf{k}\cdot\mathbf{r}}\, df\, d\mathbf{r} \tag{100}$$

The delay-wavevector spectrum is a useful albeit cumbersome tool for studying the propagation characteristics of the wireless channel. It should be noted that integrating the delay-wavevector spectrum, $S_h(\tau, \mathbf{k})$, with respect to delay, τ, will yield the wavevector spectrum, $S_h(\mathbf{k})$; likewise, integrating with respect to the wavevector, $\mathbf{k}$, will yield the delay spectrum, $S_h(\tau)$.

3.4.5.3 Power Delay-Angle Spectrum

Under the assumption that only homogeneous plane waves are contributing to the measured wireless channel, the 3-dimensional delay-wavevector spectrum, $S_h(\tau, \mathbf{k})$, may be mapped to a 2-dimensional power delay-angle spectrum, $p(\tau, \phi)$. The procedure follows that for deriving the power angle spectrum, $p(\phi)$, in Eq. (93). The delay-wavevector spectrum is first integrated with respect to wavenumber, k:

$$S_h(\tau, \beta) = \int_0^\infty S_h(\tau, \mathbf{k}) k\, dk \tag{101}$$

Then the direction-of-propagation, β, is mapped to angle-of-arrival, ϕ:

$$p(\tau, \phi) = S_h(\tau, \phi + \pi) \tag{102}$$

The power delay-angle spectrum, $p(\tau, \phi)$, reveals how the received power is distributed across delay, τ, and incident angle, ϕ, due to homogeneous plane waves arriving with different times- and angles-of-arrival. Integrating $p(\tau, \phi)$ with respect to delay, τ, will yield the conventional power angle spectrum, $p(\phi)$.

Figure 37 presents the power delay-angle spectrum for the measured indoor wireless channel. In the plot, radial distance corresponds to excess delay, τ, whereas angle corresponds to the incident angle, ϕ. The Cartesian axes provide a scale for excess delay. Comparing the power delay-angle spectrum with Fig. 26's diagram of the measurement environment, it is clear that the first arriving multipath component at an incident angle of $\phi = 330°$ corresponds to the line-of-sight path between the transmitter and the measurement region. The next major cluster of multipath components arriving at $\tau = 7$ ns and $\phi = 340°$ is attributed to a reflection off of the interior wall to the right of the transmitter in Fig. 26. The cluster arriving at $\tau = 13$ ns and $\phi = 195°$ corresponds well with a reflection off the large exterior window on the left side of the measurement diagram. The smaller cluster at $\tau = 16$ ns and $\phi = 218°$ is attributed to scattering off of the metal exterior door just below the large exterior window in the diagram. Other multipath arriving at $\tau = 13$ ns and $\phi = 50°$ are attributed to reflections off of the upper exterior wall in Fig. 26.

3.4.6 Space-Time Processing

The previous sections discussed various analysis tools for studying the statistical properties of the wireless channel. This section will provide an overview of how the field reconstruction-based spatio-temporal channel sounder's space-time wireless channel, $h(f, \mathbf{r})$, may be processed to study the underlying radio wave propagation. The discussion will emphasize filtering techniques enabled by complete knowledge of the wireless channel with respect to frequency and 2-D space. These filtering techniques will be demonstrated through the removal of the spectral content marked in the wireless channel's power delay-angle spectrum in Figure 38. By filtering, we refer to processing techniques that maintain the size and dimensionality of the data. Additional processing techniques will be briefly discussed at the end of this section. It should be emphasized that there has been very little prior research into space-time

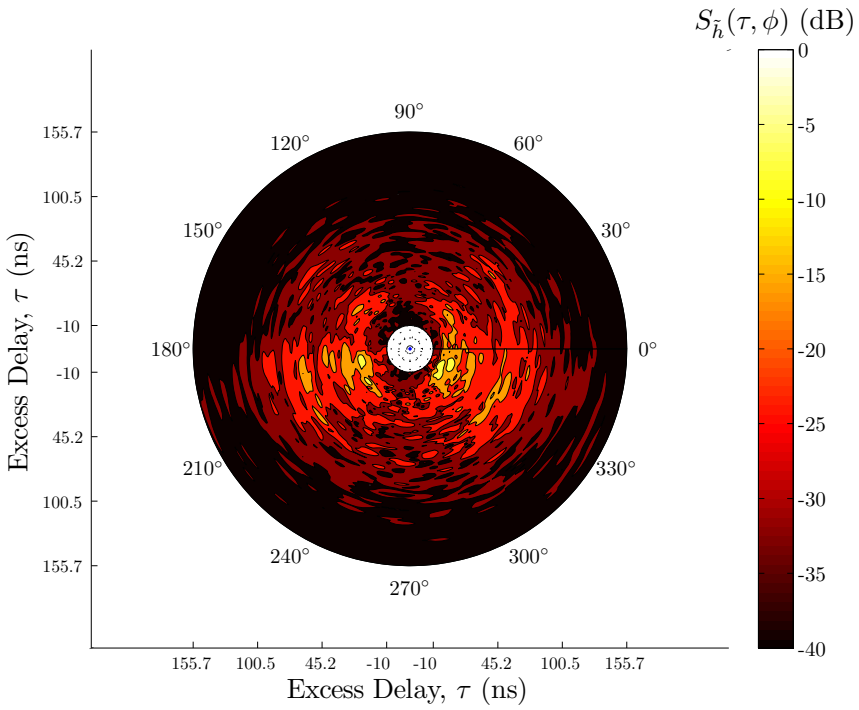

Figure 37: The wireless channel's power delay-angle spectrum describes the distribution of received power with respect to delay, τ, and incident angle, ϕ

filtering techniques for either wireless channels or electromagnetic fields. Thus, the discussion presented here is considered introductory and by no means complete.

3.4.6.1 Temporal Filtering

Temporal filtering is most commonly performed by time-gating the wireless channel's impulse response to remove unwanted multipath components based upon their time-of-arrival. Time-gating the wireless channel's impulse response is analagous to smoothing the wireless channel's frequency response and thereby reduces the frequency-selectivity of the wireless channel. In the most simplistic implementation, the wireless channel's impulse response $H(\tau;\mathbf{r})$, is masked by a rectangular window so as to remove multipath components with arrival times outside of the window. However, there are two problems with this approach, both of which may be resolved by using smooth and continuous windowing functions.

First, as is well-known from signal processing theory, the rectangular window's

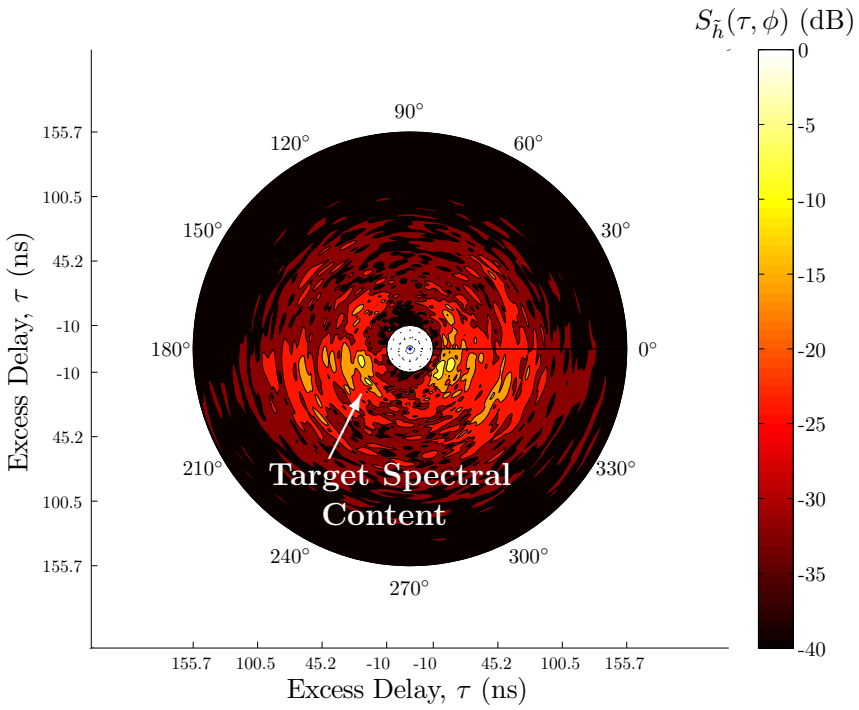

Figure 38: Filtering techniques will be applied to the indoor wireless channel in attempt to remove the spectral content indicated in the power delay-angle spectrum at $\tau = 16$ ns and $\phi = 218°$.

sharp cut-off will introduce oscillations in the wireless channel's frequency response. Smooth and continuous windows such as the Butterworth, Hamming, or Gaussian function have lower spectral side-lobes than the rectangular window, and thereby induce less oscillatory behavior in the filtered channel's frequency response.

Second, if the temporal resolution of the channel measurements exceeds the time required for a wave to propagate across the 2-D mesurement region, then imposing a rectangular window can cause a multipath component to vanish mid-flight. That is, a multipath component could be incident upon the 2-D measurement region, propagate across part of the measurement region, and then suddenly disappear because the wireless channel's impulse response has been "switched off". Similarly, at the start of this temporal window, multipath components can suddenly appear within the measurement region as the wireless channel's impulse response is "switched on". In contrast, a smooth and continuous windowing function will act as a dimmer switch

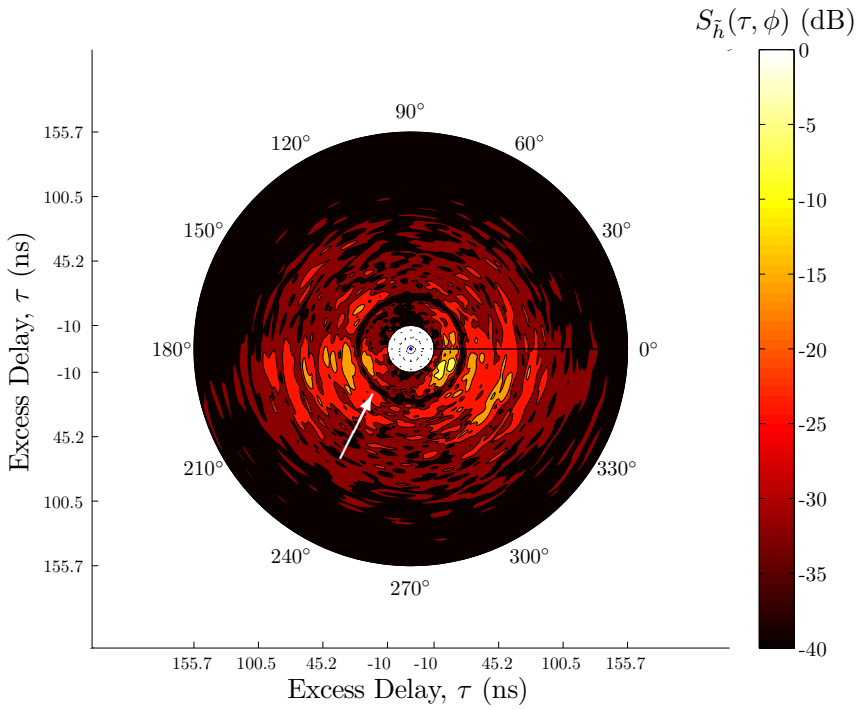

Figure 39: Temporal filtering removes all spectral content at and around a given delay, τ. The result is a ring-shaped null in the power delay-angle spectrum.

that gradually turns the wireless channel "on" or "off". In effect, this applies a delay-dependent attenuation to the measured wireless channel. Though this behavior is still non-physical, it is the best that can be achieved by considering only the wireless channel's temporal information.

Figure 39 demonstrates the effect of temporal filtering on the wireless channel's power delay-angle spectrum. A notch reject filter was constructed from a Hamming window with a -3 dB width of 8 ns centered about the target excess delay of $\tau = 16$ ns. This purely real notch filter was then applied to the channel impulse response, $H(\tau; \mathbf{r})$. As Fig. 39 indicates, temporal filtering creates a ring-shaped null in the power delay-angle spectrum that severely attenuates the intended spectral content. Though effective, temporal filtering is rather crude, because it removes *all* spectral content at the target delay.

3.4.6.2 Spatial Filtering

Two-dimensional spatial filtering provides a powerful tool for dissecting the measured wireless channel, as it allows incident waves to be isolated or removed based upon their angle-of-arrival. However, there have been no prior investigations into spatial filtering of the wireless channel, likely because there was no efficient technique for measuring the wireless channel throughout a 2-D region. The objective of spatial filtering is to apply a 2-D spectral mask to the wireless channel's plane wave spectrum, $H(\mathbf{k}; f)$, so as to attenuate spectral content corresponding to power incident from a given angle-of-arrival, ϕ, as indicated by the wavevector, $\mathbf{k}$. As with temporal filtering, the mask (i.e., window) that is applied to the plane wave spectrum should be smooth and continuous to avoid ringing in the spatial domain. As with conventional DSP filtering methods, filter synthesis must account for the data's spatial sampling rate and the boundedness of the measurement region, which limits the resolution of the plane wave spectrum. Digital image processing provides some insight for constructing spectral domain filters that pass or reject select wavevector components. It should be noted that whereas digital image filters must exhibit symmetry about the origin to maintain a real-valued image, wireless channel (i.e., electromagnetic field) spatial filters need not be symmetric. The procedure for removing spectral content around a single wavevector is relatively straightforward. A 2-D notch reject filter is constructed around the spectral content to be removed. Multiplying, or masking, the original plane wave spectrum by the 2-D notch reject filter severely attenuates the unwanted spectral content.

For narrowband wireless channel measurements, if all of the contributing plane waves are homogeneous and propagating along the horizon, the plane wave spectrum is nominally zero everywhere except along a circle of radius k_0, where k_0 is the wavenumber corresponding to the measurement frequency, f_0. To spatially filter the wireless channel across a band of frequencies, the 2-D notch reject filter's radial

position must be scaled inversely with frequency, f, such that the distance between the origin and the filter's center is the corresponding wavenumber, k. The angle of the filter's center could even be varied with frequency to handle angle- and frequency-dependent "coloring" propagation mechanisms like refraction and diffraction.

It should also be noted that for DSP-based spatial filtering, both the filter and the wireless channel must be zero-padded in the spatial domain before the filter may be multiplied with the channel's plane wave spectrum, $H(\mathbf{k}; f)$, in the wavevector domain. This zero-padding is necessary due to the inherent periodicity of the discrete filter and measurement data, as well as the spatial convolution operation that is implied by multiplication in the wavevector domain [38]. Strictly speaking, the previously discussed time-domain filtering also requires the discrete filter and measurement data to be zero-padded with respect to frequency. However, in practice, the sinc-shaped spectrum of the channel sounder's transmitted signal tends to attenuate the measurement data for large absolute frequencies, $|f|$. This natural frequency-domain roll-off made additionally frequency domain zero-padding unnecessary.

Figure 40 demonstrates the effect of spatial filtering on the wireless channel's power delay-angle spectrum. A 2-D notch reject filter was constructed from a pair of Hamming windows, each with a -3 dB width of 26 rad/m and centered about the target wavenumbers of $k_x = k\cos(218^\circ + 180^\circ)$ and $k_y = k\sin(218^\circ + 180^\circ)$. The addition of 180° converts the angle-of-arrival, ϕ, to the wavevector angle, β. The 2-D notch reject filter was then applied to the plane wave spectrum, $H(\mathbf{k}; f)$. As Fig. 40 indicates, spatial filtering created a sector-shaped null in the power delay-angle spectrum that severely attenuated the intended spectral content. As with temporal filtering, spatial filtering is effective yet crude, because it removes *all* spectral content at the target incident angle.

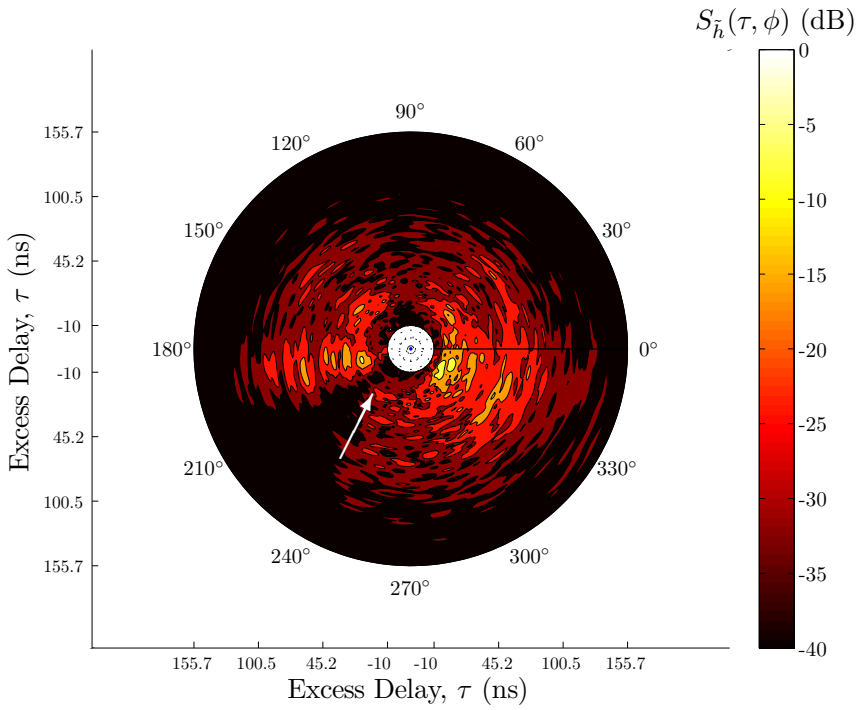

Figure 40: Spatial filtering removes all spectral content at and around a given angle-of-arrival, ϕ. The result is a sector-shaped null in the power delay-angle spectrum.

3.4.6.3 Joint Space-Time Filtering

More precise filtering may be achieved by jointly filtering the wireless channel in both space and time so as to selectively remove unwated multipath components based upon their angle- and time-of-arrival. Thus, the objective is to create delay-dependent spatial filters, or equivalently, frequency-dependent spatial filters. Basic space-time filtering may be performed directly on the channel transfer function, $H(\tau, \mathbf{k})$, by centering a smooth and continuous 3-D notch reject filter over the wavevector and delay at which the spectral content is to be removed. Multiplying, or masking, the original channel transfer function by this 3-D notch reject filter will severely attenuate the unwanted spectral content. As was previously noted, both the discrete filter and discrete measurement data must first be zero-padded with respect to space before the filter and measurement data can be multiplied together in the corresponding delay-wavevector domain.

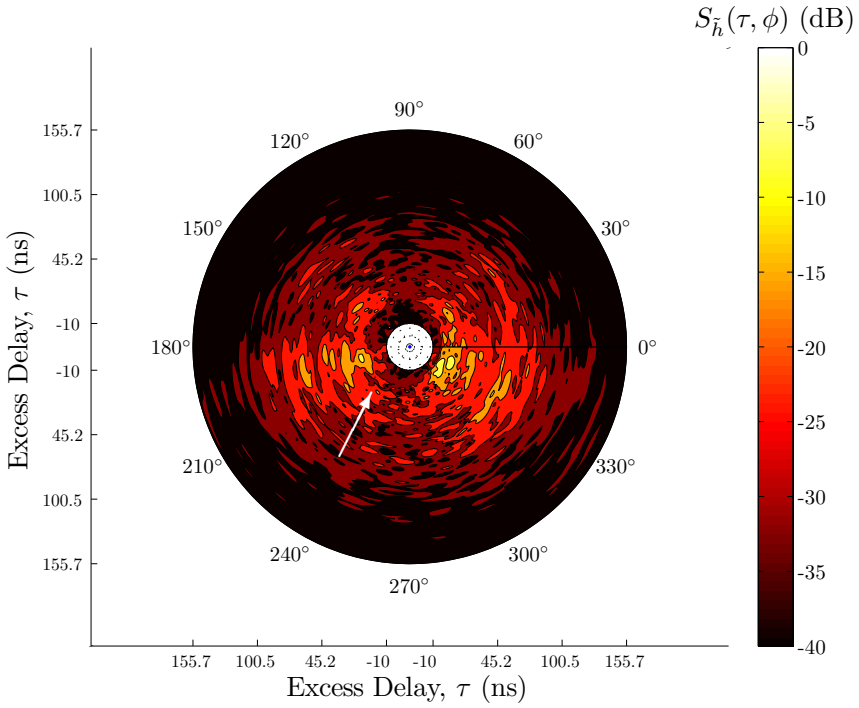

Figure 41: Space-time filtering only removes spectral content at and around a given delay and angle-of-arrival pair, (τ, ϕ). The result is a precisely positioned null in the power delay-angle spectrum.

Figure 41 demonstrates the effect of space-time filtering on the wireless channel's power delay-angle spectrum. A 3-D notch reject filter was constructed from the three Hamming windows used in the previous sections for temporal and spatial filtering. The 3-D notch reject filter was then applied to the channel transfer function, $H(\tau, \mathbf{k})$. As Fig. 41 indicates, space-time filtering creates a very precise and confined null in the power delay-angle spectrum that severely attenuates *only* the intended spectral content.

3.4.7 Other Processing Techniques

By treating the wireless channel as a large rectangular aperture, one may apply conventional array processing techniques to the measurement. Weight-and-sum beam-steering techniques may be used to apply arbitrary array patterns to the measurement aperture [87]. Subspace array processing techniques like multiple signal classification

(MUSIC) and estimation of signal parameters via rotational invariant techniques (ESPRIT) may be used to determine the angle-of-arrival of incident waves with extremely fine resolution [34].

For radio wave propagation studies, the delay-wavevector spectrum corresponding to simulated propagation mechanisms could be used to construct mechanism-specific space-time filters. Applying these mechanism-specific filters to the measurement data would allow researchers to isolate individual radio wave propagation mechanisms. A template-based extraction technique could then be used to characterize the isolated propagation mechanism by fitting the filtered data to an appropriate model.

Another interesting possibility is resampling the wireless channel using a virtual antenna whose pattern differs from the original measurement antenna. Provided that the wireless channel measurements were made with a receive antenna that approximates a Hertzian dipole, the wireless channel could be "remeasured" by a similarly polarized antenna with known complex radiation pattern. The wireless channel's cylindrical wave expansion would simply be reweighted to account for the angular harmonics of the antenna pattern. Accounting for off-the-horizon propagation would likely be complicated, if not impossible. Also, the effect of near-field measurement data and antenna-environment interactions would need to be studied to determine the range of validity of such a "remeasurement" technique.

CHAPTER IV

IN SITU DIFFRACTION MEASUREMENTS

Chapter Summary: This chapter discusses the space-time wireless channel measurements that were used to characterize diffraction by a brick building corner. The field reconstruction-based spatio-temporal channel sounder was used to "film" the wireless channel in the vicinity of a brick building corner for three different transmitter positions. The measurements were repeated for a "PEC" corner configuration wherein the brick building corner was covered with a metallic mesh to emulate a PEC wedge. Channel impulse response snapshots and power delay-angle spectra are presented for each of the six diffraction measurements.

The field reconstruction-based spatio-temporal channel sounder and accompanying space-time processing techniques described in Chapter 3 provide the tools necesary for characterizing individual propagation. Here, we describe how this measurement system was used to "film" the space-time wireless channel in the vicinity of a brick building corner. In the following chapter, we will describe the processing and analysis tools used to isolate the building corner diffraction problem and extract the corresponding diffraction coefficient. Discussion begins by determining the measurement geometry best suited for characterizing the building corner's diffraction coefficient. This is followed by a description of the "PEC" covering that was attached to the brick building corner to emulate a PEC wedge. Wireless channel measurements in the vicinity of this "PEC" wedge provided both a reference data set for evaluating the brick building corner measurements and a crucial validation of the processing and analysis techniques described in Chapter 5. Discussion of the "PEC" covering

is followed by a description of the measurement site and outline of the measurement procedure. The results of the "PEC" and brick building corner measurements are presented at the end of this chapter.

4.1 Measurement Geometry

At first glance, one might suspect that complete characterization of a building corner's diffraction coefficient, $D(\phi, \phi')$, necessitates total field measurements at all possible combinations of incident angle, ϕ', and observation angle, ϕ. Fortunately, Chapter 2's study of the UTD's impedance wedge diffraction coefficient suggests that significantly fewer measurements are necessary.

4.1.1 Reduction of Measurement Space

By employing the UTD formulation described in Eq. (41), the task of determining the diffraction coefficient, $D^{\perp}_{\parallel}{}_{\text{UTD}}(\phi, \phi')$, may be reduced to determining the two pattern functions, $C^i(\phi, \phi')$ and $C^r(\phi, \phi')$. Under the assumption of identical impedance faces these two pattern functions may be completely characterized by their behavior within any one of the eight triangular regions depicted in Fig. 5. Although this reduces the angular measurement space by a factor of eight, characterizing the pattern functions throughout one of these triangular regions remains impractical, because the measurement space is continuous with respect to both ϕ and ϕ'.

Figure 42 considers the implications of a more simplified measurement configuration wherein the transmitter is stepped through a discrete set of incident angles $\phi' \in \{\phi'_1, \phi'_2, \phi'_3\}$ while the receiver is swept through a continuous range of observation angles, $\phi \in [n\pi/2, n\pi]$. The thick solid lines in Fig. 42(a) indicate where in the ϕ-ϕ' measurement space that the measurements are actually taken; the thinner dashed lines indicate where measurements are taken indirectly by way of the pattern functions' symmetries. For illustration purposes, Fig. 42(b) depicts one possible

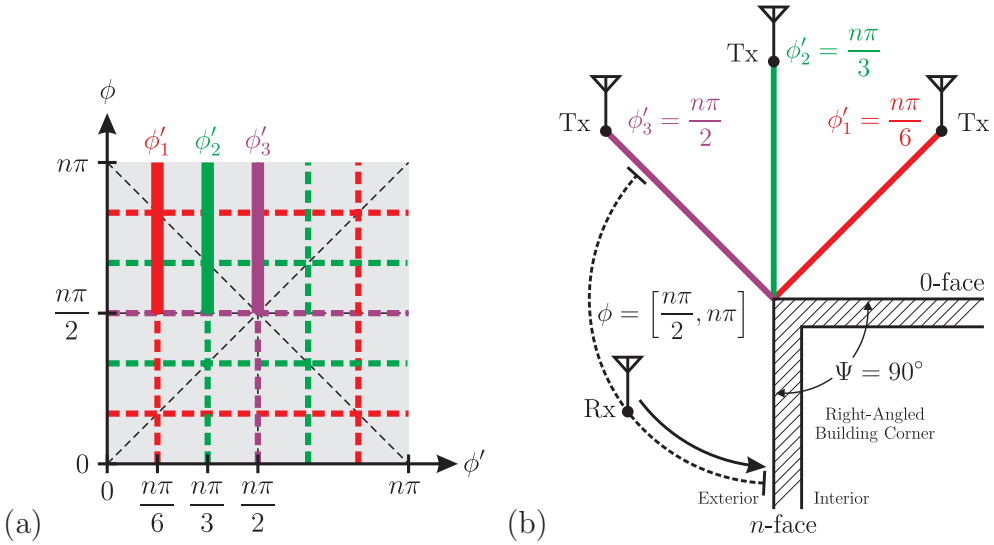

Figure 42: The implications of a simplified measurement scenario wherein the transmitter is positioned a three discrete incident angles: (a) the paths traversed by the measurements in the angular measurement space, and (b) the diagram of the corresponding measurement configuration.

measurement geometry that would correspond to Fig. 42(a). The three measurement configurations define a coarse rectangular mesh in the ϕ-ϕ' measurement space that yield a reasonably comprehensive set of total field measurements from which to determine $C^i(\phi, \phi')$ and $C^r(\phi, \phi')$.

4.1.2 Practical Considerations

To obtain equivalent information about the pattern functions using the spatio-temporal channel sounder described in Chapter 3, the square-shaped field reconstruction region must subtend $\phi \in [n\pi/2, n\pi]$. This would suggest a square field reconstruction region that circumscribes the arc in Figure 42(b). However, in order to avoid reactively coupling the receive antenna with the building face, the receive antenna must be at least one wavelength away [121]. Therefore, the square field reconstruction region must actually be shifted away from the building face, resulting in some maximum observation angle that depends on the dimensions of the reconstruction region.

4.1.3 Final Measurement Geometry

Figure 43 shows a to-scale drawing of the diffraction measurement geometry used to characterize diffraction by a brick building corner. Figure 44 provides a more detailed view of the arrangement of the linear positioner's track measurement paths. The cyan solid lines indicate the track measurement paths, whereas the blue dotted lines delineate the resulting pair of bounding rectangular contours. The square reconstruction region had sides of length $\ell = 1.13$ m and was positioned $s = 0.27$ m from the building corner's n-face. This offset, s, corresponded to

$$s = \lambda_{\max} + 4\Delta_s \tag{103}$$

which provided the $\lambda_{\max} = 0.16$ m spacing required to suppress reactive coupling and the additional $4\Delta_s = 0.11$ m of track measurement path length required to correct for track positioning errors as was discussed in Chapter 3. The separation distance between the two rectangular contours was $d = 33.9$ mm, as determined from Eq. (81). In Fig. 43, the distances ℓ_1 and ℓ_2 are given by

$$\ell_1 = \frac{\ell}{\sin(n\pi/2)} \tag{104}$$

$$\ell_2 = \ell \frac{\sin(n\pi/2)}{1 + \sin(n\pi/2)} \tag{105}$$

which, for the 90° building corner and $\ell = 1.13$ m yield $\ell_1 = 0.47$ m and $\ell_2 = 0.66$ m. The three transmit antenna locations were located at a radial distance of $R = 2.2$ m from the building corner at incident angles of $\phi' = \{45°, 90°, 135°\}$ as measured from the building's 0-face.

In addition to providing a comprehensive data set, each of the measurement configurations depicted in Fig. 43 exhibits unique and physically appealing characteristics. The first measurement configuration given by $\phi' = 45°$ provides total field measurements in three distinct regions corresponding to $E^t = \{E^i + E^r + E^d, E^i + E^d, E^d\}$ and

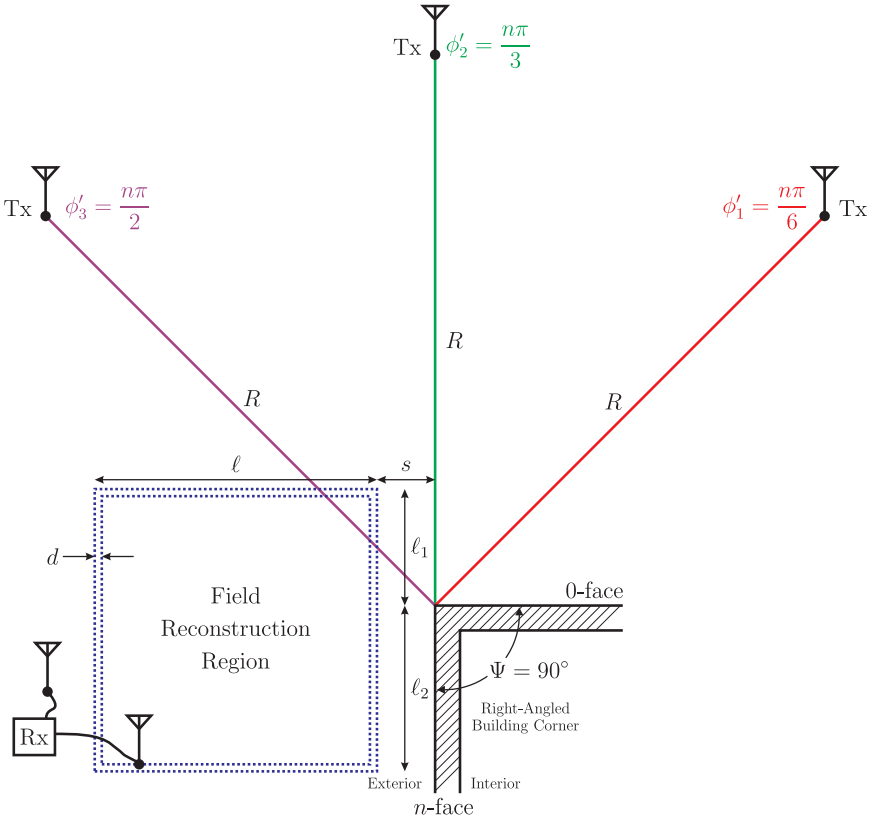

Figure 43: The corner diffraction measurements were performed using the field reconstruction technique whereby perimeter measurements were used to reconstruct the channel throughout the rectangular region.

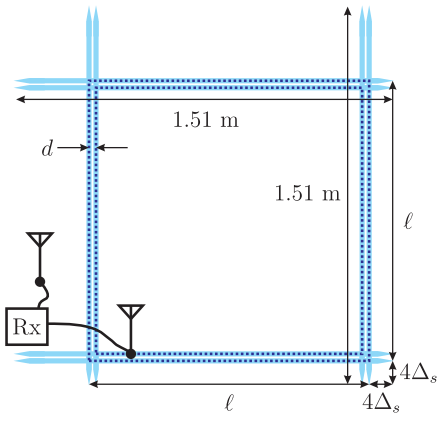

Figure 44: A more detailed diagram of the measurement geometry depicting the eight 1.51 m track measurements used to synthesize the pair of bounding rectangular contours.

spans both the incident and 0-face reflection shadow boundary. In contrast, the third measurement configuration given by $\phi' = 135°$ provides total field measurements in regions corresponding to $E^t = \{E^i + E^r + E^d, E^i + E^d\}$ and spans the n-face reflection shadow boundary. Thereby, the $\phi' = 45°$ and $\phi' = 135°$ configurations account for reflection off of each of the building corner's adjoining walls, which are presumably but not necessarily identical. Although wedge diffraction is described as an edge effect, it is strongly dependent on the reflection coefficient of each of the wedge faces. Thus, measuring the total field across across both the 0- and n-faces' RSBs provides the diffraction measurements with some facial diversity.

Finally, just as there are arguments for measuring where the reflected field exists, there are arguments for avoiding it as the $\phi' = 90°$ measurement does. As was noted, because the diffraction coefficient compensates for discontinuities in the GO's reflected field, it is strongly affected by the wedge faces' reflection coefficients. Therefore, by providing total field measurements corresponding to $E^t = \{E^i + E^d\}$ and avoiding both shadow boundaries, the $\phi' = 90°$ measurements may be more sensitive to other factors affecting the diffraction coefficient such as inhomogenieties and edge roughness.

4.2 "PEC" Validation Measurement

In addition to the brick building corner diffraction measurements described in Fig. 43, a corresponding set of three "PEC" wedge diffraction measurements were conducted by covering the building corner with a metal mesh. These "PEC" measurements provided a validation for the diffraction measurements and subsequent diffraction coefficient extraction technique. The approximation to the PEC wedge was realized by covering the diffracting building corner with a metal mesh. To provide a sharp diffracting edge for the "PEC" wedge, an 2.3 m length of angled aluminum was placed along the corner on top of the metal mesh. Figure 45 shows a photo of the

Figure 45: Photos of the "PEC" surface covering the right-angled brick building corner.

"PEC" surface covering the brick building corner. The angled aluminum was 1.6 mm thick and extended 3.8 cm from the corner. The metal mesh used to cover the building corner resembled a rectangular grid of 0.6 mm diameter wires interspaced by 0.6 cm. This corresponds to $0.06\lambda_{\text{min}}$ for the smallest transmission wavelength of $\lambda_{\text{min}} = 11$ cm. The mesh covered 0.6 m of each of the adjoining building faces and had a height of 2.4 m. The base of both the mesh and angled-aluminum were 0.3 m from the gravel rooftop. Duct tape and Gorilla Tape$^{\text{TM}}$ were used to firmly attach the "PEC" covering to the building corner.

For electric field polarizations coplanar to a rectangular mesh in free-space, a mesh spacing of less than $\lambda/10$ ensures near-total reflection at normal incidence, though the phase of the reflection coefficient will differ from 180° depending on the wire thickness [18, 94]. Based on the reflection coefficient curves presented in [94], for the smallest transmission wavelength of $\lambda_{\text{min}} = 11$ cm, the phase of the mesh's reflection coefficient is expected to be approximately 170°. It should be noted that positioning the mesh at the interface between two dielectric half-spaces will tend to increase the magnitude of the reflection coefficient when looking from the half-space with the lower permittivity toward the half-space with the greater permittivity [94]. Thus, it was

expected that the "PEC" covering would provide an acceptable approximation to the canonical PEC surface.

4.3 Diffraction Measurement Campaign

The following sections describe the measurement site and measurement procedure.

4.3.1 Measurement Site

The diffraction measurements were conducted along an exterior corner of the Van Leer Electrical and Computer Engineering Building at the Georgia Institute of Technology. The measurement corner was located at the southwest corner of the building's 5th floor, which had a smaller footprint than the rest of the building as shown by the floorplan diagram in Fig. 47. The 5th floor's smaller footprint allowed access to the measurement site by way of the 4th floor's gravel roof. Figure 46 presents a series of photos of the measurement site.

This right-angled brick building corner was chosen for its easy access, its simplicity, its architectural ubiquity, and its relative isolation from landscaping and other architectural features as demonstrated by the panoramic compilation of photos in Fig. 48. The photos were taken from the measurement corner looking out toward the surrounding environment. The 4th floor's roof also provided a relatively flat and level surface.

Figure 49 diagrams the 4.0 m high brick building corner. The central section extending 0.3 m to 3.7 m from the gravel rooftop was brick and covered an inner cinder block wall. Individual bricks measured $20 \times 6 \times 10$ cm and the inter-brick spacing was approximately 6 mm. The upper 0.3 m section was composed of concrete; the lower 0.3 m section had an outer layer of tar that was presumed to cover a concrete base. A 10 cm copper flashing separated the lower 0.3 m section from the brick. As shown in Fig. 49 and highlighted in Fig. 50, two additional features were present on the upper half of the building corner: outdoor flood lights and a metal support structure for

Figure 46: Photos of the right-angled brick building corner where the diffraction measurements were taken.

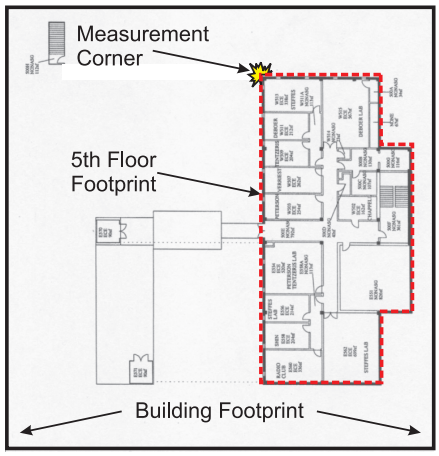

(b)

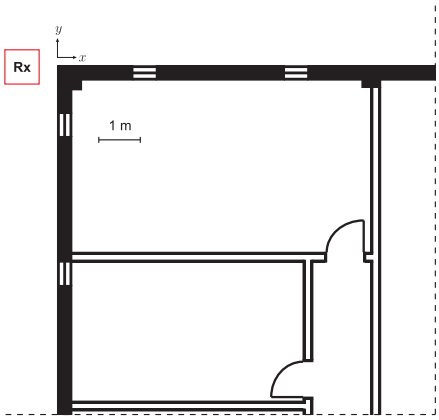

(b)

Figure 47: The 5th floor of Van Leer occupied a smaller footprint than the lower floors. This allowed access to the measurement site by way of the 4th floor's gravel rooftop. Floorplans show (a) the entire 5th floor and (b) the portion of the 5th floor near the measurement corner.

$\phi = 270°$ $\phi = 180°$ $\phi = 90°$ $\phi = 0°$

Figure 48: A panoramic compilation of photos taken from the measurement corner show the relative isolation of the measurement site.

(a)

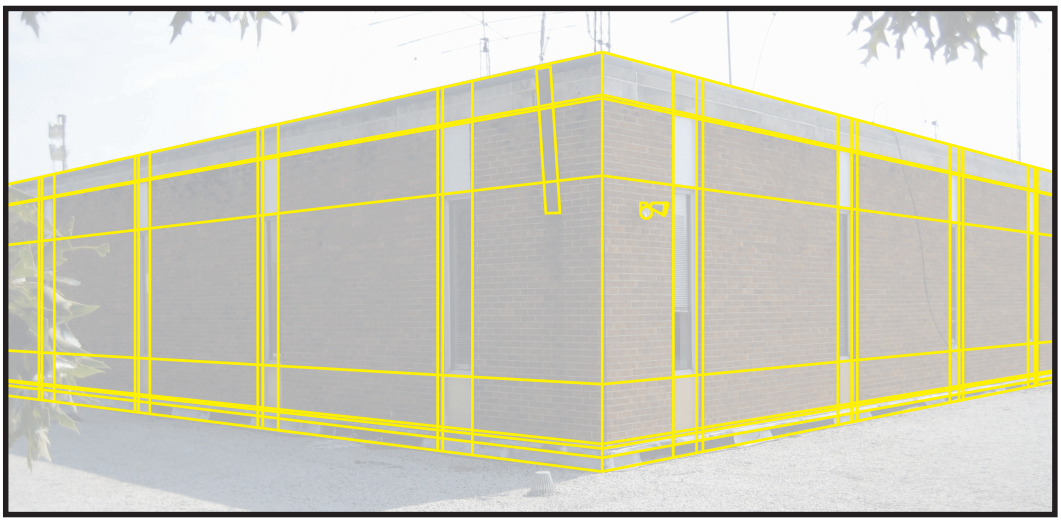

(b)

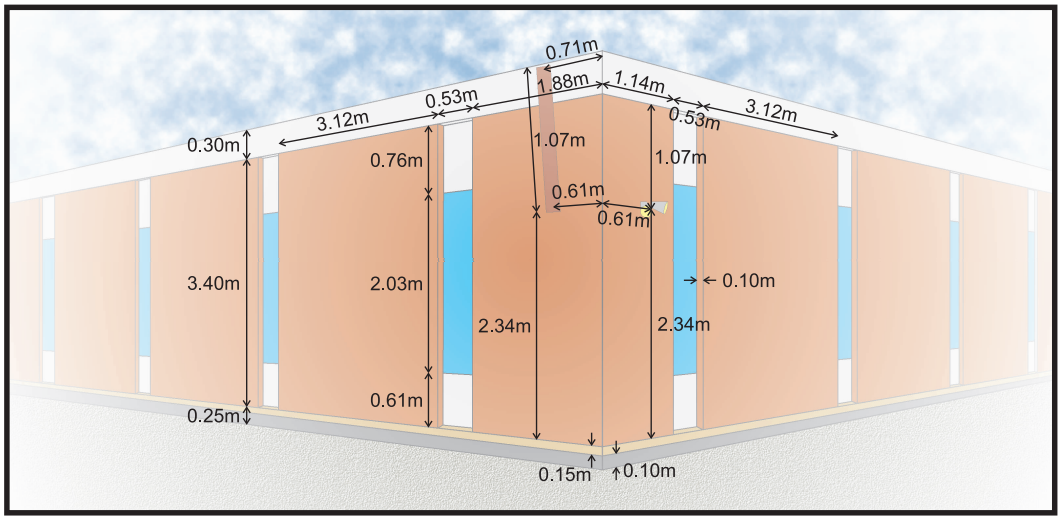

Figure 49: An (a) photo and (b) corresponding diagram of the right-angled brick building corner.

guy-wires.

4.3.2 Measurement Procedure

The eight track measurement paths illustrated in Fig. 44 were drawn onto a half-inch thick, 1.2 × 1.2 m plywood sheet that was moved into position near the building corner. Wooden shims were placed under the plywood to ensure a level surface and low-profile concrete blocks were placed atop the plywood to ensure that the surface remained stationary throughout the measurement campaign. The measurements were

Figure 50: A photo collage identifying the flood lights and metal support bracket near the top of the right-angled brick building corner.

conducted between the hours of midnight and 5 am as mandated by in-band spectrum license holders so as to minimize interference to their wireless systems. The benefits of these late-night measurements were reduced in-band interference and unoccupied offices in the vicinity of the measurement site.

The measurements were conducted over the course of three nights. Each night, the "PEC" and brick building corner configurations were measured sequentially for one of the three incident angles depicted in Fig 43. To enable direct comparisons between the "PEC" and brick configurations, the transmit antenna and "reference" receive antenna remained fixed throughout each night's measurements. A total of six measurements were conducted corresponding to the two building corner configurations ("PEC" and brick) and the three incident angles ($\phi' = \{45°, 90°, 135°\}$). Figures 51-52 present several staged photographs of the diffraction measurements – poor light conditions made it difficult to photograph the actual meaurements. Figures 51(a) and 51(b) show the "PEC" and brick corner measurements, respectively. Figure 51(c) highlights the plywood surface on which the linear positioner was placed. Figure 52 presents a photo taken from above the building corner with labels designating various components of the measurement setup.

4.4 Measurement Results

Figures 53-58 present diagrams and corresponding magnitude/phase snapshots of the wireless channel's impulse response for each of the six diffraction measurements. The diagrams indicate the position of the impulse response wavefronts for the incident (blue), reflected (red), and diffracted (green) fields. The magnitude and phase snapshots show the measured channel within the field reconstruction region. Figs. 59-64 present the power delay-angle spectra for the six measurements. Note that in both sets of figures τ denotes absolute delay. This was determined by temporally aligning

(a)  (b) 

(c) 

Figure 51: Photos of the building corner diffraction measurements: (a) a "PEC" wedge diffraction measurement, (b) a brick building corner diffraction measurement, and (c) the plywood surface with markings indicating the eight track positions.

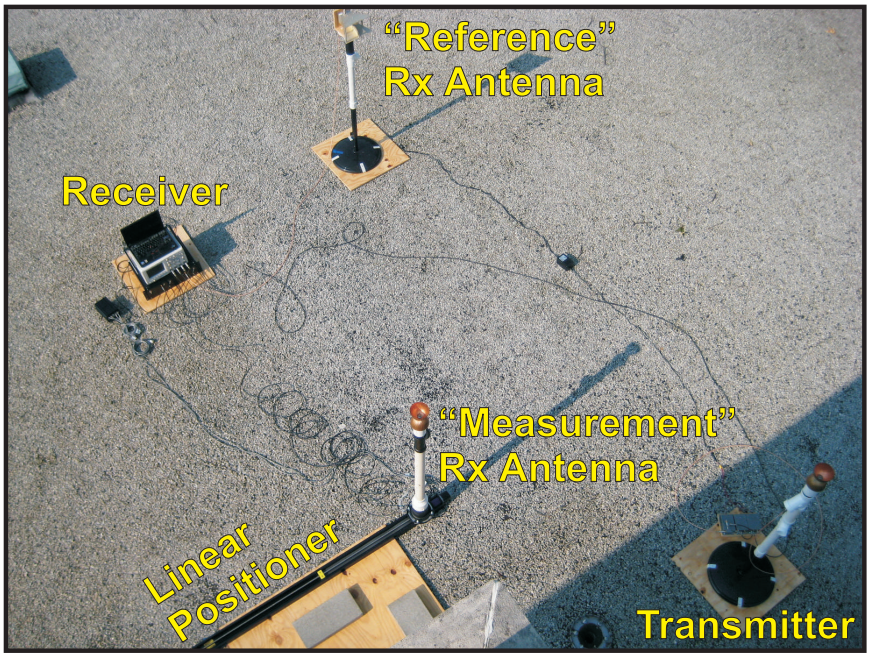

Figure 52: A top-down photo of the measurement configuration with accompanying labels for the components of the spatio-temporal channel sounder.

the measured impulse responses with the theoretical impulse responses for the corresponding PEC wedge diffraction problem. The channel impulse response snapshots corresponding to delays, τ, prior to the arrival of the band-limited sounding impulse reveal the noise floor of the space-time measurements. This noise floor of approximately -40 dB in Figs. 59-64 corresponds to -40 dB of additional path loss with respect to the 1 m free-space calibration measurement described in Appendix C. The early delay snapshots also reveal the slight ringing of the band-limited impulse due to the digital filtering techniques employed as part of the channel sounder's calibration.

Examining Figs. 53-58, it is encouraging that the sequence of diagrams and reconstructed total field plots are in agreement. The magnitude and phase of the total field consistently suggests a strong point source located at the transmitter's location, and the power delay-angle spectra confirms this observation. The interference pattern visible in the total field's magnitude is particularly encouraging, because it indicates the presence of a second field component that is likely due to diffraction. A close examination of the "PEC" measurements at $\tau = 10$ ns reveals a phase structure that suggests this second field component is due to a source located at the building corner's edge. This observation is in good agreement with the geometrical theory of diffraction, which describes the field diffracted by an edge discontinuity as a cylindrical wave emanating from the edge. The diffracted field is less apparent in the brick measurements (Figs. 54, 56, and 58), suggesting that the field diffracted by the brick corner is weaker than that diffracted by the "PEC" corner. This is also in good agreement with theoretical expectations.

The total field and power delay spectra also indicate that many weaker multipath components were incident upon the reconstruction region following the target diffraction problem. Based upon the time- and angle-of-arrival of these multipath components, few if any may be attributed to electromagnetic scattering by objects in the vicinity of the building corner. Furthermore, the structure of the total fields

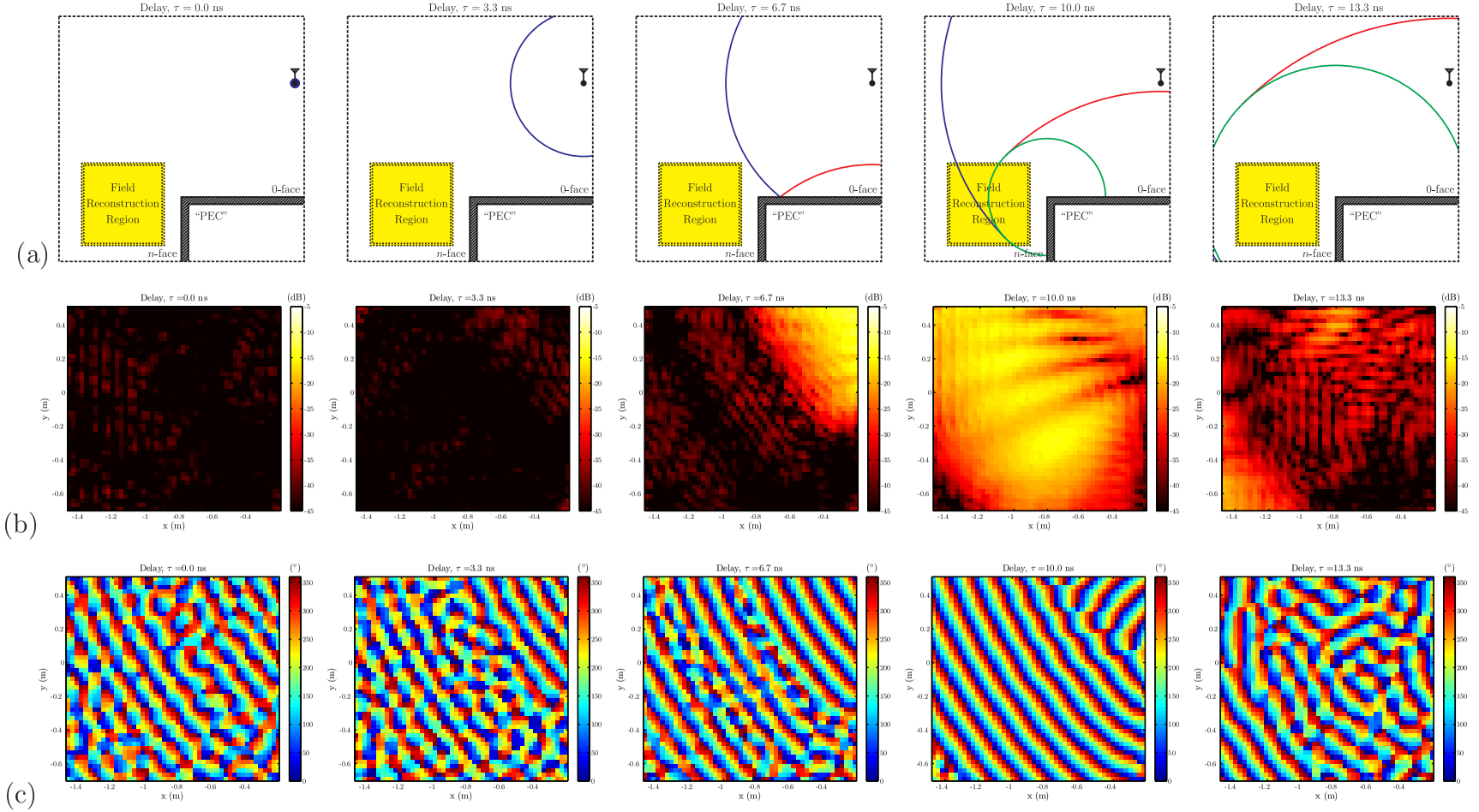

Figure 53: The wireless channel's impulse response for the measurements of diffraction by the "PEC" building corner for $\phi' = 45°$: (a) diagram, (b) magnitude, and (c) phase.

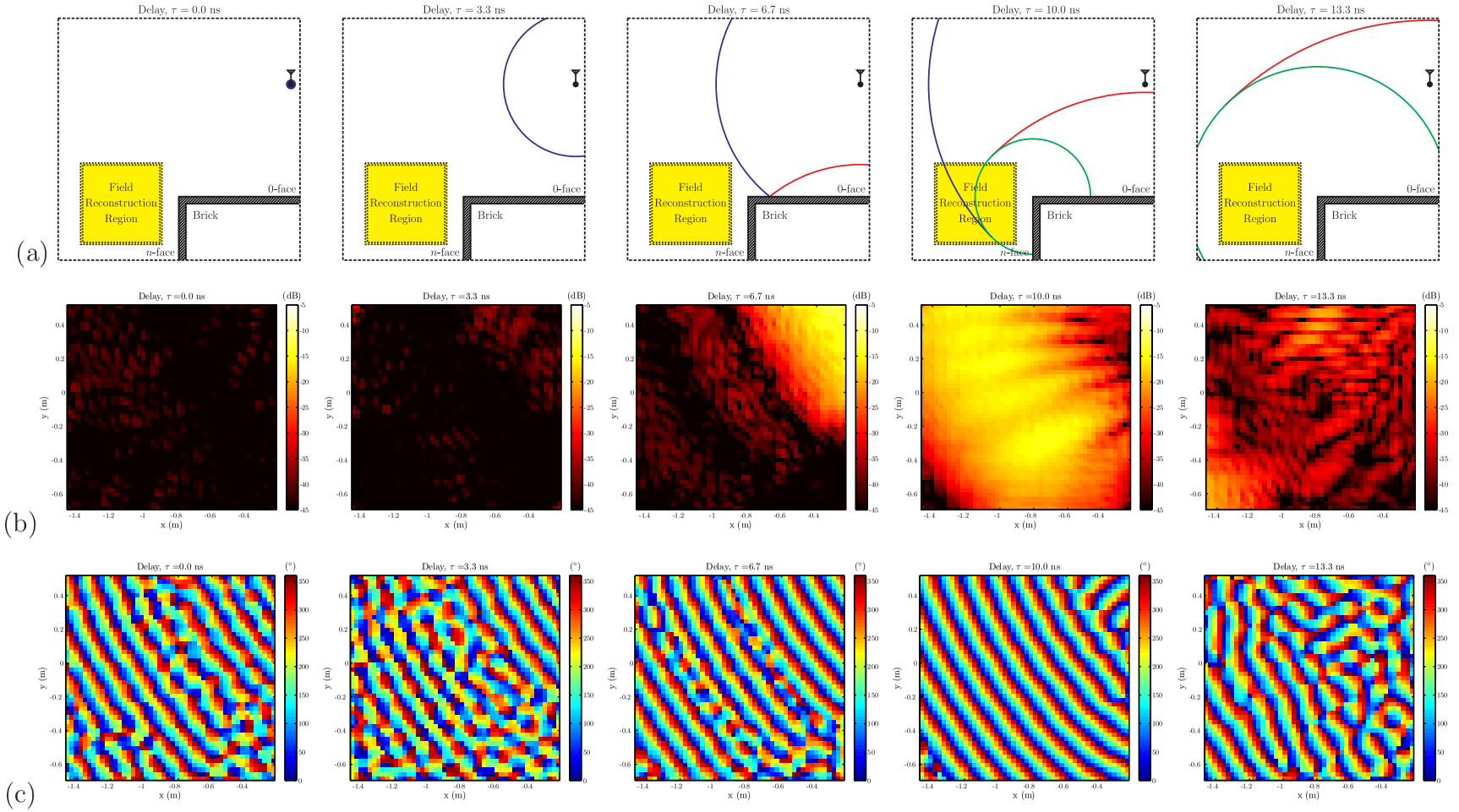

Figure 54: The wireless channel's impulse response for the measurements of diffraction by the brick building corner for $\phi' = 45°$: (a) diagram, (b) magnitude, and (c) phase.

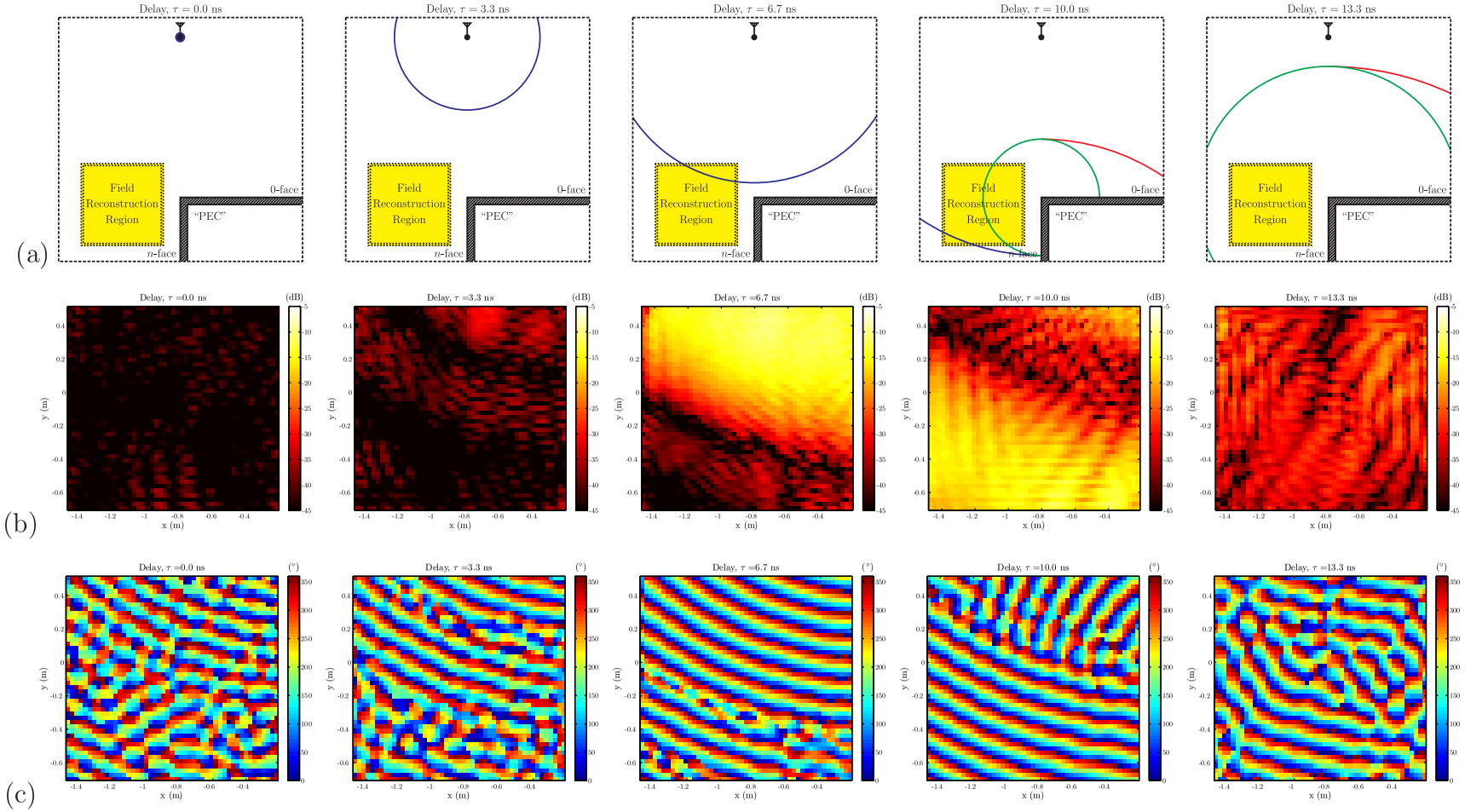

Figure 55: The wireless channel's impulse response for the measurements of diffraction by the "PEC" building corner for $\phi' = 90°$: (a) diagram, (b) magnitude, and (c) phase.

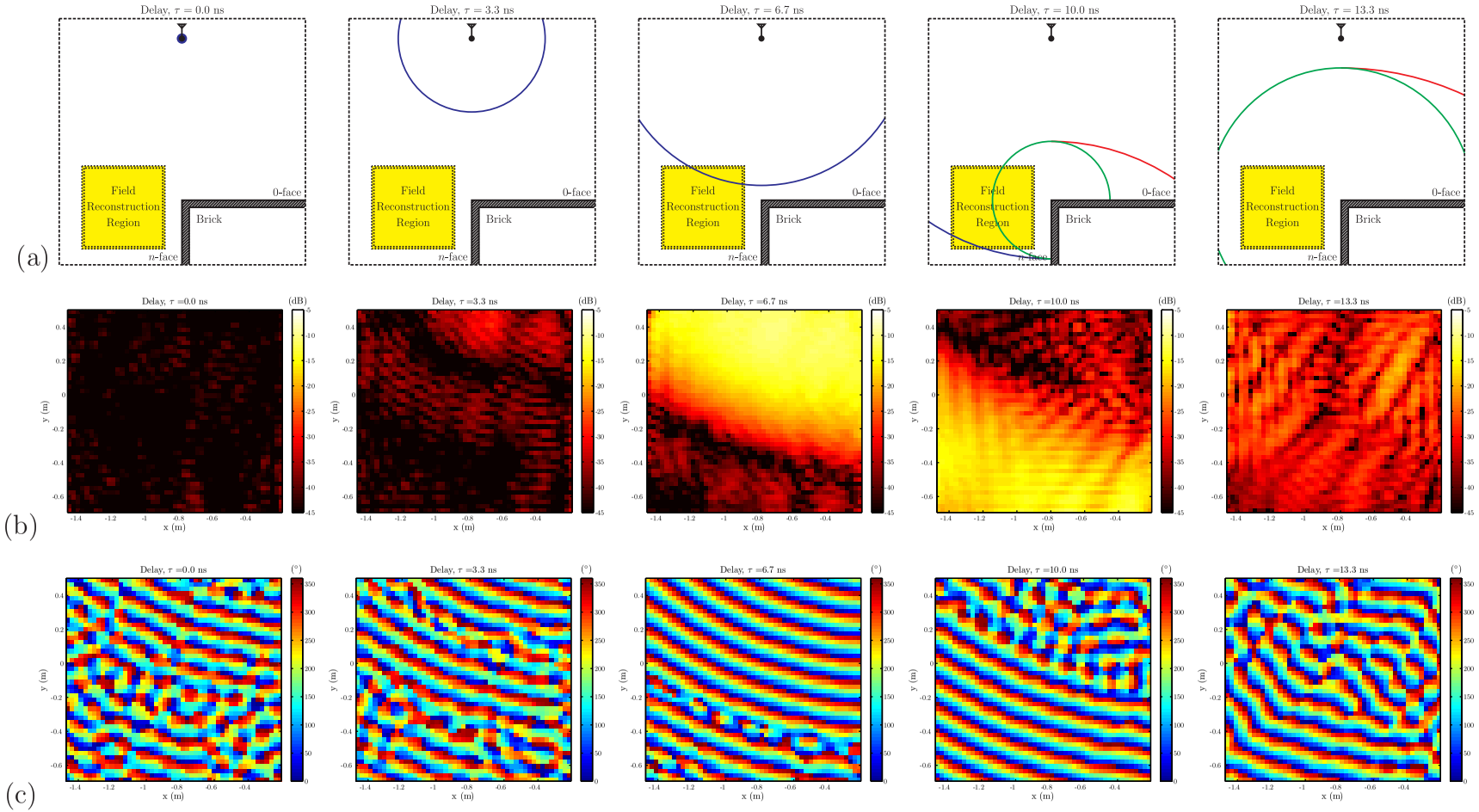

Figure 56: The wireless channel's impulse response for the measurements of diffraction by the brick building corner for $\phi' = 90°$: (a) diagram, (b) magnitude, and (c) phase.

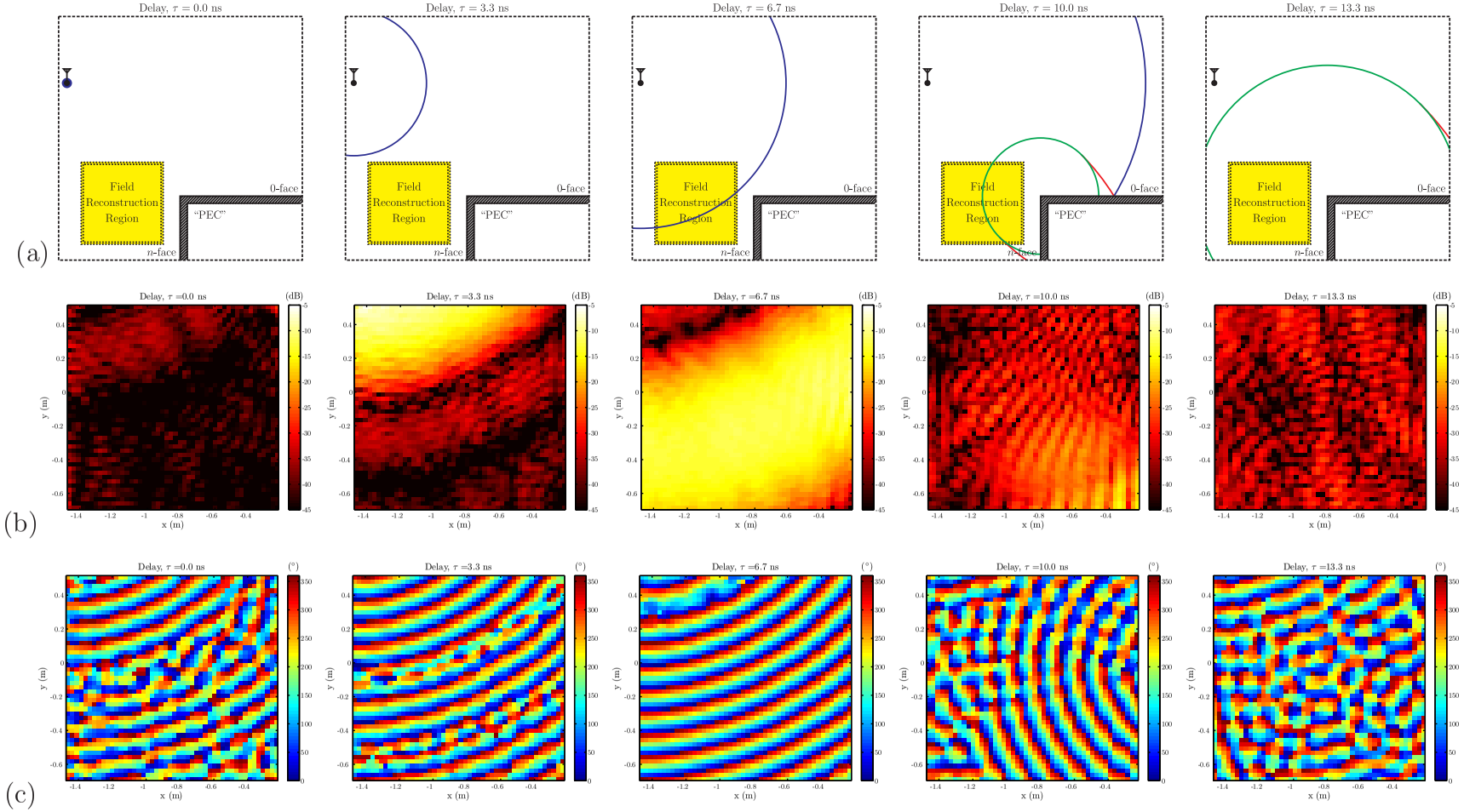

Figure 57: The wireless channel's impulse response for the measurements of diffraction by the "PEC" building corner for $\phi' = 135°$: (a) diagram, (b) magnitude, and (c) phase.

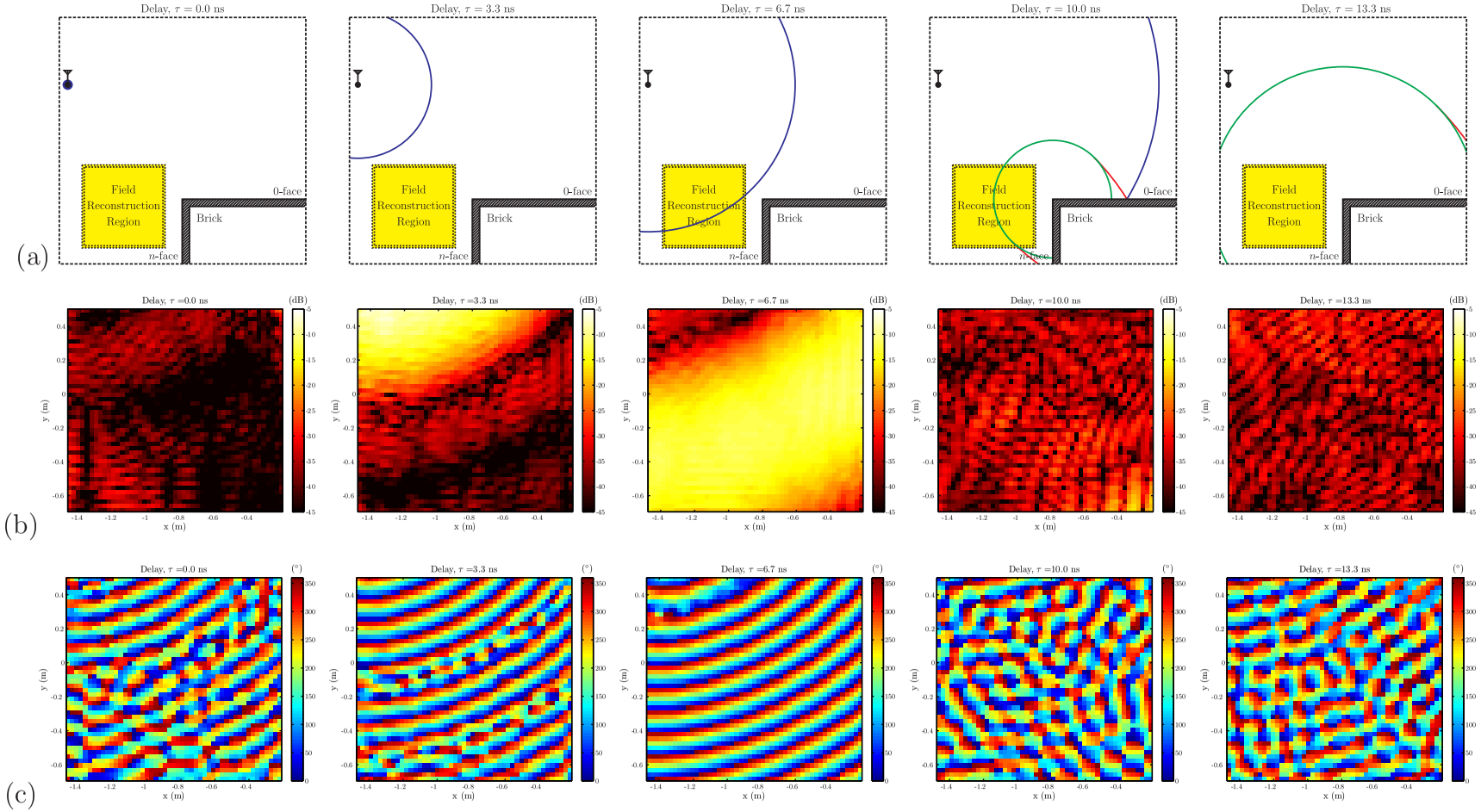

Figure 58: The wireless channel's impulse response for the measurements of diffraction by the brick building corner for $\phi' = 135°$: (a) diagram, (b) magnitude, and (c) phase.

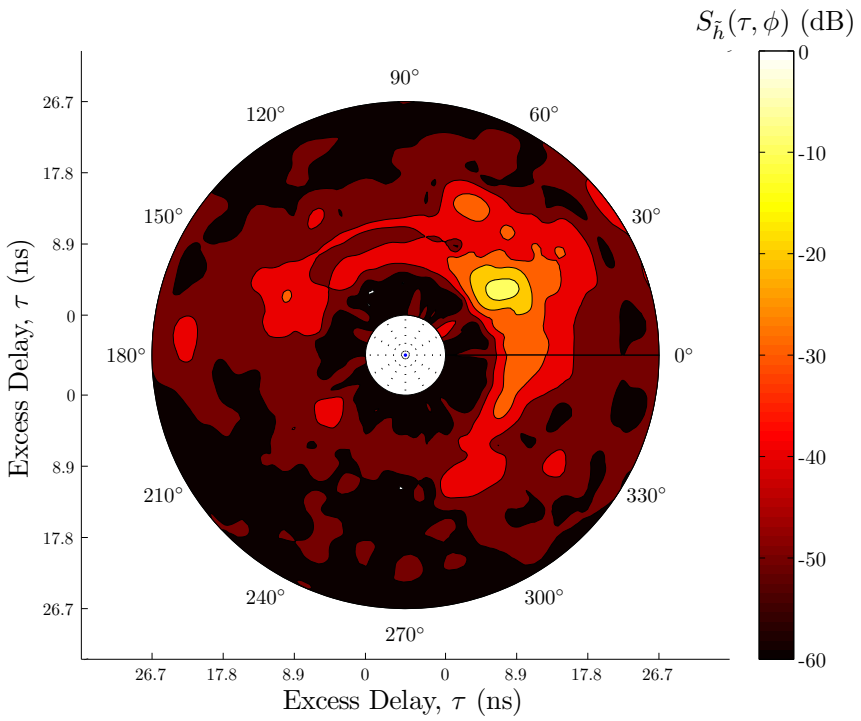

Figure 59: The power delay-angle spectrum for the "PEC" diffraction measurements with source incident angle of $\phi' = 45°$'.

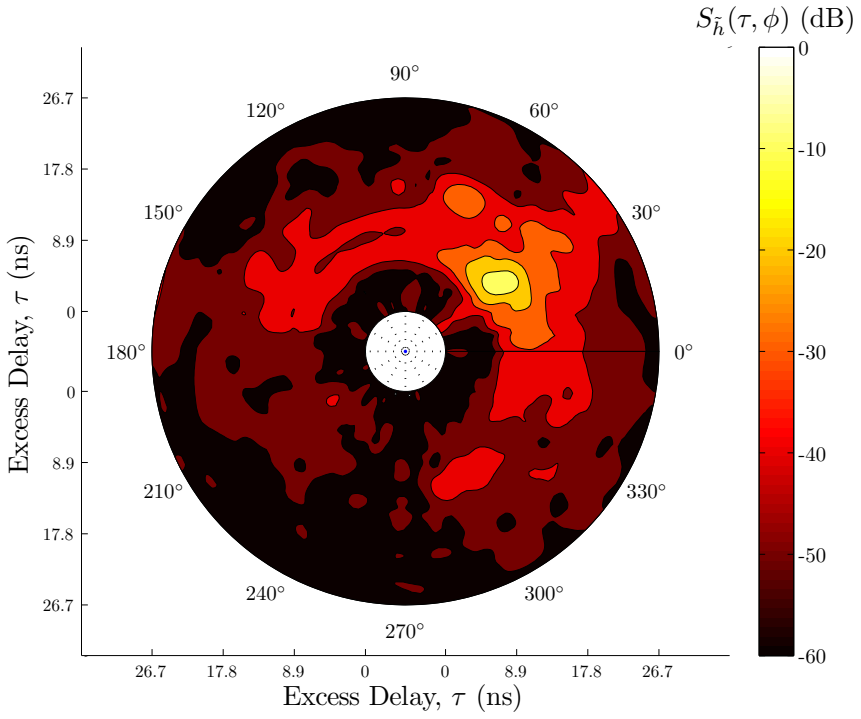

Figure 60: The power delay-angle spectrum for the brick diffraction measurements with source incident angle of $\phi' = 45°$'.

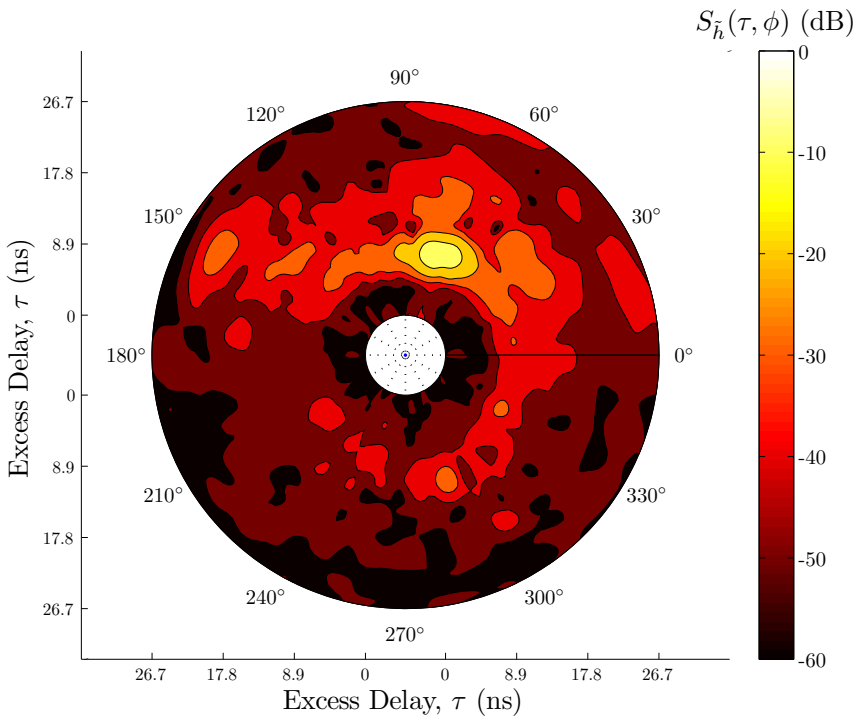

Figure 61: The power delay-angle spectrum for the "PEC" diffraction measurements with source incident angle of $\phi' = 90°$'.

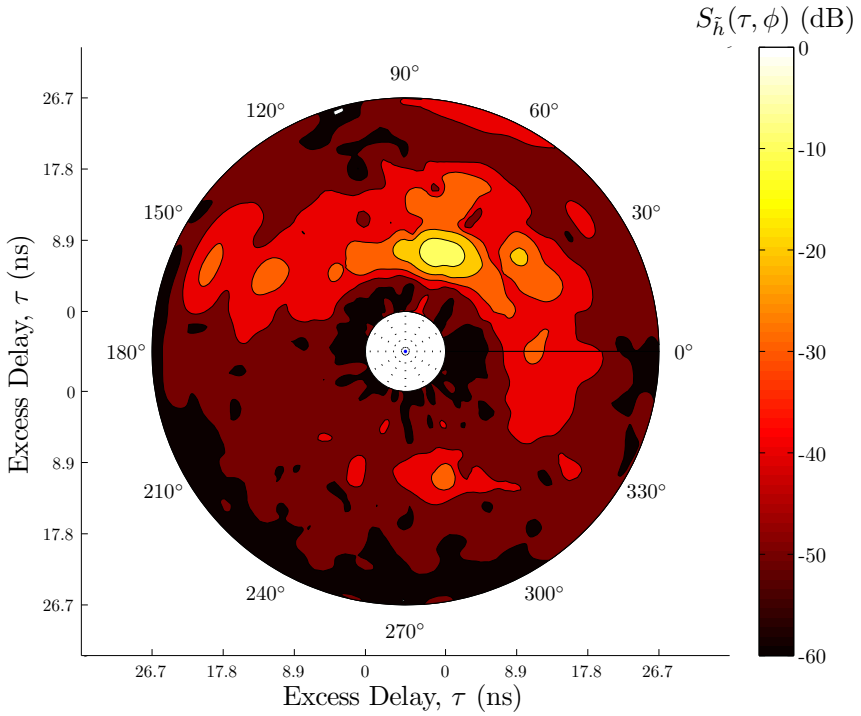

Figure 62: The power delay-angle spectrum for the brick diffraction measurements with source incident angle of $\phi' = 90°$'.

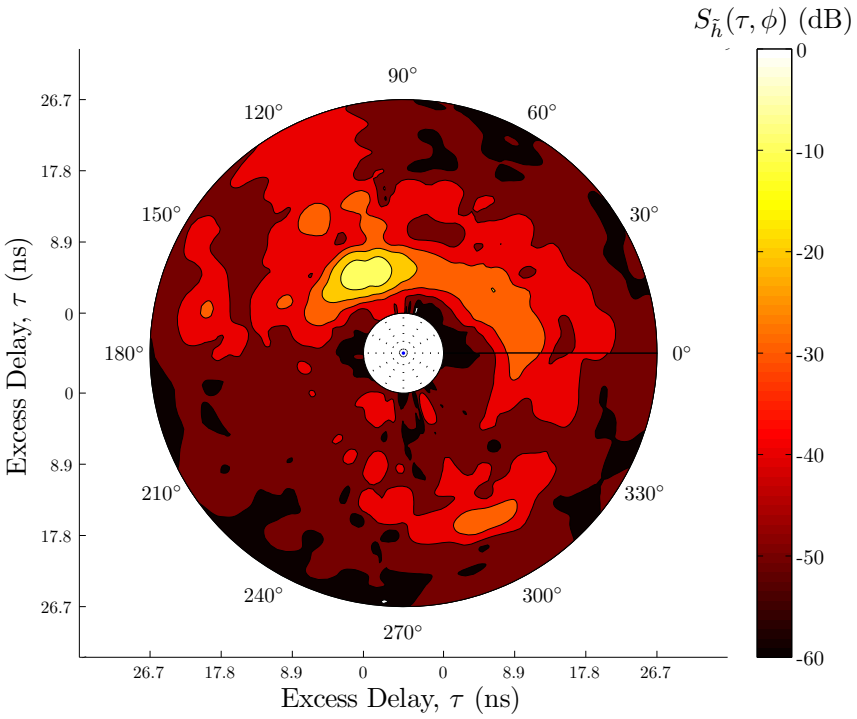

Figure 63: The power delay-angle spectrum for the "PEC" diffraction measurements with source incident angle of $\phi' = 135°$'.

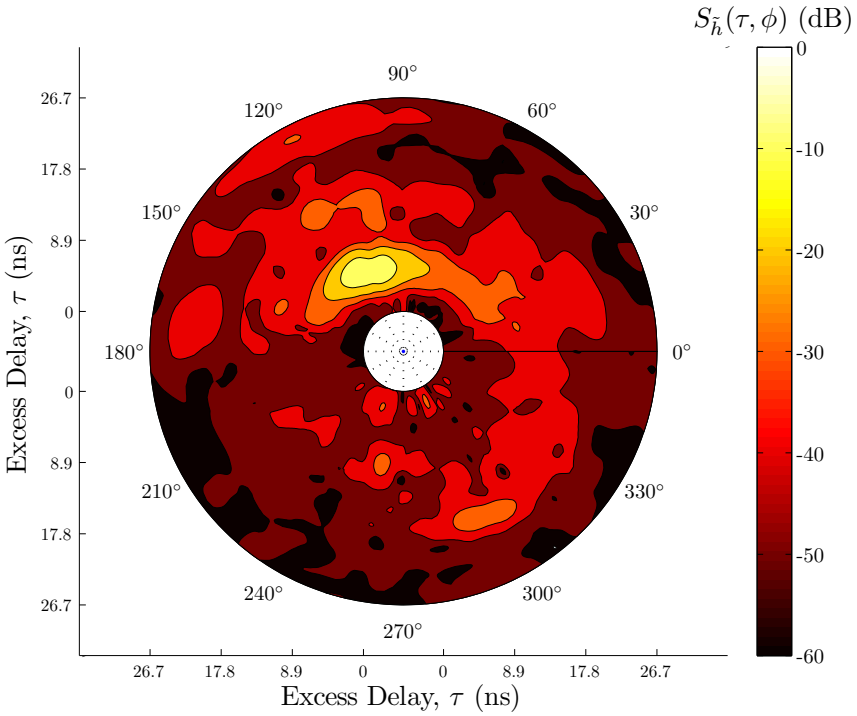

Figure 64: The power delay-angle spectrum for the brick diffraction measurements with source incident angle of $\phi' = 135°$'.

presented in Figs. 53-58 occasionally exhibits nonphysical behaviors. For example, in the $\phi' = 90°$ measurements at $\tau = 10$ ns (4th panel in Figs. 55-56), the interference pattern suggests a reflection from some fictitious interface lying parallel to the x-axis and intersecting the y-axis at $y \leq -0.66$ m. In light of these fictitious reflections, it is interesting if not surprising that for a given incident angle, ϕ', the power angle-delay spectra for the "PEC" and brick measurements are quite similar. This suggests that the nonphysical behavior of the total field and these later arriving multipath components cannot be attributed to random measurement errors.

As was discussed in Chapter 3 and Appendix A, the conjoint cylindrical wave expansion (CWE) used to reconstruct the wireless channel throughout the measurement region assumes a quasi 2-D electromagnetic field wherein contributing multipath components are incident at elevation angles tightly clustered about the horizon. Although this makes the conjoint CWE more robust in the presence of off-the-horizon propagation than the conventional and purely 2-dimensional CWE, the accuracy of the reconstructed field will still degrade in the presence of off-the-horizon propagation. The flood light and metal support structure identified in Fig. 50 are two large scatterers that may have contributed to off-the-horizon propagation. Other potential sources are the copper flashing at the base of the building corner in Fig. 49, objects within and interior to the building corner, and reflection/scattering off of the gravel rooftop.

Fortunately, both unwanted multipath components and field reconstruction artifacts may be removed by space-time filtering the wireless channel. The following chapter will discuss the space-time filtering techniques used to isolate the desired building corner diffraction problem as well as the diffraction coefficients that were extracted from the measurement data.

CHAPTER V

DIFFRACTION COEFFICIENT EXTRACTION

Chapter Summary: This chapter presents the semi-empirical diffraction coefficients that were extracted from the "PEC" and brick diffraction measurements described in the preceeding chapter. The measurements were first processed using a space-time filter to isolate the wedge diffraction problem. To compensate for diffraction geometry errors, a non-linear least-squares solver was used to determine the actual position of the transmitter and reconstruction region relative to the diffracting corner. This enabled the diffraction coefficients to be extracted from the brick and "PEC" corner measurements. The brick building corner's semi-empirical diffraction coefficient showed good agreement with a diffraction coefficient extracted from finite-difference time-domain (FDTD) simulations of the measurement configurations.

Starting with the space-time wireless channel measurements presented in Chapter 4, this chapter discusses the sequence of processing and analysis techniques that were used to isolate the desired building corner diffraction problem, correct for geometry errors in the measurement data, and extract the "PEC" and brick corners' diffraction coefficients. Discussion begins with a description of the space-time filters that were used to isolate the desired building corner diffraction problem. Following a brief review of the linear wedge diffraction model described in Chapter 2, an initial attempt at extracting semi-empirical diffraction coefficients revealed discrepancies between the intended and actual positions of the transmitter and field reconstruction region. These measurement geometry errors were resolved by determining the

UTD wedge diffraction geometry that optimized the model's fit with the measurement data. Diffraction coefficients extracted from the position-corrected measurements using the linear diffraction model from Chapter 2 and the nonlinear UTD impedance wedge diffraction model were found to be consistent. Furthermore, a comparison of the "PEC" corner's diffraction coefficient with the UTD PEC wedge diffraction coefficient showed good agreement. The brick corner diffraction coefficients were then compared to those extracted from FDTD simulations of diffraction by a brick-like hollow dielectric wedge. These measurement- and FDTD-based brick corner diffraction coefficients also showed good agreement.

5.1 Isolating the Wedge Diffraction Problem

Before the diffraction coefficients could be extracted from the measurement data, the wedge diffraction problem had to first be isolated from any interfering multipath components. To isolate the desired diffraction problem, a high-resolution space-time filter was constructed based upon the spectral content of the UTD's PEC wedge total field solution. The following sections describe the realization and application of this diffraction-specific space-time filter.

5.1.1 Synchronization

Space-time filtering removes spectral content from the total field based upon the delay (i.e., time-of-arrival) and spatial frequencies (i.e., the angle-of-arrival) of multipath components. Therefore, in order to apply a diffraction-specific space-time filter to the measurement data, it was necessary to know the *absolute* delay of the received multipath. However, as was discussed in Chapter 3, the field reconstruction-based spatio-temporal channel sounder could only determine the *relative* delay of multipath components. To convert the measurement data's relative delay to absolute delay, a linear phase taper was applied to each of the measured wireless channel frequency responses, $h(f, \mathbf{r})$, so as to temporally align the corresponding channel impulse response,

$H(\tau, \mathbf{r})$, with the impulse response of a PEC wedge assuming identical geometries. The PEC wedge impulse response was calculated by a frequency-delay Fourier transform of the UTD's frequency-dependent total field solution, $E^{t,\perp}_{\mathrm{PEC}}(\mathbf{r})$ given in Eq. (61).

5.1.2 Filter Synthesis

To construct the wedge diffraction space-time filter, the frequency-dependent UTD PEC wedge total field solution, $E^{t,\perp}_{\mathrm{PEC}}(\mathbf{r})$ corresponding to the measurement geometry was Fourier transformed with respect to frequency and 2-D space to yield the corresponding UTD PEC wedge delay-wavevector spectrum, $E^{t,\perp}_{\mathrm{PEC}}(\tau, \mathbf{k})$. A threshold, E_{thr}, was then applied to the magnitude of this delay-wavevector spectrum to produce a plateau-shaped space-time filter, $H_{\mathrm{plat}}(\tau, \mathbf{k})$:

$$H_{\mathrm{plat}}(\tau, \mathbf{k}) = \begin{cases} 1 & \text{for} \quad |E(\tau, \mathbf{k})| \geq E_{\mathrm{thr}} \\ |E(\tau, \mathbf{k})|/E_{\mathrm{thr}} & \text{for} \quad |E(\tau, \mathbf{k})| < E_{\mathrm{thr}} \end{cases} \tag{106}$$

The final wedge diffraction space-time filter, denoted $H_{\mathrm{filt}}(\tau, \mathbf{k})$, was realized by convolving the plateau-shaped filter, $H_{\mathrm{plat}}(\tau, \mathbf{k})$, with a unit area Gaussian smoothing function, $H_{\mathrm{G}}(x)$, along each of the filter's three dimensions, τ, k_x, and k_y:

$$H_{\mathrm{filt}}(\tau, \mathbf{k}) = H_{\mathrm{plat}}(\tau, \mathbf{k}) \otimes H_{\mathrm{G}}(\tau) H_{\mathrm{G}}(k_x) H_{\mathrm{G}}(k_y) \tag{107}$$

where $\mathbf{k} = (k_x, k_y)$ is the 2-D wavevector in Cartesian coordinates. For the realized wedge diffraction space-time filters, the threshold, E_{thr}, was set to 40 dB below $\max \left| E^{t,\perp}_{\mathrm{PEC}}(\tau, \mathbf{k}) \right|$, and the Gaussian smoothing functions applied along τ, k_x, and k_y were characterized by standard deviations of $\sigma_\tau = 0.9$ ns, $\sigma_{k_x} = 2.2$ rad/m, and $\sigma_{k_y} = 2.2$ rad/m, respectively. This choice of threshold, E_{thr} and smoothing function parameters, σ_τ, σ_{k_x}, and σ_{k_y} yielded a tight diffraction-specific filter that passed the nearly all of the UTD PEC wedge solution's delay-wavevector spectral content without considerably alteration to the total field. Thus, the filter acted as a sort of

band-pass filter for diffraction problems that sharply attenuated any wavevector-delay spectral content unrelated to the desired diffraction problem.

5.1.3 Filtering Results

A wedge diffraction space-time filter, $H_{\text{filt}}(\tau, \mathbf{k})$, was constructed for and applied to each of the measured wireless channels. As discussed towards the end of Chapter 3, due to the inherent periodicity of the discrete Fourier transform, a series of Fourier transforms, zero-padding, and cropping were required in order to correctly apply the space-time filter to the wireless channel measurements. Specifically, the synthesized filter, $H_{\text{filt}}(\tau, \mathbf{k})$, was Fourier transformed to the space-frequency domain where both it and the wireless channel, $h(f, \mathbf{r})$, were zero-padded along 2-D space. The zero-padded filter and wireless channel were then Fourier transformed to the delay-wavevector domain and multiplied together. The resulting product was Fourier transformed back to the space-frequency domain wherein the filtered wireless channel was cropped from the zero-padding.

Following the space-time diffraction filtering, additional precision space-time filtering was performed using the methods discussed in Chapter 3 to remove artifacts of the field reconstruction arising due to off-the-horizon propagation. These artifacts were identified in the power delay-angle spectra in Figs. 59-64 as multipath components that were either nonphysical or unrelated to the desired diffraction problem. We note that for a given incident angle, ϕ', the field reconstruction artifact filtering was performed identically for the"PEC" and brick measurements. Figures 65-70 present the results of the space-time filtering. The top row of each figure shows the magnitude and phase the wireless channel before filtering, the middle row shows the magnitude and phase after applying the diffraction-specific space-time filter, and the last row shows the magnitude and phase after additional precision filtering. Time-domain snapshots of the filtered space-time diffraction measurements may be found

Table 2: RMS Change to Total Field Due to Space-Time Filtering (%)

ϕ'	Filter	"PEC"	Brick	UTD's PEC Wedge
45°	Diffraction	46.3	44.5	5.7
	ST	5.8	5.2	4.1
	Diffraction+ST	46.6	44.8	7.2
90°	Diffraction	41.8	40.7	5.3
	ST	10.1	11.5	7.5
	Diffraction+ST	43.4	42.0	9.4
135°	Diffraction	35.1	33.6	5.2
	ST	6.4	5.0	3.6
	Diffraction+ST	35.4	34.1	6.4

in Appendix F.

As is evidenced by Figs. 65-70, space-time filtering does a remarkable job of isolating the desired building corner diffraction problem. The magnitude and phase of the filtered wireless channels closely resemble the electromagnetic field arising due to diffraction by an impedance wedge. Encouragingly, the filtered "PEC" measurements tend to show a more pronounced diffraction-like interference pattern than the corresponding brick measurements. This indicates that the "PEC" corner diffracts more power than the brick corner as would be expected for a corresponding pair of PEC and impedance wedges.

Somewhat less encouraging are the filtering results for the $\phi' = 90°$ measurements. Examining Figs. 67 and 68, the characteristic interference bands associated with diffraction seem poorly defined, especially in comparison to the $\phi' = 45°$ and $\phi' = 135°$ measurements. Furthermore, as a comparison of subfigures (b) and (c) in Figs. 67-68 indicates, the $\phi' = 90°$ measurements had considerably more field reconstruction artifacts than $\phi' = 45°$ and $\phi' = 135°$ measurements and necessitated considerably more precision space-time filtering to "clean up" the data.

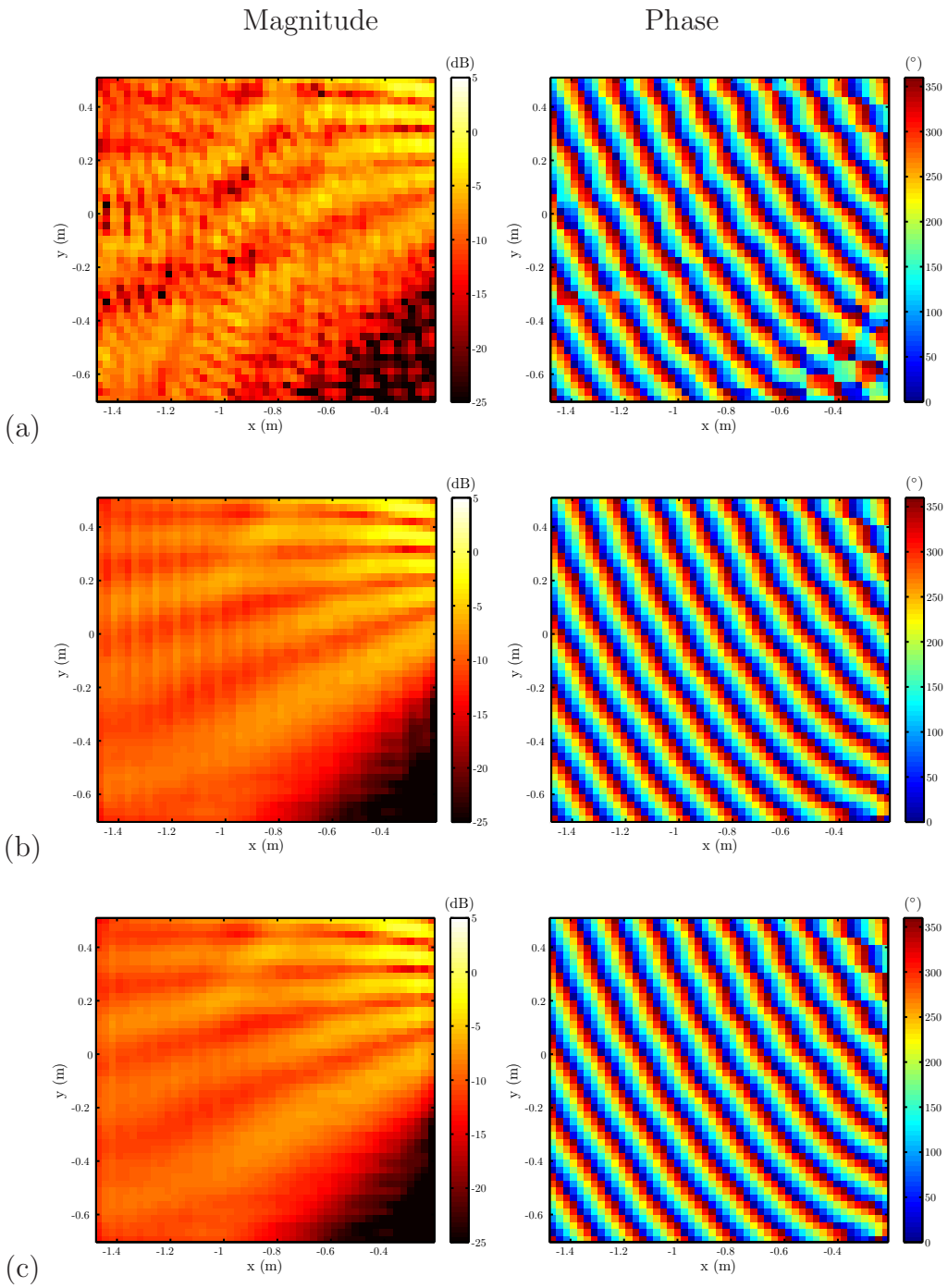

Figure 65: Space-time filters were used to isolate the wedge diffraction problem from the total field measurements. The plots present the magnitude and phase of the filtered "PEC" measurement data for an incident angle of $\phi' = 45°$ at 2.3 GHz: (a) measured, (b) after applying the diffraction-specific filter, and (c) after additional space-time filtering.

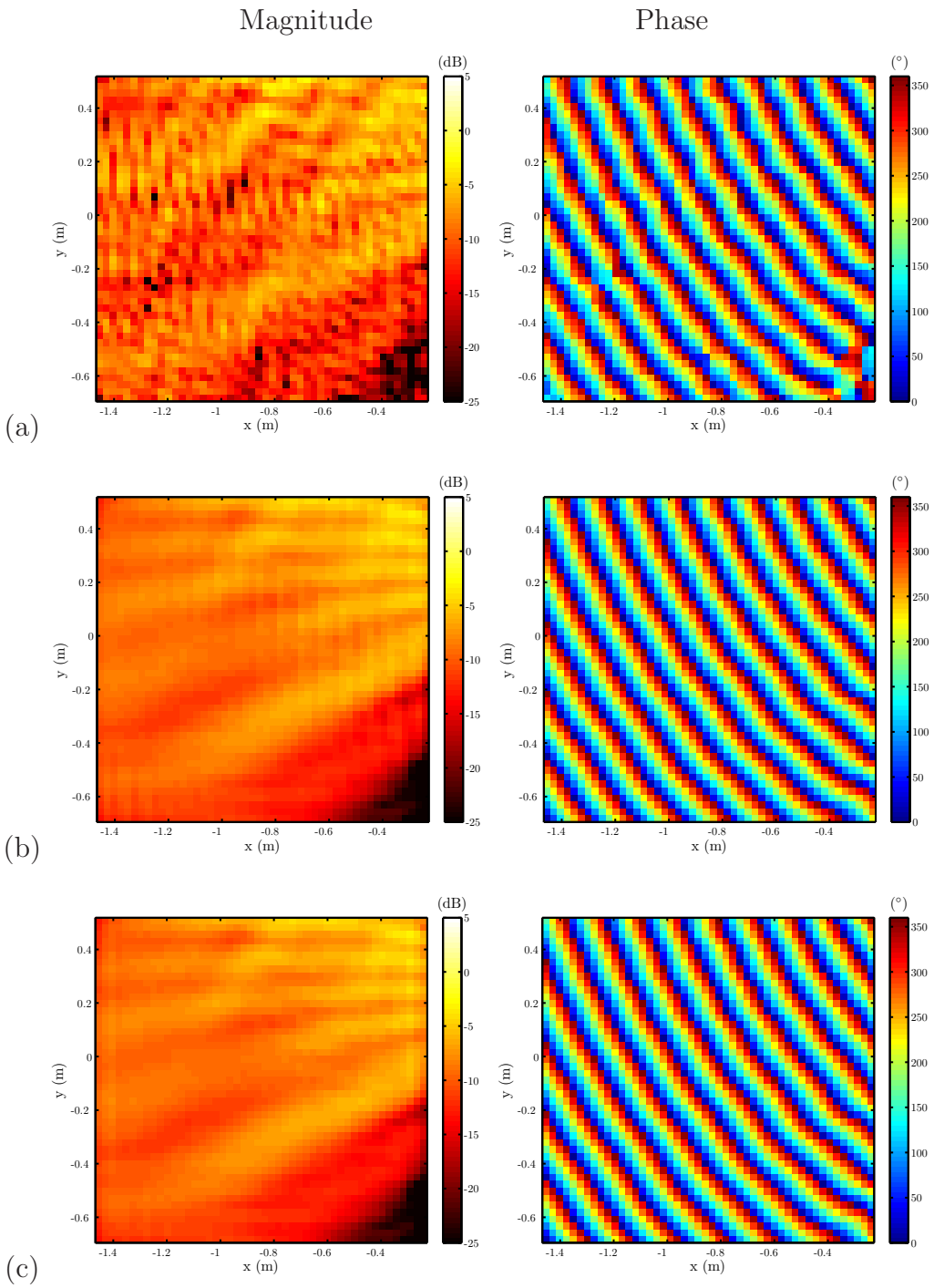

Figure 66: Space-time filters were used to isolate the wedge diffraction problem from the total field measurements. The plots present the magnitude and phase of the filtered brick measurement data for an incident angle of $\phi' = 45°$ at 2.3 GHz: (a) measured, (b) after applying the diffraction-specific filter, and (c) after additional space-time filtering.

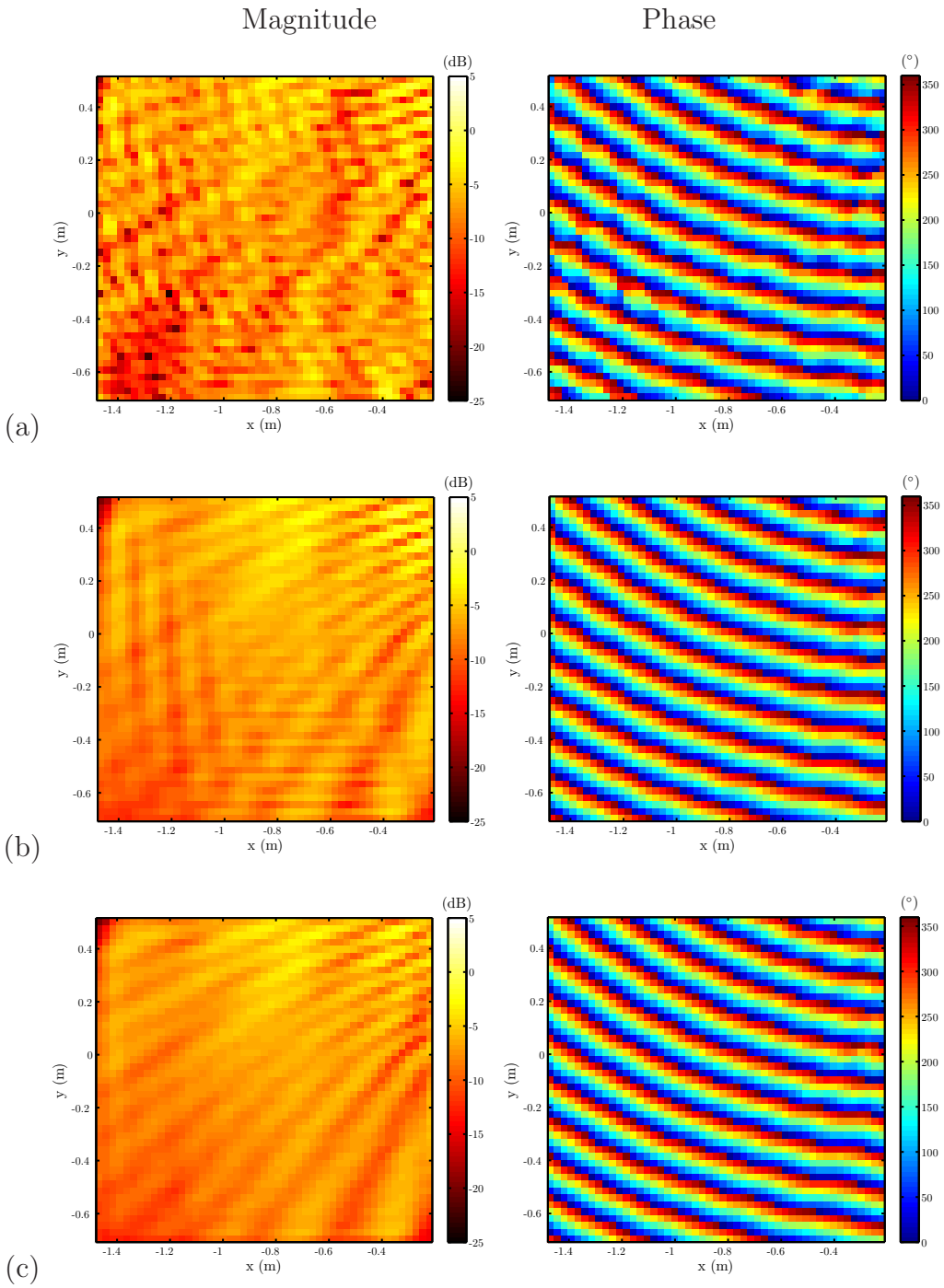

Figure 67: Space-time filters were used to isolate the wedge diffraction problem from the total field measurements. The plots present the magnitude and phase of the filtered "PEC" measurement data for an incident angle of $\phi' = 90°$ at 2.3 GHz: (a) measured, (b) after applying the diffraction-specific filter, and (c) after additional space-time filtering.

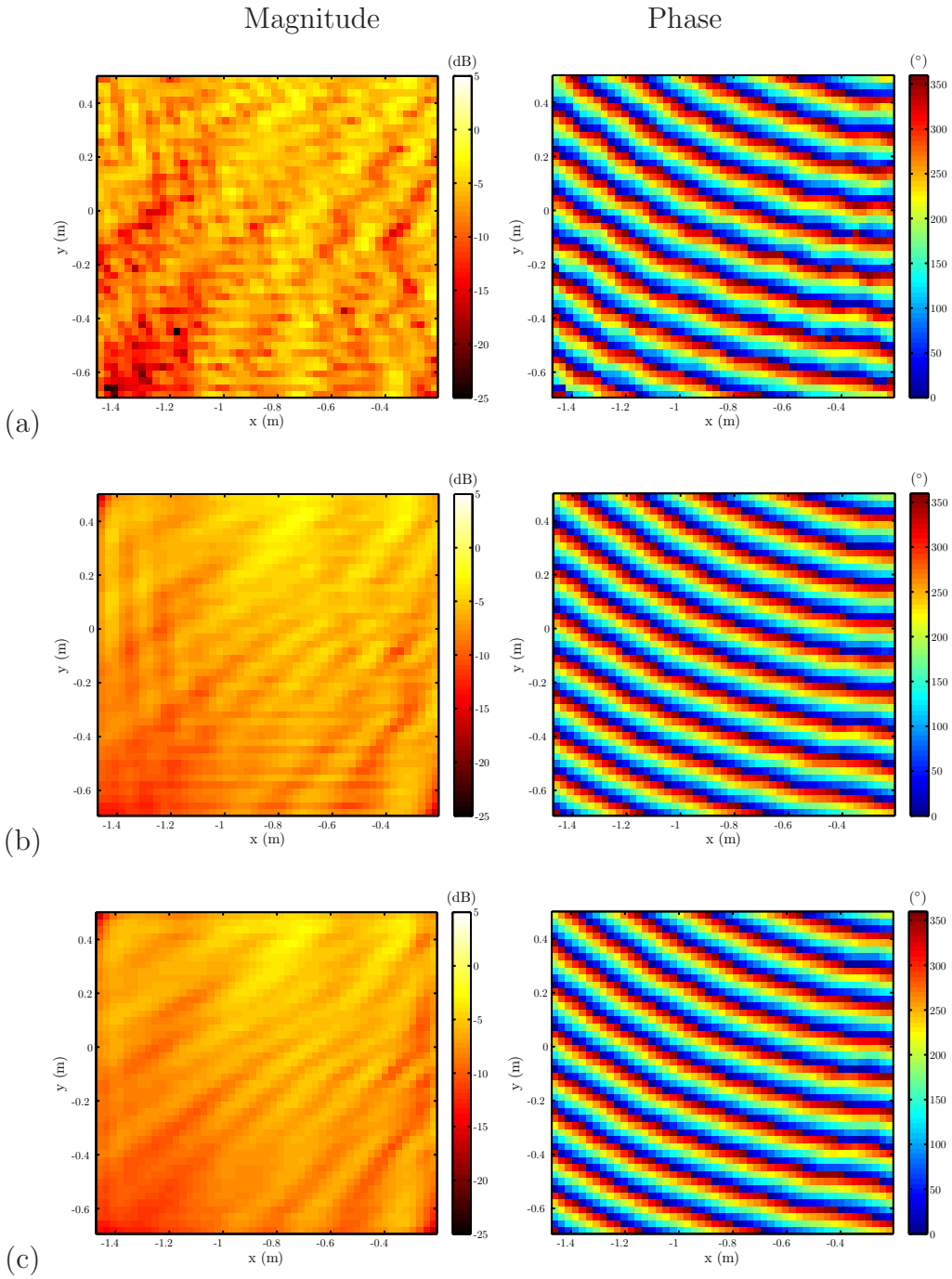

Figure 68: Space-time filters were used to isolate the wedge diffraction problem from the total field measurements. The plots present the magnitude and phase of the filtered brick measurement data for an incident angle of $\phi' = 90°$ at 2.3 GHz: (a) measured, (b) after applying the diffraction-specific filter, and (c) after additional space-time filtering.

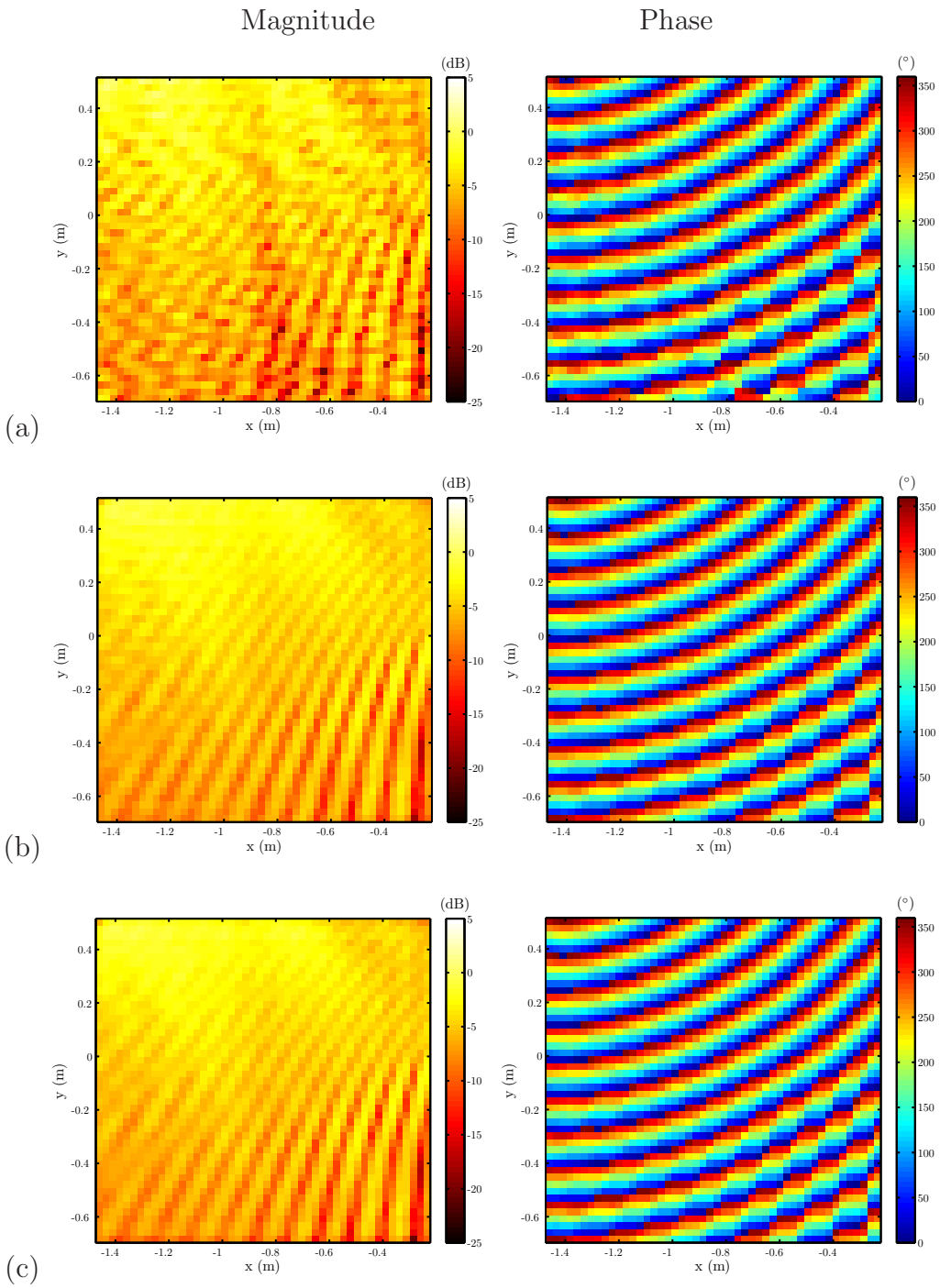

Figure 69: Space-time filters were used to isolate the wedge diffraction problem from the total field measurements. The plots present the magnitude and phase of the filtered "PEC" measurement data for an incident angle of $\phi' = 135°$ at 2.3 GHz: (a) measured, (b) after applying the diffraction-specific filter, and (c) after additional space-time filtering.

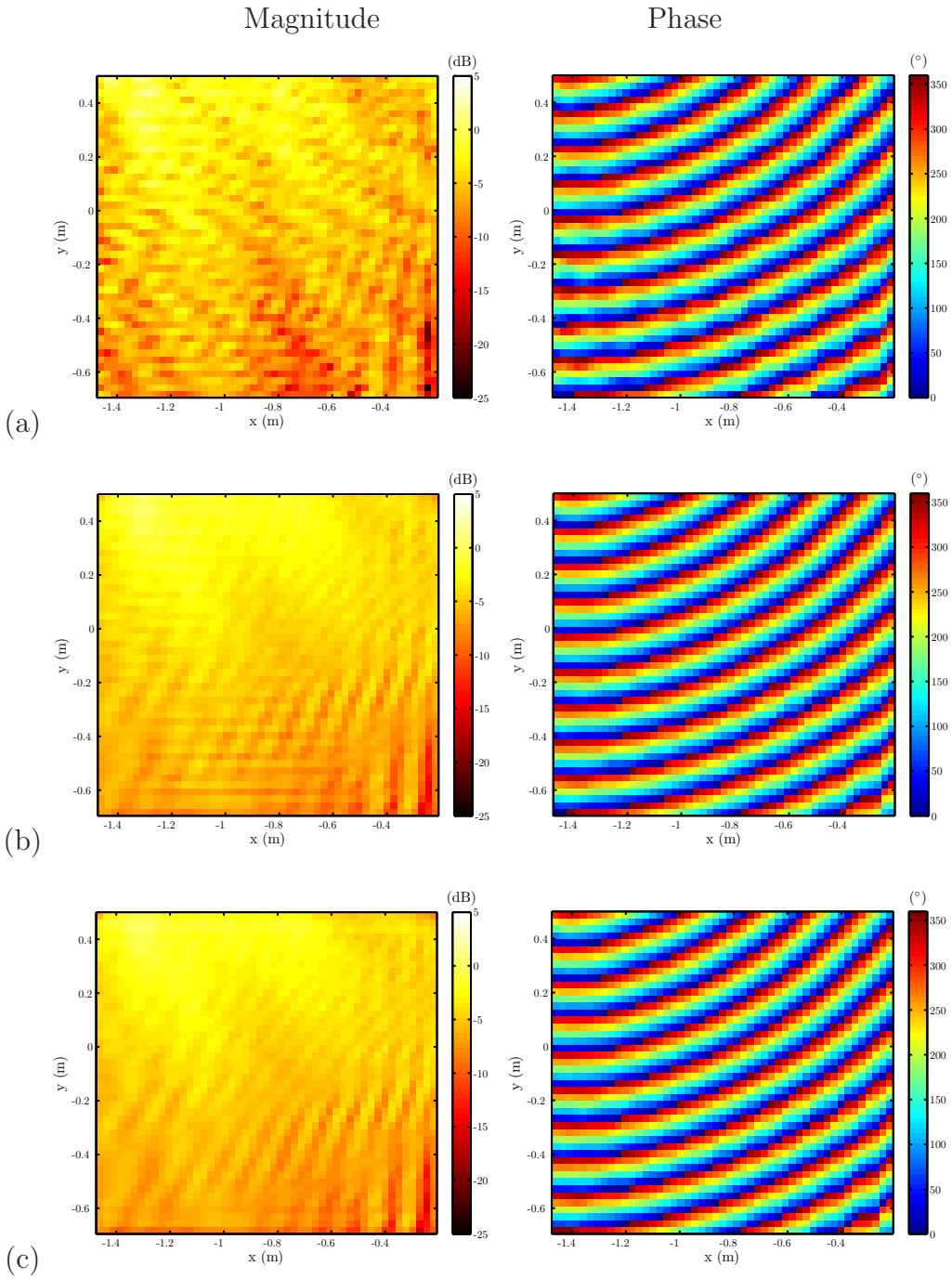

Figure 70: Space-time filters were used to isolate the wedge diffraction problem from the total field measurements. The plots present the magnitude and phase of the filtered brick measurement data for an incident angle of $\phi' = 135°$ at 2.3 GHz: (a) measured, (b) after applying the diffraction-specific filter, and (c) after additional space-time filtering.

Table 2 summarizes the percent change in the measurement data due to filtering. In the table, "Diffraction" designates changes to the total field due to the diffraction-specific space-time filter, "ST" designates changes due to precision space-time filtering, and "Diffraction+ST" designates changes due to the combination of diffraction-specific filtering and precision space-time filtering. For comparison, Table 2 also shows the RMS change when these filters were applied to the UTD PEC wedge simulation used to construct the diffraction-specific space-time filter.

The large RMS changes to the brick and "PEC" measurements as well as the filtering results presented in Figs. 65-70 illustrate how critical space-time filtering can be for in situ measurements of radio wave propagation mechanisms. Without proper filtering, field contributions due to unwanted multipath components may severely distort the field contributions associated with the propagation mechanism of interest. Given the low power spectral density of the transmitter's spread spectrum signal as well as the presence of other wireless systems in the measurement band, it is also likely that the diffraction-specific space-time filters helped to suppress measurement noise corresponding to either the receiver's noise floor or in-band interference. The removal of this measurement noise also helps to explain the rather large RMS changes to the measured complex-baseband wireless channels and suggests a low signal-to-noise-and-interference ratio for the fields corresponding to the building corner diffraction problem. Importantly, the last column in Table 2 indicates that the filters had little effect on spectral components associated with wedge diffraction. This is largely confirmed by the filtering results presented in Figs. 65-70.

5.2 Diffraction Models

Once the wedge diffraction problem was isolated, the diffraction cofficients could be extracted from the filtered measurement data by way of an appropriate wedge diffraction model. Three different diffraction models were used to extract the diffraction

coefficients: 1) the linear diffraction model developed in Chapter 2, 2) a more constrictive nonlinear variation of Chapter 2's linear model, and 3) the UTD's impedance wedge diffraction model. This section briefly summarizes the three diffraction models and evaluates their performance using UTD simulations of the measurements.

5.2.1 Linear Model (a_{1-3})

The linear diffraction model developed and presented in Chapter 2 describes the total field, $\tilde{E}^t(\mathbf{r})$, as a weighted sum of four terms:

$$\begin{aligned}\tilde{E}^t(\mathbf{r}) &= (E_0)\hat{E}^{t,\perp}_{\mathrm{PEC}}(\mathbf{r}) \\ &+(a_1E_0)\left[\,\tilde{C}(\theta)\hat{E}^{r,\perp}_{\mathrm{PEC}}(\mathbf{r})+\tilde{C}(\phi,\phi')\hat{E}^{d,\perp}_{\mathrm{PEC}}(\mathbf{r})\,\right] \\ &-(a_2E_0)\left[\,2\tilde{\chi}^{\perp}_{\parallel}(\theta)\hat{E}^{r,\perp}_{\mathrm{PEC}}(\mathbf{r})\right. \\ &\left.+2\tilde{\chi}^{\perp}_{\parallel}(\phi,\phi')\hat{E}^{i}(\mathbf{0})A(\rho)e^{-jk\rho}\{D_0^-(\phi-\phi')+D_0^-(\phi+\phi')\}\,\right] \\ &-(a_3E_0)\left[\,2\tilde{C}(\theta)\tilde{\chi}^{\perp}_{\parallel}(\theta)\hat{E}^{r,\perp}_{\mathrm{PEC}}(\mathbf{r})\right. \\ &\left.+2\tilde{C}(\phi,\phi')\tilde{\chi}^{\perp}_{\parallel}(\phi,\phi')\hat{E}^{i}(\mathbf{0})A(\rho)e^{-jk\rho}\{D_0^-(\phi-\phi')+D_0^-(\phi+\phi')\}\,\right]\end{aligned} \tag{108}$$

All terms are weighted by the source magnitude and phase, E_0. The latter three terms are also weighted by the model coefficients, a_{1-3}, that are used to construct the semi-empirical diffraction coefficient, $\tilde{D}^{\perp}_{\parallel\,\mathrm{UTD}}(\phi,\phi')$:

$$\begin{aligned}\tilde{D}^{\perp}_{\parallel\,\mathrm{UTD}}(\phi,\phi') &= D^{\perp}_{\mathrm{PEC}}(\phi,\phi') \\ &+a_1\tilde{C}(\phi,\phi')D^{\perp}_{\mathrm{PEC}}(\phi,\phi') \\ &+a_2 2\tilde{\chi}^{\perp}_{\parallel}(\phi,\phi')\{D_0^-(\phi-\phi')+D_0^-(\phi+\phi')\} \\ &+a_3 2\tilde{C}(\phi,\phi')\tilde{\chi}^{\perp}_{\parallel}(\phi,\phi')\{D_0^-(\phi-\phi')+D_0^-(\phi+\phi')\}\end{aligned} \tag{109}$$

The model coefficients, a_{1-3}, may be determined by performing a least-squares fit of the measurements to the linear total field model in Eq. (108) and normalizing the

least-squares solution vector by E_0.

5.2.2 Nonlinear Model (a_{1-2}, $a_3 = a_1 a_2$)

In the development of the linear diffraction model presented in Chapter 2, it was noted that the model coefficients, a_{1-3}, are nominally related by the equality $a_3 = a_1 a_2$. Thus, the nonlinear variation of Chapter 2's model merely enforces this equality. Thereby, the total field for this alternative diffraction model is given by

$$\begin{aligned}
\tilde{E}^t(\mathbf{r}) = (E_0)\hat{E}^{t,\perp}_{\mathrm{PEC}}(\mathbf{r}) \\
&+(a_1 E_0)\left[\,\tilde{C}(\theta)\hat{E}^{r,\perp}_{\mathrm{PEC}}(\mathbf{r}) + \tilde{C}(\phi,\phi')\hat{E}^{d,\perp}_{\mathrm{PEC}}(\mathbf{r})\,\right] \\
&-(a_2 E_0)\left[\,2\tilde{\chi}^{\perp}_{\parallel}(\theta)\hat{E}^{r,\perp}_{\mathrm{PEC}}(\mathbf{r})\right. \\
&\left.+2\tilde{\chi}^{\perp}_{\parallel}(\phi,\phi')\hat{E}^{i}(\mathbf{0})A(\rho)e^{-jk\rho}\{D_0^-(\phi-\phi') + D_0^-(\phi+\phi')\}\,\right] \\
&-(a_1 a_2 E_0)\left[\,2\tilde{C}(\theta)\tilde{\chi}^{\perp}_{\parallel}(\theta)\hat{E}^{r,\perp}_{\mathrm{PEC}}(\mathbf{r})\right. \\
&\left.+2\tilde{C}(\phi,\phi')\tilde{\chi}^{\perp}_{\parallel}(\phi,\phi')\hat{E}^{i}(\mathbf{0})A(\rho)e^{-jk\rho}\{D_0^-(\phi-\phi') + D_0^-(\phi+\phi')\}\,\right]
\end{aligned} \tag{110}$$

Explicitly enforcing $a_3 = a_1 a_2$ leads to a more constrictive diffraction model that should be more robust in the presence of measurement errors. Furthermore, because a_3 is nominally given by $a_1 a_2$, this substitution should have little impact on the model's accuracy. However, enforcing $a_3 = a_1 a_2$ also means that the unknown model coefficients, a_{1-2}, can only be determined using a nonlinear least-squares solver. The corresponding semi-empirical diffraction coefficient may be determined by substituting $a_1 a_2$ for a_3 in Eq. (109):

$$\tilde{D}^{\perp}_{\parallel\,\mathrm{UTD}}(\phi,\phi') = D^{\perp}_{\mathrm{PEC}}(\phi,\phi') \tag{111}$$
$$+a_1\tilde{C}(\phi,\phi')D^{\perp}_{\mathrm{PEC}}(\phi,\phi')$$
$$+a_2 2\tilde{\chi}^{\perp}_{\parallel}(\phi,\phi')\{D_0^-(\phi-\phi')+D_0^-(\phi+\phi')\}$$
$$+a_1a_2 2\tilde{C}(\phi,\phi')\tilde{\chi}^{\perp}_{\parallel}(\phi,\phi')\{D_0^-(\phi-\phi')+D_0^-(\phi+\phi')\}$$

5.2.3 UTD Impedance Wedge Model: (ϵ_R)

The third diffraction model used to extract semi-empirical diffraction coefficients was the UTD impedance wedge model. This model's total field solution is given by Eq. (12) for some normalized impedance angle, $\left|\theta^{\perp}_{\parallel}\right|$, as determined by Eqs. (21) and (22) for some wedge face impedance, Z_s. The corresponding UTD impedance wedge diffraction coefficient is given by Eq. (25). As in Chapter 2), we will equate Z_s to intrinsic impedance, η, as given by Eq. (14) for some unknown relative permittivity, ϵ_R, assuming a relative permeability of $\mu_R = 1$. As with the nonlinear model described in Eq. (110), the UTD impedance wedge model's unknown relative permittivity, ϵ_R, can only be solved using a nonlinear least-squares solver.

5.2.4 Diffraction Coefficient Extraction Simulation

In Chapter 2, the linear wedge diffraction model was evaluated as a tool for extracting the diffraction coefficient from total field data. This evaluation was repeated for the three diffraction models (linear, nonlinear, and UTD impedance wedge) using UTD simulations of the three different measurement geometries assuming a PEC wedge for the "PEC" measurements and a brick-like impedance wedge for the brick measurements. Based upon the range of conductivities and permittivities cited in the literature [58, 23, 73, 40], a complex relative permittivity of $\epsilon_R = 4 - j0.2$ was used to describe the brick-like impedance wedge. At the simulation frequency of 2.3 GHz, which corresponds to the diffraction measurements' center frequency, an imaginary

relative permittivity of 0.2 is equivalent to specifying a conductivity of $\sigma = 0.026$ S/m. For the ultra-wideband measurements described in Chapter 4, assuming a brick conductivity of $\sigma = 0.026$ S/m would imply that the brick's complex permittivity ranges from $\epsilon_R = 4 - j0.24$ at 1.85 GHz to $\epsilon_R = 4 - j0.16$ at 2.75 GHz. From these observations and the rather weak frequency dependence of brick at microwave frequencies [103], any frequency-dependent changes in the permittivity of brick due to dielectric relaxation effects or conductivity is unlikely to be observed in the diffraction measurements.

It should also be noted that at the measurement band spanning 1.85 GHz to 2.75 GHz, a dielectric medium with a permittivity of $\epsilon_R = 4 - j0.2$ will have a skin depth, δ_s, between 0.52 m and 0.35 m. This range of skin depths is significantly larger than the 0.1 m thickness of the building corner's exterior brickwork and corresponds to less than 3 dB of attenuation for a wave that is normally incident on a 0.1 m thick brick wall. Although this low attenuation might suggest that a significant amount of power could propagate *through* the building corner, it is important to recognize that refraction by and reflections within the brick wall will also play a role. For a solid right-angled dielectric wedge with a permittivity of $\epsilon_R \geq 4$, any waves propagating into the wedge at one face will undergo total internal reflection (TIR) at the opposing face whereby no power actually propagates through the wedge. However, scattering within an actual building corner due to inhomogeneities and even the interior "air" corner will invariably cause some of the power trapped by TIR within the brickwork to "leak" out.

Strictly speaking, the impedance wedge model may only be used to model the field exterior to a diffracting wedge when the fields propagating into the wedge have no effect on the exterior fields. That is, any waves penetrating the wedge faces must be severely attenuated due to losses or remain trapped within the wedge due to TIR.

Although the potential for waves to propagate into and be scattered out of an inhomogeneous building corner conflicts with this requirement, the impedance wedge is the only existing analytical model applicable to the building corner diffraction problem. Furthermore, provided $\epsilon_R \geq 4$ and neglecting inhomogeneities within the brickwork, propagation through a brick building corner is solely dependent on scattering processes *interior* to the brickwork. Thus, any diffracted field contributions arising due to waves undergoing scattering within the building corner should be significantly smaller than the diffracted field resulting from the source's incident field, $E^i(\mathbf{r})$, impinging on the building corner's diffracting edge. Therefore, it is expected that the impedance wedge model should provide a reasonably accurate description of the fields diffracted by a brick building corner and thereby, the corner's corresponding diffraction coefficient. Depending on the extent of scattering within the building corner, the impedance wedge model may also provide an acceptable description of the building corner diffraction problem's total field.

Figure 71 presents the diffraction coefficients that were extracted from the UTD simulations. For completeness and continuity with later diffraction coefficient plots, both the PEC wedge and the brick-like impedance wedge ($\epsilon_R = 4 - j0.2$) were simulated. The first column of plots correspond to the diffraction coefficients extracted from the PEC wedge simulation; the second column, the brick-like impedance wedge. From the top down, the corresponding incident angles are 45°, 90°, and 135°. To facilitate comparisons, all plots show the UTD's diffraction coefficients for a PEC and brick-like impedance wedge. The gray region in the plots identifies the observation angular sector, $\phi \in [128°, 250°]$, subtended by the rectangular measurement region described in Fig. 43.

The diffraction coefficients extracted from the PEC and brick-like impedance wedge simulation are in excellent agreement with their theoretical counterparts. As might be expected, the diffraction coefficients extracted using the UTD impedance

wedge model are consistently the most accurate. The diffraction coefficient extracted from the PEC wedge simulations also tend to be more accurate than those extracted from the brick-like impedance wedge simulation. This is particurlarly true for the linear and nonlinear diffraction models, which were formulated as additive corrections to the PEC wedge solution.

5.3 Semi-Empirical Diffraction Coefficients

A two-stage least-squares fitting procedure was used to fit the space-time filtered "PEC" and brick measurements to each of the three diffraction models (linear, nonlinear, and UTD impedance wedge). First, the wideband measurement data was normalized at each of the measurement frequencies by the the source phasor, E_0. For the linear and nonlinear models, E_0 was determined by fitting the measurements directly to the model. For the UTD impedance wedge model, the source phasor, E_0, was determined by fitting the measurements to the UTD PEC wedge model. After normalizing the measurements, the model unknowns (a_{1-3}, a_{1-2}, and ϵ_R) were determined that provided the best fit across the entire measurement band. Thus, the least-squares fitting procedure tacitly assumed that the material-dependent model unknowns were frequency independent. Based upon the range of brick permittivities and conductivities quoted in the literature, this is a reasonable assumption.

Figure 72 presents the semi-empirical diffraction coefficients resulting from the wideband least-squares fit of the diffraction models to the measurement data. At best, the extracted diffraction coefficients may be said to have a tendency to follow the corresponding UTD PEC and brick-like impedance wedge diffraction coefficients. However, generally the agreement between the measurement data and the theoretical curves is extremely poor. The inconsistency and poor fit of the extracted diffraction coefficients could be attributed to a number of factors, but the most likely culprit is measurement geometry errors. In Chapter 2, it was noted that in order to apply

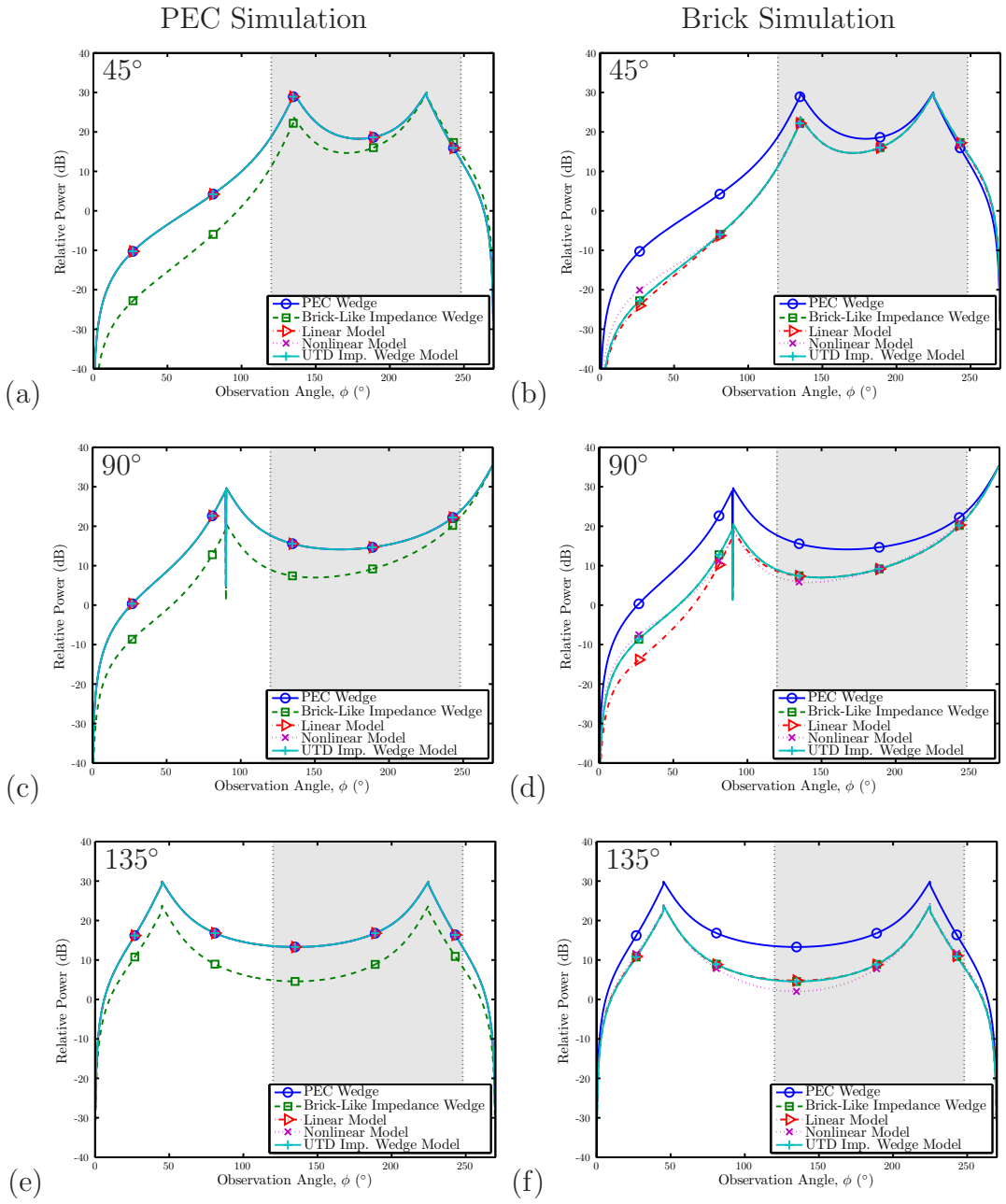

Figure 71: The semi-empirical diffraction coefficients extracted from simulations of the UTD's PEC and brick-like impedance wedge total field solution. For comparison, the UTD's PEC and brick-like impedance wedge diffraction coefficients are also presented. (a) $\phi' = 45°$, PEC wedge; (b) $\phi' = 45°$, brick-like impedance wedge; (c) $\phi' = 90°$, PEC wedge; (d) $\phi' = 90°$, brick-like impedance wedge; (e) $\phi' = 135°$, PEC wedge; (f) $\phi' = 135°$, brick-like impedance wedge.

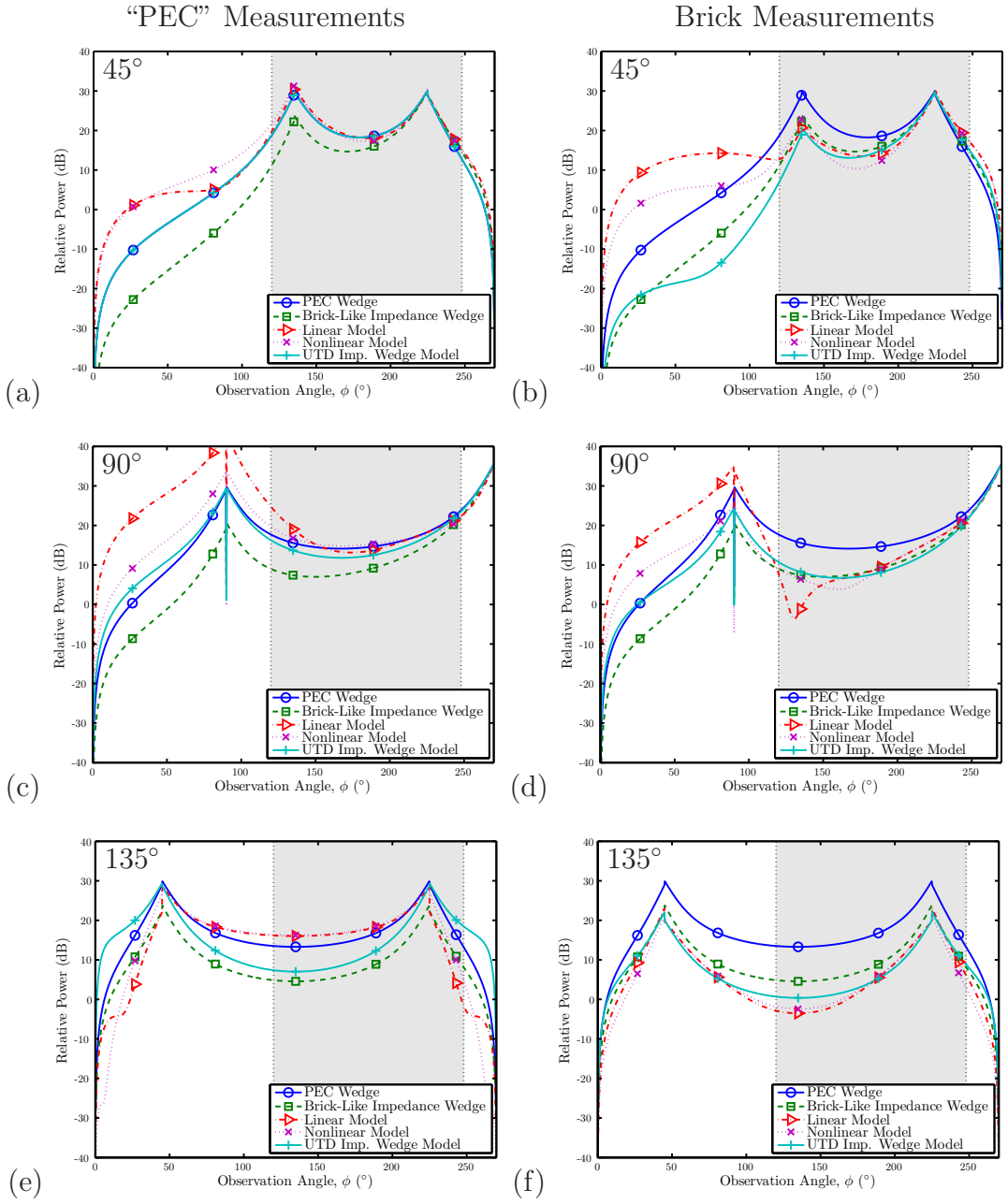

Figure 72: The semi-empirical diffraction coefficients extracted from the "PEC" and brick corner diffraction measurements using Model I. For comparison, the UTD's PEC and impedance ($\epsilon = 5 - j0.1$, $\sigma = 0.03$ S/m) wedge diffraction coefficients are also presented. (a) $\phi' = 45°$, "PEC"; (b) $\phi' = 45°$, brick; (c) $\phi' = 90°$, "PEC"; (d) $\phi' = 90°$, brick; (e) $\phi' = 135°$, "PEC"; (f) $\phi' = 135°$, brick.

the linear model for wedge diffraction, the exact geometry of the problem must be known. Specifically, one must know the wedge's interior angle and the positions of the transmitter and receiver relative to the diffracting edge. For the diffraction measurements described in Chapter 4, the *intended* problem geometry was described in Fig. 43. However, the actual positions of the transmitter and receiver invariably differed from these intended positions.

5.3.1 Geometry Error Simulations

To confirm that the behavior of semi-empirical diffraction coefficients presented in Fig. 72 may be attributed to measurement geometry errors, the previous diffraction coefficient extraction simulations were repeated with the inclusion of a random displacement of the source and measurement region. The diffraction coefficients were then extracted from this new set of simulated total field data under the false assumption that the measurement geometry agreed with the intended geometry described in Fig. 43. The source and measurement region's x and y displacements were described by four independent and identically distributed Gaussian random variables with zero mean and a standard deviation of 3 cm. The simulation was repeated 100 times for each of the three incident angles for both the PEC and impedance wedge. To ensure a fair comparison across all combinations of incident angle and wedge type, a common set of 100 pairs of 2-D source and measurement region displacements were used.

Figs. 73, 74, and 75 present the diffraction coefficients extracted from the geometry error simulations using the linear, nonlinear, and UTD impedance wedge diffraction model, respectively. The overlapping gray curves correspond to the diffraction coefficients that were extracted from each of the 100 simulations. Superimposed atop these erroneous diffraction coefficients are the UTD's PEC and brick-like impedance wedge diffraction coefficients as well as the semi-empirical diffraction coefficients that were extracted from the measurements.

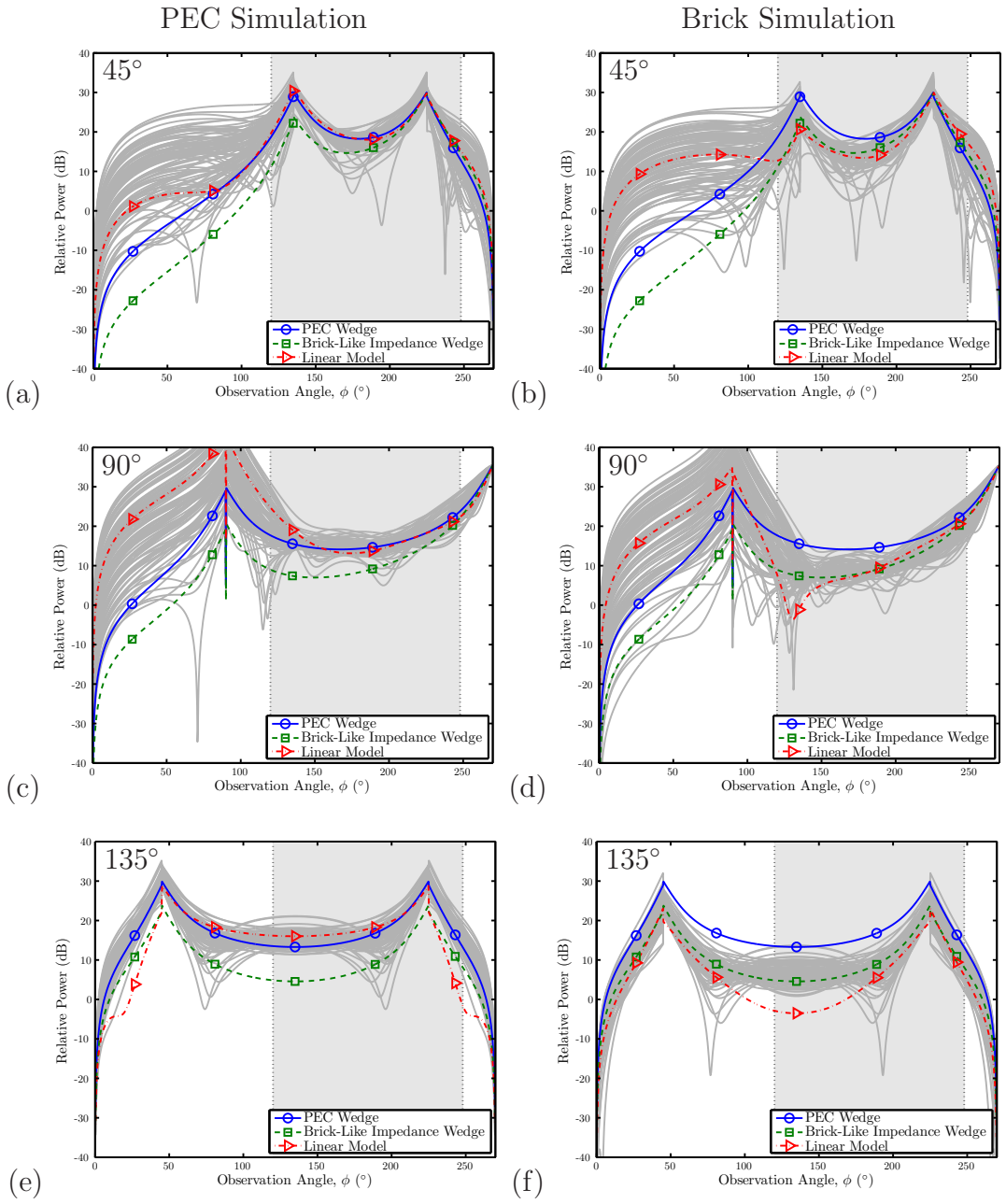

Figure 73: The semi-empirical diffraction coefficients extracted from simulations of the UTD's PEC and brick wedge total field solution after introducing geometry errors. Diffraction coefficients were extracted using the linear model. For comparison, the UTD's PEC and impedance wedge diffraction coefficients are also presented. (a) $\phi' = 45°$, "PEC"; (b) $\phi' = 45°$, brick; (c) $\phi' = 90°$, "PEC"; (d) $\phi' = 90°$, brick; (e) $\phi' = 135°$, "PEC"; (f) $\phi' = 135°$, brick.

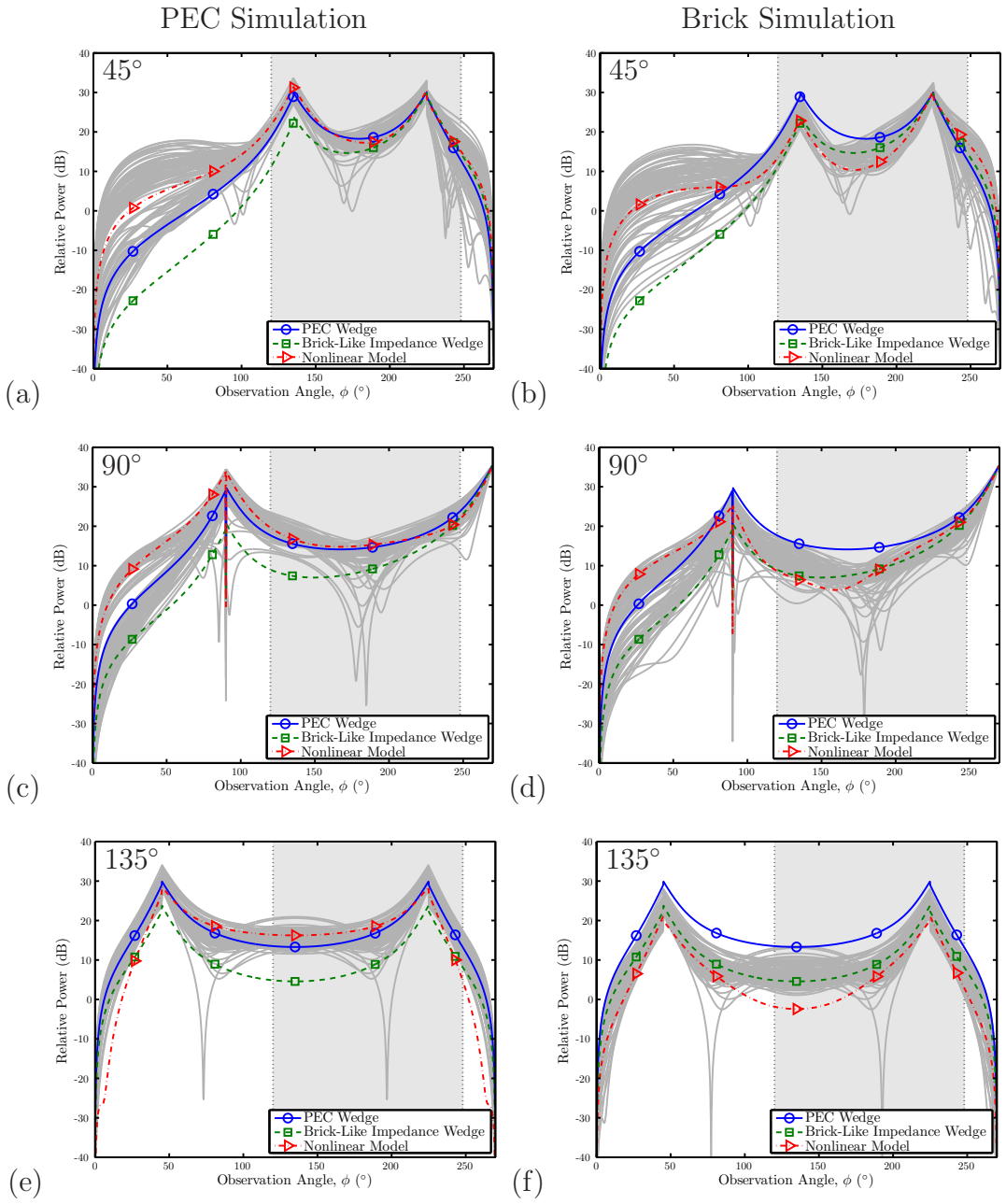

Figure 74: The semi-empirical diffraction coefficients extracted from simulations of the UTD's PEC and brick wedge total field solution after introducing geometry errors. Diffraction coefficients were extracted using the nonlinear model. For comparison, the UTD's PEC and impedance wedge diffraction coefficients are also presented. (a) $\phi' = 45°$, "PEC"; (b) $\phi' = 45°$, brick; (c) $\phi' = 90°$, "PEC"; (d) $\phi' = 90°$, brick; (e) $\phi' = 135°$, "PEC"; (f) $\phi' = 135°$, brick.

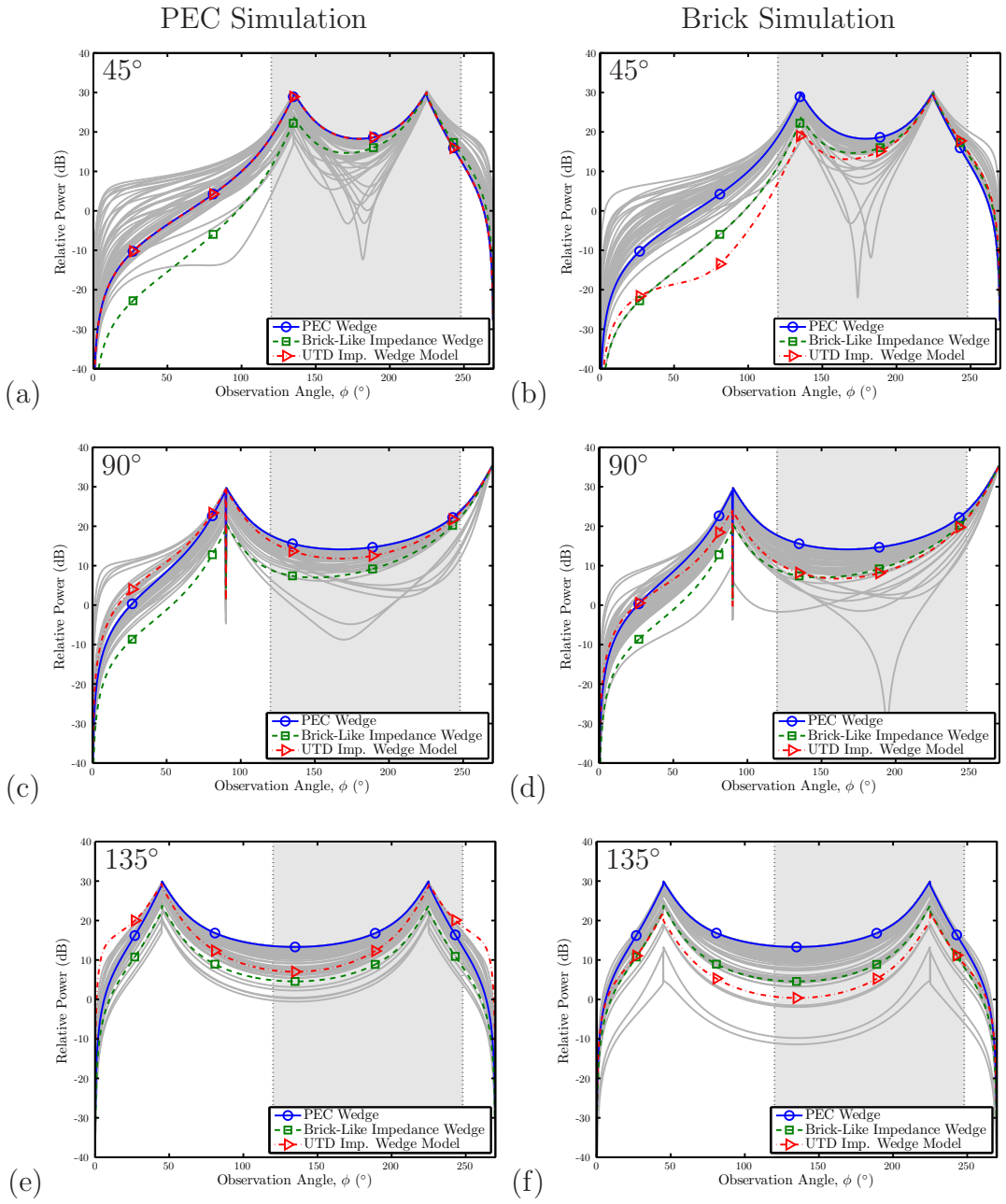

Figure 75: The semi-empirical diffraction coefficients extracted from simulations of the UTD's PEC and brick wedge total field solution after introducing geometry errors. Diffraction coefficients were extracted using the UTD impedance wedge model. For comparison, the UTD's PEC and impedance wedge diffraction coefficients are also presented. (a) $\phi' = 45°$, "PEC"; (b) $\phi' = 45°$, brick; (c) $\phi' = 90°$, "PEC"; (d) $\phi' = 90°$, brick; (e) $\phi' = 135°$, "PEC"; (f) $\phi' = 135°$, brick.

Three important observations can be made based on the data presented in Figs. 73-75. First, the measurement-based semi-empirical diffraction coefficients are generally within the range of variations of the erroneous diffraction coefficients, indicating that the behavior of the extracted diffraction coefficients may be attributed to measurement geometry errors. The exceptions are Figs. 73-74(f), which indicate the diffraction coefficients extracted from the brick measurements for $\phi' = 135°$ are several dB below the lowest gray error curve. This suggests that either the geometry errors for the $\phi' = 135°$ brick measurement were outside the range of the simulated errors or that the actual building corner's diffraction coefficient is smaller in magnitude than the UTD's brick-like impedance wedge diffraction coefficient. It is worth noting that the $\phi' = 135°$ diffraction coefficient extracted using the UTD impedance wedge model was also smaller in magnitude than the brick-like impedance wedge diffraction coefficient.

Second, the more constrained diffraction models tend to be more robust in the presence of measurement geometry errors. Diffraction coefficients extracted from the erroneous simulation data using the linear model (Fig. 73) showed the greatest range of variations, whereas the diffraction coefficients extracted using the UTD impedance wedge model (Fig. 75) showed the smallest range of variations. The rather peculiar exception to this generalization is the $\phi' = 135°$ measurements, wherein it seems that the UTD impedance wedge model is the least robust. This is encouraging given that the diffraction coefficients extracted from the $\phi' = 135°$ "PEC" measurements using the UTD impedance wedge model (Figs. 73(e)) showed little similarity to the UTD's PEC wedge diffraction coefficient.

Third, despite the geometry errors, the erroneous diffraction coefficients tend to follow the behavior of the actual UTD coefficients, especially in the gray rectangular region that delineates the angular sector subtended by the measurement/simulation region. Thus, even with geometry errors, the extracted semi-empirical diffraction

coefficients provide a vague sense of the actual "PEC" and brick building corners' diffraction coefficients. However, given this position error, it is difficult to say much more about the extracted semi-empirical diffraction coefficients beyond the fact that the "PEC" and brick measurements *loosely* resemble the UTD's PEC and impedance wedge diffraction coefficients.

5.3.2 Geometry Error Correction

To improve the accuracy of the extracted diffraction coefficients, a geometry correction technique was developed to ascertain the actual geometry of the diffraction measurements. There were two key assumptions in the development and application of this geometry correction technique. First, it was assumed that the space-time filtered measurement data resembled the total field due to diffraction by an arbitrary wedge. This is largely confirmed by the filtered measurement data presented in Figs. 65-70 and Appendix F. Second, it was assumed that an extremely simple wedge diffraction model could be used as a fitting function for determining the transmitter and measurement region positions via a least-squares fit. That is, a low-complexity diffraction model would provide the best fit to the measurement data only when the model's source and observation positions coincided with the actual positions of the transmitter and the field reconstruction region. This assumption is reasonable given that the incident, reflected, and diffracted fields are all characterized by circular wavefronts as illustrated by the diagrams in Figs. 59-64. Thereby, the phase structure of the space-time wireless channel within the measurement region contains information about the geometry of the diffraction problem.

The geometry error correction technique processed the "PEC" and brick measurements in pairs of identical incident angles, ϕ', to exploit the measurements' mutual information on the transmitter location. As was noted in Chapter 4, for a given incident angle, the transmitter location was fixed and identical for the "PEC" and brick

measurements. Four different combinations of the the UTD's PEC and brick-like impedance wedge solution were used as low-complexity fitting models for determining the true positions of the transmitter and measurement region. In the first of the four model combinations, both the "PEC" and brick measurements were fit to the UTD's PEC wedge solution. In the second case, the UTD's brick-like impedance wedge solution was used as the fitting model for both the "PEC" and brick measurements. The third case applied the PEC model to the "PEC" measurements and the brick-like impedance model to the brick measurements. Assuming that the "PEC" and brick measurements actually resemble the UTD's PEC and brick-like impedance wedge solutions, this fitting model combination is expected to yield the most accurate position corrections. Finally, to thoroughly assess the effect of the choice of the fitting model, the third combination was reversed whereby the PEC model was applied to the brick measurements and the brick-like impedance wedge solution was applied to the "PEC" measurements. The target minimization function for the geometry error correction technique returned the residual of a least-squares fit of the PEC/brick-like impedance wedge diffraction model to the measurements for a specified diffraction model geometry. The wideband least-squares fitting procedure for these low-complexity diffraction models was analogous to that used for the UTD impedance wedge model in the preceding section.

Table 3 summarizes the results of this geometry error correction for the various diffraction models and incident angles. It is encouraging to observe that, aside from the transmitter position for $\phi' = 45°$, there is a fair amount of consistency in the measurement geometry corrections despite the variations in the fitting models. Less encouraging, however, is the large displacement corrections for the transmitter location with $\phi' = 90°$.

Figures 76, 77, and 78 present the diffraction coefficients that were extracted from the "PEC" and brick corner diffraction measurements using the linear, nonlinear,

Table 3: Paired Geometry Error Correction Results (cm)

ϕ'	**"PEC"/Brick Model Pair**	**"PEC" Rx**		**Brick Rx**		**Tx**	
		Δx	Δy	Δx	Δy	Δx	Δy
45°	PEC/PEC	1.3	-0.8	2.0	-0.5	-5.8	-3.1
	Imp./Imp.	2.2	-0.6	3.7	-0.1	0.7	0.4
	PEC/Imp.	1.9	-0.7	3.3	-0.2	-1.9	-1.1
	Imp./PEC	1.4	-0.7	2.2	-0.4	-3.5	-1.8
90°	PEC/PEC	2.6	-0.6	3.4	2.2	5.5	11.2
	Imp./Imp.	3.0	0.4	3.9	2.5	5.8	11.1
	PEC/Imp.	2.7	-0.5	3.6	2.3	5.7	11.2
	Imp./PEC	2.8	-0.5	3.6	2.4	5.6	11.1
135°	PEC/PEC	3.8	2.4	3.3	2.9	5.1	6.1
	Imp./Imp.	3.8	1.6	3.3	1.8	5.1	5.1
	PEC/Imp.	3.7	2.1	3.3	2.1	5.1	5.5
	Imp./PEC	3.9	2.3	3.3	2.8	5.2	6.0

and UTD impedance wedge model, respectively, following the application of this geometry error correction technique. As might be expected given the consistency of the geometry error corrections in Table 3, there is a fair amount of consistency in the extracted diffraction coefficients across the various fitting model combinations, though particularly within the angular sector subtended by the measurement region. More importantly, Figs. 76-78 reveal that fitting the measurement data to the UTD's PEC or brick-like impedance wedge solution does not force the resulting diffraction coefficients to resemble the PEC or brick-like impedance wedge coefficient.

Excluding the $\phi' = 90°$ measurement data, the diffraction coefficients presented in Figs. 76-78 appear relatively similar within the angular sector subtended by the measurement region. Outside of this observation angular sector, the diffraction coefficients extracted using the linear model tend to be inconsistent with those extracted using the nonlinear and UTD impedance wedge model. Furthermore, whereas the diffraction coefficients extracted from the $\phi' = 90°$ measurements using the UTD

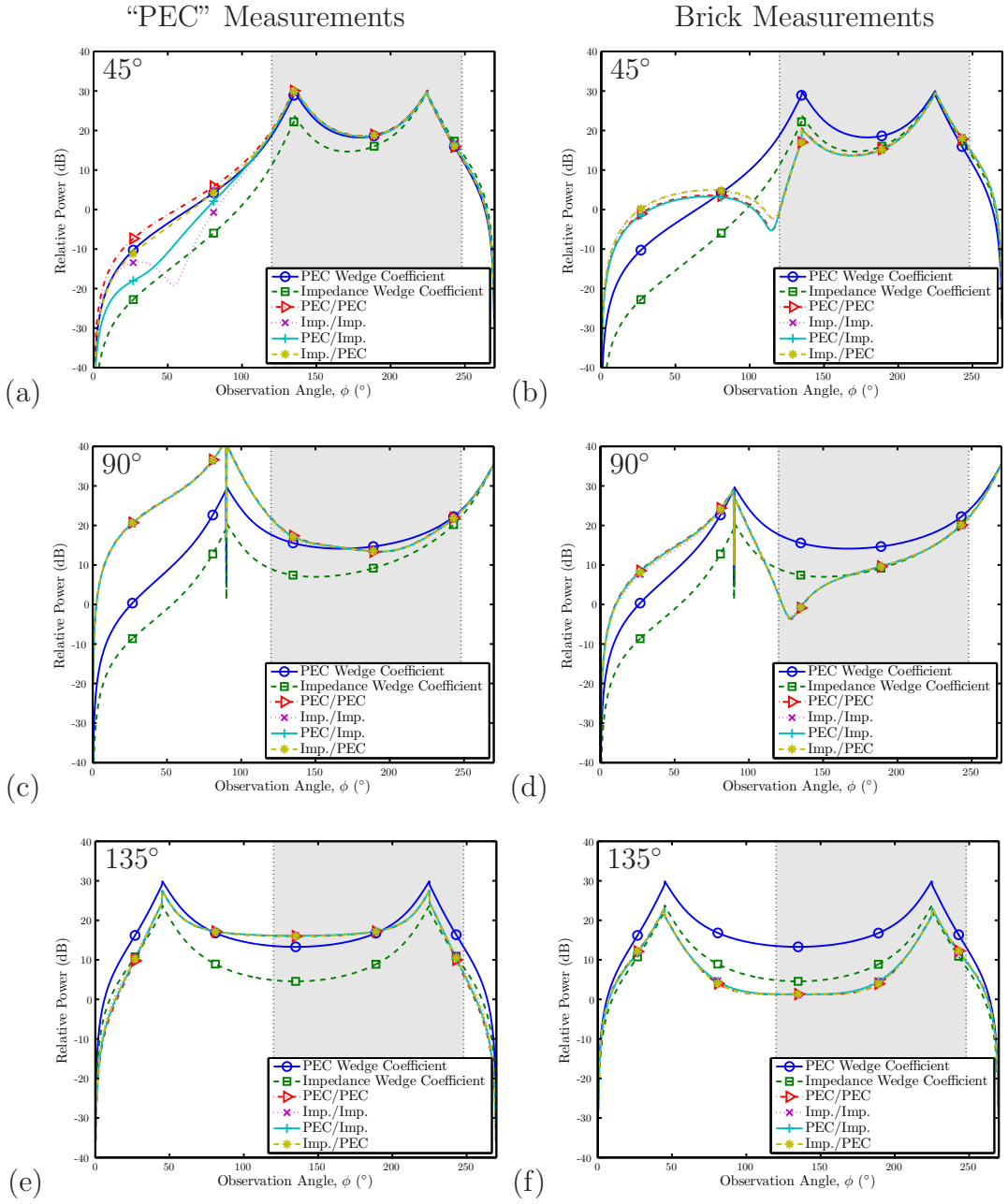

Figure 76: The semi-empirical diffraction coefficients extracted from the position-corrected "PEC" and brick corner diffraction measurements using the linear model. For comparison, the UTD's PEC and brick-like impedance wedge diffraction coefficients are also presented. (a) $\phi' = 45°$, "PEC"; (b) $\phi' = 45°$, brick; (c) $\phi' = 90°$, "PEC"; (d) $\phi' = 90°$, brick; (e) $\phi' = 135°$, "PEC"; (f) $\phi' = 135°$, brick.

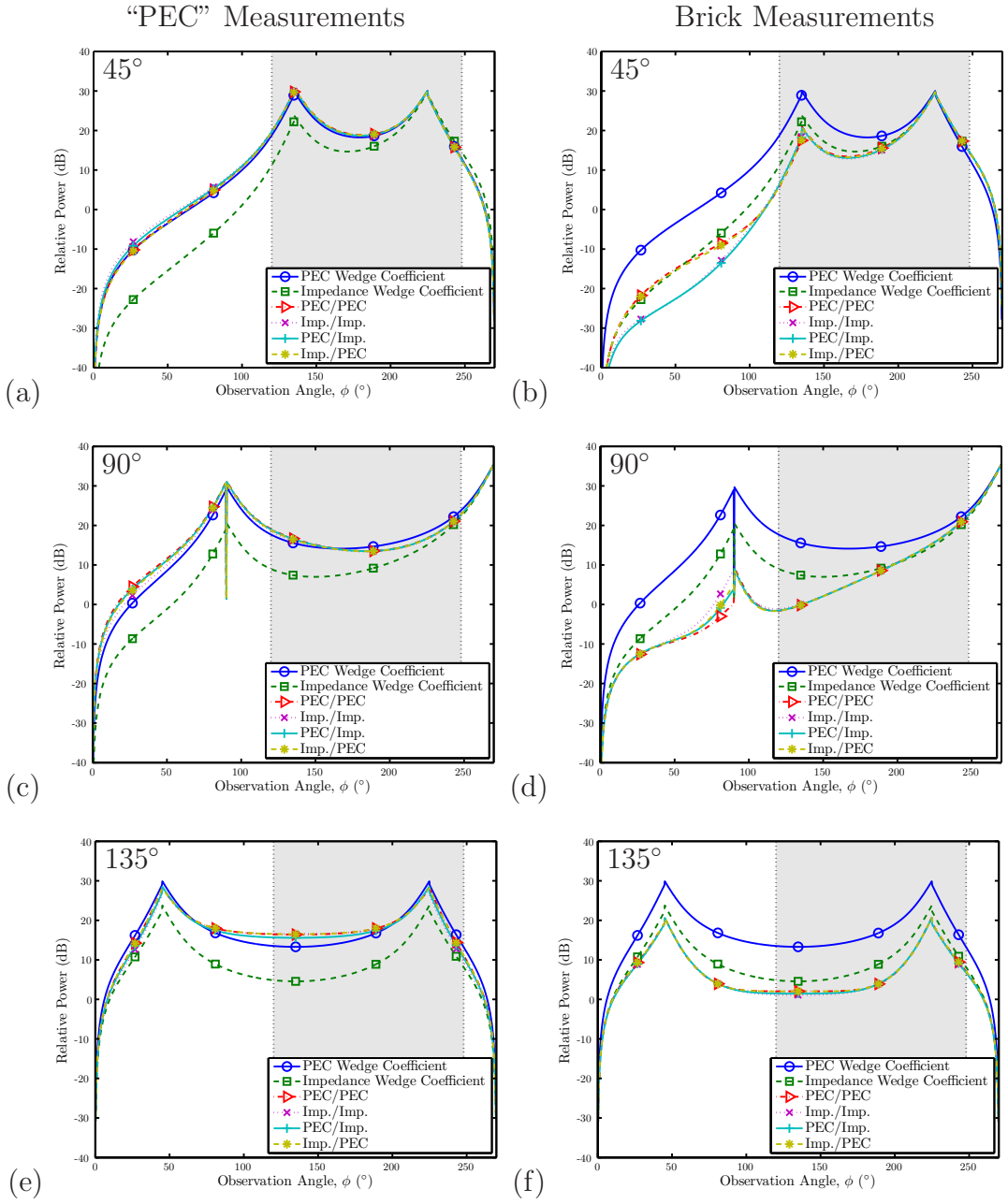

Figure 77: The semi-empirical diffraction coefficients extracted from the position-corrected "PEC" and brick corner diffraction measurements using the nonlinear model. For comparison, the UTD's PEC and brick-like impedance wedge diffraction coefficients are also presented. (a) $\phi' = 45°$, "PEC"; (b) $\phi' = 45°$, brick; (c) $\phi' = 90°$, "PEC"; (d) $\phi' = 90°$, brick; (e) $\phi' = 135°$, "PEC"; (f) $\phi' = 135°$, brick.

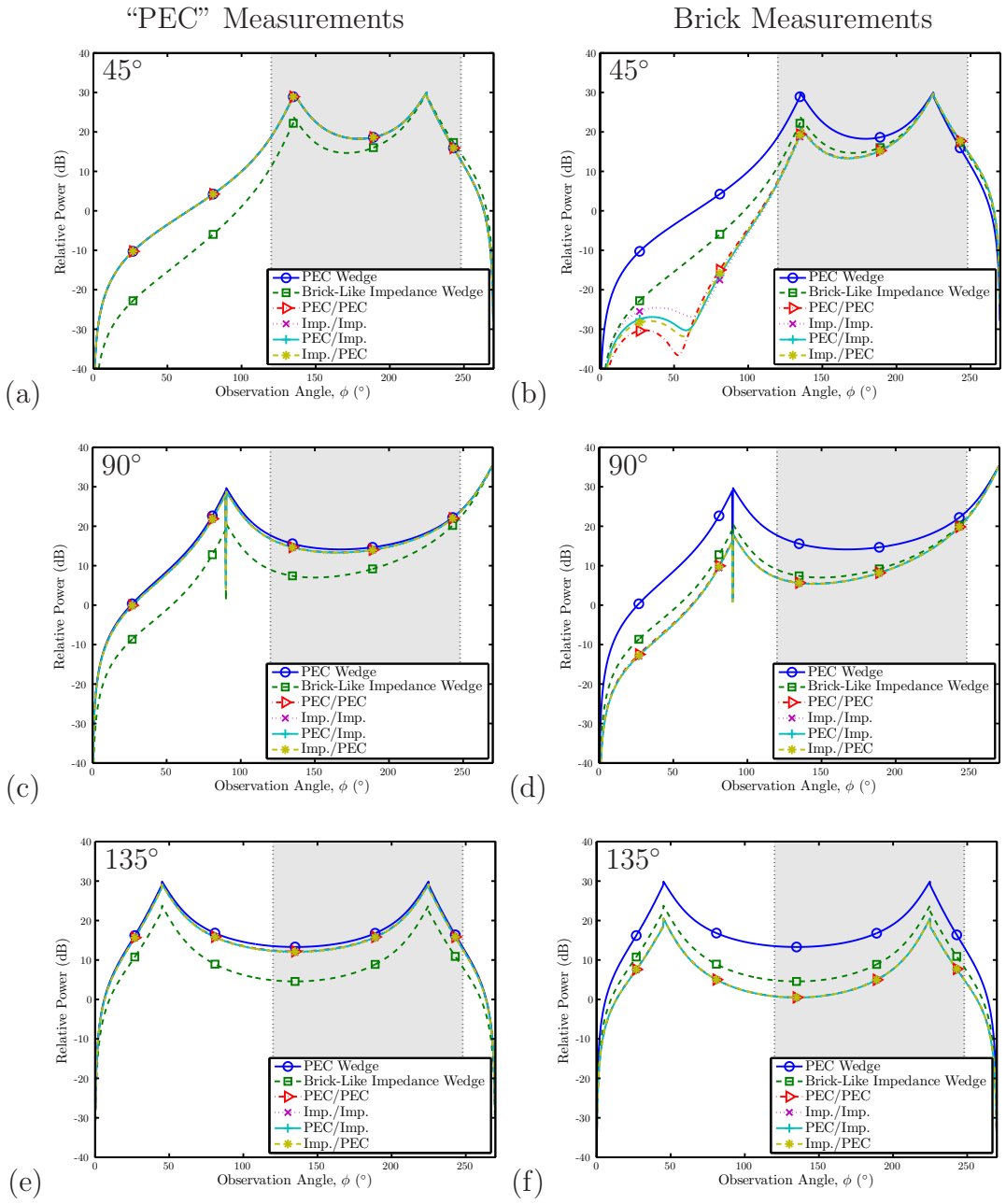

Figure 78: The semi-empirical diffraction coefficients extracted from the position-corrected "PEC" and brick corner diffraction measurements using the UTD impedance wedge model. For comparison, the UTD's PEC and brick-like impedance wedge diffraction coefficients are also presented. (a) $\phi' = 45°$, "PEC"; (b) $\phi' = 45°$, brick; (c) $\phi' = 90°$, "PEC"; (d) $\phi' = 90°$, brick; (e) $\phi' = 135°$, "PEC"; (f) $\phi' = 135°$, brick.

impedance wedge model and to an extent the nonlinear model seem reasonable, those extracted using the linear model appear quite bizarre. In light of these observations and the fact that the linear model was found to be the least robust in the presence of measurement errors, the behavior of the diffraction coefficients in Figs. 76-78 as well as the inconsistency of the $\phi' = 90^\circ$ diffraction coefficients might be attributable to the degrees-of-freedom of the different diffraction models. However, this does not help to explain the large (> 10 cm) and somewhat dubious corrections to the transmitter position for $\phi' = 90^\circ$ measurement.

Encouragingly, the "PEC" wedge diffraction coefficients look increasingly similar to the UTD's PEC wedge diffraction coefficients, whereas the brick wedge diffraction coefficients are consistently smaller than the brick-like impedance wedge diffraction coefficients. Thus, whereas diffraction by a PEC wedge seems to describe the "PEC" measurements with reasonable accuracy, diffraction by a brick-like impedance wedge ($\epsilon_R = 4 - j0.2$) appears inadequate for modeling the total field due to diffraction by a brick building corner. This is supported by Table 4, which presents relative permittivities, ϵ_R, corresponding to the diffraction coefficients in Fig. 78 that were extracted using the UTD impedance wedge model. As with the geometry error corrections presented in Table 3, there is a noticeable consistency in the relative permittivities, ϵ_R presented in Table 4 for the different position corrections. Comparing the complex relative permittivities presented in Table 4, $\epsilon_R = 2$ seems to be a reasonable relative permittivity for modeling diffraction by a brick corner using the UTD impedance wedge model.

It should be noted that the peculiar null in the diffraction coefficients in Fig. 78(b) for the brick measurements at incident angle of $\phi' = 45^\circ$ is actually an artifact of the impedance wedge model, and not in any way attributable to the measurement data. Strictly speaking, the first-order impedance boundary condition used to construct the UTD impedance wedge diffraction model is only valid if $|\sqrt{\epsilon_R \mu_R}| \gg 1$ [99]. Thus,

Table 4: UTD Impedance Wedge Model's Best-Fit Brick Relative Permittivity, ϵ_R

Model Pair	**Incident Angle,** ϕ'		
	45°	90°	135°
PEC/PEC	$2.2 - j0.1$	$2.8 + j0.2$	$1.8 + j0.3$
Imp./Imp.	$2.0 - j0.2$	$2.6 - j0.4$	$1.9 + j0.1$
PEC/Imp.	$2.1 - j0.2$	$2.7 - j0.1$	$1.9 + j0.0$
Imp./PEC	$2.1 - j0.2$	$2.7 - j0.0$	$1.8 + j0.8$

for the small relative permittivities presented in Table 4, which assume a relative permeability of $\mu_R = 1$, the UTD impedance wedge solution is not valid inasmuch as it would provide a poor approximation to the total field arising due to diffraction by a dielectric wedge with a small relative permittivity. Importantly, this only means that the UTD impedance wedge solution cannot be used to *predict* the total field for dielectric wedges with small permittivities; it says nothing about whether or not the UTD impedance wedge solution can used to *model* the diffraction problem provided that the surface impedance model is adjusted appropriately. However, as evidenced by the diffraction coefficients in Fig. 78(b), it is evident that the impedance wedge model itself begins to break down for small (or conversely, large) incident angles, ϕ', and observation angles, ϕ, when the relative permittivity is small.

5.3.3 Final Diffraction Coefficients

The geometry error correction technique was repeated for the PEC/Impedance wedge model combination using a new brick-like surface impedance characterized by a relative permittivity of $\epsilon_R = 2$. Table 5 summarizes the results of this final geometry error correction. As might be expected given the relative insensitivity of the geometry error correction technique to the specific diffraction fitting model, the geometry corrections in Table 5 are quite similar to those for the PEC/Impedance case in Table 3.

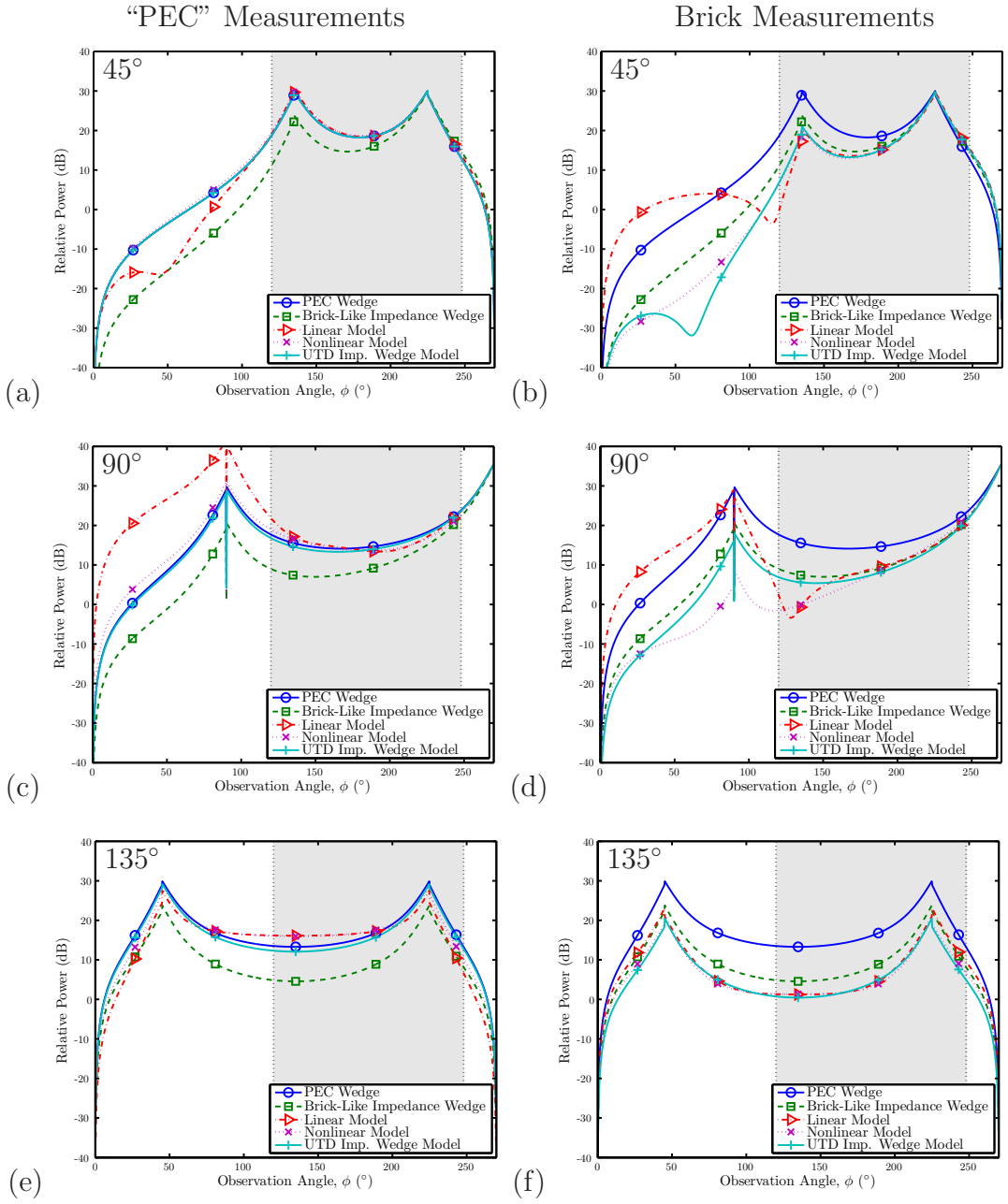

Figure 79: The *individual* semi-empirical diffraction coefficients extracted from the position-corrected "PEC" and brick corner diffraction measurements. For comparison, the UTD's PEC and brick-like impedance wedge diffraction coefficients are also presented. (a) $\phi' = 45°$, "PEC"; (b) $\phi' = 45°$, brick; (c) $\phi' = 90°$, "PEC"; (d) $\phi' = 90°$, brick; (e) $\phi' = 135°$, "PEC"; (f) $\phi' = 135°$, brick.

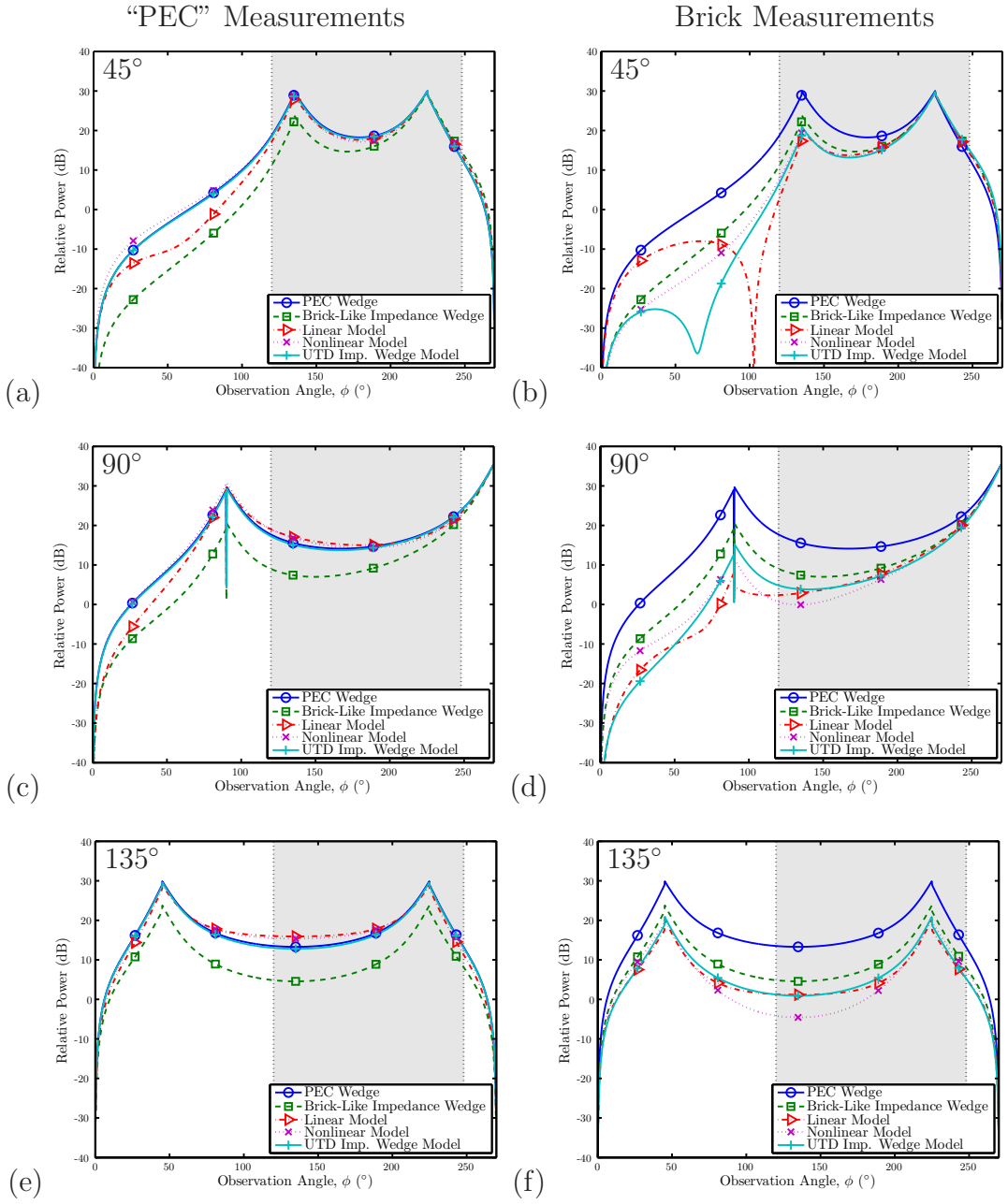

Figure 80: The *global* semi-empirical diffraction coefficients extracted from the position-corrected "PEC" and brick corner diffraction measurements. For comparison, the UTD's PEC and brick-like impedance wedge diffraction coefficients are also presented. (a) $\phi' = 45°$, "PEC"; (b) $\phi' = 45°$, brick; (c) $\phi' = 90°$, "PEC"; (d) $\phi' = 90°$, brick; (e) $\phi' = 135°$, "PEC"; (f) $\phi' = 135°$, brick.

Table 5: PEC/Imp. Geometry Error Correction Results Using $\epsilon_R = 2$ (cm)

ϕ'	**"PEC" Rx**		**Brick Rx**		**Tx**	
	Δx	Δy	Δx	Δy	Δx	Δy
45°	2.1	-0.6	3.6	-0.1	0.6	0.5
90°	2.9	-0.3	3.8	2.6	6.1	12.0
135°	3.7	2.0	3.4	2.0	5.2	5.3

Figure 79 presents the diffraction coefficients extracted from the new position-corrected measurements. Overall, Fig. 79 reinforces many of the previous observations about the diffraction measurement data and corresponding coefficients. First, the "PEC" wedge measurements tend to yield a diffraction coefficient that strongly resembles the UTD PEC wedge diffraction coefficient. Second, the brick wedge measurements tend to yield a set of diffraction coefficients with magnitudes that are below those of the brick-like UTD impedance wedge diffraction coefficient. Third, excepting for the $\phi' = 135°$, the diffraction coefficients extracted with the linear model are inconsistent with those extracted from the $\phi' = 45°$ and $\phi' = 135°$ measurements. This may be indicative of residual measurement geometry errors, or it might reveal some underlying problems with the linear model's formulation.

To further evaluate the linear model's diffraction coefficients Fig. 80 compares the *global* diffraction coefficients that were extracted from the "PEC" and brick corner measurements using each of the diffraction models. The diffraction model parameters (a_{1-3}, a_{1-2}, and ϵ_R) for these global diffraction coefficients were determined through a wideband least-squares fit across all incident angles ($\phi' = \{45°, 90°, 135°\}$). Thereby, these global diffraction coefficients should effectively average out the variations among the different incident angle measurements. Table 6 summarizes the model parameters corresponding to the individual and global diffraction coefficients in Figs. 79 and 80, respectively.

Table 6: Diffraction Model Parameters for the Brick Corner

Incident Angle, ϕ'	**Linear**			**Nonlinear**		**UTD Imp. Wedge**
	a_1	a_2	a_3	a_1	a_2	ϵ_R
$45°$	$0.88\angle{-16°}$	$2.21\angle{2°}$	$1.86\angle{-166°}$	$0.35\angle{175°}$	$0.60\angle{2°}$	$2.0 - j0.2$
$90°$	$3.08\angle{-39°}$	$3.52\angle{-32°}$	$1.16\angle{145°}$	$0.25\angle{-29°}$	$0.63\angle{-1°}$	$2.7 - j0.2$
$135°$	$4.13\angle{172°}$	$1.25\angle{150°}$	$1.17\angle{-164°}$	$1.09\angle{162°}$	$0.57\angle{46°}$	$1.8 - j0.1$
$\{45°, 90°, 135°\}$	$0.26\angle{-14.1°}$	$1.05\angle{5°}$	$0.42\angle{-149°}$	$0.44\angle{-127°}$	$0.63\angle{-8°}$	$2.0 - j0.1$

Overall, Fig. 80's global diffraction coefficients show trends similar to those observed in the *individual* diffraction coefficients presented in Fig. 79. Namely, the "PEC" diffraction coefficients resemble the UTD's PEC wedge diffraction coefficient, the brick diffraction coefficients are smaller in magnitude than the brick-like UTD impedance wedge diffraction coefficient, and the linear model's diffraction coefficients tend to deviate from the other models' diffraction coefficients. The latter point is also evidenced by the linear model's coefficients, a_{1-3}, in Table 6, which show little consistency for the different incident angles, ϕ'. Furthermore, the linear model's coefficients, a_{1-3}, neither resemble the nonlinear model's coefficients, a_{1-2}, nor come close to satisfying the equality, $a_3 = a_1 a_2$, that the nonlinear model explicitly enforces.

The variation in the diffraction model parameters in Table 6 also indicate that residual measurement geometry errors persisted in the measurements. Nominally, the diffraction model parameters extracted from any of the four incident angle combinations listed in Table 6 would be identical, indicating that the individual measurements describe diffraction by the same type of wedge. Small position errors would alter the extracted diffraction coefficient just as introducing small displacements to the position of a planar impedance surface may be used to simulate changes in the planar surface's impedance. It is conceivable that other factors such as the brick corner's inhomogeneity may yield diffraction coefficients that simply do not translate from the measurement incident angle to other incident angles, though this would be difficult to discern without extremely accurate measurement data. Deficiencies in the models as well as the nature of the least-squares fitting procedure, which tends to optimize the fit between measurements and models wherever the measurement data is large, may also contribute to variations among the diffraction coefficients extracted from each of the three incident angles.

Throughout this analysis, considerable uncertainty has surrounded the $\phi' = 90°$

measurement data due to the poorly pronounced diffraction interference pattern, considerable field reconstruction artifacts, and large transmitter position error. However, the sometimes bizarre behavior of the linear model's $\phi' = 90°$ diffraction coefficients seem to be more a fault of the linear model than the measurement data. Furthermore, based on the model parameters presented in Table 6 and the diffraction coefficients extracted using the nonlinear and UTD impedance wedge models in Figs. 79 and 80, the $\phi' = 90°$ measurements seem no more anomalous than the results of $\phi' = 45°$ and $\phi' = 135°$ measurements.

In light of these observations and given that the global diffraction coefficients average out some of the variations in the individual diffraction coefficients, it is expected that the global diffraction coefficients extracted from the $\phi' = \{45°, 90°, 135°\}$ measurements are the most trustworthy diffraction coefficients. Furthermore, given that the UTD impedance wedge model is the most constrained and thereby the most robust of the diffraction models, it is expected that diffraction coefficients extracted using the UTD impedance wedge model are the most reliable. Finally, we note that the model parameters in Table 6 may be used to construct the brick building corner's semi-empirical diffraction coefficient using any of the three diffraction models.

5.4 Comparison to FDTD Simulations

As a final evaluation, three 2-D finite-difference time-domain (FDTD) simulations were performed to compare the coefficients extracted from a simulated hollow dielectric corner against the coefficients extracted from the measurement data. The FDTD simulation data was provided courtesy of Andrew C. M. Austin, a researcher with the Radio Systems Group under the supervision of Profs. Michael J. Neve and Gerard Rowe at the University of Auckland, Auckland, New Zealand. The FDTD simulation used a lattice measuring 4x4 m with a cell size of 0.25 cm and a vertically

(i.e., perpendicularly) polarized sinusoidal excitation at 2.3 GHz. The simulation geometry corresponded to the three measurement configurations presented in Fig. 43. The building corner was modeled as a hollow dielectric wedge with a wall thickness of 10 cm correponding to the thickness of the exterior brickwork and a complex relative permittivity of $\epsilon_R = 4 - j0.2$; the interior of the building corner was modeled as free-space.

Figure 81 compares the global diffraction coefficients extracted from the FDTD simulations and brick measurements. Overall, Fig. 81 indicates that: 1) the measurement-based diffraction coefficients are reasonably similar to the FDTD-based diffraction coefficients and 2) both the FDTD- and measurement-based diffraction coefficients tend to be smaller in magnitude than the brick-like UTD impedance wedge diffraction coefficient. This is particularly true within the gray region denoting the observation angular sector subtended by the field reconstruction region in Fig. 43.

Interestingly, based on both the measurement- and FDTD-based diffraction coefficients presented in Fig. 81, it is apparent that the UTD impedance wedge model does not provide an accurate description of diffraction by a brick building corner when seemingly appropriate brick material properties ($\epsilon_R = 4 - j0.2$) are used. Of course, this is rather unsurprising given that the first-order impedance boundary condition is only accurate for $|\sqrt{\epsilon_R \mu_R}| \gg 1$ [99]. For perpendicular polarization, a comparison of the Fresnel reflection coefficient and the first-order impedance boundary condition's reflection coefficient reveals that for a given incident angle, the impedance boundary condition tends to overestimate the magnitude of the reflected field when $|\sqrt{\epsilon_R \mu_R}| \gg 1$ is not satisfied. Based on the diffraction coefficients in Fig. 81, it seems that the impedance boundary condition also tends to overestimate the magnitude of the diffracted field when $|\sqrt{\epsilon_R \mu_R}| \gg 1$ is not satisfied.

In some respects, the good agreement between the measurement- and FDTD-based diffraction coefficients is surprising given that the FDTD simulations were for

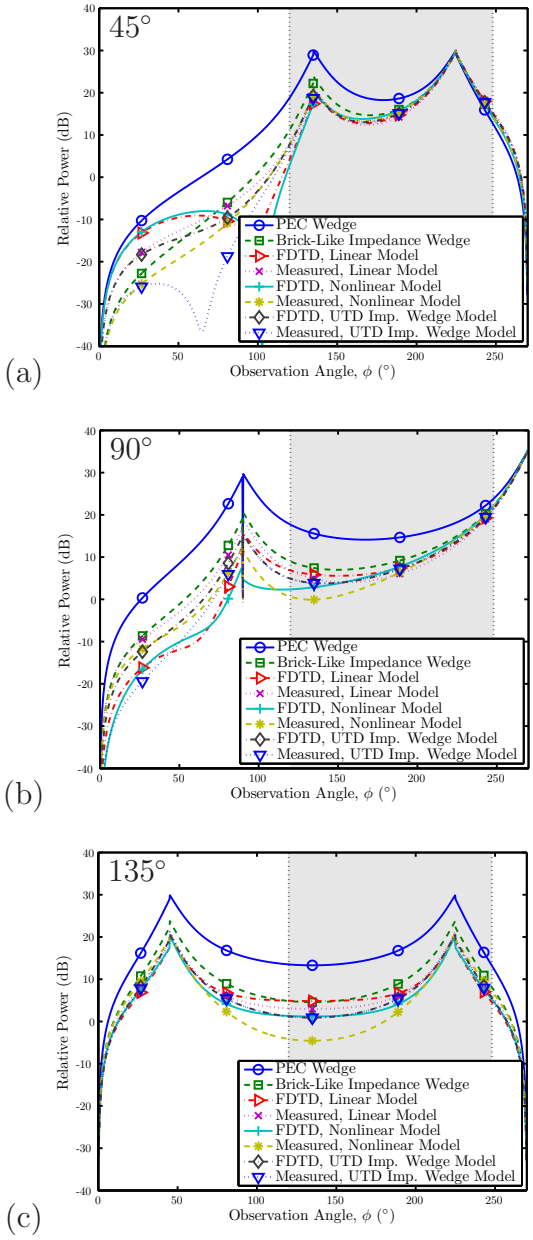

Figure 81: A comparison of the global semi-empirical diffraction coefficients extracted from the FDTD simulations and brick corner diffraction measurements. For comparison, the UTD's PEC and brick-like impedance wedge diffraction coefficients are also presented. (a) $\phi' = 45°$; (b) $\phi' = 90°$; (c) $\phi' = 135°$

an extremely simplified representation of the building corner. Thereby, the FDTD simulations neglected the inhomogeneities, inherent periodicities, and surface/edge roughness of the brick building corner. Based on analyses of reflection and diffraction by rough surfaces and rough knife-edges, respectively, it is expected that surface or edge roughness would reduce the magnitude of the reflected and diffracted fields and superimpose a comparatively weak and diffuse scattered field [25, 35, 112, 113]. For roughness characterized by surface or edge variations much smaller than a wavelength, the reduction in the reflected and diffracted fields and corresponding increase in the diffuse fields is expected to be quite small. Predicting the effects of inhomogeneities is considerably more difficult due to the range of possible configurations. However, provided there are no highly reflective planar interfaces within the building corner (i.e., metal-backed insulation) or strongly scattering structures near the diffracting edge, inhomogeneities would likely have a negligible effect on the reflected and diffracted field and would primarily contribute to an increase in the diffuse field via scattering of the fields propagating into the building corner.

Comparing the diffraction coefficients extracted with each of the diffraction models, Fig. 81 does indicate that the measurement-based diffraction coefficients are consistently equal to or less than the FDTD-based diffraction coefficients. Although this could be attributed to the building corner's edge or surface roughness, it could also be due to various other factors such as residual measurement geometry errors or a brick building corner relative permittivity that was smaller than the $\epsilon_R = 4 - j0.2$ used in the FDTD simulations. In principle, it should be possible to determine if the reduction in the diffraction coefficient's magnitude is due to surface roughness by subtracting the UTD-based coherent field components (incident, reflected, and diffracted) from the observed total field and examining the resulting diffuse field. However, the diffuse power tends to be several orders of magnitude less than the coherent power and

would likely be masked by or indiscernible from the measurements' noise floor. Furthermore, any inaccuracies in the extracted incident, reflected, and diffracted fields due to model limitations or residual measurement geometry errors would make it impossible to completely subtract out these coherent field contributions.

Verifying the presence of a diffuse field due to edge roughness would be even more difficult, because the resulting diffuse diffracted field would still behave as a cluster of rays emanating from the diffracting edge. In fact, the only difference between these diffuse and coherent diffracted fields is that rays corresponding to the diffuse diffracted field are not restricted to the so-called "Keller cone". It may be noted that the diffusely diffracted field's 3-D rays contradict the field reconstruction technique's requirement that the electromagnetic field be quasi 2-D field; this is also true of the fields scattered by rough surfaces and volume inhomogeneities.

To summarize, even if the possibility of measurement geometry errors could be ruled out, it remains unclear how one might distinguish between reductions in the diffraction coefficient due to roughness and permittivity. Therefore, it is impossible to say anything else conclusively beyond that which has already been said. Namely, the FDTD simulations indicate that the brick building corner may be accurately modeled by a hollow dielectric wedge with a permittivity of $\epsilon_R = 4 - j0.2$, and that a UTD impedance wedge diffraction coefficient based on brick-like material properties will overestimate the magnitude of the diffracted field.

5.5 Measurement Conclusions

It is important to consider the brick-like impedance wedge's overestimation of the diffracted field in the context of potential applications. Using the diffraction coefficients extracted with the UTD impedance wedge model, the discrepancy between the UTD's brick-like impedance wedge diffraction coefficients and those extracted from

the measurements and FDTD simulations within the range of observation angles subtended by the measurement/simulation region (i.e., the gray region in Fig. 81) is approximately 3 dB. Though this may seem significant in itself, a 3 dB reduction in the diffracted field would only result in a 1 dB change to the observed total field. For applications in wireless communication or radio wave propagation prediction, a 1 dB change in the *predicted* received power due to an erroneous diffraction model will 1) almost always be negligible when compared to the errors arising due to the model's incompleteness (i.e., neglecting structural details, inhomogeneities, etc.) and 2) will have a negligible impact on the predicted signal-to-noise ratio, data throughput, and channel capacity. This negligibility even applies to the predicted capacity of a multiple-input multiple-output (MIMO) communication system, which is far more sensitive to how power is distributed among multipath components than conventional single-input single-output (SISO) systems. In fact, the only scenario where a 1 dB error in predicted power might be important is received signal strength indicator (RSSI)-based radiolocation, which can be extremely sensitive to prediction errors when there are few basestations in the receiver's vicinity.

Thus, for most all applications the UTD's brick-like impedance wedge model provides a reasonably accurate description of the fields diffracted by a brick building corner. These results should be encouraging to wireless engineers who have long used the UTD impedance wedge model to plan and optimize their networks. Based on the measurements and analysis presented here, it is plausible that other building corners whose exteriors are composed of materials with permittivities equal to or greater than brick may also be accurately modeled as an impedance wedge. On the other hand, for building corner exteriors composed of materials having a permittivity less than that of brick (i.e., $\epsilon_R < 4$), the error between the predicted and actual diffracted power will invariably be larger than was observed in the brick corner measurements. Although

this error in itself may be considerable, the more significant source of prediction error would undoubtedly be due to waves propagating *through* the semi-transparent building corner. Thus, whereas applying the impedance wedge model to building corners with exterior permittivities of $\epsilon_R \geq 4$ should yield acceptable results, using the impedance wedge model on corners with permittivities of $\epsilon_R < 4$ is inadvisable.

CHAPTER VI

CONCLUSIONS

Chapter Summary: This chapter summarizes the original contributions of this research, identifies potential improvements to the techniques described in this dissertation, and discusses possible applications. The chapter concludes with a list of publications and presentations by the author.

This dissertation presented a measurement system and accompanying analysis tools for studying radio wave propagation mechanisms in real-world environments. The measurement system combined an ultra-wideband channel sounder with a quasi 2-D field reconstruction technique to map the space-time wireless channel throughout a planar region. This comprehensive wireless channel "filming" technique enabled the selective removal of multipath components through DSP-based space-time filters. Using a set of building corner diffraction measurements, it was also demonstrated how space-time filters could be used to isolate individual propagation mechanisms. Fitting these filtered diffraction measurements to three different diffraction models resulted in the first ever semi-empirical diffraction coefficients describing diffraction by a brick building corner.

6.1 Original Contributions

The following list summarizes the original contributions of this dissertation:

- Linear wedge diffraction model (Chapter 2)
- Conjoint cylindrical wave expansion (Appendices A and B)

- UWB SIMO sliding correlator channel sounder (Appendix C)
- Field reconstruction-based spatio-temporal channel sounder (Chapter 3)
- General and mechanism-specific space-time filtering (Chapters 3 and 5)
- Space-time diffraction measurements (Chapter 4 and Appendix F)
- Diffraction coefficient extraction technique (Chapters 2 and 5)
- Diffraction coefficients for brick building corners (Chapter 5)

6.2 Potential Improvements

The following sections highlight specific aspects of this research that either fell short of expectations or could be reworked to achieve significantly better results.

6.2.1 Measurement Position Accuracy

A reoccurring problem with the measurement data reported here was position errors. For the field reconstruction technique, errors in the placement of the linear positioner required the development of the intersection-based position correction technique discussed in Chapter 3. For the extraction of the semi-empirical diffraction coefficients, errors in the diffraction measurement geometry required the development of the geometry error correction technique discussed in Chapter 5. Developing, refining, and debugging these computationally intensive and highly specialized position correction techniques required a significant amount of time and effort that would have been better spent on other aspects of this research. The clarity of hindsight makes this particularly unfortunate, because 1) the sensitivity of coherent field measurements to position is well known (cf. [41, 80]), and 2) precision range measurement tools that would have eliminated these position errors may be purchased for a few hundred dollars (cf. the Bosch DLR165K Digital Laser Rangefinder Kit). Thus, it is

highly recommended that any future research employing the wireless channel "filming" technique described in Chapters 3 and 4 use a laser-based range measurement tool to guarantee accurate and precise position data.

6.2.2 Flexibility of Measurement Technique

The current spatio-temporal channel sounder uses the linear track positioner to synthesize the required pair of concentric measurement contours. Though precise in its displacements, the track positioner is cumbersome to move and inconvenient for measuring radio propagation in arbitrary environments. It would be advantageous to integrate the SIMO channel sounder with a more flexible position tracking system based on inertial navigation [7] or camera pose estimation [5], which would allow the measurement contours to be synthesized by sweeping the receive antenna along the planar region's perimeter. Although, these position tracking systems have traditionally been prohibitively expensive, recent advances in micro-electromechanical systems (MEMS) and, oddly enough video game systems, have made *joint* inertial navigation and camera pose estimation extremely affordable. Specifically, Nintendo®'s Wii Remote and MotionPlus add-on contain an infrared camera and MEMS-based multi-axis accelerometers/gyroscopes, all of which may be read via the Wii Remote's Bluetooth link. In [43], a spatial channel sounder was demonstrated that combined a vector network analyzer with a Nintendo Wii Remote to map the 915 MHz wireless channel throughout a 1x1 m region space. Although the system in [43] only used the Wii Remote's infrared camera for pose estimation, it was still able to achieve a mean position error of 1.75 cm. With additional refinement and integration of the translation/rotation data provided by the MEMS accelerometers/gyroscopes, it is expected that this position error could be significantly reduced.

6.2.3 Field Reconstruction Using Randomly Positioned Measurements

Although the field reconstruction technique described in Chapter 3 and Appendix A used a pair of bounding contour measurements, it is conceivable that the electromagnetic fields could also be reconstructed using a set of arbitrarily positioned measurements with certain spatial distributions (i.e., uniformly distributed) or measurement geometries (i.e., along a spiral or squiggle). In principle, provided that the measurement locations yield an independent system of equations for the conjoint cylindrical wave expansion, it should be possible to reconstruct the field throughout the vicinity. A space-time measurement system that used camera pose estimation and/or inertial navigation system would be well-suited for recording channel measurements at arbitrary locations in space. Fusing these two ideas, one envisions researchers being able to rapidly map the space-time wireless channel throughout a region of space by simply waving around a custom space-time measurement "wand" that contains both an antenna and a position tracking system. This is even more exciting when one realizes that it could be used for full-blown field reconstructions in 3-D! With a six degrees-of-freedom position tracking system, one could make wideband measurements at arbitrary location within a volume of space and reconstruct the entire space-time channel using the spherical wave expansion [104]. This would be an incredibly powerful measurement tool for studying and characterizing radio wave propagation.

6.3 Applications and Extensions of this Research

Here, we outline two innovative applications of this research. In the first application, we reconsider the semi-empirical radio wave propagation model that was presented in Chapter 1. In the second application, we discuss how wireless channel "filming" may be used in classrooms to both augment and reinforce traditional electromagnetics visualization tools.

6.3.1 Semi-Empirical Radio Wave Propagation Model

This research demonstrated how the spatio-temporal channel sounder may be used to extract a semi-empirical diffraction coefficient describing diffraction by a brick building corner. Using similar techniques, one could obtain semi-empirical diffraction and reflection coefficients for common scatterers in the radio wave propagation environment. This would enable the ray-based semi-empirical radio wave propagation model that was described in Chapter 1. As was discussed in Chapter 5, measuring the diffuse scattered field that arises due to roughness and inhomogeneities would be difficult if not impossible with the current measurement system. However, by modifying the system as previously discussed so as to reconstruct the space-time wireless channel throughout a 3-D volume, it should be possible to distinguish between the coherent and diffuse scattered fields by way of their elevation angle-of-arrival. This would enable an in situ study of the effects of roughness that could be wrapped into the semi-empirical propagation model via an appropriate radiosity model.

6.3.2 Wireless Channel "Filming" as an Educational Tool

There is a consensus among science education researchers that student learning is greatly facilitated by showing otherwise invisible phenomena [36]. This notion of making the invisible visible is especially pertinent to electromagnetics, which not only works with physically intangible quantities but also tends to be intensely mathematical. The electromagnetics community has a laudable history of bringing electromagnetism visualization tools into the classroom to show students the fields resulting from both canonical and complex radio wave propagation problems [49]. However, at the end of the day, these simulations are still solutions to mathematical models and are thus incapable of showing students what's really "out there". A simulation's idealization of reality can also be dissatisfying to students, particularly when they

learn that multipath propagation can make a complete mess of the simulations' oftentimes orderly electromagnetic fields. Without real-world measurements to put the simulation results into context, students are left to wonder about the accuracy and applicability of these simulated fields. Thus, in addition to the obvious "cool" factor and the potential for increased student engagement, showing students films of actual space-time wireless channels helps them develop a realistic mental picture of radio wave propagation as well as a truth reference against which they can compare the simulation results. Furthermore, with a few modifications to the measurement system described in Chapter 3, instructors could even map the space-time wireless channel in real-time so as to demonstrate how changes to the environment affect the observed wireless channel.

6.4 List of Publications and Presentations

The following sections provide chronological lists of publications and conference presentations stemming from the author's M.S. thesis, this Ph.D. dissertation, and various other research projects.

6.4.1 Journal Articles

[1] R. J. Pirkl and G. D. Durgin, "Optimal sliding correlator channel sounder design," *IEEE Transactions on Wireless Communications*, vol. 7, no. 9, pp. 3488-3497, Sept 2008.

[2] R. J. Pirkl and G. D. Durgin, "Quasi 2-D field reconstruction using the conjoint cylindrical wave expansion," *IEEE Transactions on Antennas and Propagation*, vol. 57, no. 4, April 2009, pp. 1095- 1104, April 2009.

[3] A. C. M. Austin, M. J. Neve, G. B. Rowe, and R. J. Pirkl, "Modeling the effects of nearby buildings on inter-floor radio-wave propagation," *IEEE Transactions on Antennas and Propagation*, vol. 57, no. 7, pp. 2155-2161,

July 2009.

[4] R. J. Pirkl and G. D. Durgin, "Revisiting the spread spectrum sliding correlator: why filtering matters," *IEEE Transactions on Wireless Communications*, vol. 8, no. 7, pp. 3454-3457, July 2009.

6.4.2 Conference Presentations

[1] R. J. Pirkl and G. D. Durgin, "Isolating individual radio wave propagation mechanisms using space-time filters," *2010 USNC/URSI Nat. Rad. Sci. Meeting., Boulder, CO*, 6-9 Jan 2010.

[2] R. J. Pirkl and G. D. Durgin, "How to build an optimal channel sounder," *APS '07 Antennas and Propagation Symposium, Honolulu, HI*, pp. 601-604, 9-15 June 2007.

[3] R. J. Pirkl and G. D. Durgin, "Interpolation of perimeter wireless channel measurements into the measurement region," *APS '08 Antennas and Propagation Symposium, San Diego, CA*, pp. 1-4, 5-11 July 2008.

[4] M. Yamanaka, M. Enomoto, R. J. Pirkl, G. D. Durgin, S. Sampei, and N. Morinaga, "The minimum number of adaptive array antenna elements for interference suppression in ubiquitous communication environments," *11th Int. Symp. Wireless Personal Multimedia Comm.*, pp. 1-6, 5-8 April 2009.

[5] R. J. Pirkl, G. D. Durgin, A. C. M. Austin, and M. J. Neve, "Extracting UTD wedge diffraction coefficients from electric field measurements," *2009 USNC/URSI Nat. Rad. Sci. Meeting., Boulder, CO*, 5-8 Jan 2009.

[6] R. J. Pirkl and G. D. Durgin, "2-D field reconstruction: a measurement

"sandbox" for spatial correlation analysis," *2009 EuCAP, Berlin, Germany*, 23-28 March 2009.

[7] S. Hassig, R. Q. Soria, R. J. Pirkl, and G. D. Durgin, "A "Wiimote"-based spatio-temporal wireless channel sounder," *IEEE SoutheastCon, Atlanta, GA*, 5-8 March 2009.

APPENDIX A

QUASI 2-D FIELD RECONSTRUCTION USING THE CONJOINT CYLINDRICAL WAVE EXPANSION

Let us assume a 2-D electromagnetic field that is invariant in the z-direction. Without loss of generality, we restrict our analysis to the z-component of a time-harmonic electric field, denoted $E_z(\rho, \phi)$ in cylindrical coordinates. Within a homogeneous and source-free medium, $E_z(\rho, \phi)$ may be expanded as a summation of cylindrical waves according to [104]

$$E_z(\rho, \phi) = \sum_n a_n J_n(k\rho)\, e^{jn\phi} \tag{112}$$

where $J_n(x)$ is the nth order Bessel function of the first kind, a_n is the nth term's coefficient, and k is the time-harmonic field's wavenumber given by

$$k = 2\pi/\lambda \tag{113}$$

where λ is the wavelength of the time-harmonic field within the medium. From the uniqueness theorem, it is known that for a lossy medium, knowledge of E_z along any closed contour, Γ, allows for perfect reconstruction of E_z within the region bounded by Γ [104]. Thereby, it is possible to uniquely determine all a_n from a *single* closed contour. While theoretically sound, numerical solutions for a_n based on E_z along a single contour result in an electric field that is dominated by the resonant modes of the region's geometry [79]. Using only the electric field, one may suppress these resonant modes through the *dual-surface* approach, which augments the original closed contour, Γ with an additional contour, Γ', concentric to and approximately $\lambda/4$ within

Γ [118, 100]. Thus, for practical applications, the CWE will require knowledge of the electric field along at least *two* concentric closed contours interspaced by $\lambda/4$.

The conventional CWE is only intended for the canonical case of true 2-D fields. Therefore, care must be taken when appying this 2-D expansion to the 3-D fields encountered in real-world wireless channels. Even so-called "2-D" wireless channels will exhibit small variations in the z-direction due to plane waves propagating at nonzero elevation angles. For these quasi 2-D (Q2D) fields, the conjoint cylindrical wave expansion provides a more accurate field reconstruction than the conventional cylindrical wave expansion [82, 81]. This is achieved by augmenting the conventional CWE with an additional CWE that uses a slightly smaller wavenumber k' given by

$$k' = k - \Delta\pi \tag{114}$$

where Δ is the *wavenumber stepsize* given by

$$\frac{1}{2D} \leq \Delta \leq \frac{1}{D} \tag{115}$$

where D is the largest distance between any two points along the planar region's perimeter. For the case of a circular region, D corresponds to the region's diameter. Equation (115) allows the wavenumber stepsize to be optimized for a given propagation environment. If plane waves with large elevation AoA are expected to contribute significantly to the measured fields, a Δ nearer to $1/D$ is preferrable; if the AoA is expected to cluster tightly about the horizon, then a Δ of $1/(2D)$ would likely perform best. The conjoint cylindrical wave expansion is then given by

$$E_z(\rho,\phi) = \sum_n [b_n J_n(k\rho) + c_n J_n(k'\rho)] e^{jn\phi} \tag{116}$$

where b_n and c_n are the complex coefficients of the expansion. The two concentric measurement contours required to suppress resonant modes also provide the necessary

information for uniquely solving for b_n and c_n. However, numerical implementations of Eq. (116) are somewhat more difficult due to the resulting ill-conditioned matrix equation and necessitate a singular value decomposition (SVD) to solve for the coefficients. Following an analytical analysis of the accuracy of the conventional and conjoint CWEs, we will address the issues of numerical implementation and conclude with an example application of this quasi 2-D field reconstruction technique.

A.1 Analytical Accuracy Analysis

Let us determine the mean-squared error, ε^2, of the conventional and conjoint CWEs for an arbitrary electric field, $E(\vec{r})$, given by

$$E(\vec{r}) = \sum_{i=1}^{N} E_{0,i} e^{j\Phi_i} e^{-jk\rho\cos\alpha_i\cos(\beta_i-\phi)} \tag{117}$$

throughout a circular region Ω of radius $\rho_0 = D/2$ provided a pair of concentric circular measurement contours, Γ, at radii $\rho = \{\rho_0, \rho_0'\}$ with $\rho_0' = \rho_0 - \lambda/4$. Eq. (117) describes the field due to N plane waves, each with a magnitude $E_{0,i}$, complex phase $e^{j\Phi_i}$, real wavevector elevation angle α_i, and arbitrary wavevector azimuth angle β_i. Generally, the problem is to compute

$$\varepsilon^2 = \frac{L_2\{E(\vec{r}) - A(\vec{r})\}_\Omega^2}{\pi\rho_0^2} \tag{118}$$

where $L_2\{(\cdot)\}_\Omega$ is the continuous L-2 norm operator given by [86]

$$L_2\{(\cdot)\}_\Omega = \left[\int_\Omega \|(\cdot)\|^2 d\Omega\right]^{1/2} \tag{119}$$

and $A(\vec{r})$ is the conventional or conjoint CWE given by

$$A(\vec{r}) = \sum_n f_n(\rho) e^{jn\phi} \tag{120}$$

where

$$f_n(\rho) = \begin{cases} a_n J_n(k\rho) & \text{for} \quad \Delta D = 0 \\ b_n J_n(k\rho) + c_n J_n(k'\rho) & \text{for} \quad \Delta D \neq 0 \end{cases} \tag{121}$$

The coefficients b_n (for $\Delta D = 0$) or c_n and d_n (for $\Delta D \neq 0$) are determined from the minimization problem

$$\min L_2\{E(\vec{r}) - A(\vec{r})\}|_{\vec{r}\in\Gamma} \tag{122}$$

along the two measurement contours, Γ. We note that an analytical expression may be found for ε^2, but its application requires explicit knowledge of Φ_i. A simpler and more practical solution may be found by assuming that Eq. (117) describes *uncorrelated scattering* and deriving the *expected value* of ε^2. Uncorrelated scattering assumes that Φ_i is a random variable realized from a probability density function uniformly distributed from 0 to 2π and

$$\mathrm{E}\left\{e^{j(\Phi_p - \Phi_q)}\right\} = \begin{cases} 1 & \text{for} \quad p = q \\ 0 & \text{for} \quad p \neq q \end{cases} \tag{123}$$

where $\mathrm{E}\{(\cdot)\}$ denotes the expected value (or ensemble average) of $(\cdot)$ [76]. The expected value of ε^2 is then given by

$$\overline{\varepsilon^2} = \mathrm{E}\left\{ \frac{L_2\{E(\vec{r}) - A(\vec{r})\}_\Omega^2}{\pi\rho_0^2} \right\} \tag{124}$$

Physically, Eq. (123) implies that each of the incident waves arise due to different scattering mechanisms [33]. Given the complexity of real-world propagation environments, this is generally considered to be a sound assumption.

A rigorous albeit highly compressed analysis in the Appendix illustatrates how $\overline{\varepsilon^2}$ may be derived for both the conventional and conjoint CWEs for an electric field described by Eq. (117). Consideration of these analytical solutions provides powerful

insight for applying both the conventional and conjoint CWEs to real-world field reconstruction problems.

We first consider Figure 82, which presents the mean-squared reconstruction error for a single, unit amplitude plane propagating with a wavevector elevation angle α across a circular region of diameter D as given by Eqs. (145) and (148). The curves denoted by $\Delta D = 0$ correspond to the conventional CWE given by Eq. (112). Effectively, both expansions seek to approximate a plane wave of wavenumber $k\cos\alpha$ by a plane wave of wavenumber k (and/or k'). Thus, as $k\cos\alpha$ approaches k (or k'), we observe a null in the reconstruction error that indicates an accurate approximation. More so, when observed over increasingly larger regions, errors in the approximation of $k\cos\alpha$ by k (and/or k') become more apparent because the approximation's phase error grows linearly with distance. Thereby, smaller diameter regions tend to have smaller reconstruction errors, as evidenced by a comparison of Fig. 82(a) and 82(b).

Secondly, we observe from Eqs. (145) and (148) that the mean-squared reconstruction error for the field due to a single, unit amplitude plane wave, denoted ε_0^2, is independent of both the wave's phase and azimuth AoA. Therefore, the error curves in Figure 82 are applicable to any unit amplitude plane wave including inhomogeneous plane waves provided that the wavevector elevation angle α is real.

For the arbitrary field described by Eq. (117), provided that the uncorrelated scattering assumption holds, the expected value of ε^2 is given by

$$\overline{\varepsilon^2} = \sum_{i}^{N} E_{0,i}^2 \varepsilon_0^2(\alpha_i) \tag{125}$$

Equation (125) reveals that $\overline{\varepsilon^2}$ is just a summation of the α-dependent mean-squared reconstruction errors for the N plane waves, with each $\varepsilon_0^2(\alpha_i)$ weighted by the corresponding waves's power, $E_{0,i}^2$. Therefore, provided an elevation power angle spectrum, $p(\theta)$, the uncorrelated scattering assumption, and ε_0^2 for either the conventional or conjoint CWE, $\overline{\varepsilon^2}$ is also given by

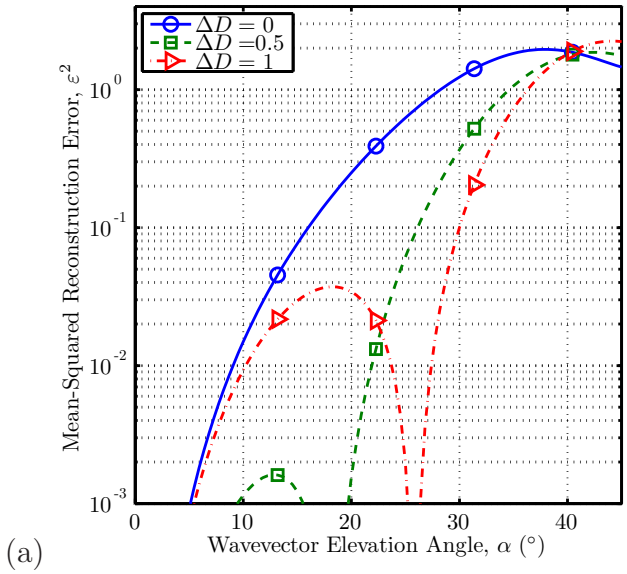

(a)

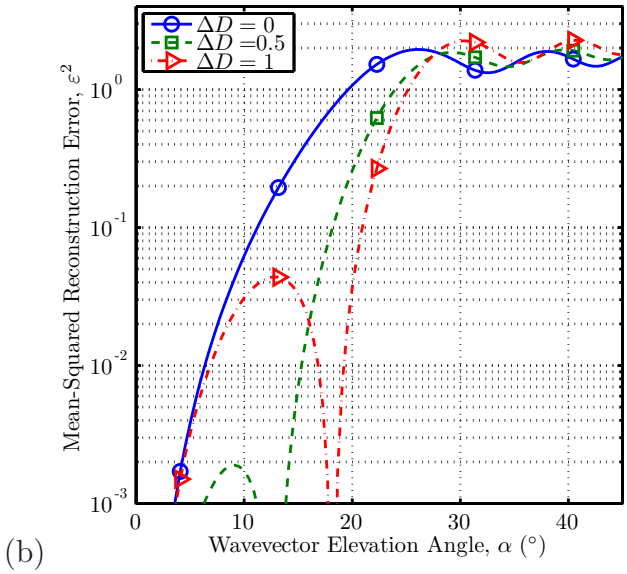

(b)

Figure 82: The conventional and conjoint CWE's mean-squared reconstruction error, ε^2, for a single, unit amplitude plane wave propagating with a wavevector elevation angle α across a circular region of diameter D: (a) $D = 5\lambda$, (b) $D = 10\lambda$. $\Delta D = 0$ corresponds to the conventional CWE.

$$\overline{\varepsilon^2} = \int_{-\pi/2}^{\pi/2} \varepsilon_0^2(\alpha) p(-\alpha) d\alpha \tag{126}$$

In practice, it may be more convenient to work with a power-normalized form of the total mean squared error:

$$\widehat{\overline{\varepsilon^2}} = \frac{\int_{-\pi/2}^{\pi/2} \varepsilon_0^2(\alpha) p(-\alpha) d\alpha}{\int_{-\pi/2}^{\pi/2} p(-\alpha) d\alpha} \tag{127}$$

This formulation allows for comparison of reconstruction errors between measurement sites with different total received powers. The approximate power angle spectrum, $p(\theta)$, may be determined from the perimeter measurement data using Fourier-based beamsteering techniques, though this approach will invariably overestimate the error due to the planar array geometry's large beamwidth in elevation. Alternatively, $p(\theta)$ may be determined from ray-based propagation prediction techniques or from statistical distributions of power versus elevation for specific propagation environments [53]. The latter two approaches are particularly useful for predicting reconstruction errors during the planning stages of a measurement campaign.

A.2 Numerical Implementation

In contrast to the conventional CWE's basis functions, the conjoint CWE's basis functions are not orthogonal along a pair of circular contours. In fact, when the conjoint CWE's basis functions are evaluated at a discrete set of measurement locations along two concentric closed contours so as to cast Eq. (116) into a matrix equation of the form

$$\mathbf{Ax} = \mathbf{b} \tag{128}$$

the basis function matrix $\mathbf{A}$ will frequently be ill-conditioned due to the similarity of the *two* nth order Bessel functions in (116); this is particularly problematic for large n. It is important to account for the ill-conditioned state of $\mathbf{A}$, lest the evaluation of the basis function coefficient vector, $\mathbf{x}$, be dominated by the noise in the electric field measurement vector, $\mathbf{b}$. To quantify the impact of measurement noise on the evaluation of $\mathbf{x}$, we first define the *condition number*, κ, of the matrix $\mathbf{A}$. In the L-2 norm, the condition number of the matrix $\mathbf{A}$ is equal to the ratio of its largest to smallest singular values, $\sigma_{\mathbf{A}}$, as given by [37]

$$\kappa(\mathbf{A}) = \frac{\max(\sigma_{\mathbf{A}})}{\min(\sigma_{\mathbf{A}})} \tag{129}$$

The singular values of $\mathbf{A}$ are the nonzero elements of the diagonal matrix $\mathbf{S}$ as determined by the SVD of $\mathbf{A}$:

$$\mathbf{A} = \mathbf{USV}^H \tag{130}$$

In Eq. (130), $\mathbf{V}^H$ denotes the conjugate transpose of $\mathbf{V}$. The condition number provides a measure of the degree of independence of the matrix columns, with orthogonal matrices having a condition number of 1 and singular matrices having a condition number of ∞ [37]. For the least-squares problem of determining $\mathbf{x}$ from $\mathbf{A}$ and $\mathbf{b}$ in (128), the condition number also relates errors in the solution vector, $\mathbf{x}$, to errors in $\mathbf{A}$ and $\mathbf{b}$. Let us suppose that the electric field measurement vector, $\mathbf{b}$, is given by

$$\mathbf{b} = \mathbf{b_0} + \mathbf{b}_\delta \tag{131}$$

where $\mathbf{b_0}$ represents the true electric field at the measurement locations, and $\mathbf{b}_\delta$ is a vector describing measurement errors stemming from a poor signal-to-noise ratio (SNR), interference, and various other system limitations. Analogously, let us define the basis function coefficient vector, $\mathbf{x}$, as

$$\mathbf{x} = \mathbf{x_0} + \mathbf{x}_\delta \tag{132}$$

where $\mathbf{x_0}$ describes the set of coefficients, a_n (or b_n and c_n), corresponding to the true electric field, and $\mathbf{x}_\delta$ is the error in the coefficients due to the measurement error, $\mathbf{b}_\delta$. For the linear least-squares problem of determining $\mathbf{x}$ from $\mathbf{A}$ and $\mathbf{b}$, the precise relationship between $\mathbf{x}_\delta$ and $\mathbf{b}_\delta$ depends upon how much of the measurement error, $\mathbf{b}_\delta$, is described by the column space of $\mathbf{A}$. Without a thorough characterization of the measurement error, a direct relationship is not very useful. However, we are able to define an upper bound on the L-2 norm of $\mathbf{x}_\delta$ using the L-2 norm of $\mathbf{b}_\delta$ [60]:

$$\|\mathbf{x}_\delta\| \leq \frac{\kappa}{\|\mathbf{A}\|}\|\mathbf{b}_\delta\| \tag{133}$$

In Eq. (133), $\|\cdot\|$ denotes the L-2 norm operator. Eq. (133) provides a bound for errors in the basis function coefficients, $\mathbf{x}$, but what would be more useful is a bound on the error of the reconstructed field as given by $\mathbf{Ax}$. Using the relation [60]

$$\|\mathbf{A}\mathbf{x}_\delta\| \leq \|\mathbf{A}\|\|\mathbf{x}_\delta\| \tag{134}$$

Eq. (133) may be rewritten as

$$\|\mathbf{A}\mathbf{x}_\delta\| \leq \kappa\|\mathbf{b}_\delta\| \tag{135}$$

Thus, we see that, in the worst case, the reconstructed field's error norm, $\|\mathbf{A}\mathbf{x}_\delta\|$, will equal the product of the measurement error's norm, $\|\mathbf{b}_\delta\|$ and the matrix condition number, κ. This further indicates that the condition number should be kept small so as to minimize the impact of measurement errors on the accuracy of the reconstructed field.

A large condition number may be reduced by simply removing the nearly-dependent columns of $\mathbf{A}$. Specifying a maximum condition number, κ_{max}, and employing

Eq. (129), we can easily determine the largest set of ℓ singular values which will yield a $\kappa \leq \kappa_{max}$. Using a subset selection technique based on the QR-decomposition with column-pivoting [37, p. 590], we could retain the ℓ "most independent" columns and discard the remainder. However, this technique does not guarantee that the new condition number will be less than κ_{max}, although heuristic evidence indicates that this is typically true.

An alternative and more elegant solution employs the SVD to compute a rank ℓ approximation to the pseudo-inverse of $\mathbf{A}$ that enables one to directly solve the matrix equation described by (128). Using the SVD, the pseudo-inverse of $\mathbf{A}$, denoted $\mathbf{A}^+$, is given by

$$\mathbf{A}^+ = \mathbf{V}\mathbf{S}^+\mathbf{U}^H \tag{136}$$

where $\mathbf{S}^+$ is the pseudo-inverse of the diagonal matrix $\mathbf{S}$ [37]. The best rank ℓ approximation to $\mathbf{A}^+$ is given by

$$\mathbf{A}_\ell^+ = \mathbf{V}_\ell\mathbf{S}_\ell^+\mathbf{U}_\ell^H \tag{137}$$

where ℓ is again determined by Eq. (129) for some maximum condition number, κ_{max}, $\mathbf{U}_\ell^H$ and $\mathbf{V}_\ell$ denote the first ℓ rows and columns of $\mathbf{U}^H$ and $\mathbf{V}$, respectively, and $\mathbf{S}_\ell^+$ is the upper left most ℓ-by-ℓ submatrix of $\mathbf{S}^+$. This rank ℓ approximation matrix may then be used to directly solve for the coefficient vector $\mathbf{x}$ in Eq. (128):

$$\mathbf{x}_\ell = \mathbf{b}\mathbf{A}_\ell^+ \tag{138}$$

Here, $\mathbf{x}_\ell$ indicates that the coefficient vector is computed using $\mathbf{A}_\ell^+$ as opposed to the actual pseudo-inverse. By using the rank ℓ approximation to $\mathbf{A}^+$, the condition number amplifying the measurement error in Eqs. (133) and (135) is guaranteed to be at most κ_{max}.

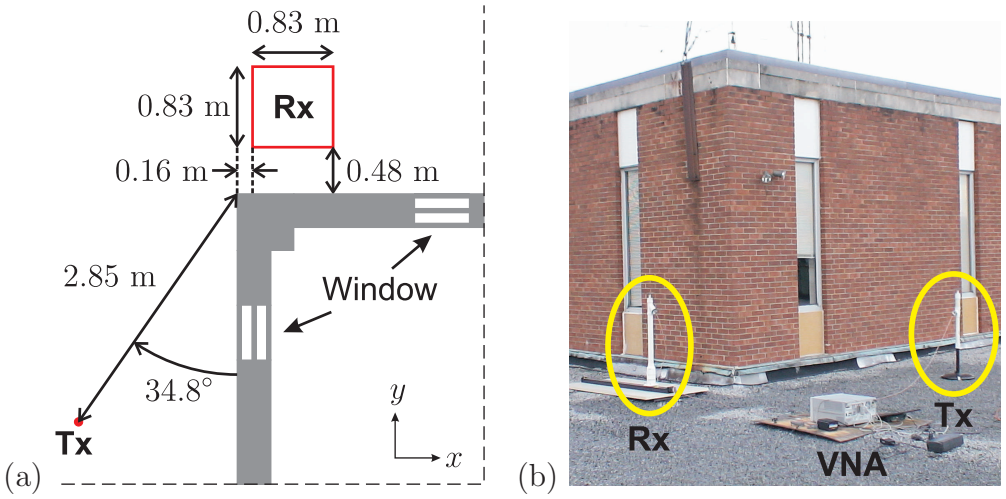

Figure 83: Using a VNA, S_{21} measurements were made on a 28 by 28 point measurement grid near the corner of an exterior wall. *Rx* denotes the receiver measurement grid, and *Tx*, the transmitter. (a) overhead diagram and (b) photo of measurement.

A.3 Experimental Validation

As a final validation and demonstration of the utility of the proposed technique, the conjoint CWE was applied to field measurements obtained near the corner of an exterior wall composed of brick on the outside and cinder block on the inside. Figure 83(a) diagrams the measurement area photographed in Figure 83(b). The measurement area comprised the 5th floor of an academic building as well as the gravel roof atop the 4th floor. Note that the 5th floor occupies a fraction of the building's full footprint and thereby allowed access to the 4th floor roof. Also, we note that the gravel rooftop made for an electromagnetically rough surface that likely scattered the coherent specular ground reflection into diffuse waves with slightly negative elevation AoAs.

A vector network analyzer (VNA) and linear positioner were used to make S_{21} measurements of the 2.45 GHz industrial, scientific, and medical (ISM) band wireless channel. For a static channel and a fixed transmitter, complex S_{21} measurements are directly proportional to the time-harmonic electric field. Both the transmit and receive antennas were vertically polarized quarter-wavelength monopole antennas

mounted atop a 1.15 m polyvinyl chloride (PVC) mast. The receive antenna's mast was attached to the linear positioner, which had a position accuracy of 1×10^{-5} m; the transmit antenna's mast was attached to a stationary stand. A 2.45 GHz bandpass filter and 10 ft coaxial cable was connected to ports 1 and 2 of the VNA. Following a 2-port calibration, the cable ends were connected to the antennas. For each measurement location, the VNA was swept from 2.4 GHz to 2.488 GHz in 1 MHz increments. Measurements were taken at $\lambda/4$ intervals on a rectangular grid that measured 6.75λ by 6.75λ, with $\lambda = 0.1224$ m corresponding to the free-space wavelength at 2.45 GHz. Temporal averaging of measurement data minimized the effect of time-varying scatterers. Figure 84(a) shows the magnitude and phase of the measured S_{21} at 2.45 GHz in dB and degrees, respectively. For comparison, Figure 84(b) presents the corresponding UTD solution for a unit amplitude plane wave incident on a perfectly electrically conducting (PEC) 90° wedge. Observe that there is good agreement between the S_{21} measurements and the ideal UTD solution.

Using only perimeter S_{21} data corresponding to the measurement grid's two outermost rectangular contours, the S_{21} was reconstructed within the rectangular measurement region using the conjoint CWE with select normalized wavenumber stepsizes, ΔD. The diameter, D, was set to the length of the measurement region's diagonal: $D = \sqrt{2} \cdot 6.75\lambda$. Figure 85 presents the error (dB) of the reconstructed S_{21} at 2.45 GHz. The reconstruction error was calculated as the magnitude of the difference between the measured and reconstructed S_{21}. Note that the error maps in Fig. 85 have been drawn with the same dB colormap as the measured S_{21} magnitude presented in Fig. 84(a) so as to facilitate comparisons. This allows us to observe that although the reconstruction error tends to follow the magnitude of the measured S_{21}, the reconstruction error is generally smaller. Overall, we find that the conjoint CWEs ($\Delta D \neq 0$) have a smaller reconstruction error than the conventional CWE ($\Delta D = 0$). Significant improvements are observed near the region's perimeter as

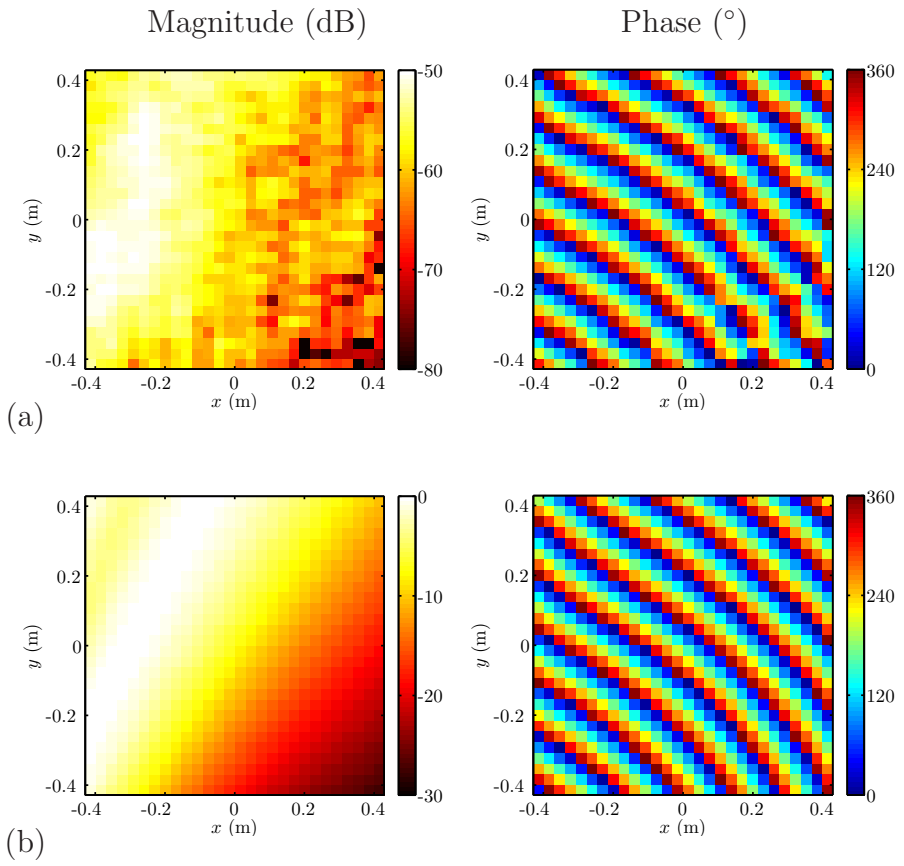

Figure 84: The magnitude (dB) and phase (°) of S_{21} for the diffraction measurement setup at 2.45 GHz: (a) the measured S_{21} and (b) the ideal UTD-based calculation.

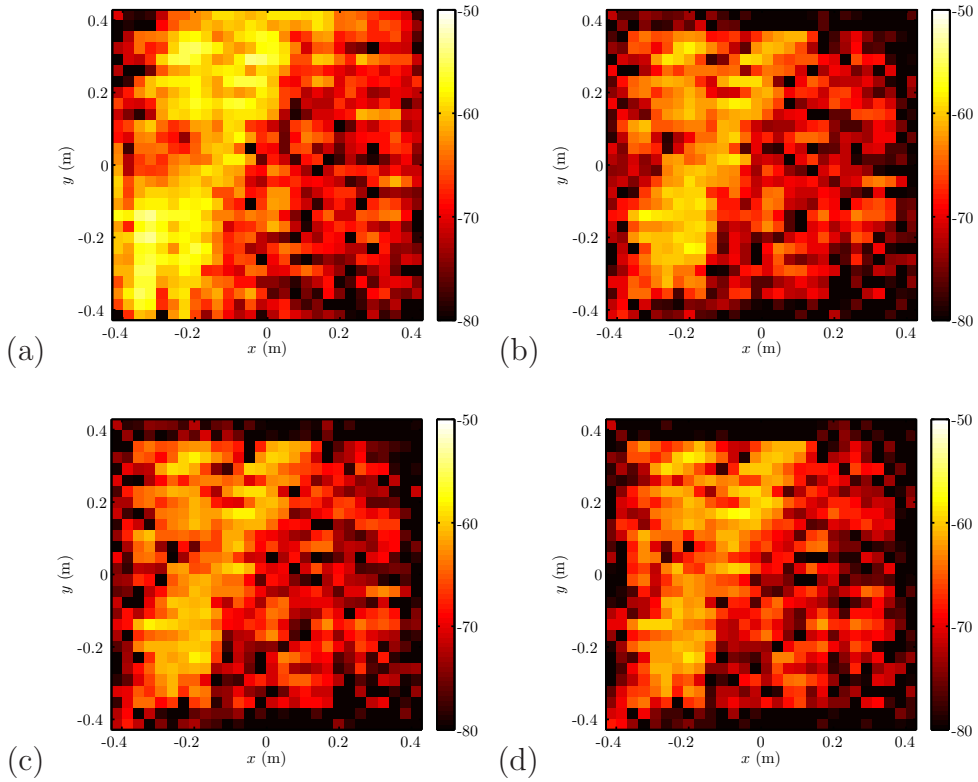

Figure 85: Spatial error maps for the reconstructed S_{21} in dB at 2.45 GHz for select wavenumber stepsizes: (a) $\Delta D = 0$, (b) $\Delta D = 1/2$, (c) $\Delta D = 3/4$, (d) $\Delta D = 1$.

might be expected given the conjoint CWE's larger set of basis functions. To better compare the accuracy of the conjoint and conventional CWEs, cumulative distribution function (CDF) error curves were calculated from the *interior* of the rectangular region. By "interior", we refer to the measurement sites bounded by the two outer closed contours and thereby exclude the perimeter points where the conjoint CWEs showed substantial error reductions so as to more fairly compare the error CDFs. Figure 86 presents the resulting CDFs. Despite excluding the perimeter region for which the conjoint CWE showed significant gains, we still observe that the conjoint CWE ($\Delta D \neq 0$) reduces both the 95th percentile and maximum reconstruction error by at least 3 dB.

Figure 87 examines the mean-squared reconstruction error throughout the "interior" region as a function of frequency. The mean-squared reconstruction error at

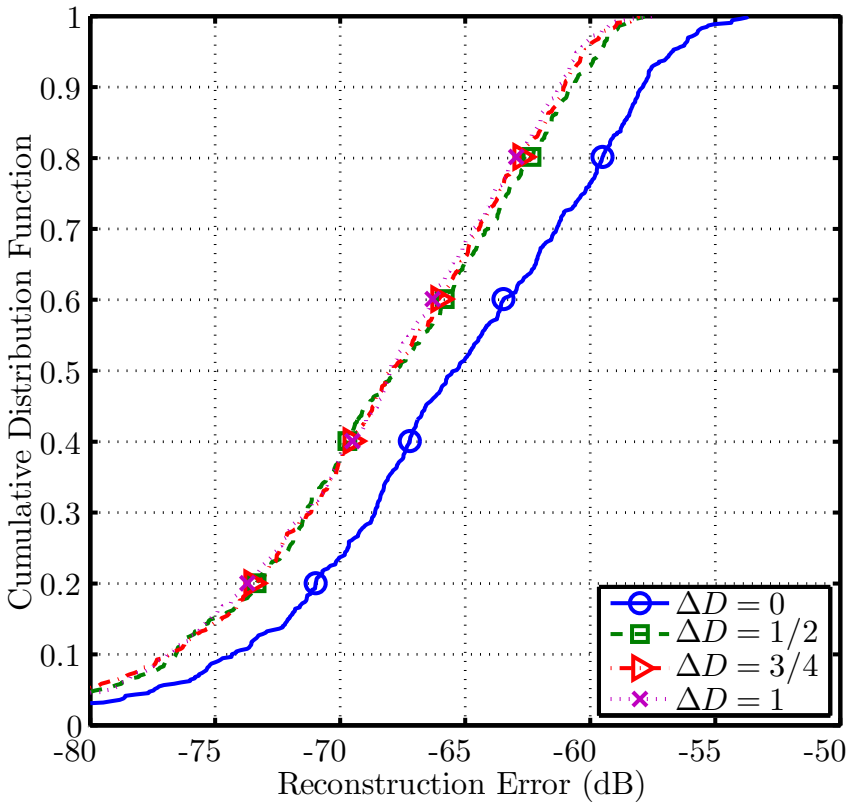

Figure 86: A comparison of the error cumulative distribution functions for the reconstructed S_{21} in the measurement region's "interior" at 2.45 GHz.

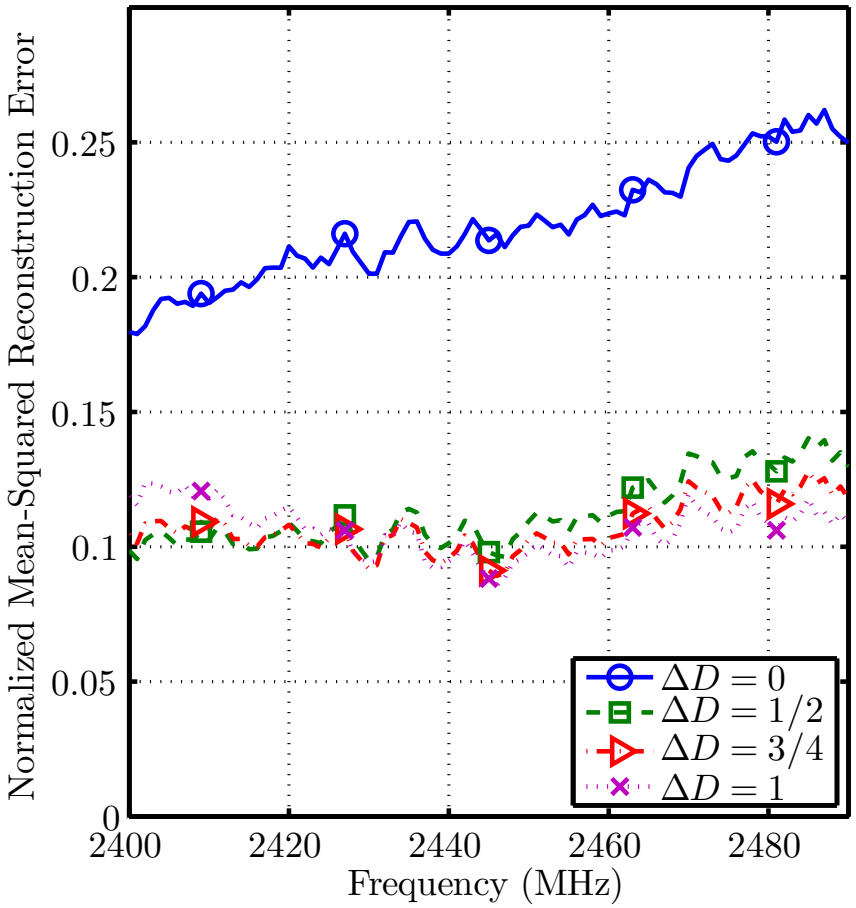

Figure 87: Normalized mean-squared reconstruction error in the measurement region's "interior" for $\Delta D = \{0, 1/2, 3/4, 1\}$.

each frequency was normalized by the interior's mean-squared S_{21}. As Fig. 87 shows, the conjoint CWEs yielded consistently smaller reconstruction errors across the entire measurement band. The overall trend of increasing error with frequency is attributed to the increasing electromagnetic size of the measurement region. At higher frequencies, the electromagnetic size of the region is larger, leading to larger reconstruction errors as suggested by the error curves in Fig. 82.

APPENDIX B

ANALYTICAL RECONSTRUCTION ERROR FOR CONVENTIONAL AND CONJOINT CWES

B.1 Conventional CWE's Mean-Squared Error

Using the expansion

$$e^{-j\rho\cos\theta} = \sum_n J_n(\rho)\, e^{-jn(\theta+\pi/2)} \tag{139}$$

Equation (117) may be rewritten as

$$E(\vec{r}) = \sum_{i=1}^{N}\sum_n a_{n,i} J_n(k\rho\cos\alpha_i) e^{jn\phi} \tag{140}$$

where the coefficient $a_{n,i}$ is given by

$$a_{n,i} = E_{0,i} e^{j\Phi_i} e^{jn(\beta_i-\pi/2)} \tag{141}$$

Substituting (140) and (141) into (118) and evaluating the L-2 norm yields

$$
\begin{aligned}
&L_2\{E(\vec{r}) - A(\vec{r})\}^2|_{\vec{r}\in\Gamma} = \qquad (142)\\
&\quad 2\pi \sum_n \Bigg[\rho_0 |a_n|^2 J_n^2(k\rho_0) + \rho_0' |a_n|^2 J_n^2(k\rho_0')\\
&\quad -\rho_0 \sum_{i=1}^{N} \left(a_{n,i} a_n^* + a_{n,i}^* a_n \right) J_n(k\rho_0) J_n(k\rho_0 \cos\alpha_i)\\
&\quad -\rho_0' \sum_{i=1}^{N} \left(a_{n,i} a_n^* + a_{n,i}^* a_n \right) J_n(k\rho_0') J_n(k\rho_0' \cos\alpha_i)\\
&\quad +\rho_0 \sum_{p=1}^{N} \sum_{q=1}^{N} a_{n,p} a_{n,q}^* J_n(k\rho_0 \cos\alpha_p) J_n(k\rho_0 \cos\alpha_q)\\
&\quad +\rho_0' \sum_{p=1}^{N} \sum_{q=1}^{N} a_{n,p} a_{n,q}^* J_n(k\rho_0 \cos\alpha_p) J_n(k\rho_0' \cos\alpha_q) \Bigg]
\end{aligned}
$$

The coefficient a_n that minimizes (142) is found to be

$$
a_n = \sum_{i=1}^{N} \chi_n^a(\alpha_i) a_{n,i} \qquad (143)
$$

where

$$
\chi_n^a(\alpha) = \frac{\rho_0 J_n(k\rho_0 \cos\alpha) J_n(k\rho_0) + \rho_0' J_n(k\rho_0' \cos\alpha) J_n(k\rho_0')}{\rho_0 J_n^2(k\rho_0) + \rho_0' J_n^2(k\rho_0')} \qquad (144)
$$

Solving Eq. (124) with the minimizing coefficient and the aid of [39] yields the expected value of the mean-squared error given in Eq. (125) where $\varepsilon_0^2(\alpha)$ may be shown to be the mean-squared error due to a single, unit amplitude plane wave propagating at a wavevector elevation angle α as given by

$$
\begin{aligned}
&\varepsilon_0^2(\alpha) = \qquad (145)\\
&\quad 1 + \sum_n \Bigg[(\chi_n^a(\alpha))^2 F_n(k) - 4\chi_n^a(\alpha) G_n(k, k\cos\alpha) \Bigg]
\end{aligned}
$$

and F_n and G_n are helper functions defined as

$$F_n(k) = \left[J_n^2(k\rho_0) - J_{n-1}(k\rho_0)J_{n+1}(k\rho_0)\right] \tag{146}$$

$$G_n(k_1, k_2) = \frac{k_2 J_{n-1}(k_2\rho_0)J_n(k_1\rho_0) - k_1 J_{n-1}(k_1\rho_0)J_n(k_2\rho_0)}{\rho_0(k_1^2 - k_2^2)} \tag{147}$$

B.2 Conjoint CWE's Mean-Squared Error

Through similar albeit more tedious mathematical manipulations one may determine that $\overline{\varepsilon^2}$ for the conjoint CWE is again given by Eq. (125) where the unit amplitude plane wave's mean-squared error is given by

$$\begin{aligned}\varepsilon_0^2(\alpha) = 1 + \sum_n \Big[& (\chi_n^b(\alpha))^2 F_n(k) + (\chi_n^c(\alpha))^2 F_n(k') \\ & -4\chi_n^b(\alpha) G_n(k, k\cos\alpha) - 4\chi_n^c(\alpha) G_n(k', k\cos\alpha) \\ & +4\chi_n^b(\alpha)\chi_n^c(\alpha) G_n(k, k') \Big]\end{aligned} \tag{148}$$

and

$$\chi_n^b(\alpha) = \frac{J_n(k'\rho_0')J_n(k\rho_0\cos\alpha) - J_n(k'\rho_0)J_n(k\rho_0'\cos\alpha)}{J_n(k\rho_0)J_n(k'\rho_0') - J_n(k'\rho_0)J_n(k\rho_0')} \tag{149}$$

$$\chi_n^c(\alpha) = \frac{J_n(k\rho_0')J_n(k\rho_0\cos\alpha) - J_n(k\rho_0)J_n(k\rho_0'\cos\alpha)}{J_n(k'\rho_0)J_n(k\rho_0') - J_n(k\rho_0)J_n(k'\rho_0')} \tag{150}$$

The minimizing coefficients are given by

$$b_n = \sum_{i=1}^{N} a_{n,i}\chi_n^b(\alpha_i) \tag{151}$$

$$c_n = \sum_{i=1}^{N} a_{n,i}\chi_n^c(\alpha_i) \tag{152}$$

APPENDIX C

SINGLE-INPUT MULTIPLE-OUTPUT SLIDING CORRELATOR CHANNEL SOUNDER

This chapter focuses on the details of the constructed SIMO sliding correlator channel sounder. For an in-depth discussion of the sliding correlator's theoretical operation, see [82].

C.1 Hardware

The channel sounder hardware consists of two separable systems: a direct sequence spread spectrum transmitter and a dual-channel sliding correlator-based receiver.

C.1.1 Transmitter

Figure 88 presents a system diagram of the channel sounder's transmitter. A custom frequency synthesizer outputs a 450 MHz sinusoid at 5 dBm. The frequency synthesizer's output power is not directly controllable, so this 450 MHz signal was passed through a 10 dB attenuator before being fed into a custom $L = 511$-bit pseudo-random noise (PN) generator. The 10 dB attenuator ensured the 450 MHz sinusoid was within the acceptable input power range of the PN generators. This input signal served as the clock for the PN generator, thereby setting the chip rate to $f_c = 450$ MHz. For further details on the PN generator, see Appendix D.

The PN generator's spread spectrum output was passed through a Mini-Circuits VLF-225 low-pass filter with a -3 dB cut-off at 350 MHz and a -20 dB stop-band beginning at 460 MHz [68]. This low-pass filter suppressed the spectral sidelobes of the PN's sinc-shaped spectral envelope as well as attenuated the PN generator's 450 MHz clock that coupled onto the output pseudo-random noise. Figure 89 compares the

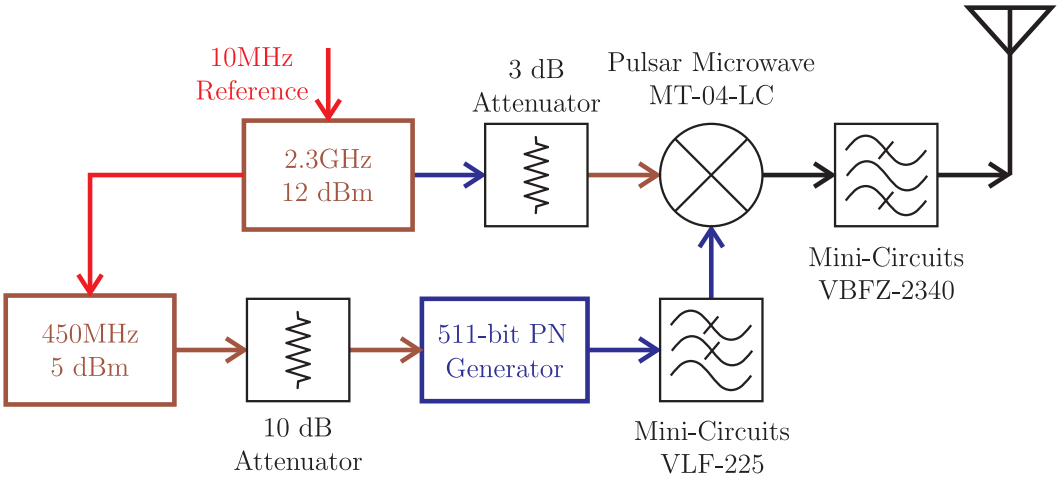

Figure 88: System diagram of the transmitter.

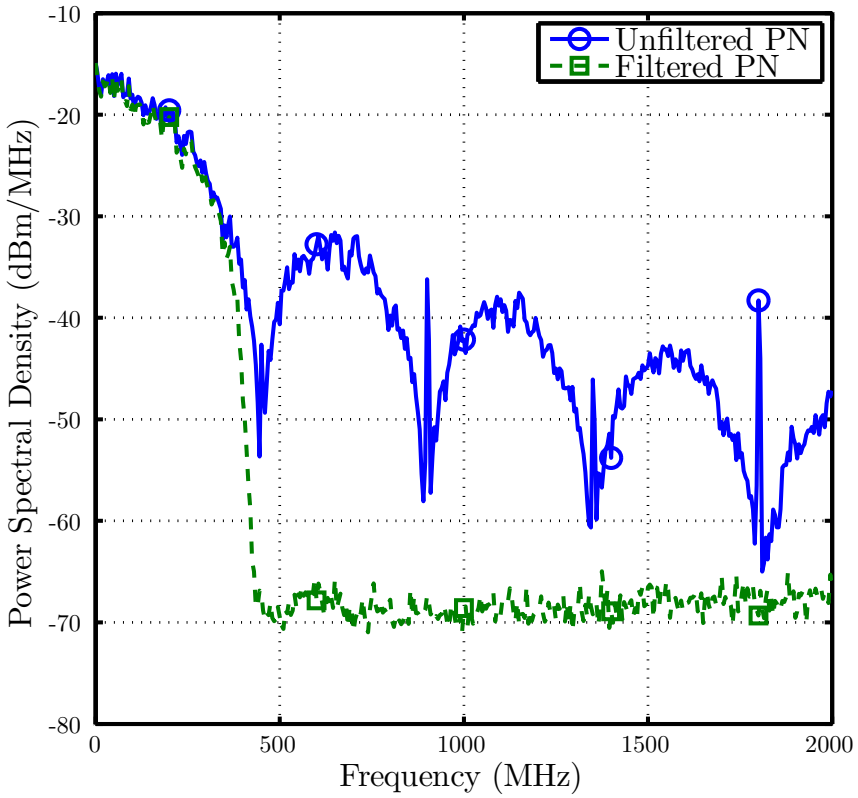

Figure 89: The transmitter PN's output spectrum before and after filtering.

output spectrum of the 511-bit PN generator clocked at 450 MHz before and after the low-pass filter. The sidelobes were heavily attenuated by the filter while the main spectral lobe remained more-or-less in tact.

The filtered PN was fed into the intermediate frequency (IF) port of a Pulsar Microwave MT-04-LC mixer, which upconverted the PN to 2.3 GHz. The mixer's local oscillator (LO) was provided by a custom 2.3 GHz frequency synthesizer with an output power of 12 dBm. The frequency synthesizer's output was attenuated by 3 dB before being passed to the mixer. The resulting 9 dBm signal was below the nominal 13 dBm of LO power expected by the mixer. However the slightly weaker LO also reduced the LO power that coupled onto the mixer's RF port and thereby led to an overall flatter and more uniform RF spectrum.

The resulting modulated PN was then passed through a Mini-Circuits VBFZ-2340 band-pass filter, which had -2.2 dB pass-band extending from 2.02 GHz to 2.66 GHz [64]. This filter suppressed the harmonics of the 2.3 GHz LO as well as removed any of the baseband PN that had coupled from the mixer's IF port to its RF port. The filtered RF signal was then fed into a wideband antenna via a 12 ft coaxial cable with 2.8 dB of loss at 2.3 GHz. Figure 90 presents the output spectrum of the channel sounder's transmitter. The total transmitter power was approximately -4 dBm. Figure 91 shows a photo of the constructed transmitter.

Finally, as indicated by Fig. 88, both the 450 MHz and 2.3 GHz frequency synthesizers were fed by a 10 MHz reference signal. This 10 MHz reference was provided by a reference clock at the receiver that ultimately originated from an Agilent DSO6104A oscilloscope. Thereby all of the frequency sources were phase-locked to the same 10 MHz reference signal.

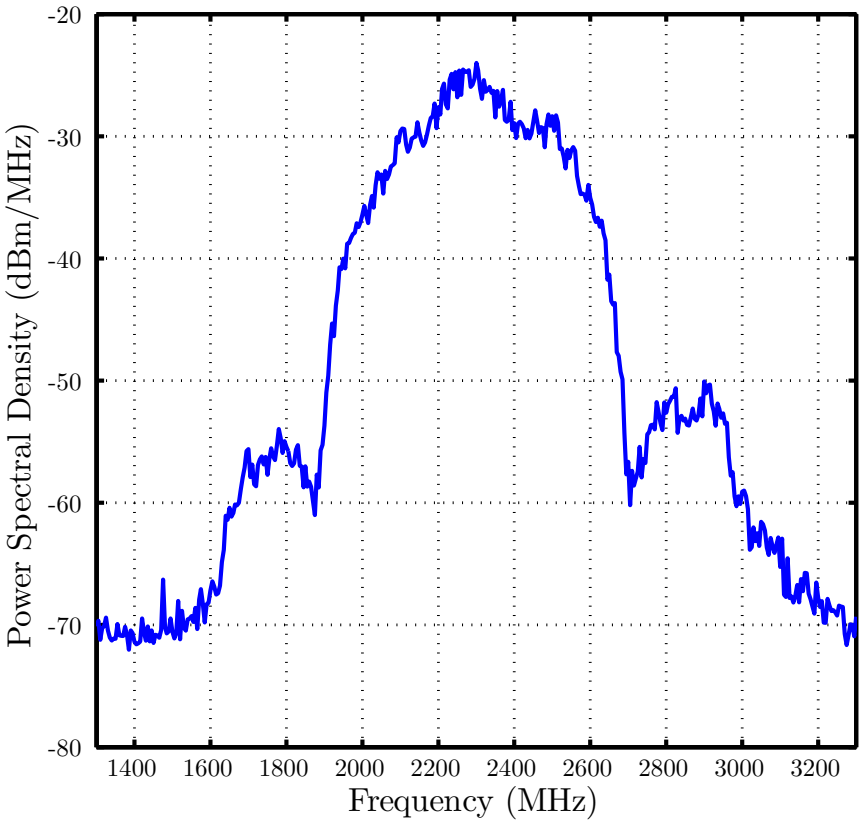

Figure 90: The spectrum of the channel sounder's transmitter.

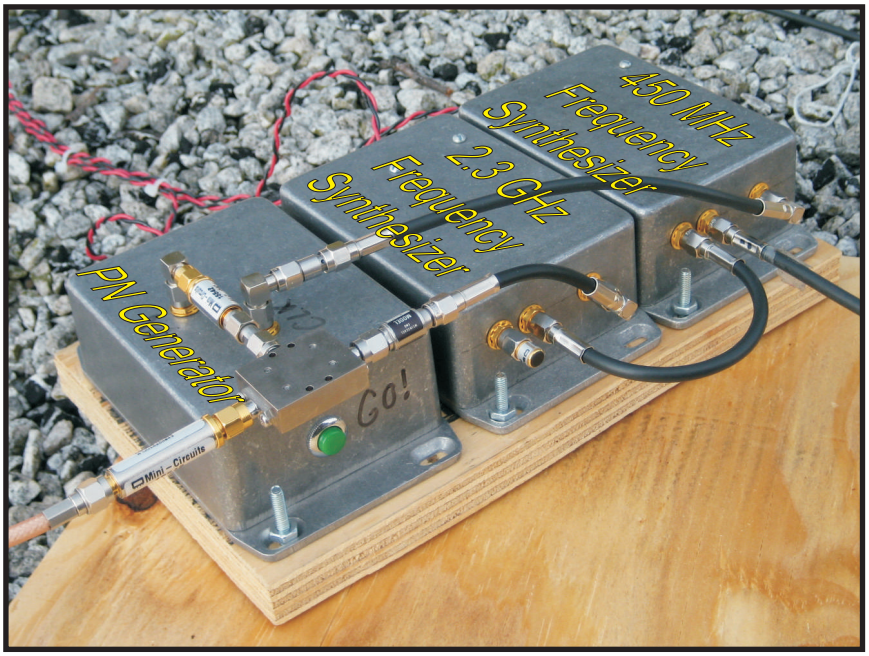

Figure 91: A photo of the channel sounder's spread spectrum transmitter indicating the PN generator and frequency synthesizers.

C.1.2 Receiver

Figures 92 through 94 describe the architecture of the channel sounder's receiver. As can be seen from Fig. 92, the receiver consists of two independent RF chains, each starting with an antenna and ending with a pair of baseband outputs for the inphase and quadrature signal components. A pair of Mini-Circuits VBFZ-2340 band-pass filters were placed after the antennas' coaxial cables to remove any out-of-band interference. Then, the pair of RF signals were each fed into a *sliding correlator and downconversion block*, which is presented in greater detail in Fig. 92.

The signals were first passed to a Mini-Circuits ZVE-8G amplifier, which served as a wideband low-noise amplifier with gain of 30 dB, a noise floor of 4 dB, and a 1 dB compression point at 30 dBm [63]. Then, the signal was mixed with a modulated PN produced by the *PN modulation block* detailed in Fig. 93. The PN modulation block's architecture is nearly identical to the transmitter architecture presented in Fig. 88 excepting for the absence of a transmit antenna and a 3 dB attenuator at the mixer's LO input. For the PN modulation block, the PN chip rate was $f_c' = 449.6$ MHz, the LO frequency was 3.18 GHz, and the RF filtering was provided by the cascade of a Mini-Circuits VHP-19 high-pass filter and a Mini-Circuits VLP-41 low-pass filter. The VLP-41 had a -3 dB cut-off at 4.1 GHz and a -20 dB stop-band beginning at 5.6 GHz [71]. The VHP-19 had a -3 dB cut-off at 1.99 GHz and a -20 dB stop-band ending at 1.65 GHz [70].

With $f_c = 450$ MHz and $f_c' = 449.6$ MHz, the channel sounder's *slide factor*, γ, was calculated to be 1125 using Eq. (153) [22].

$$\gamma = \frac{f_c}{f_c - f_c'} \tag{153}$$

The slide factor defines the temporal dilation and, thereby, the bandwidth compression afforded by the sliding correlation of two PN signals with slightly different chip rates.

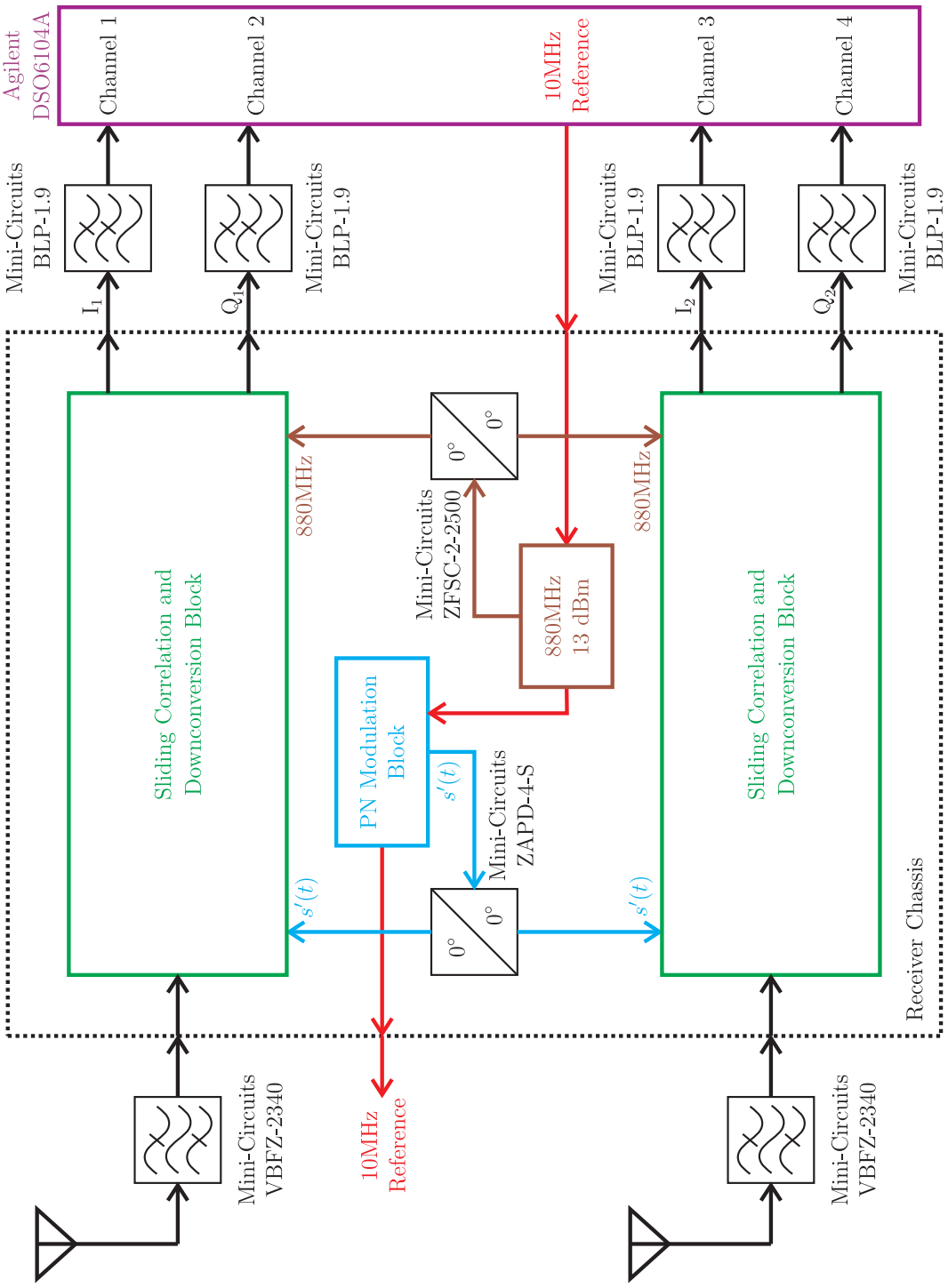

Figure 92: System diagram of the receiver.

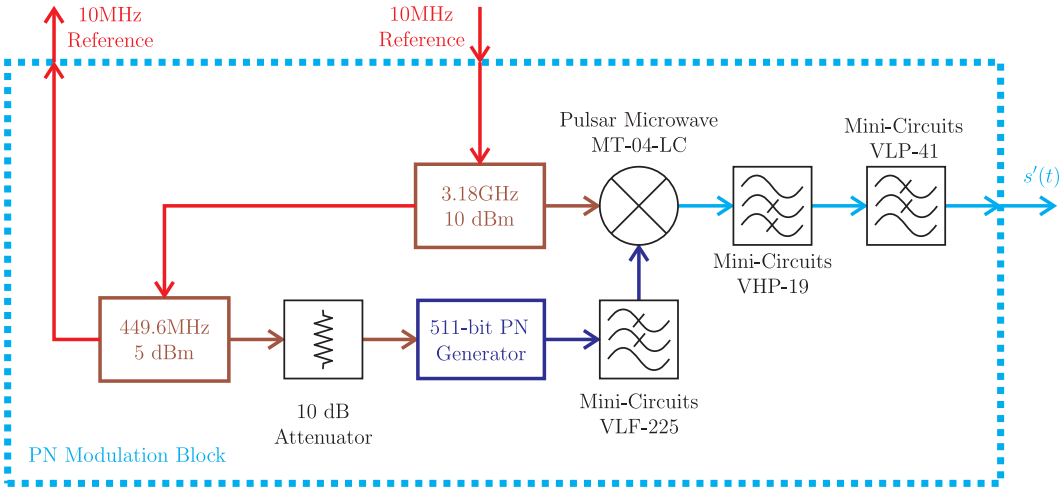

Figure 93: System diagram of the receiver's PN modulation block.

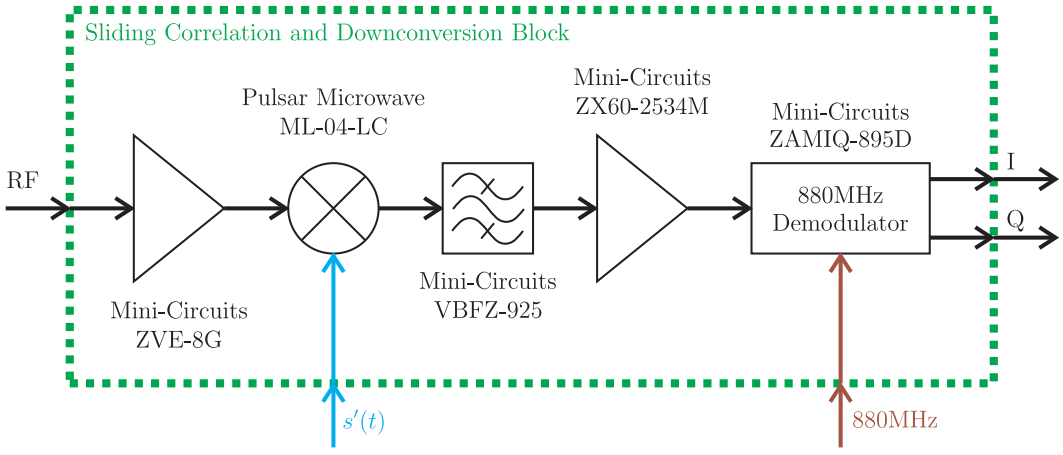

Figure 94: System diagram of the receiver's sliding correlation and downconversion block.

As shown in Fig. 92, the PN modulation block's output was split by a Mini-Circuits ZAPD-4-S splitter before being fed into the sliding correlation and downconversion blocks. Thereby, both RF chains were processed identically. After mixing the amplified RF signals with the modulated PN, the resulting signal was the classic time-dilated impulse response of the sliding correlator channel sounder, albeit at an IF of 880 MHz and severely corrupted by the sliding correlator's ever-troublesome *distortion signal*. The time-dilated impulse response had a baseband bandwidth of approximately $f_c/\gamma = 300$ kHz and a period of $\gamma L/f_c = 1.3$ ms.

A Mini-Circuits VBFZ-925 band-pass filter provided some modest filtering of the distortion signal before being amplified by a Mini-Circuits ZX60-2534M amplifier. The filter's -2.4 dB pass-band extended from 800 MHz to 1.05 GHz [65]. The amplifier featured 38 dB of gain, a noise figure of 3.1 dB, and 1 dB compression point at 15.9 dBm [69]. Finally, the IF signal was downconverted to baseband inphase (I) and quadrature (Q) components via a Mini-Circuits ZAMIQ-895D demodulator, which featured a typical amplitude and phase unbalance of 0.15 dB and 1.5°, respectively [66]. The demodulator's LO was provided by a custom 880 MHz frequency synthesizer with an output power of 13 dBm. As Fig. 92 illustrates, the 880 MHz signal was split by a Mini-Circuits ZFSC-2-2500 splitter before being fed into the ZAMIQ-895D demodulators within the sliding correlation and downconversion blocks. Thus, each demodulator received the nominal 10 dBm LO signal.

After downconversion to I and Q, each of the four baseband signals were filtered by a Mini-Circuits BLP-1.9 low-pass filter, which had a -3 dB cut-off at 2.5 MHz and a -20 dB stop-band beginning at 3.4 MHz [67]. Then, the four analog signals were sampled by an Agilent DSO6104A digital oscilloscope, which featured an 8-bit analog-to-digital converter with a maximum sampling rate of 1 GS/s [1]. The sampling rate for each of the four oscilloscope channels was set to 5 MS/s, corresponding to a maximum non-aliased frequency of 2.5 MHz. Note that the aliasing of

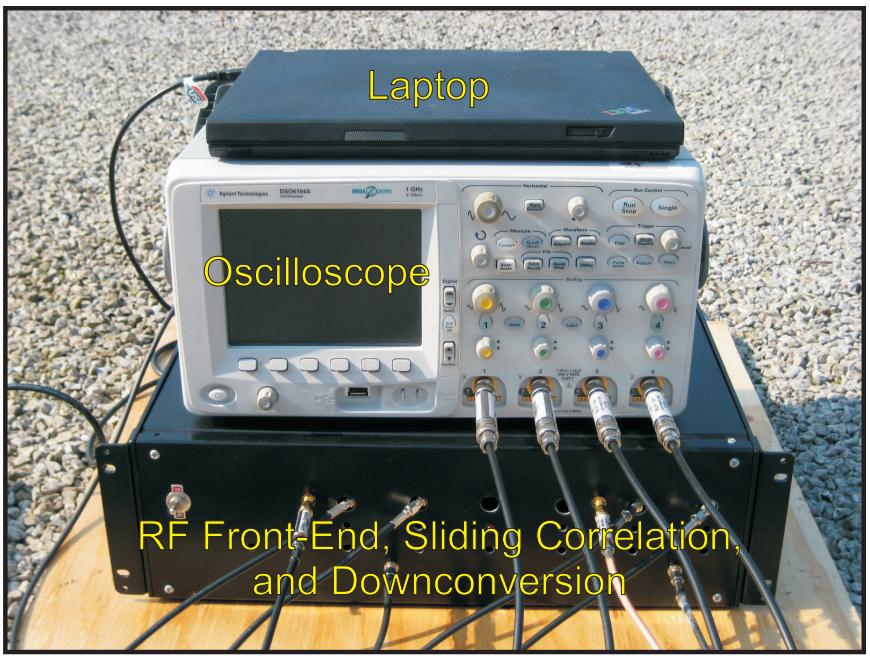

Figure 95: A photo of the constructed SIMO receiver.

frequency content from 2.5 MHz to approximately 3.4 MHz would not affect the accurate recording of the time-dilated impulse response, which had spectral content from DC to approximately 400 kHz. The four oscilloscope channels were simultaneously sampled at 5 MS/s for 100 ms. Thus, on each channel, the oscilloscope captured 78.2 periods of the sliding correlator's time-dilated impulse response.

For the measurements discussed throughout this work, a 38.5 ft coaxial cable with 6.2 dB of attenuation at 2.3 GHz connected the receiver's "measurement" channel antenna to the receiver and a 12 ft coaxial cable with 2.8 dB of attenuation at 2.3 GHz connected the receiver's "reference" channel antenna to the the receiver. Figures 95-97 present photos of the constructed receiver. Figure 95 shows the entire receiver. Figure 96 provides a labeled photograph of the hardware contained inside the receiver chassis. Figure 97(b) identifies additional components in the receiver chassis located beneath the aluminum mounting plate in Figure 97(a).

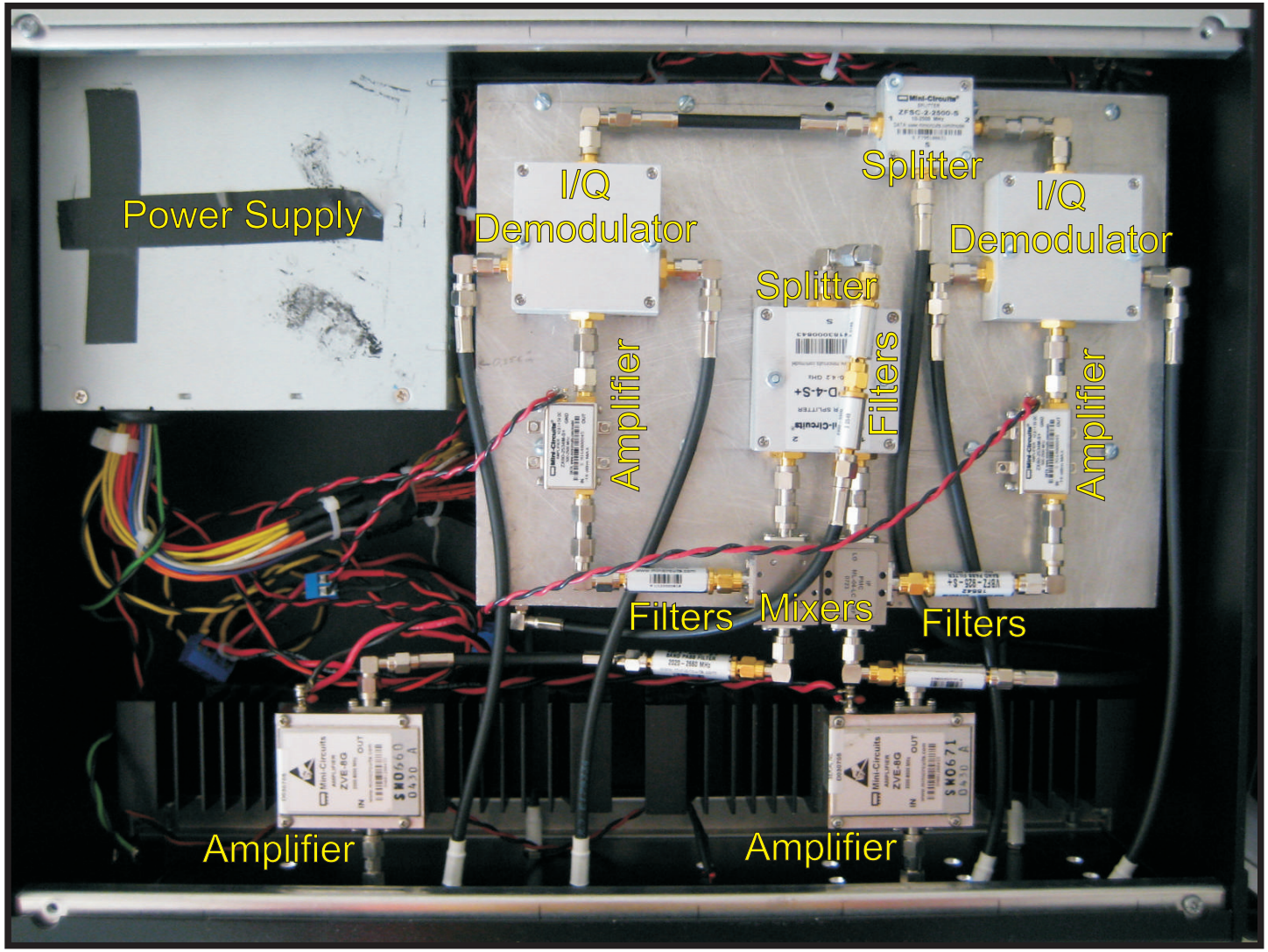

Figure 96: A photo of the hardware inside the receiver chassis.

(a) 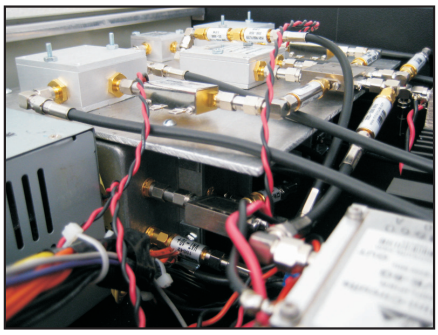 (b) 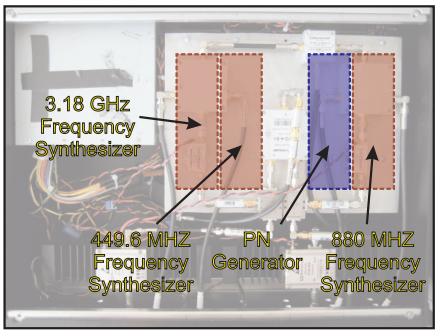

Figure 97: A photo and diagram of the receiver hardware beneath the alumninum mounting plate.

C.2 Antennas

The channel sounder required three wideband antennas for performing phase- and delay-stable measurements: one transmit antenna and two receive antennas. In a typical setup, the transmit antenna was omnidirectional, the "measurement" channel's receive antenna was omnidirectional, and the "reference" channel's receive antenna was directional and pointed toward the transmitter. Using a directional antenna on the receiver's "reference" channel made the measurements less susceptible to the effects of any time-varying scatterers in the environment.

An off-the-shelf dual-ridged horn antenna was used as the directional antenna, whereas a pair of custom bicone-like antennas were constructed for use as the omnidirectional antennas. The following sections present various measurement and simulation data for these antennas.

C.2.1 Omndirectional: Toiletenna

Figure 98 presents a diagram of the bicone-like omnidirectional antenna. The antenna was composed of two hollow, copper semi-ellipsoids, which were cut from two copper toilet floats – thus the name "toiletenna". The threaded socket of each of the toilet float halves was screwed onto the barrel of a nylon screw. A brass pin connected the upper semi-ellipsoid to the center pin of an SMA connector. Figure 99 presents

photos of the constructed toiletenna. Figures 100-102 compare the simulated and measured performance of the two constructed toiletennas. The antennas simulations were performed using Ansoft HFSS. The S_{11} measurements and gain patterns were obtained using a vector network analyzer. The gain patterns were measured at the Georgia Tech Propagation Group's far-field antenna range located on the 5th floor of the Van Leer Building. Discrepancies among the simulated and measured antennas are largely attributed to imperfections and variations in the antennas' construction.

The -10 dB bandwidth of toiletenna #1's S_{11} extended from 700 MHz to 2.5 GHz; at 2.75 GHz, which is the highest frequency in the channel sounder's meaurement band, toiletenna #1's S_{11} was -8 dB. Toiletenna #2's -10 dB bandwidth more closely matched the simulation results, extending from 700 MHz to beyond 3 GHz. The Smith charts in Fig. 101 show the classic spiraling pattern of the complex S_{11} that is expected of a bicone antenna, though the measurements indicate the real part of the antennas' impedance was slightly lower than intended. The bicone-like behavior of the toiletennas is further confirmed by the elevation plane gain patterns presented in Fig. 102. From measurement data not shown here, it was determined that the cross-polarization ratio of the toiletennas at $\pm 90^\circ$ from zenith was less than -24 dB across the entire measurement band. For comparison, the simulation-based cross-polarization ratio at $\pm 90^\circ$ from zenith was below -42 dB for the same range of frequencies.

C.2.2 Directional: Ridged-Horn Antenna

Figure 103 presents a photo of the dual-ridged horn antenna. As with the omnidirectional antennas, the directional antenna's characteristics were measured using a vector network analyzer, and the gain pattern was measured at the Georgia Tech Propagation Group's far-field antenna range. The dual-ridged horn antenna had a specified bandwidth of 1-18 GHz with a relatively constant albeit poor $|S_{11}|$ as Fig. 104

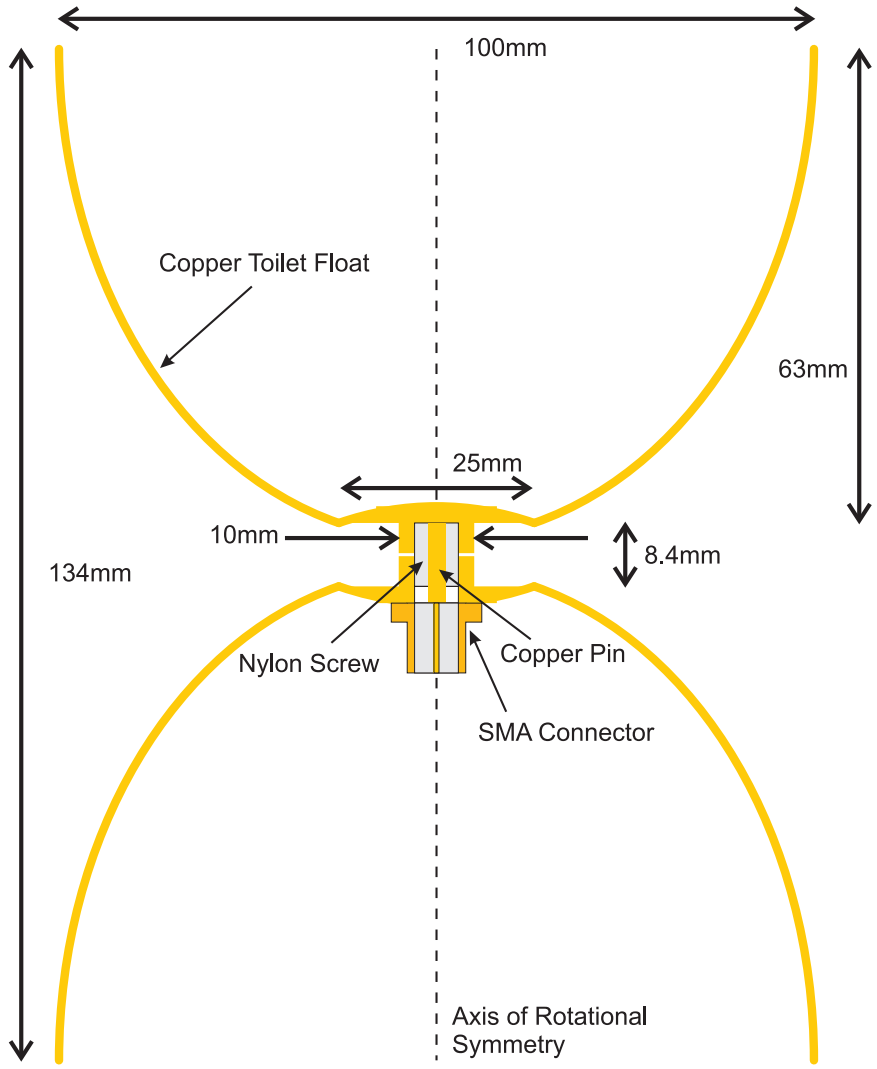

Figure 98: A diagram of the toiletenna, which emulates a bicone antenna.

(a) (b)

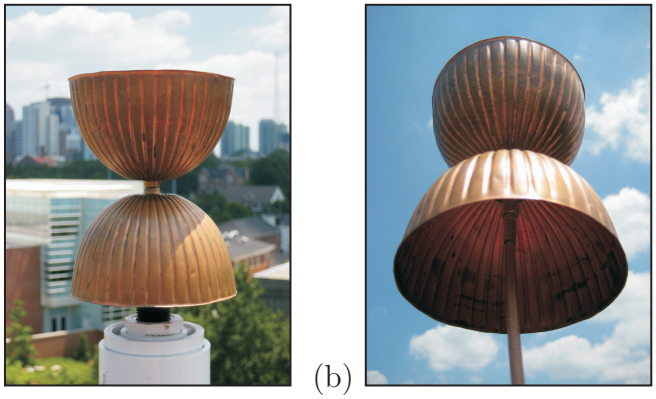

Figure 99: Photos of one of the toiletennas.

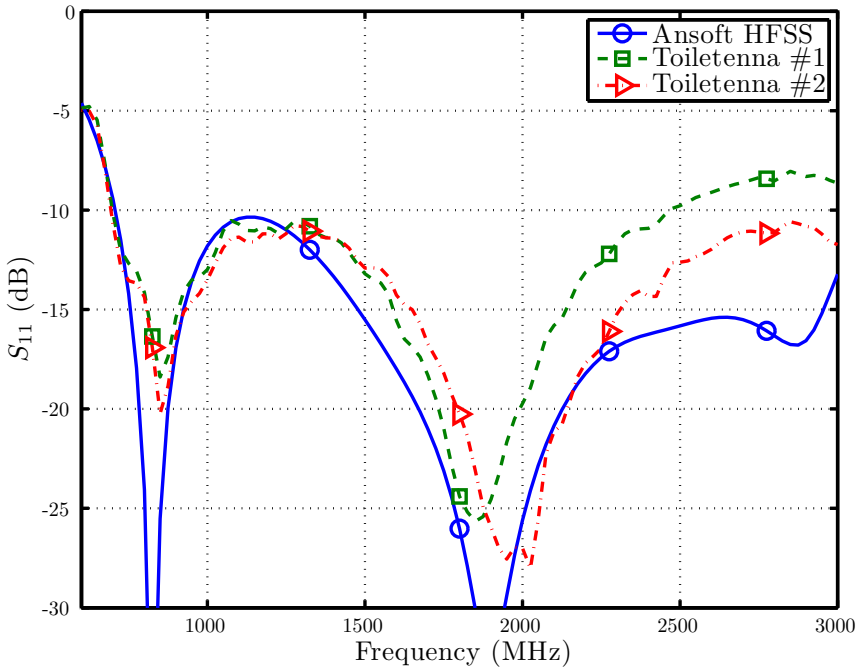

Figure 100: A comparison of the simulated and measured S_{11} for the toiletennas.

indicates. Figure 105 presents the gain pattern of the dual-ridged horn antenna as measured at 2.45 GHz along azimuth. The measured -3 dB and -10 dB beamwidths at 2.45 GHz were 50° and 110°, respectively. The antenna gain along boresight at 2.45 GHz was determined to be 8 dB.

C.3 Software

The software side of the channel sounder fell into two categories: data acquisition and post-processing. The data acquisition software provided the necessary communication tools for configuring and triggering the oscilloscope, as well as for downloading a measurement off of the oscilloscope and storing it on a computer. The post-processing software provided offline calibration and digital filtering of the recorded impulse response measurements.

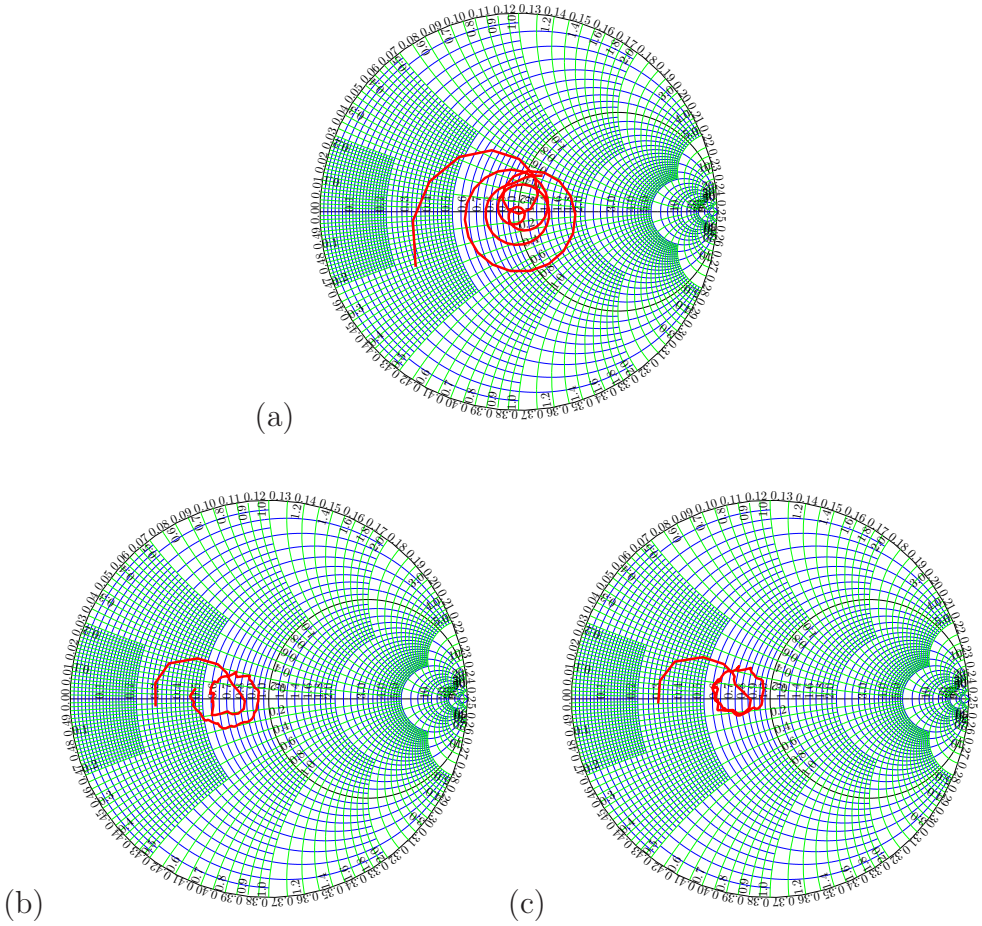

Figure 101: The S_{11} plotted on a Smith chart: (a) simulated, (b) Toiletenna #1, and (c) Toiletenna #2.

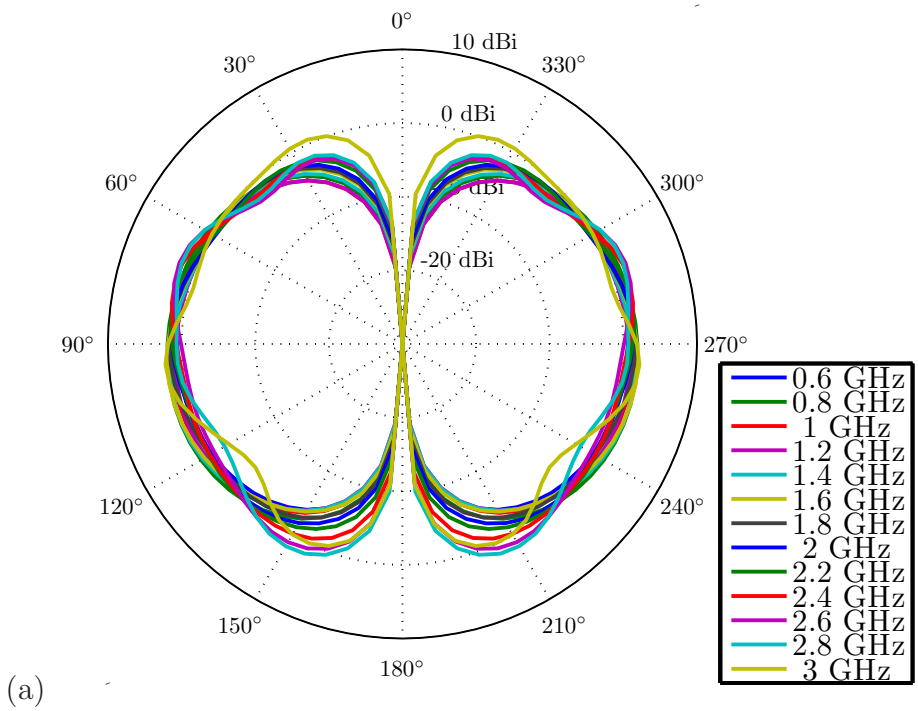

(a)

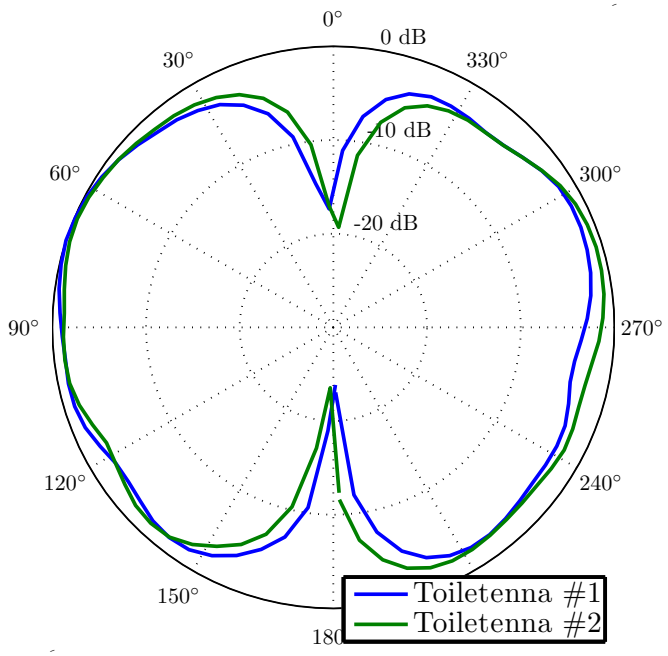

(b)

Figure 102: The elevation plane gain pattern for the toiletenna: (a) the simulated gain pattern at various frequencies and (b) the measured normalized gain pattern at 2.45 GHz.

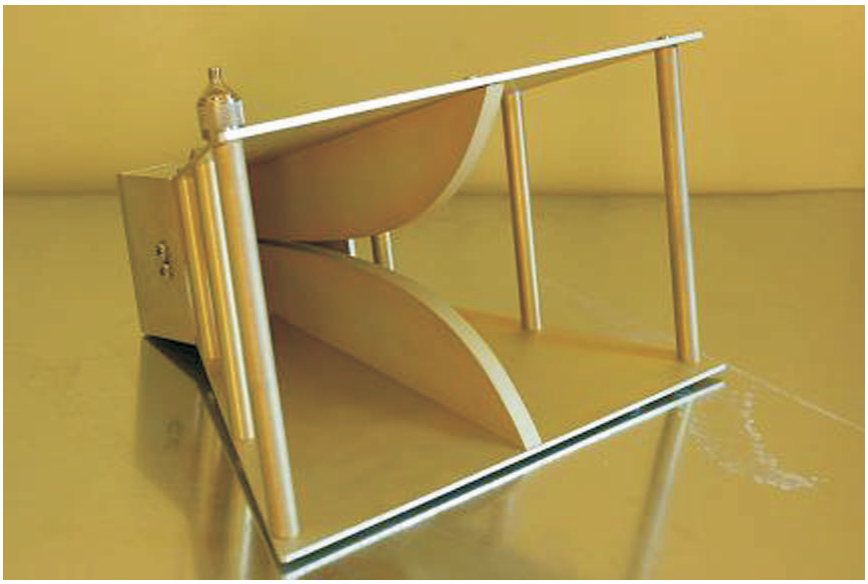

Figure 103: A photo of the dual-ridged horn antenna.

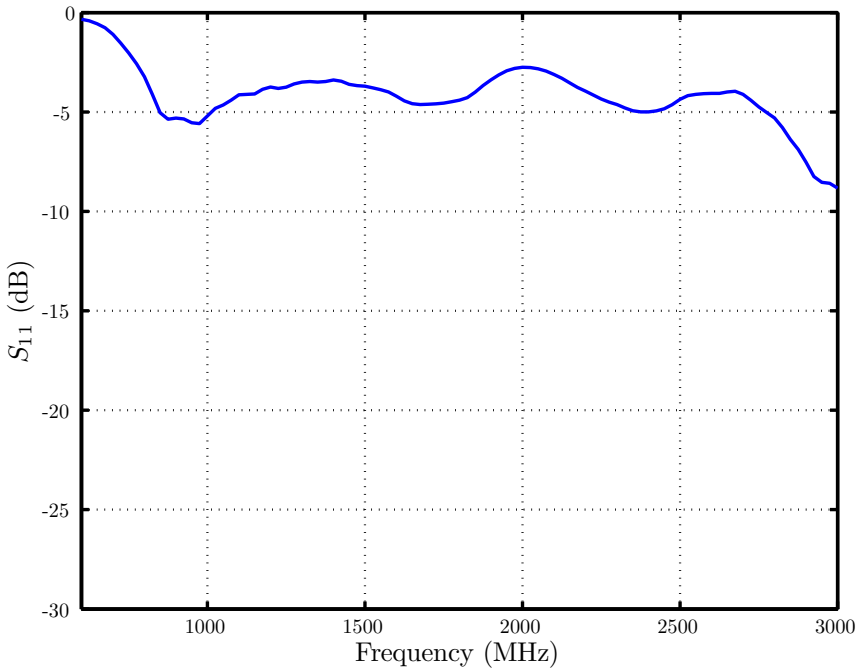

Figure 104: The measured S_{11} for the dual-ridged horn antenna.

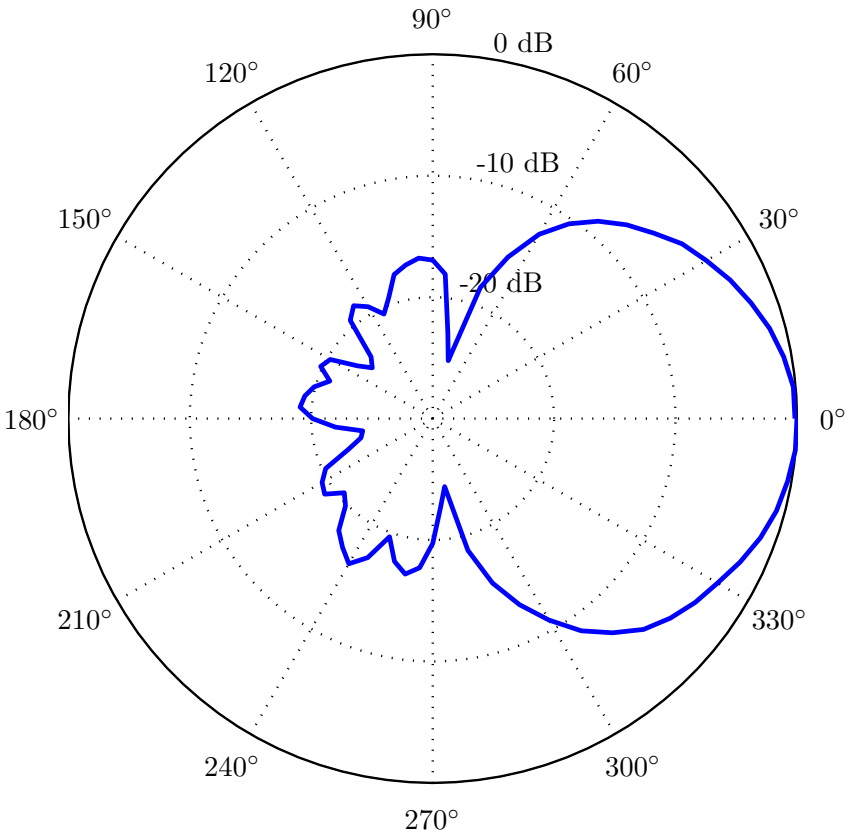

Figure 105: The measured azimuth plane gain pattern for the dual-ridged horn antenna at 2.45 GHz.

C.3.1 Data Acquisition

Data acquisition was controlled by a laptop via USB. The laptop was connected to the Agilent DSO6104A digital oscilloscope using a USB cable, and a custom MATLAB-C software suite was written to communicate with the oscilloscope. The software suite was built around the *Agilent IO Libraries Suite* and thus enabled remote communication with *any* Agilent instrument that supported SICL-based commands. It should be noted that the software is compatible with a range of communication links including USB, GPIB, RS-232, and TCP/IP.

C.3.1.1 Instrument Communication Software Suite

The software suite was originally devised for GPIB-based communication using an Agilent 82357 USB-to-GPIB cable. Thus, much of the terminology is oriented toward GPIB connections. However, it should be emphasized that this in no way restricts the range of supported communication protocols. As already noted, a number of communication protocols are supported.

The software suite provides a number of useful MATLAB functions for pulling data off of specific instruments. These instrument-specific functions are:

- `getSATrace.m`: Downloads the current trace and supplementary data from a spectrum analyzer.
- `getScopeTrace.m`: Downloads the current trace and supplementary data from an oscilloscope.
- `getVNATrace.m`: Downloads the current trace and supplementary data from a vector network analyzer.
- `getVNASparam.m`: Downloads a specific S-parameter from the vector network analyzer.

All of these functions rely on a lower level MATLAB function called `gpibtalk.m`, which is used to issue commands and query a specified instrument. Actual communication takes place using a pair of custom MATLAB-to-C function wrappers called `gpibprintf.m` and `gpibprompt.m`. `gpibprintf.m` sends commands to the specified instrument whereas `gpibprompt.m` sends queries. Both executables return information back to MATLAB by way of a log/data file called `myfile.txt`. When commands are sent to the instrument, `myfile.txt` is used to inform MATLAB if the communication was successful; when queries are sent, the data returned by the instrument is written to `myfile.txt`, which is subsequently imported by MATLAB.

Each instrument is identified by a "SICL address", which can be determined from the *Agilent Connection Expert* program within the *Agilent IO Libraries Suite*. An instrument's SICL address depends on the interface used to connect to the instrument and thus will change depending on whether, for example, a USB cable or a GPIB cable is used to connect the computer to the instrument. For select devices, the MATLAB function `getDeviceGPIBAdress.m` may be used to determine the appropriate SICL address for the instrument. See the help comments within `getDeviceGPIBAddress.m` for further details.

Finally, it should be noted that ASCII is the default data format. Though convenient due to its transparency, ASCII can be very inefficient, particulary when a large number of data points are to be downloaded from the instrument. Some instruments such as the Agilent DSO6104A allow trace/waveform data to be transferred using an 8-bit byte or 16-bit word format. If it is desired to use an 8- or 16-bit binary data format, one of the two auxiliary query functions, `gpibpromptbyte.m` and `gpibpromptword.m`, may be used. To do so, the trace/waveform query command must be issued using either of these two functions, not `gpibtalk.m`. Furthermore, the instrument should be instructed to transfer data in the appropriate binary format. Note that most instruments only allow trace and/or waveform data to be transferred

using a binary data format. More basic queries that return a single scalar will continue to be transferred in ASCII.

C.3.1.2 Channel Impulse Response Measurement

Once the channel sounder was powered on and operating correctly, the oscilloscope may be configured for taking measurements by calling the MATLAB function `setupScope.m`. After the oscilloscope has been properly configured, a new measurement may be triggered by calling `triggerScope.m`. Once the waveform data has been acquired, the SIMO channel impulse response (CIR) may be downloaded from the oscilloscope using the MATLAB function `getCIR.m`. This function downloads waveform data from each of the oscilloscopes four input channels and compiles them into two complex-baseband CIR measurements.

It should be noted that `setupScope.m` only needs to be called once per measurement campaign. Should the vertical scaling of any of the oscilloscope channels require adjustment, this can be achieved using the MATLAB function `setupScopeVScale.m`. Then, a new CIR measurement may be triggered using `triggerScope.m` and downloaded using `getCIR.m`.

C.3.2 Post-Processing

The SIMO channel sounder hardware provides only modest analog filtering. Additional filtering is necessary to remove the sliding correlator's distortion signal and realize the system's large measurement dynamic range. After digital filtering, the CIR will be "cleaner" but will still be contaminated by the impulse response of the measurement system. This necessitates a back-to-back calibration measurement wherein the transmitter is connected to the receiver via an attenuator and splitter. The resulting attenuator-splitter impulse response measured by the SIMO channel sounder may then be used to calibrate the actual CIR measurements. However, this attenuator-splitter back-to-back calibration neglects any mismatches at the antennas as well as

the antennas' frequency-dependent gain. Thus, the preferred calibration measurement is a free-space wireless channel measurement. For the SIMO channel sounder, co-polarized antenna measurements at a separation distance of 1 m were used to calibrate out the channel sounder's system response.

Post-processing of the raw, time-dilated CIR measurements returned by `getCIR.m` is achieved using the MATLAB function `processCIR.m`. Both the digital filtering and the calibration are handled by this function. The next two sections discuss how `processCIR.m` performs both the digital filtering and the calibration. Finally, we note that, to simplify our discussion the remaining sections assume the raw, time-dilated CIR returned by `getCIR.m` has been appropriately rescaled in time by the slide factor, γ, so as to recover the true CIR. This may be achieved by multiplying either the waveform's time vector or its sampling rate by the slide factor, γ. In practice, this temporal rescaling is performed within `processCIR.m`.

C.3.2.1 Digital Filtering

For a stationary transmitter and receiver in a static wireless channel, the impulse response, $H(\tau)$, recorded by a sliding correlator channel sounder will be periodic with a period of L/f_c. This allows the signal to be represented in terms of its Fourier coefficients as determined using Fourier analysis. Typically, the Fourier coefficients of the periodic CIR $H(\tau)$ would be determined from

$$a_k = \frac{1}{nT} \int_{t_0}^{t_0+nT} dt H(\tau) e^{-j2\pi \frac{f_c}{L} kt} \tag{154}$$

where a_k is the Fourier coefficient corresponding to some integer k, $T = L/f_c$ corresponds to single period of the CIR, and $n = 1$. However, assuming that $H(\tau)$ is in fact periodic with period L/f_c, n may actually be any positive integer.

This is significant, because in practice the measured static CIR will be corrupted by system noise, in-band interference, and channel fluctuations due to time-varying

scatters, which we collectively lump together as some complex temporal noise, $N(\tau)$. Though possible, it is highly unlikely that $N(\tau)$ will have significant spectral content at integer multiples of f_c/L. This suggests that applying Fourier analysis to $H(\tau) + N(\tau)$ for some large (and nominally infinite) n will lead to Fourier coefficients similar to those that would be calculated from Eq. (154).

It should be noted that this "Fourier analysis" approach to filtering is identical to time-averaging n periods of the CIR. However, whereas Fourier analysis may be directly applied to the approximately 78 periods of the CIR sampled by the oscilloscope, time-averaging across periods requires the measurement to be divided up into its 78 periods and will generally require each period to be interpolated to a common time vector.

Fourier analysis was implemented with the MATLAB function `fourierAnalysis.m`. The 78.2 CIR periods returned by `getCIR.m` were truncated to exactly 78 periods. Then, Eq. (154) was used to extract the Fourier coefficients of the 78-period CIR for $k \in (-L, L)$, which corresponds to the CIR's main spectral lobe [82]. Note that $k = \pm L$ is excluded because these correspond to the nulls in the CIR's sinc-squared spectral mask [82].

A complementary function, `fourierSynthesis.m`, may be used to reconstruct the time-domain impulse response from the Fourier coefficients calculated by `fourierAnalysis.m`. However, it is generally more convenient to leave the CIR in its Fourier coefficient representation due to the resulting data compression. The two complex baseband CIR waveforms returned by `getCIR.m` each consist of 500,000 complex data points. In contrast, for integer $k \in (-L, L)$ where $L = 511$, each CIR may be represented with just 1,023 complex data points. In addition, it makes calibration very straightforward.

C.3.2.2 Calibration

As discussed in [82], the sliding correlator channel sounder's probing signal is a triangular pulse train resulting from the autocorrelation of PN. Denoting the spectrum of this probing signal as $x(f)$, the impulse response recorded by the channel sounder has a spectrum $y(f)$ given by

$$y(f) = x(f)h_s(f)h_c(f) + n(f) \tag{155}$$

where $h_s(f)$ is the frequency response of the channel sounder, $h_c(f)$ is the frequency response of the wireless channel, and $n(f)$ is additive noise and interference.

Under the assumption that the noise/interference spectrum, $n(f)$, corresponds to Gaussian white noise, the system response, $h_s(f)$, maybe removed from the measured channel response by via Wiener deconvolution [38]. First, a reference measurement, $y_s(f)$, is made in a channel having a constant magnitude and linear phase. This enables the estimation of the system response as

$$\tilde{h}_s(f) \approx \frac{y_s(f)}{x(f)} \left[\frac{|x(f)|^2}{|x(f)|^2 + \max |x(f)|^2 / [\mathrm{SNR_s(f)}]} \right] \tag{156}$$

where $\mathrm{SNR_s(f)}$ is the frequency-dependent signal-to-noise ratio (SNR) of the reference measurement. Using this estimate of the system's response, the wireless channel may be estimated from a channel measurement as

$$\tilde{h}_c(f) \approx \frac{y(f)}{x(f)h_s(f)} \left[\frac{|x(f)h_s(f)|^2}{|x(f)h_s(f)|^2 + \max |x(f)h_s(f)|^2 / [\mathrm{SNR_c(f)}]} \right] \tag{157}$$

where $y(f)$ is the received signal's spectrum and $\mathrm{SNR_c(f)}$ is the frequency-dependent SNR of the wireless channel measurement. Substituting Eq. (156) for $h_s(f)$ and simplifying yields

Table 7: SIMO Channel Sounder Capabilities

System Capability	Realized Performance
Doppler Resolution, $f_{D,\max}$	391 Hz
Dynamic Range, D_R	34 dB
Temporal Resolution, T_{res}	2.22 ns
Max Multipath Delay, $\tau_{\max}$	1.14 μs
Max Path Length, $d_{\max}$	341 m

$$h_c(f) \approx \frac{y(f)}{y_s(f)} \left\{ \frac{|y_s(f)|^2 \left[\frac{|x(f)|^2}{|x(f)|^2 + \max|x(f)|^2/[\text{SNR}_\text{s}(\text{f})]} \right]}{|y_s(f)|^2 \left[\frac{|x(f)|^2}{|x(f)|^2 + \max|x(f)|^2/[\text{SNR}_\text{s}(\text{f})]} \right]^2 + \frac{\max|x(f)h_s(f)|^2}{\text{SNR}_\text{c}(\text{f})}} \right\} \tag{158}$$

Effectively, Wiener deconvolution applies an SNR-dependent spectral mask (i.e., a window) to the otherwise noisy channel response estimate given by $y(f)/y_s(f)$. If the desired end result is a high temporal resolution channel impulse response, additional frequency-domain windowing may be necessary to suppress the temporal "sidelobes" due to the implicit rectangular window. In addition to traditional windows like the Hamming window, the magnitude of the probing signal's spectrum, $x(f)$ may also be used with good results.

C.4 Channel Sounder Capabilities

Table 7 summarizes the capabilities of the SIMO sliding correlator channel sounder. For an explanation of the channel sounder capabilities listed in Table 7, see [82].

APPENDIX D

PSEUDO-RANDOM NOISE GENERATOR

The heart of a sliding correlator channel sounder is a pseudo-random noise (PN) generator. For the SIMO sliding correlator channel sounder described in Appendix C, the PN generator was realized as a 9-bit linear feedback shift register (LFSR). To attain the highest possible chip rate, the propagation delays around the LFSR's feedback loop were minimized by using high-speed emitter-coupled logic (ECL) integrated circuits.

D.1 Emitter-Coupled Logic

ECL is generally considered the best choice for high-speed digital design and offers propagation delays on the order of picoseconds [96]. To maximize performance, ECL requires RF-like design consideration so as to minimize reflections due to impedance mismatches. Other design constraints are imposed by the very nature of ECL, which achieves its short propagation delays by biasing transistors in the forward active region [97]. Because outputs are always sourcing current, power consumption can be high. Further, ECL requires all outputs be terminated through a resistance, R_{TT}, to a voltage, $V_{TT} = V_{cc} - 2$, where V_{cc} is the positive voltage rail, so as to remain in the forward active region during both high and low outputs [98]. Ideally, R_{TT} should match the trace and ouput impedance of the device, both of which are typically 50 Ω. The termination voltage, V_{TT}, acts as a current sink for the ECL outputs. For $V_{cc} = 5$ V, a 3 V current sink may be designed using an op amp and a PNP transistor as shown in Figure 106. Configured as a voltage-follower, the op amp applies 2.27 V to the base of the transistors. Current flowing from the ECL outputs into the emitter

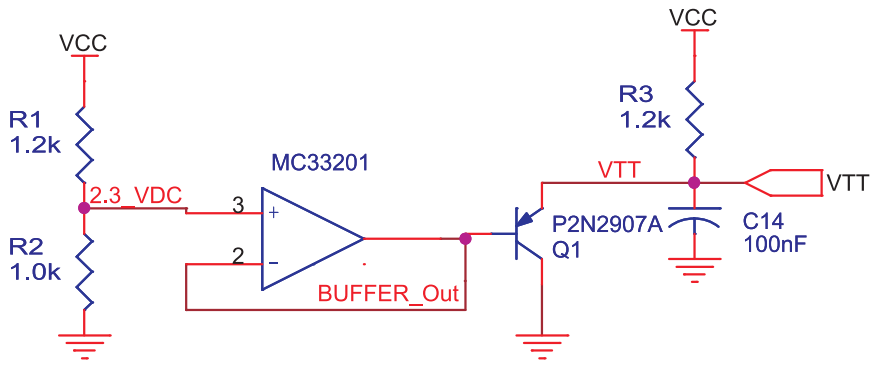

Figure 106: A schematic of the 3 V current sink used for V_{TT}.

will forward bias the transistor, thereby setting V_{BE} to approximately 0.7 V and V_{TT} to approximately 3 V.

D.2 Linear Feedback Shift Register

A 9-bit LFSR was implemented using the simple shift register generator (SSRG) architecture and ECL integrated circuits as shown in Figure 107(a). A *MC10EP142* 9-bit shift register provided the backbone for the LFSR. Using the feedback registers, $\{9, 5\}$, the LFSR produced an m-sequence of length $L = 2^9 - 1 = 511$ chips [32]. Modulus 2 addition was perfomed using an *MC10EL07 XOR* gate, and the *XOR*'s output of which was fed into the shift register's input. To initialize the LFSR, a single-pull single-throw (SPST) switch connected to V_{HI} was used to toggle shift register between parallel and serial input modes. Closing the switch put the shift register in parallel input mode and caused the register's first bit to be set to V_{HI}. Subsequently opening the switch returned the shift register to serial input mode and initiated the PN generation.

D.3 PN Generator Clock Converter

To allow for flexibility in selecting a high-speed clock source, the PN generator was designed to accept both square and sinusoidal clocks. The clock input was AC-coupled and included a 50 Ω termination for use with typical RF signal sources.

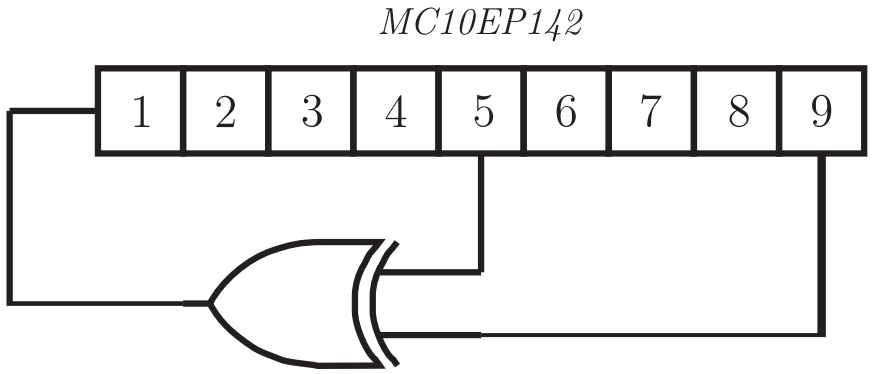

(a)

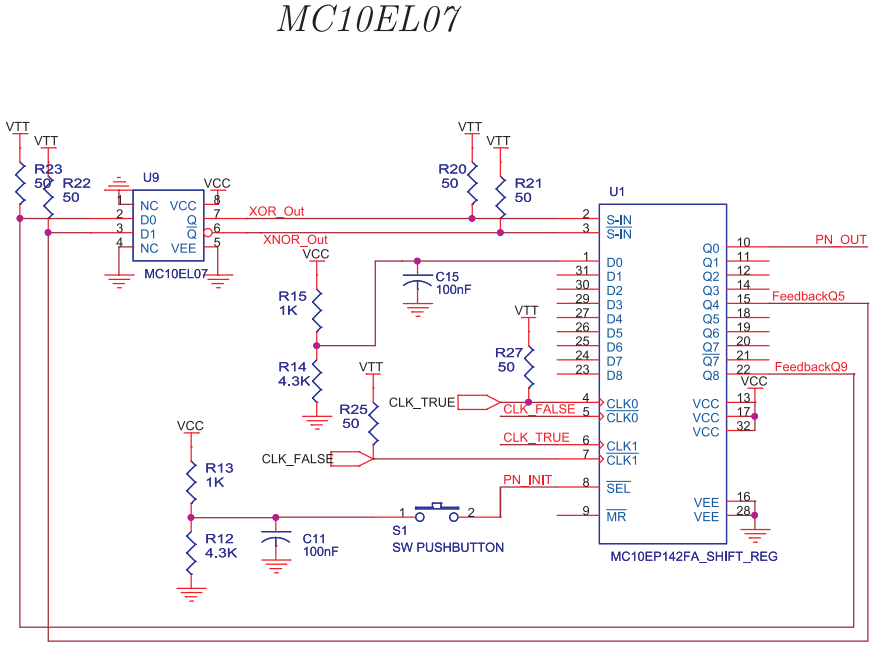

(b)

Figure 107: The 9-bit linear feedback shift register produces an m-sequence of length $L = 511$ chips: (a) diagram of the circuit and (b) a simplified schematic.

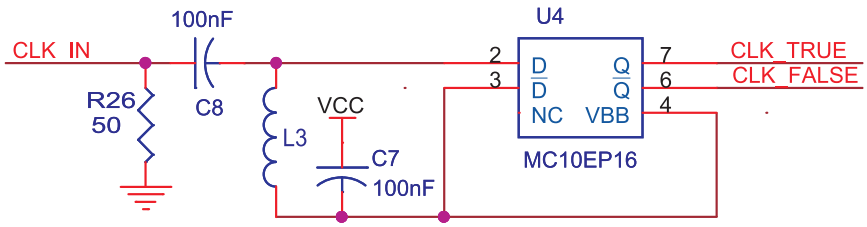

Figure 108: A schematic of the shift register clock converter based around the *MC10EP16* differentical receiver chip. The circuit allows the PN generator to accept sinusoidal clocks from high frequency signal generators.

As shown in Fig. 108, the applied clock source was DC-biased to V_{BB}, which was provided by the *MC10EP16* differential receiver. The DC-biased clock signal was then fed into one of the differential receiver's inputs. The other input was connected directly to V_{BB}. This configuration converted the single-ended AC-coupled clock to a differential ECL clock. The *MC10EP16* buffered this differential clock for distribution to the *MC10EP142* shift register. The *MC10EP16* differential receiver allowed for a maximum input voltage of 2 V_{pp}. For a sinusoidal clock source, this corresponds to a maximum input power of 10 dBm. The miminum input power for a sinusoidal clock was experimentally determined to be -10 dBm, which correponds to 1.414 mV_{pp}.

D.4 PN Output Termination

The ECL-based LFSR required a 50 Ω termination to $V_{TT} = Vcc - 2$ to maintain proper biasing. However, most RF devices such as amplifiers, mixers, and filters are designed for 50 Ω terminations to GND. Resolving this disparity required a DC path to ground for biasing the ECL's emitter-follower output while also allowing for a 50 Ω AC termination to GND as provided by a typical RF device. When terminated through 50 Ω to V_{TT}, the emitter-follower sourced 21.1 mA for V_{HI} and 5.1 mA for V_{LO}. When the ECL output was connected to the parallel combination of a 274 Ω resistor to GND and a large capacitor to a 50 Ω device as depicted in Fig. 109, the emitter-follower sourced 22.8 mA for V_{HI} and 3.8 mA for V_{LO} [57]. These currents were sufficiently similar to the currents sourced by an ECL output terminated through

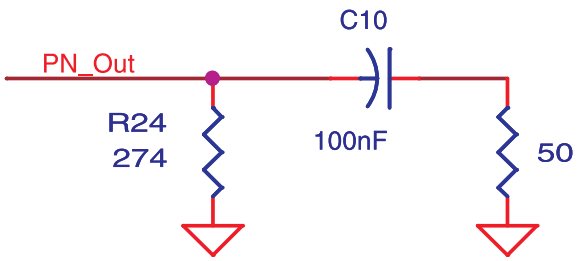

Figure 109: A schematic of the PN output circuit for connecting the ECL's emitter-follower to a 50 Ω RF termination.

50 Ω to V_{TT} so as to ensure the ECL output remained biased in the forward active region.

D.5 Verification of the PN

Figure 110 examines the power spectral density of the output signal with the LFSR clocked at $f_c = 800$ MHz. The characteristic sinc-shaped envelope is visible with nulls occurring at multiples of 800 MHz [32]. Spikes at these nulls indicate clock feed-through. Figure 111 takes a closer look at this power spectral density and reveals the individual spectral components that define the spectrum's envelope. The spectral components have a spacing of 1.565 MHz, which is in agreement with the theoretical spacing given by f_c/L where $L = 511$ and $f_c = 800$ MHz [32]. This indicates that the LFSR was operating correctly and generating the expected PN. Figure 112 shows a photographs of the constructed PN generator.

D.6 Schematics

Figures 113 through 114 present circuit schematics for the PN generators.

D.7 PCB Layout

Figures 116 and 117 present the top and bottom layers, respectively, of the PN generator's PCB layout.

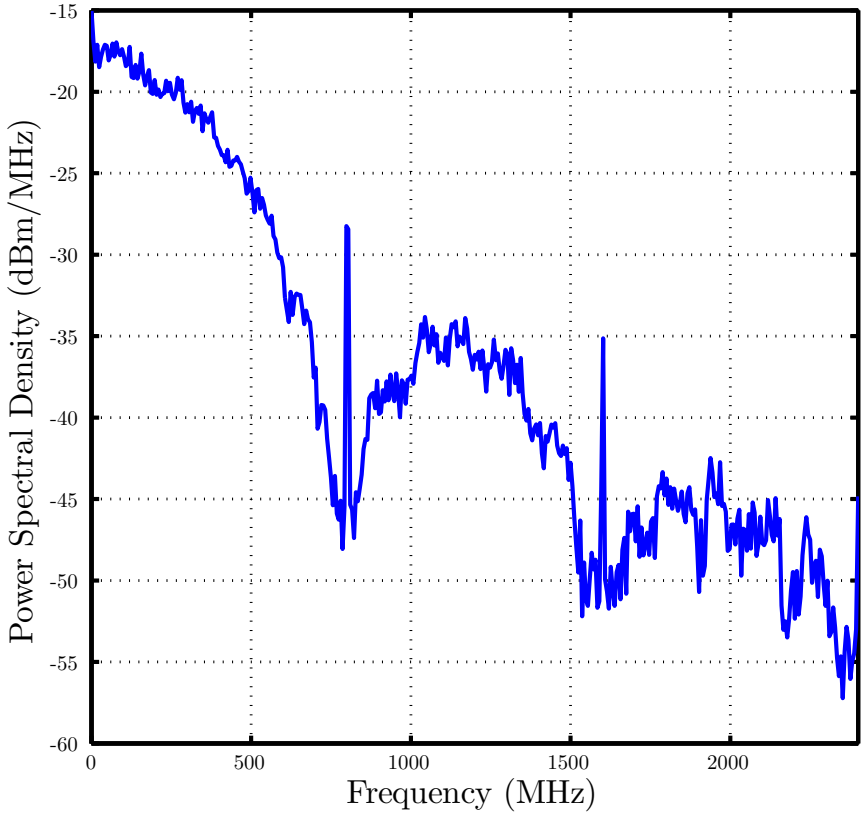

Figure 110: The spectrum of the PN produced by the 9-bit LFSR with a chip rate of $f_c = 800$ MHz. The spectrum had the characteristic sinc-shaped envelope.

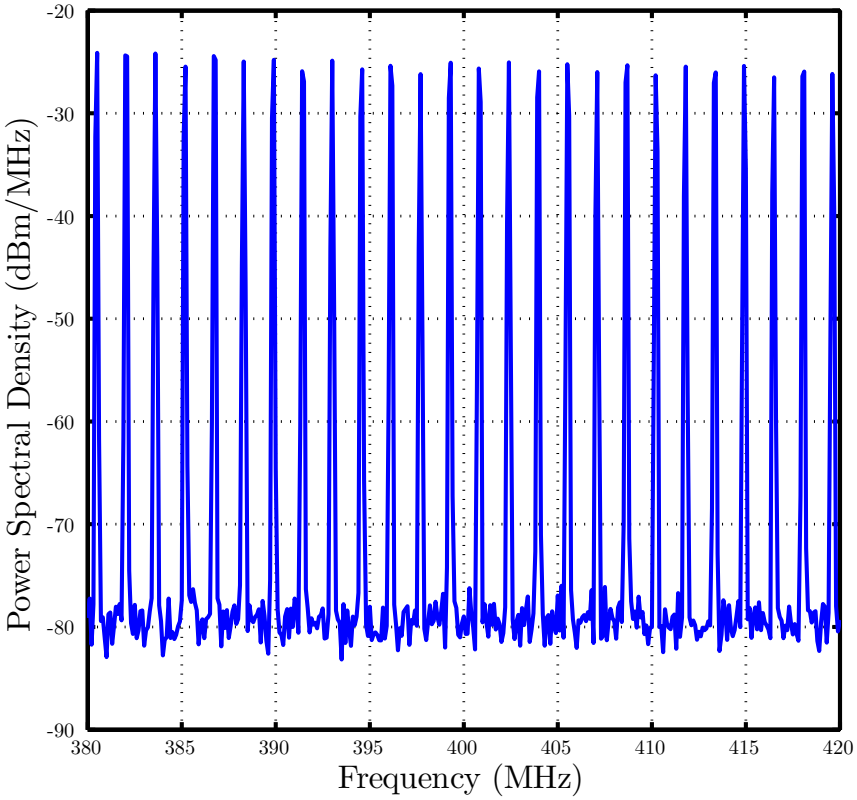

Figure 111: A closer look at the spectrum produced by the 9-bit LFSR with a chip rate of $f_c = 800$ MHz reveals the spectral components that make up the sinc-shaped envelope. The interval between spectral components was 1.565 MHz.

(a)

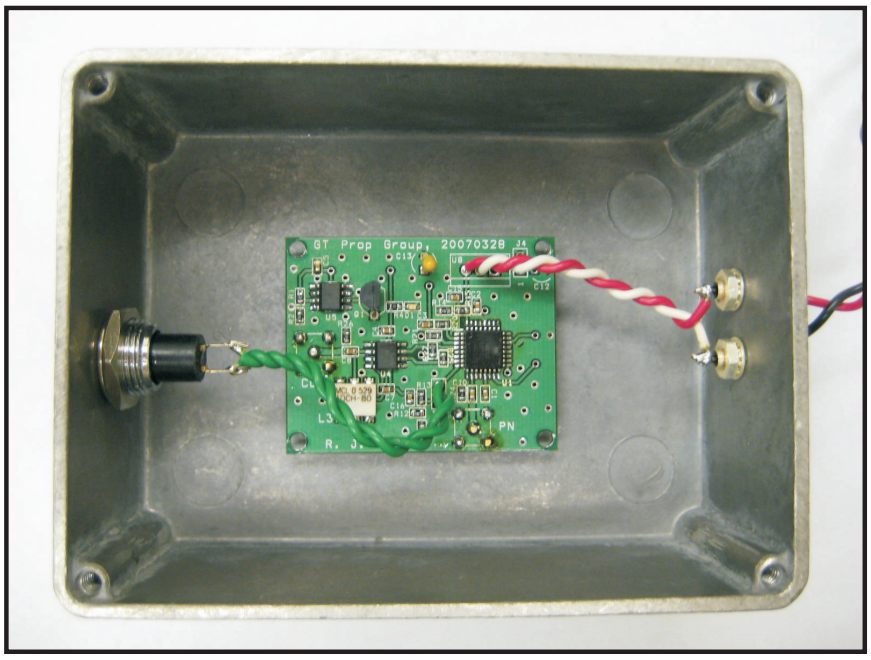

(b)

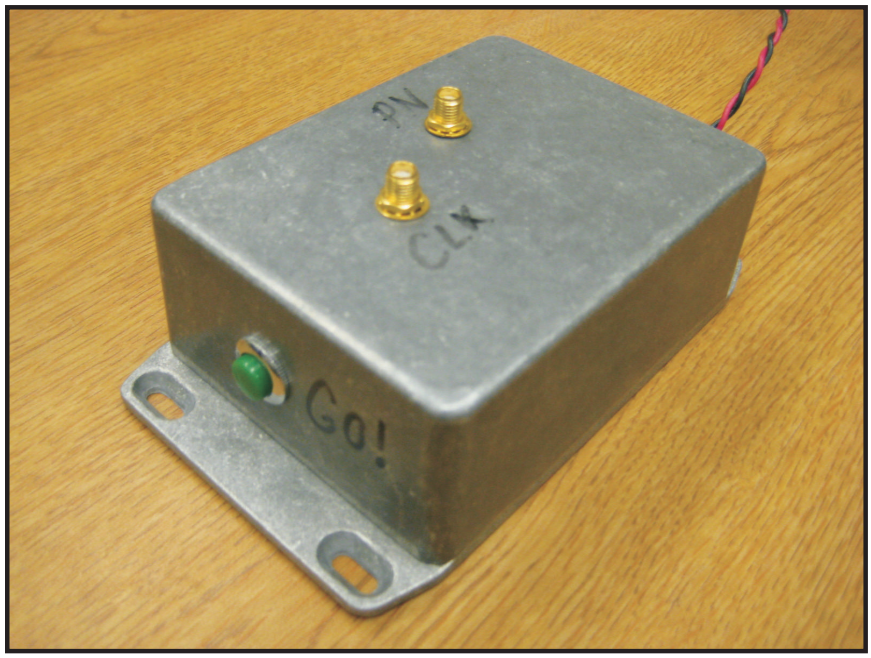

Figure 112: Photos of the 9-bit LFSR-based PN generator designed with ECL: (a) populated circuit board and (b) enclosed PN generator. The PN generator produced a sequence length of $L = 511$ chips at a maximum chip rate of approximately 800 MHz.

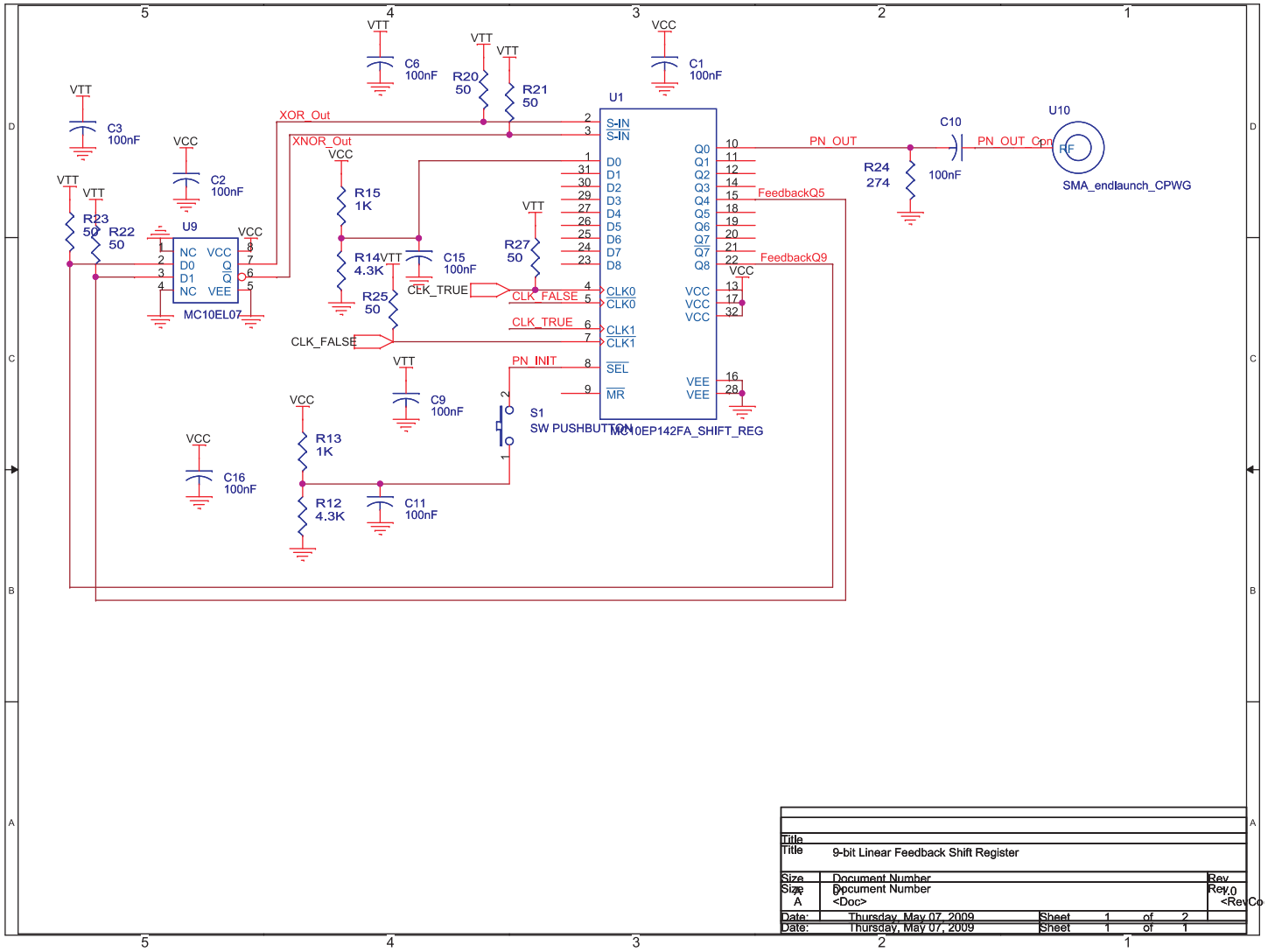

Figure 113: PN schematic showing the 9-bit linear feedback shift register used to produce the 511-bit pseudo-random noise.

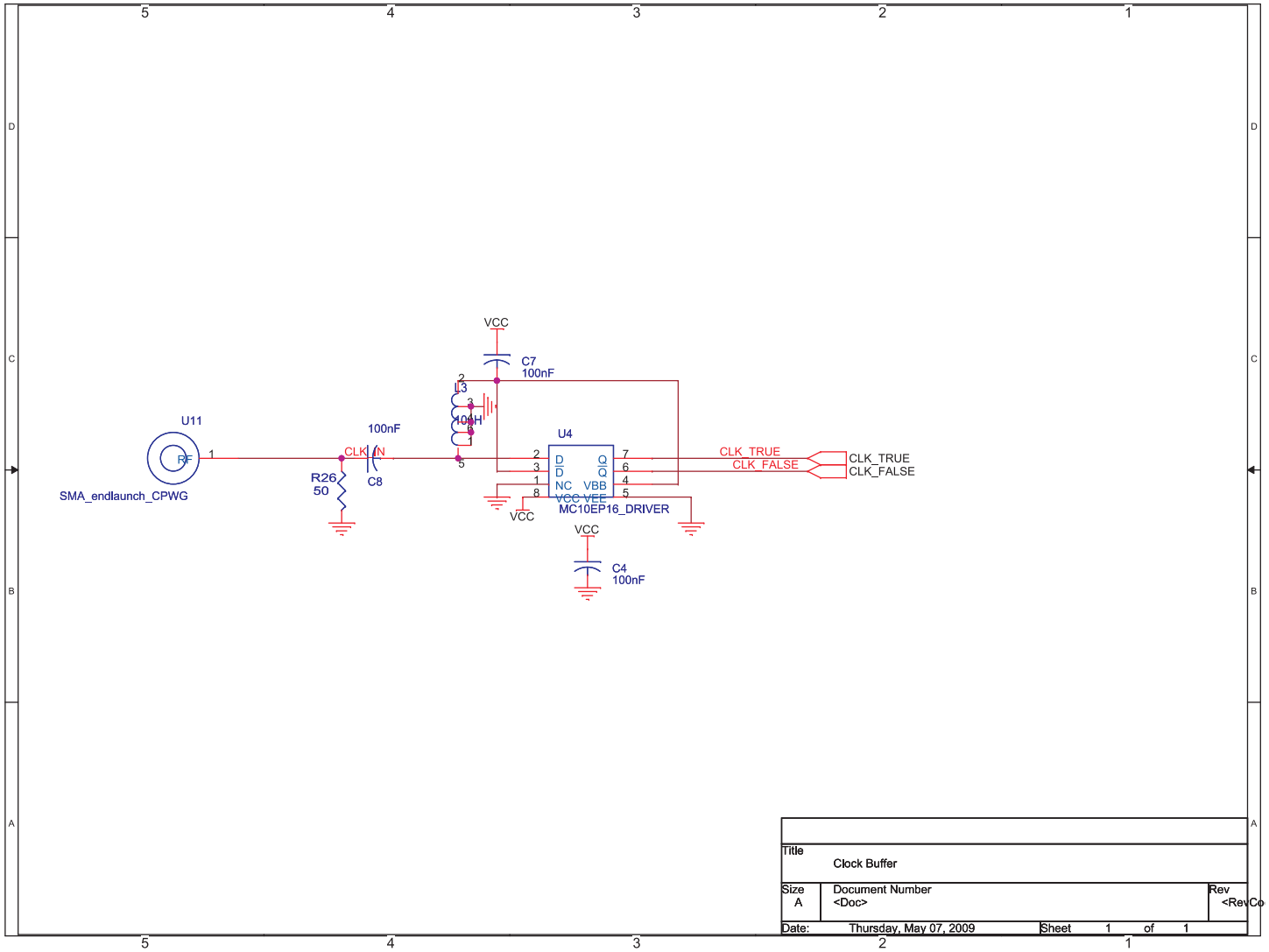

Figure 114: PN schematic showing clock converter used to convert an AC-coupled sinusoidal source into an ECL differential clock.

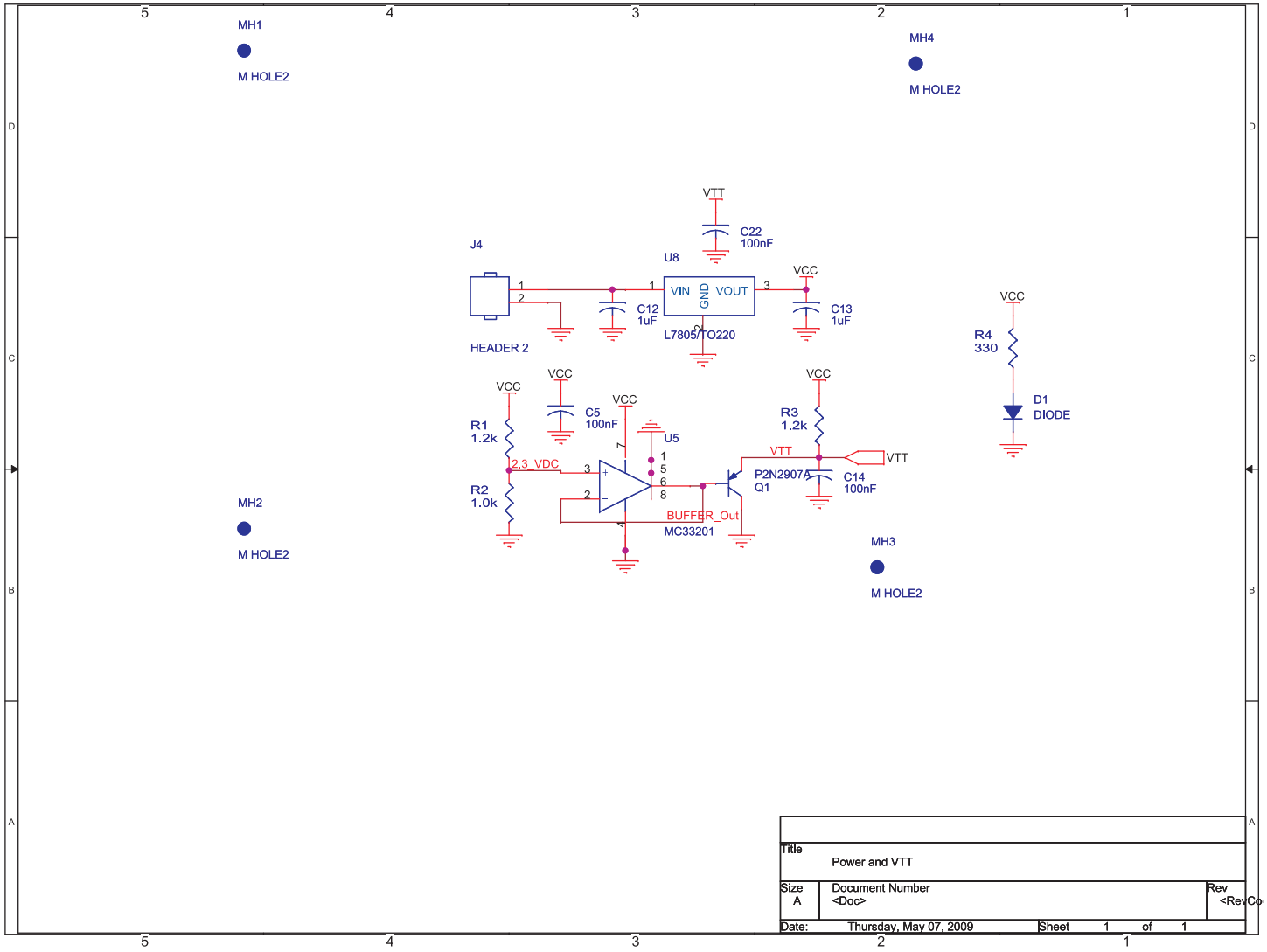

Figure 115: PN schematic showing the 5 V power rail and the 3 V current sink, V_{TT}.

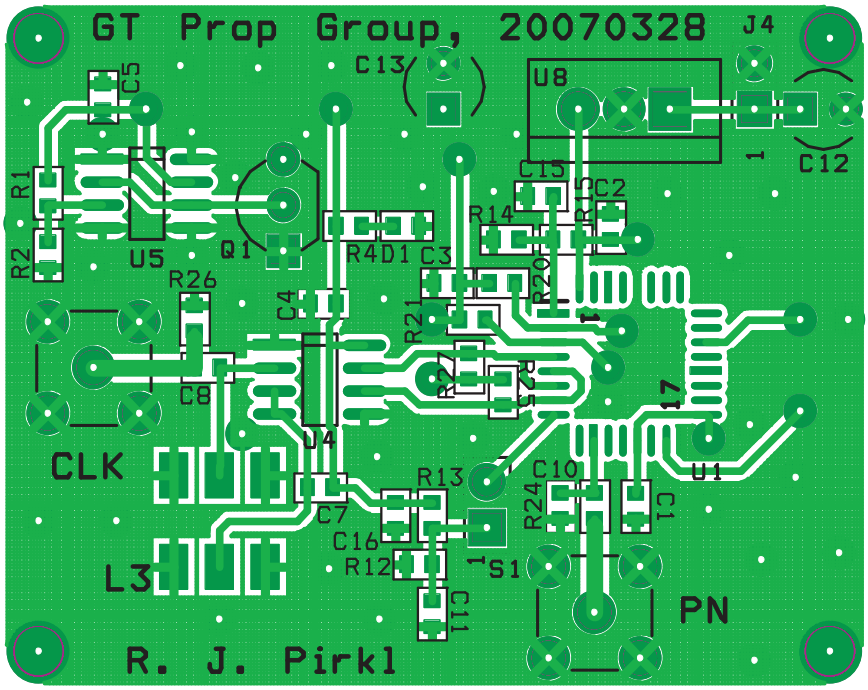

Figure 116: The PN generator board's top copper layer, solder mask, and silk screen.

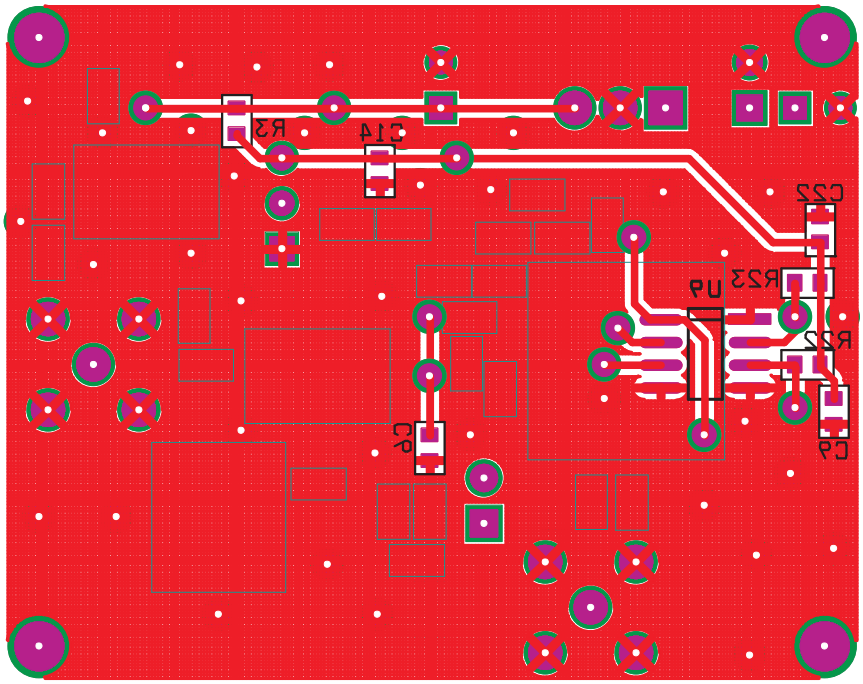

Figure 117: The PN generator board's bottom copper layer, solder mask, and silk screen.

APPENDIX E

FREQUENCY SYNTHESIZER

The frequency synthesizers described here provide compact, inexpensive, and extremely flexible RF signal sources that have been used for a myriad of applications. It should be noted that this design was a collaborative effort between the author and Chris J. Durkin.

E.1 Hardware

Figure 118 presents photos of one of the constructed frequency synthesizers. Schematics for various system blocks of the frequency synthesizer are depicted in Figures 119, 120, and 121. The following sections will provide a brief overview of each of the system blocks.

E.1.1 Phase-Locked Loop

The phase-locked loop describes the combination of a voltage-controlled oscillator (VCO), and frequency synthesizer, which contains the phase frequency detector, frequency dividers, and charge pump.

E.1.1.1 Voltage-Controlled Oscillator

The frequency synthesizer board accepts any surface mount VCO with a 16-pin 0.5 in by 0.5 in footprint provided that the necessary tuning voltage is 0-5 V, and the required power voltage is 5 V. Appropriate VCOs at a myriad of frequency bands are available through companies such as Mini-Circuits and Crystek Microwave.

(a)

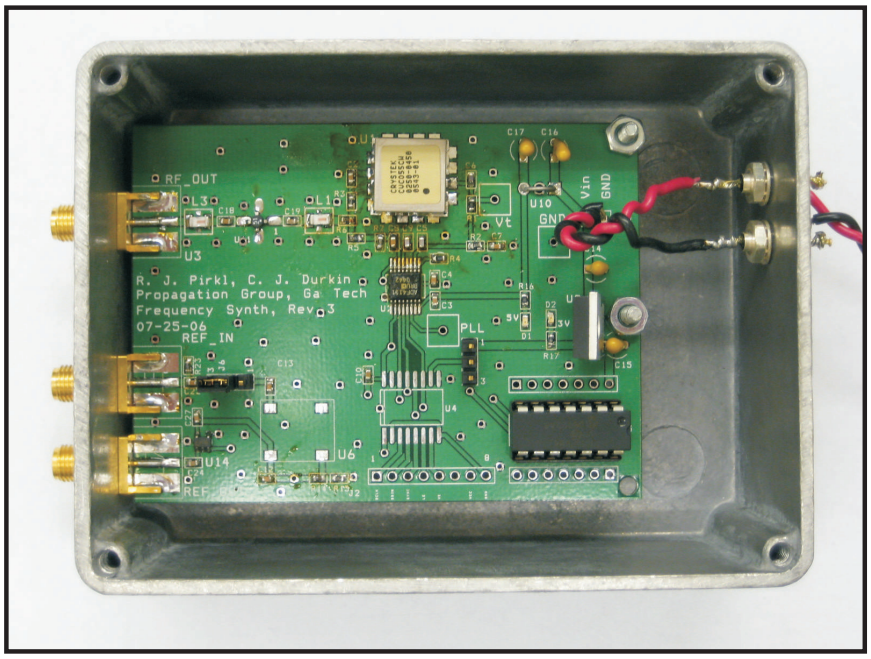

(b)

Figure 118: Photos of a constructed frequency synthesizer: (a) populated circuit board and (b) enclosed frequency synthesizer.

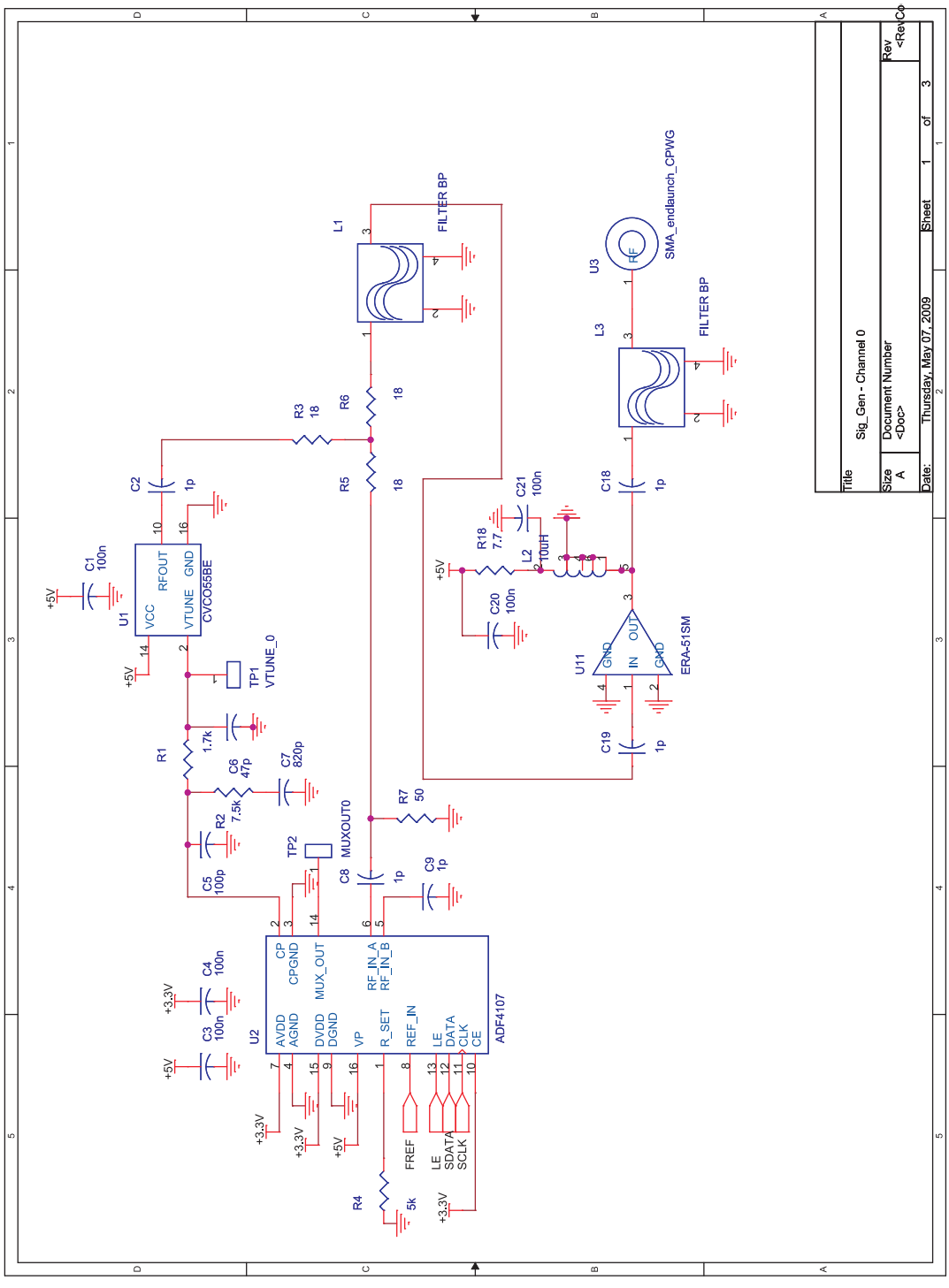

Figure 119: Frequency synthesizer board schematic showing the phase-locked loop, output filters, and amplifier.

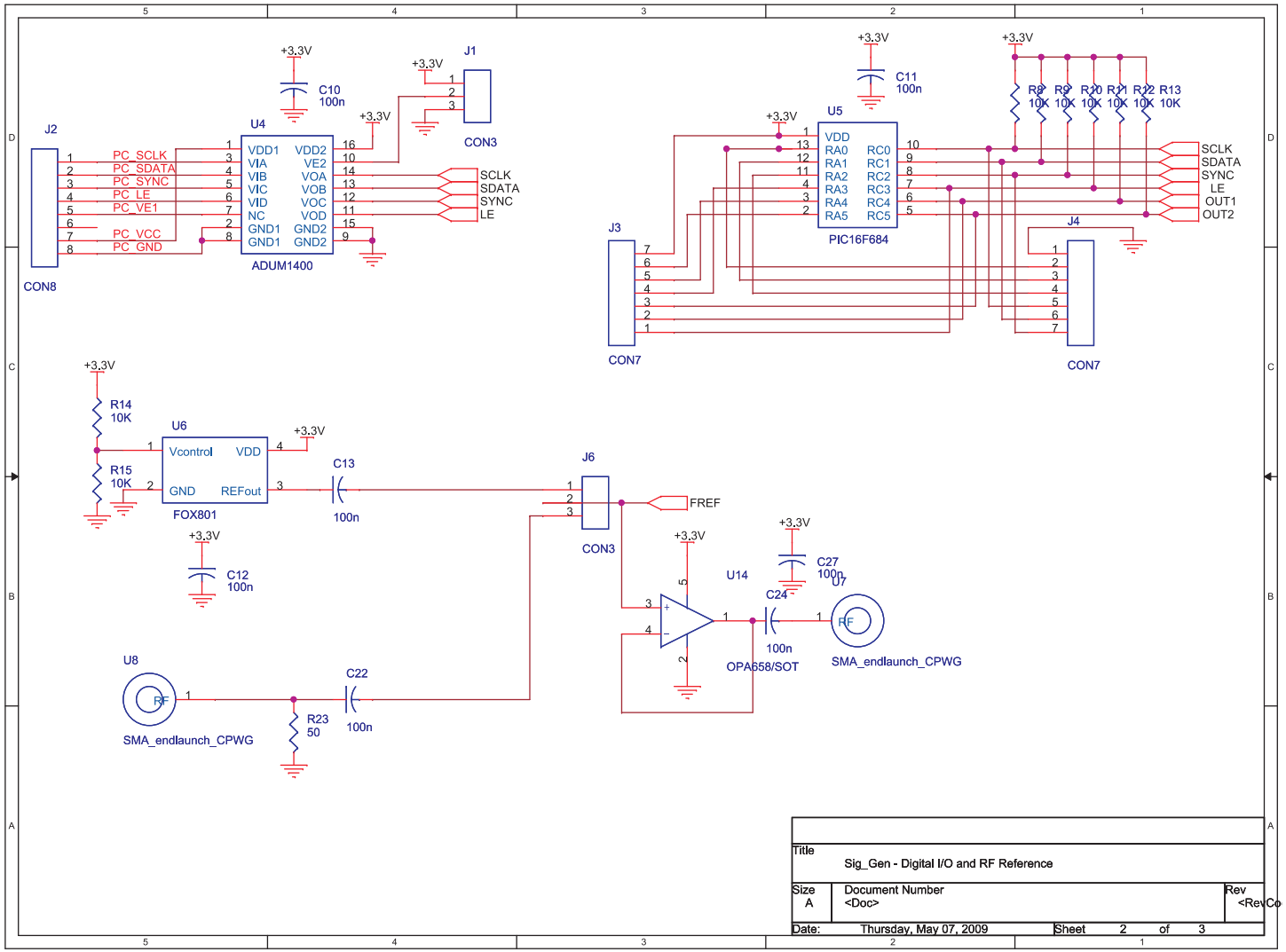

Figure 120: Frequency synthesizer board schematic showing the optoisolator, PIC microcontroller, and 10 MHz reference buffer.

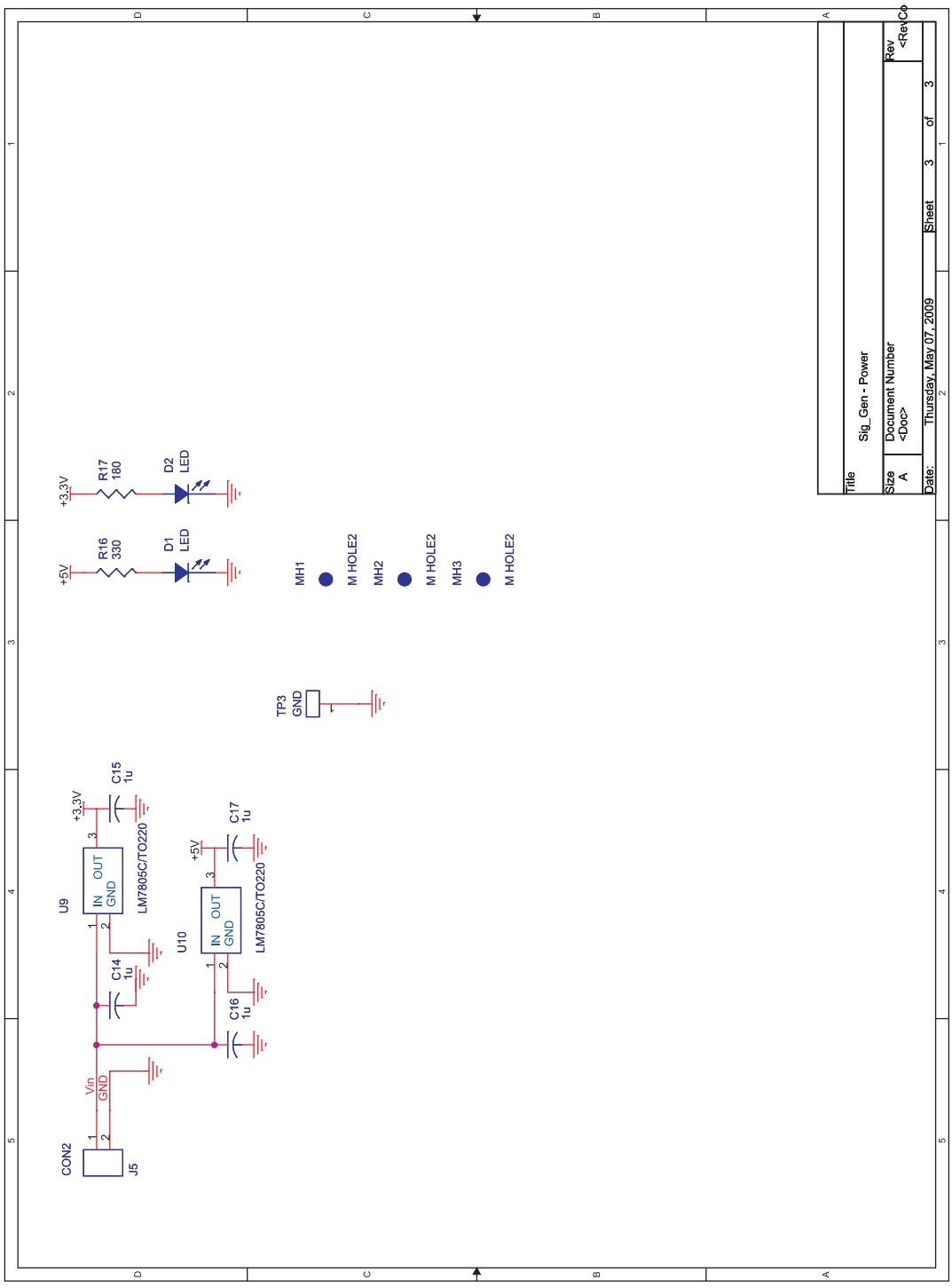

Figure 121: Frequency synthesizer schematic showing the voltage regulators and power rail LEDs.

E.1.1.2 Frequency Synthesizer

The board accepts a range of frequency synthesizer ICs produced by Analog Devices with a 16-lead TSSOP footprint. The board should work with many (though not all) of the frequency synthesizer ICs in the ADF40XX and ADF41XX family. However, the board has only been tested with the following ICs:

- ADF4001
- ADF4111
- ADF4107

Generally, it is required that the frequency synthesizer IC be a single "integer-N type" with four 24-bit registers (or latches). The registers will be described as follows:

- Reference counter latch
- N counter latch
- Function latch
- Initialization latch

The reference counter, R, is used to divide down some reference frequency, f_{REF}, which is nominally 10 MHz as is the convention for RF equipment. The N counter latch is used to divide the VCO's output frequency, f_{VCO}, to some more manageable frequency for phase frequency detection. The N counter latch may be composed of either a single 13-bit counter, N, or the combination of a 13-bit counter, B, and a 6-bit counter, A. For the latter case, the first two bits of the *function latch* and *initialization latch* are used to assign a prescalar, P, and N is effectively given by

$$N = PB + A$$

For either case, the VCO frequency will be given by

$$f_{\mathrm{VCO}} = N\frac{f_{\mathrm{REF}}}{R}$$

Thus, by appropriately choosing N (or P, B, and A) and R, one has a great deal of flexibility in setting the VCO's frequency.

When correctly programmed, the frequency synthesizer IC will compare the phase and frequency between f_{VCO}/N and f_{REF}/R and attempt to adjust VCO's tuning voltage via the frequency synthesizers charge pump so as to correct for any disparity.

E.1.1.3 Loop Filter

Differences in phase and/or frequency will cause the charge pump to produce proportional transient output signals that "drive" the loop filter. The loop filter converts the charge pump's transient output to a smooth and nominally constant VCO tuning voltage. The loop filter shown in Fig. 119 was a third order low-pass filter as described in [31, p. 18] that had a bandwidth of 70 kHz. For a given frequency synthesizer IC and desired output frequency, Analog Devices's "ADIsimPLL 3.1 Design and Evaluation Software" may be used to determine the appropriate loop filter. This software is freely available online through the Analog Devices website.

E.1.2 RF Filter

The RF filters remove harmonics generated by either the VCO or the amplifier. The frequency synthesizer board accepts any of Mini-Circuit's surface mount low-pass filters that use their custom "FV1206" footprint. The filter should have a cut-off just above the desired VCO frequency to ensure that the harmonics are adequately attenuated.

E.1.3 RF Amplifier

The output of the VCO is typically around 0 ± 3 dBm. Following the 6 dB of loss due to the wideband resistive power divider (i.e., the three 18 Ω resistors), the RF signal power is too weak to drive most mixers. Therefore, an amplifier and its associated biasing network are used to boost the frequency synthesizer board's output power. The frequency synthesizer board accepts any of Mini-Circuit's surface mount monolithic gain block amplifiers that use their custom "WW107" footprint. Aside from bandwidth, gain, and 1 dBm compression point, it is important to consider the amplifier's operating voltage, which must be below 5 V. A biasing resistor with an appropriate power rating is used to set the amplifier's biasing current. In Fig. 119, a 7.7 Ω resistor is used to bias a Mini-Circuits ERA-51SM amplifier to 4.5 V and 65 mA. The biasing network's inductor, which was a Mini-Circuits ADCH-80 RF choke, ensured the VCO's high frequency output did not couple onto the frequency synthesizer board's 5 V supply.

E.1.4 10 MHz Reference

The lower half of Fig. 119 shows the circuitry used to produce the nominally 10 MHz reference, f_{REF}, for the phase-locked loop. The board allows for either an external frequency reference or an on-board temperature-compensated crystal oscillator (TXCO). For the external frequency reference, the external source should be matched to 50 Ω. For the on-board TCXO, the frequency synthesizer board accepts a Fox Electronics FOX801A TCXO; similar models should work provided the footprint and required supply voltage are the same. A voltage-divider may be used to fine-tune the TCXO's output frequency. The jumper *J6* may be used to select between the on-board reference and an external reference. It should be noted that the voltage swing of any reference frequency signal must be within the acceptable limits of both the frequency synthesizer IC and the voltage-follower op amp, which buffers f_{REF} for use by other

frequency synthesizer boards or RF equipment. Thus, just as with conventional RF equipment, the frequency synthesizer boards feature a reference frequency input and output to allow multiple devices to be phase-locked to the same f_{REF}.

The capacitors following the on-board frequency reference and external reference input are used to AC-couple the reference signal going into the frequency synthesizer IC. When presented with an AC-coupled reference signal, the frequency synthesizer IC applies a DC offset at the reference input pin. Thereby, the reference frequency signal seen at the op amp's noninverting input is DC-biased and generally nonnegative. The DC-biased reference frequency signal is buffered by a high-speed op amp before being AC-coupled to the board's reference frequency output. The frequency synthesizer board accepts a 5-pin surface mount op amp using the SOT23-5 footprint such as the Fairchild FHP3130.

E.1.5 Digital I/O

The primary function of the digital I/O circuitry shown in the upper half of Fig. 120 is to correctly program the frequency synthesizer IC's four registers so that the phase-locked loop will yield the desired output frequency. The digital I/O is based around a serial peripheral interface (SPI), which requires a clock signal, a data signal, and a latch signal. The board features two digital I/O circuits: an optoisolator and a PIC microcontroller. The optoisolator allows for programming by an external device and is useful for testing purposes. For general use, a programmed PIC16F684 microcontroller provides all the necessary control over the frequency synthesizer board. The board has a 14-pin DIP footprint for the microcontroller. Typically a 14-pin DIP socket is soldered onto the board, after which the microcontroller IC inserted into the DIP socket. This allows the microcontroller IC to be removed for reprogramming as needed.

E.1.6 Power

As shown in Fig. 121, the board uses a pair of voltage regulators to produce the necessary 5 V and 3.3 V power rails. A pair of LEDs provide feedback concerning the board's power status. Typically, the input voltage provided at jumper *J5* is already 5 V, so the LM7805 voltage regulator is not used.

E.2 PLL/Microcontroller Programming

The PLL's frequency synthesizer IC is generally programmed by a Microchip PIC16F684 microcontroller. The microntroller code is designed to program the frequency synthesizer IC when the frequency synthesizer board is powered on. Adapting the microcontroller code to achieve different output frequencies for various frequency synthesizer ICs and reference frequencies is relatively straightforward.

There are three basic steps to programming the microcontroller. First, the appropriate register data is determined for the frequency synthesizer IC's 24-bit registers using a custom MATLAB function, `setfreq.m`. Then, this data is entered into the header file, `siggen.h`, for the microcontroller program. Finally, the microcontroller code, `siggen.c` is compiled, and the "Microchip PICkit 1 Flash Starter Kit" is used to (re)program the microcontroller's flash memory.

E.2.1 Determining Register Data

The appropriate register data may be determined by using the MATLAB function, `setfreq.m`. This function takes in the desired VCO frequency, the name of the frequency synthesizer IC, and the reference frequency and returns four 24-bit hexademical numbers. Sequentially writing these four 24-bit hexadecimal numbers to the frequency synthesizer IC will cause the PLL to lock onto the specified VCO frequency. Note that all specified frequencies are in MHz.

As an example, suppose an ADF4107 frequency synthesizer IC and appropriate

VCO are to be used with a 10 MHz reference frequency to generate a 2.45 GHz output. The corresponding call to `setfreq.m` would be:

```
>> PLLHexData = setfreq(2450, 'ADF4107', 10);
P = 16
R = 1
A = 5
B = 15
4000A6
010004
000F15
4000A2
```

Thus, the four 24-bit hexadecimal numbers are `4000A6`, `010004`, `000F15`, and `4000A2`. Note that the program also displays the corresponding values of the prescalar, P, and counters R, A, and B.

As originally written, `setfreq.m` only works with the ADF4107, ADF4111, and ADF4001 frequency synthesizer ICs. However, adding a new frequency synthesizer IC is simply a matter of adding a new `case` to the `switch` statement at the beginning of the function and modifying the corresponding values of `Plist`, `hasAB`, `minRF`, `maxRF`, and `maxPrescalarOutFreq`. The appropriate value for each these variables may be determined from the IC's datasheet and comment's within the functon. Finally, it should be noted that Analog Devices's "ADIsimPLL 3.1 Design and Evaluation Software" provides what is undoubtedly a more comprehensive tool for determinining the appropriate prescalar and counter values for *any* of the Analog Devices frequency synthesizer ICs. This software is freely available online through the Analog Devices website.

E.2.2 Entering Register Data in the Program Header

The four 24-bit hexademical numbers returned by the `setfreq.m` must then be entered into the microcontroller program's `siggen.h` header file. The byte array `pll_bytes` is assigned to the four 24-bit hexademical numbers. For the previous example, wherein an ADF4107 frequency synthesizer IC and 10 MHz reference are used to generate a 2.45 GHz signal, the value of `pll_bytes` would be changed to:

```
const static byte pll_bytes[PLLROWS][PLLCOLS]= {
  { 0x40, 0x00, 0xA6 },
  { 0x01, 0x00, 0x04 },
  { 0x00, 0x0F, 0x15 },
  { 0x40, 0x00, 0xA2 }
};
```

Thus, each 24-bit hexadecimal number is broken into three 8-bit bytes that together occupy one row of the array.

E.2.3 Compiling the Program and Flashing the Microcontroller

With `siggen.h` appropriately modified, the main program file, `siggen.c`, may then be compiled. After compiling, the PIC16F684 should be inserted into the "Microchip PICkit 1 Flash Starter Kit", which may then be connected to the computer via a USB cable. After connecting the programming board, the PIC16F684's flash memory is then reprogrammed with the newly compiled microcontroller coder. Disconnecting the USB cable will then power down the programming board, after which the newly prorammed PIC164684 can be removed from the "Microchip PICkit 1 Flash Starter Kit" and inserted into the frequency synthesizer board's 14-pin DIP socket.

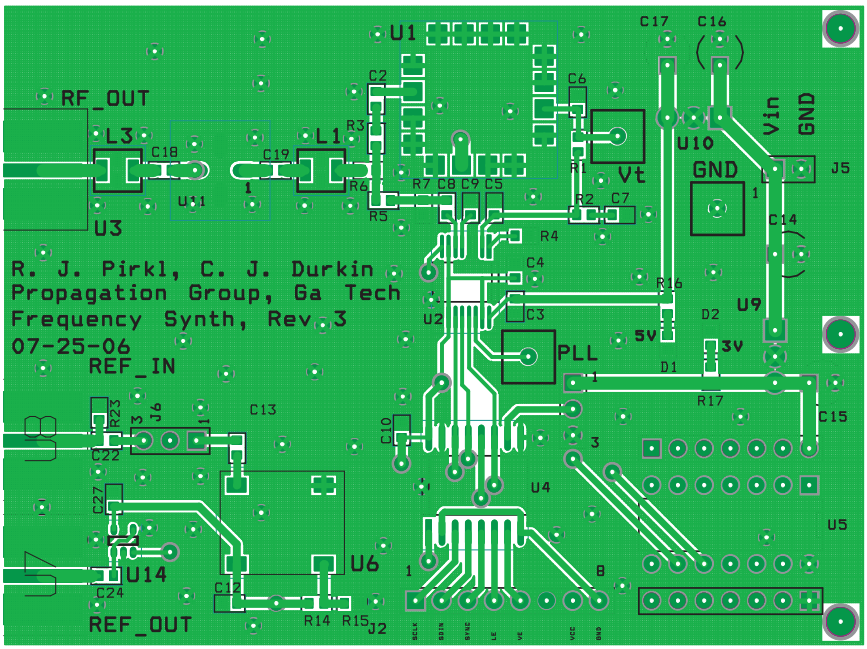

Figure 122: The frequency synthesizer board's top copper layer, solder mask, and silk screen.

E.3 PCB Layout

Figures 122 and 123 present the top and bottom copper layers, respectively, for the frequency synthesizer's PCB layout.

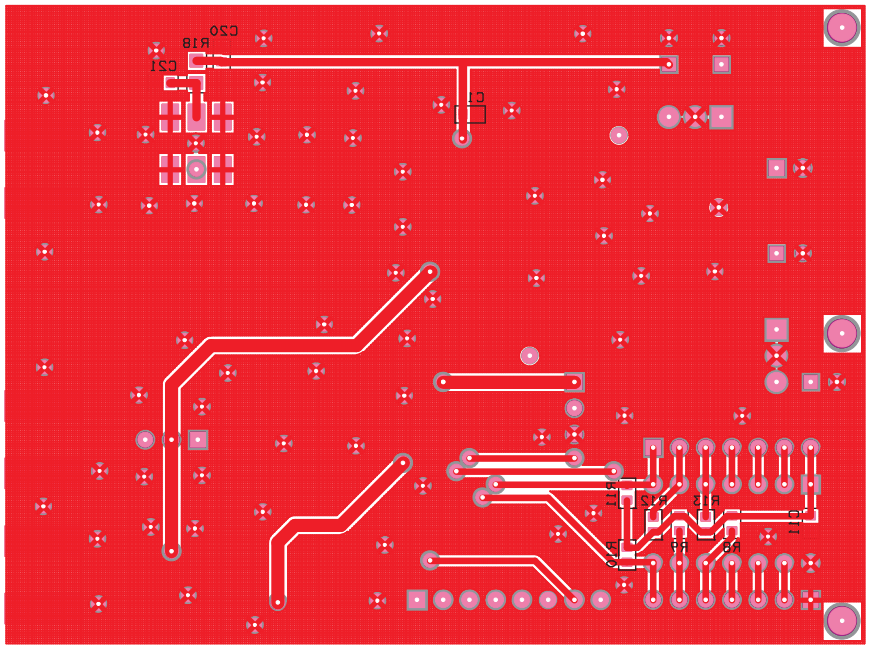

Figure 123: The frequency synthesizer board's bottom copper layer, solder mask, and silk screen.

APPENDIX F

TIME-DOMAIN DIFFRACTION SNAPSHOTS

Figures 124-126 present snapshots of the wireless channels' impulse responses following the application of the diffraction-specific space-time filter. Subfigures (a) and (b) correspond to the magnitude and phase of the filtered "PEC" measurements; subfigures (c) and (d), the magnitude and phase of the filtered brick measurements.

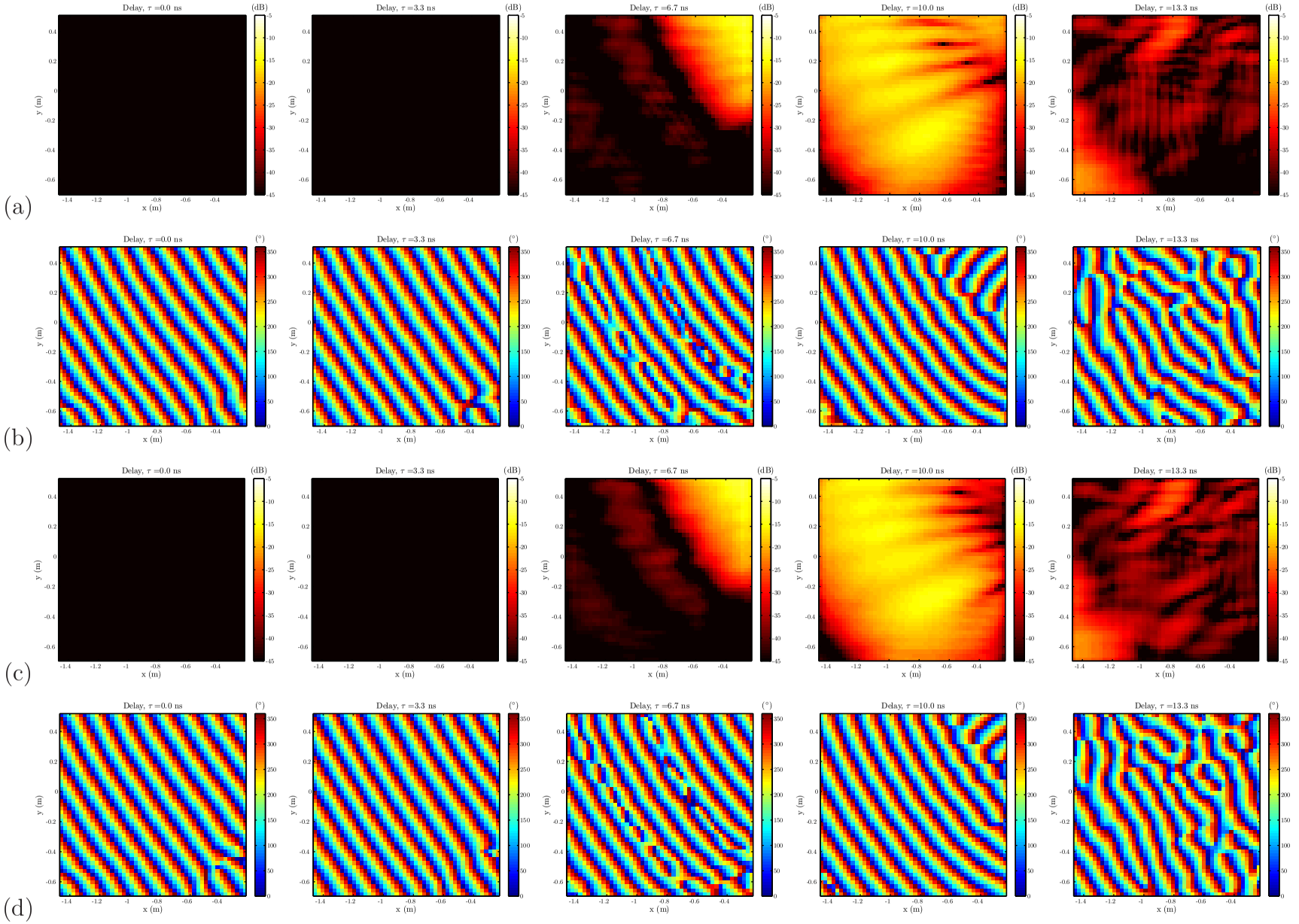

Figure 124: The filtered space-time wireless channel measurements for $\phi' = 45°$ measurements: (a) "PEC" magnitude, (b) "PEC" phase, (c) brick magnitude, and (d) brick phase.

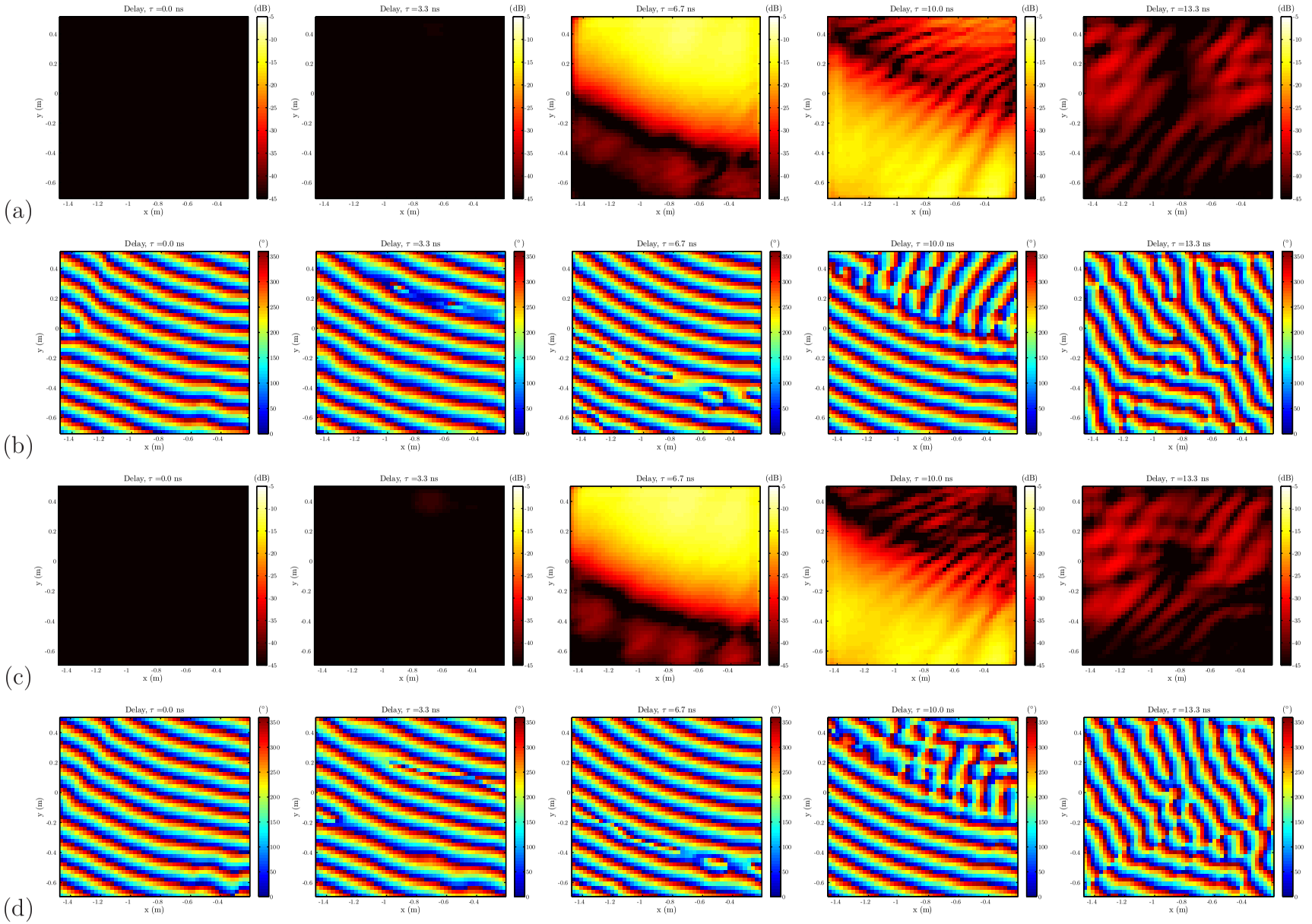

Figure 125: The filtered space-time wireless channel measurements for $\phi' = 90°$ measurements: (a) "PEC" magnitude, (b) "PEC" phase, (c) brick magnitude, and (d) brick phase.

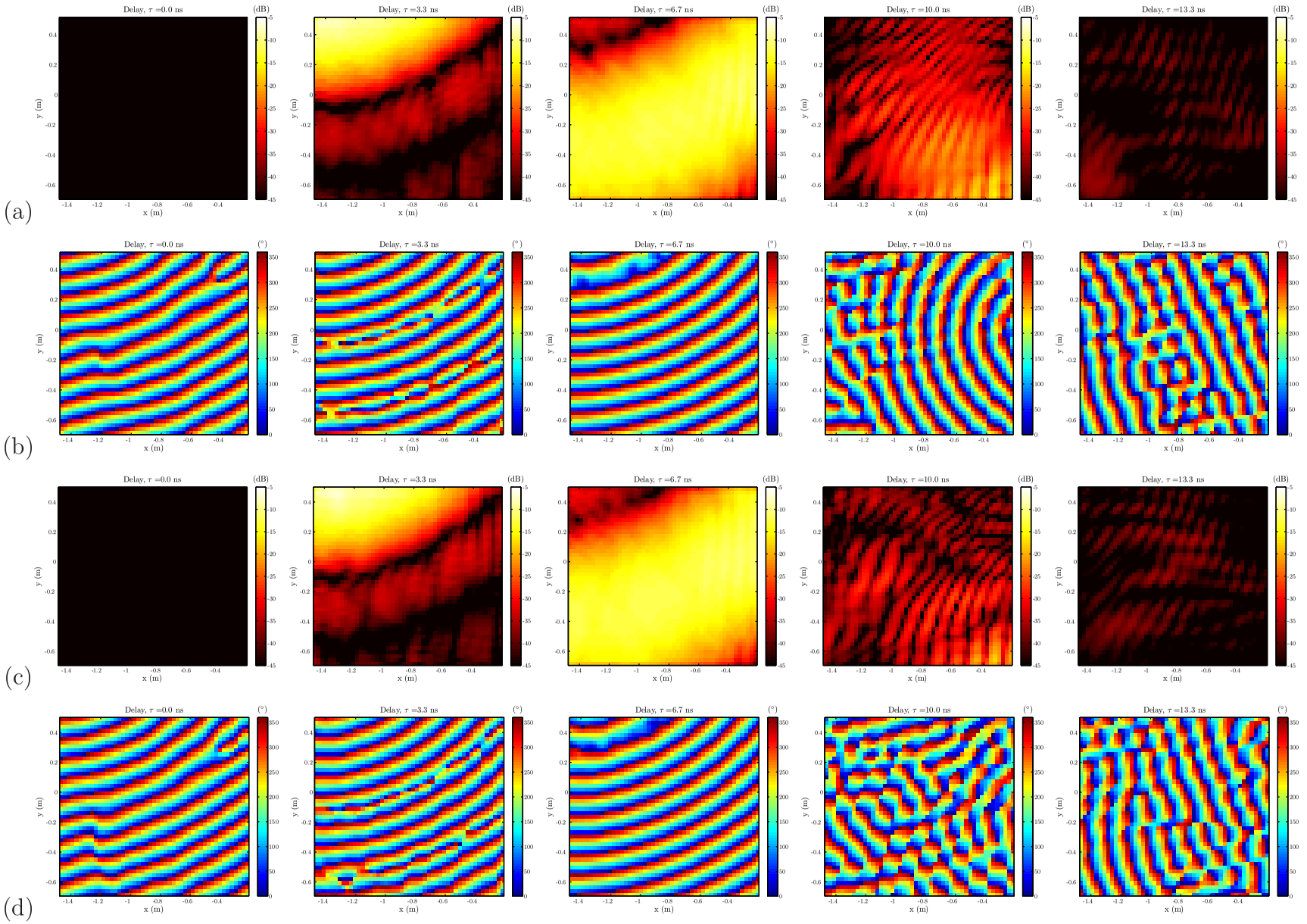

Figure 126: The filtered space-time wireless channel measurements for $\phi' = 135°$ measurements: (a) "PEC" magnitude, (b) "PEC" phase, (c) brick magnitude, and (d) brick phase.

REFERENCES

[1] Agilent Technologies, *Agilent 6000 Series Oscilloscope*, July 2005.

[2] Al-Nuaimi, M. O. and Haslett, C. J., "Measurements of diffraction and shielding from buildings," in *IEE Colloquium on Radio Frequency Co-Channel Interference Measurements and Modelling*, pp. 7/1–7/5, September 20 1988.

[3] Andersen, J. B., Rappaport, T. S., and Yoshida, S., "Propagation measurements and models for wireless communication channels," *IEEE Communications Magazine*, pp. 42–49, January 1995.

[4] Anderson, H. R., "Building corner diffraction measurements and predictions using UTD," *IEEE Transactions on Antennas and Propagation*, vol. 46, pp. 292–293, February 1998.

[5] Ansar, A. and Daniilidis, K., "Linear pose estimation from points or lines," *IEEE Transactions on Pattern Analysis and Machine Intelligence*, vol. 25, pp. 578–589, May 2003.

[6] Ayadi, M., Tabbane, S., and Behadj, Z., "Hierarchical radiosity model for the prediction of propagation in micro-cellular urba environment," in *Third International Conference on Wireless and Mobile Communications*, 4-9 March 2007.

[7] Barbour, N. and Schmidt, G., "Inertial sensor technology trends," *IEEE Sensors Journal*, vol. 1, pp. 332–339, December 2001.

[8] Bernardi, P., Cicchetti, R., and Testa, O., "A three-dimensional UTD heuristic diffraction coefficient for complex penetrable wedges," *IEEE Transactions on Antennas and Propagation*, vol. 50, pp. 217–224, February 2002.

[9] Bernardi, P., Cicchetti, R., and Testa, O., "An accurate UTD model for the analysis of complex indoor radio environments in microwave WLAN systems," *IEEE Transactions on Antennas and Propagation*, vol. 52, pp. 1509–1520, June 2004.

[10] Bertoni, H. L., Honcharenko, W., Rocha, L., and Xia, H. H., "UHF propagation prediction for wireless personal communications," *Proceedings of the IEEE*, vol. 82, pp. 1333–1359, September 1994.

[11] Blaunstein, N., Toeltsch, M., Christodoulou, C. G., Laurila, J., Tsalolihin, E., Bonek, E., Vainikainen, P., Tsouri, N., Kalliloa, K., and Laitinen, H., "Azimuth, elevation, and time-delay distributions in

wireless communication channels," *IEEE Antennas and Propagation Magazine*, vol. 48, pp. 160–167, February 2006.

[12] Borovikov, V. A. and Kinber, B. Y., *Geometrical Theory of Diffraction*, vol. 37 of *IEE Electromagnetic Waves Series*. London, UK: The Institute of Electrical Engineers, 1994.

[13] Bracewell, R. N., *The Fourier Transform and Its Applications*. New York: McGraw Hill, 3rd ed., 1999.

[14] Bullington, K., "Radio propagation at frequencies above 30 megacycles," *Proceedings of the Institue of Radio Engineers*, vol. 35, pp. 1122–1136, October 1947.

[15] Bultitude, R. J. C., Mahmoud, S. A., and Sullivan, W. A., "A comparison of indoor radio propagation characteristics at 910 MHz and 1.7 GHz," *IEEE Journal on Selected Areas in Communications*, vol. 7, pp. 20–30, January 1989.

[16] Burge, R. E., Yuan, X.-C., Carroll, B. D., Fisher, N. E., Hall, T. J., Lester, G. A., Taket, N. D., and Oliver, C. J., "Microwave scattering from dielectric wedges with planar surfaces: a diffraction coefficient based on a physical optics version of GTD," *IEEE Transactions on Antennas and Propagation*, vol. 47, pp. 1515–1527, October 1999.

[17] Chamberlin, K. A. and Luebbers, R. J., "An evaluation of Longley-Rice and GTD propagation models," *IEEE Transactions on Antennas and Propagation*, vol. AP-30, pp. 1093–1098, November 1982.

[18] Christodoulou, C. G. and Kauffman, J. F., "On the electromagnetic scattering from infinite rectangular grids with finite conductivity," *IEEE Transactions on Antennas and Propagation*, vol. 34, pp. 144–154, February 1986.

[19] Clarke, R. H., "A statistical theory of mobile-radio reception," *Bell System Technical Journal*, vol. 47, pp. 957–1000, July 1968.

[20] Collin, R. E., "Hertzian dipole radiating over a lossy earth or sea: some early and late 20th-century controversies," *IEEE Antennas and Propagation Magazine*, vol. 46, pp. 64–79, April 2004.

[21] Constantinou, C. C., Mehler, M. J., and Demetrescu, C., "Bricks: a theorist's point of view," in *IEE National Conference on Antennas and Propagation*, pp. 112–115, 30 March - 1 April 1999.

[22] Cox, D. C., "Delay Doppler characteristics of multipath propagation at 910 MHz in a suburban mobile radio environment," *IEEE Transactions on Antennas and Propagation*, vol. 20, pp. 625–635, September 1972.

[23] Cuinas, I. and Sanchez, M. G., "Measuring, modeling, and characterizing of indoor radio channels at 5.8 GHz," *IEEE Transactions on Vehicular Technology*, vol. 50, pp. 526–535, March 2001.

[24] Cuinas, I. and Sanchez, M. G., "Permittivity and conductivity measurements of building materials at 5.8 GHz and 41.5 GHz," *Wireless Personal Communications*, vol. 20, pp. 93–100, 2002.

[25] Davis, B. A. and Brown, G. S., "Diffraction by a randomly rough knife-edge," *IEEE Transactions on Antennas and Propagation*, vol. 50, pp. 1769–1778, December 2002.

[26] Degli-Esposti, V., Fuschini, F., Vitucci, E. M., and Falciasecca, G., "Measurements and modelling of scattering from buildings," *IEEE Transactions on Antennas and Propagation*, vol. 55, pp. 143–153, January 2007.

[27] Demetrescu, C., Budaev, B. V., Constantinou, C. C., and Mehler, M. J., "TM electromagnetic scattering by a transparent wedge with resistive faces," *IEEE Transactions on Antennas and Propagation*, vol. 47, pp. 47–54, January 1999.

[28] Demetrescu, C., Constantinou, C. C., and Mehler, M. J., "Scattering by a right-angled lossy dielectric wedge," *IEE Proc.-Microw. Antennas Propag*, vol. 144, pp. 392–396, October 1997.

[29] Demetrescu, C., Constantinou, C. C., and Mehler, M. J., "Corner and rooftop diffraction in radiowave propagation prediction tools: a review," in *48th IEEE Vehicular Technology Conference*, pp. 515–519, 18-21 May 1998.

[30] Devasirtham, D. M. J., "Time delay spread and signal level measurements of 850 MHz radio waves in building environments," *IEEE Transactions on Antennas and Propagation*, vol. 34, pp. 1300–1305, November 1986.

[31] Devices, A., "PLL Frequency Synthesizer ADF4107," 2007. Online: http://www.analog.com/static/imported-files/data_sheets/ADF4107.pdf.

[32] Dixon, R. C., *Spread Spectrum Systems with Commerical Applications*. John Wiley and Sons, Inc., 1994.

[33] Durgin, G. D., *Space-Time Wireless Channels*. Upper Saddle River, NJ: Prentice Hall Inc., 2003.

[34] Durkin, C. J. and Durgin, G. D., "Phased array multipath detection: power delay profile vs. information theoretic criteria," in *IEEE Antennas and Propagation Society International Symposium*, pp. 1120–1123, 9-15 June 2007.

[35] Franceschetti, G., Iodice, A., Natale, A., and Riccio, D., "Stochastic theory of edge diffraction," vol. 56, pp. 437–449, February 2008.

[36] Goldberg, F. and Bendall, S., "Making the invisible visible: a teaching/learning environment that builds on a new view of the physics learner," *American Journal of Physics*, vol. 63, pp. 978–991, November 1995.

[37] Golub, G. H. and Van Loan, C. F., *Matrix Computations*. Baltimore, MD: The Johns Hopkins University Press, 1983.

[38] Gonzalez, R. C. and Woods, R. E., *Digital Image Processing*. Upper Saddle River, NJ: Prentice Hall, 2nd ed., 2002.

[39] Gradshteyn, I. S. and Ryzhik, I. M., *Table of Integrals, Series, and Products*. San Diego, CA: Academic Press, 2000.

[40] Grosvenor, C. A., Johnk, R. T., Baker-Jarvis, J., Janezic, M. D., and Riddle, B., "Time-domain free-field measurements of the relative permittivity of building materials," *IEEE Transactions on Instrumentation and Measurement*, vol. 58, pp. 2275–2282, July 2009.

[41] Hald, J., Hansen, J. E., Jensen, F., and Larsen, F. H., *Spherical Near-Field Antenna Measurements*. London: Peter Peregrinus, Ltd., 1988.

[42] Hashemi, H. and Tholl, D., "Delay spread of indoor radio propagation channels," *IEEE Transactions on Vehicular Technology*, vol. 43, pp. 110–120, Feb. 1994.

[43] Hassig, S., Soria, R. Q., Bhandari, S., Pirkl, R. J., and Durgin, G. D., "Q "Wiimote"-based spatio-temporal wireless channel sounder," in *IEEE Southeastcon, 2009*, p. 444, 5-8 March 2009.

[44] Hata, M., "Empirical formula for propagation loss in land mobile radio services," *IEEE Transactions on Vehicular Technology*, vol. VT-29, pp. 317–325, August 1980.

[45] Herman, M. I., Volakis, J. L., and Senior, T. B. A., "Analytical expressions for a function occurring in diffraction theory," *IEEE Transactions on Antennas and Propagation*, vol. 35, pp. 1083–1086, September 1987.

[46] Herrmann, G. F., "Numerical computation of diffraction coefficients," *IEEE Transactions on Antennas and Propagation*, vol. 35, pp. 53–61, January 1987.

[47] Herrmann, G. F. and Strain, S. M., "Numerical diffraction coefficients in the shadow transition region," *IEEE Transactions on Antennas and Propagation*, vol. 36, pp. 1244–1251, September 1988.

[48] Ikegami, F., Takeuchi, T., and Yoshida, S., "Theoretical prediction of mean field strength for urban mobile radio," *IEEE Transactions on Antennas and Propagation*, vol. 39, pp. 299–302, March 1991.

[49] Iskander, M. F., "Technology-based electromagnetic education," *IEEE Transactions on Microwave Theory and Techniques*, vol. 50, pp. 1015–1020, March 2002.

[50] James, G. L., "Uniform diffraction coefficients for an impedance wedge," *Electronic Letters*, vol. 13, pp. 403–404, July 1977.

[51] James, G. L., *Geometrical Theory of Diffraction*. London, UK: Peter Perigrinus Ltd., 3rd ed., 1986.

[52] Jones, D. S. and Pidduck, F. B., "Diffraction by a metal wedge at large angles," *The Quarterly Journal of Mathematics*, vol. 1, no. 1, pp. 229–237, 1950.

[53] Kalliola, K., Laitinen, H., Vainikainen, P., Toeltsch, M., Laurila, J., and Bonek, E., "3-D double-directional radio channel characterization for urban macrocellular applications," *IEEE Transactions on Antennas and Propagation*, vol. 51, pp. 3122–3133, November 2003.

[54] Keller, J. B., "Geometrical theory of diffraction," *Journal of the Optical Society of America*, vol. 52, pp. 116–130, February 1962.

[55] Kenrick, G. W. and Pickard, G. W., "Summary of progress in the study of radio wave propagation phenomena," *Proceedings of the Institute of Radio Engineers*, vol. 18, pp. 649–668, April 1930.

[56] Kouyoumjian, R. G. and Pathak, P. H., "A uniform geometrical theory of diffraction for an edge in a perfectly conducting surface," *Proceedings of the IEEE*, vol. 62, pp. 1448–1462, November 1974.

[57] Labs, P. R., "Prl faqs: Ecl and pecl: Answers 9-12." Online: http://www.pulseresearchlab.com/faqs/ecl_ques/ecl_Q9-Q12.htm.

[58] Landron, O., Feuerstein, M. J., and Rappaport, T. S., "A comparison of theoretical and empirical reflection coefficients for typical exterior wall surfaces in a mobile radio environment," *IEEE Transactions on Antennas and Propagation*, vol. 44, pp. 341–351, March 1996.

[59] Laurila, J., Kalliola, K., Toeltsch, M., Hugl, K., Vainikainen, P., and Bonek, E., "Wide-band 3-D characterization of mobile radio channels in urban environment," *IEEE Transactions on Antennas and Propagation*, vol. 50, pp. 233–243, February 2002.

[60] Lawson, C. L. and Hanson, R. J., *Solving Least Squares Problems*. Englewood Cliffs, NJ: Prentice Hall, Inc., 1974.

[61] Luebbers, R. J., "Finite conductivity uniform GTD versus knife edge diffraction in prediction of propagation path loss," *IEEE Transactions on Antennas and Propagation*, vol. 32, pp. 70–76, January 1984.

[62] Luebbers, R. J., "Propagation prediction for hilly terrain using GTD wedge diffraction," *IEEE Transactions on Antennas and Propagation*, vol. 32, pp. 951–955, September 1984.

[63] Mini-Circuits, "Coaxial amplifier ZVE-8G." Online: http://www.minicircuits.com/pdfs/ZVE-8G.pdf.

[64] Mini-Circuits, "Coaxial Bandpass Filter VBFZ-2340+." Online: http://www.minicircuits.com/pdfs/VBFZ-2340+.pdf.

[65] Mini-Circuits, "Coaxial Bandpass Filter VBFZ-925." Online: http://www.minicircuits.com/pdfs/VBFZ-925+.pdf.

[66] Mini-Circuits, "Coaxial I & Q Demodulator ZAMIQ-895D." Online: http://www.minicircuits.com/pdfs/ZAMIQ-895D.pdf.

[67] Mini-Circuits, "Coaxial Low Pass Filter BLP-1.9." Online: http://www.minicircuits.com/pdfs/BLP-1.9+.pdf.

[68] Mini-Circuits, "Coaxial Low Pass Filter VLF-225." Online: http://www.minicircuits.com/pdfs/VLF-225.pdf.

[69] Mini-Circuits, "Connectorized Amplifier ZX60-2534M." Online: http://www.minicircuits.com/pdfs/ZX60-2534M+.pdf.

[70] Mini-Circuits, "Ultra-Reliable High Pass Filter VHP-19." Online: http://www.minicircuits.com/pdfs/VHP-19.pdf.

[71] Mini-Circuits, "Ultra Reliable Low Pass Filter VLP-41." Online: http://www.minicircuits.com/pdfs/VLP-41.pdf.

[72] Montiel, E., Aguado, A. S., and Sillion, F. X., "A radiance model for predicting radio wave propagation in irregular dense urban areas," *IEEE Transactions on Antennas and Propagation*, vol. 51, pp. 3097–3108, November 2003.

[73] Muqaibel, A., Safaai-Jazi, A., Bayram, A., Attiya, A. M., and Riad, S. M., "Ultrawideband through-the-wall propagation," *IEE Proc.-Microw. Antennas Propag.*, vol. 152, pp. 581–588, December 2005.

[74] Nechayev, Y. I. and Constantinou, C. C., "Improved heuristic diffraction coefficients for an impedance wedge at normal incidence," *IEE Proc.-Microw. Antennas Propag.*, vol. 153, pp. 125–132, April 2006.

[75] Nechayev, Y. I., Constantinou, C. C., and Lukama, L., "Comparison of measured and theoretical diffracted fields around building corners at 2.4 GHz," in *IEEE VTS 54th Vehicular Technology Conference, 2001*, vol. 2, pp. 728–732, 7-11 October 2001.

[76] Papoulis, A., *Probability, Random Variables, and Stochastic Processes*. McGraw-Hill, Inc, 1965.

[77] Pelosi, G., Coccioli, R., and Manara, G., "An FEM-based numerical diffraction coefficent for irregular wedge configurations," *IEEE Transactions on Antennas and Propagation*, vol. 45, pp. 563–564, March 1997.

[78] Pelosi, G., Coccioli, R., Manara, G., and Monorchio, A., "Scattering from a wedge with cavity backed apertures in its faces and related configurations: TE case," *IEE Proc.-Microw. Antennas Propag.*, vol. 142, pp. 183–188, April 1995.

[79] Peterson, A. F., "The interior resonance problem associated with surface integral equations of electromagnetics: Numerical consequences and a survey of remedies," *Electromagnetics*, vol. 10, no. 3, pp. 293–312, 1990.

[80] Peterson, A. F., Ray, S. L., and Mittra, R., *Computational Methods for Electromagnetics*. New York: IEEE Press, 1998.

[81] Pirkl, R. J. and Durgin, G. D., "Interpolation of perimeter wireless channel measurements into the measurement region," in *IEEE Antennas and Propagation Society International Symposium*, pp. 1–4, 5-11 July 2008.

[82] Pirkl, R. J. and Durgin, G. D., "Quasi 2-D field reconstruction using the conjoint cylindrical wave expansion," *IEEE Transactions on Antennas and Propagation*, 2008. Accepted for publication.

[83] Pirkl, R. J., Durgin, G. D., Austin, A. C. M., and Neve, M. J., "Extracting UTD wedge diffraction coefficients from electric field measurements," in *USNC/URSI National Radio Science Meeting Abstracts*, (Boulder, CO), 5-8 January 2009.

[84] Rappaport, T. S., Seidel, S. Y., and Takamizawa, K., "Statistical impulse response models for factory and open plan building radio communication system design," *IEEE Transactions on Communications*, vol. 39, pp. 794–807, May 1991.

[85] Remley, K. A., Anderson, H. R., and Weisshar, A., "Improving the accuracy of ray-tracing techniques for indoor propagation modeling," *IEEE Transactions on Vehicular Technologies*, vol. 49, pp. 2350–2358, November 2000.

[86] Rice, J. R., *The Approximation of Functions*. Reading, MA: Addison-Wesley Publishing Company, 1964.

[87] Rossi, J.-P., Barbot, J.-P., and Levy, A. J., "Theory and measurement of the angle of arrival and time delay of UHF radiowaves using a ring array," *IEEE Transactions on Antennas and Propagation*, vol. 45, pp. 876–884, May 1997.

[88] Rossi, J.-P., Wiart, J., and Eynard, F., "In situ measurement of reflection and diffraction coefficients of UHF radio waves on buildings using a ring array," *Radio Science*, vol. 35, pp. 361–369, March 2000.

[89] Rouviere, J.-F., Douchin, N., and Combes, P. F., "Improvement of the UTD formulation for diffraction of an electromagnetic wave by a dielectric wedge," *Electronics Letters*, vol. 33, pp. 373–375, February 1997.

[90] Rouviere, J.-F., Douchin, N., and Combes, P. F., "Diffraction by lossy dielectric wedges using both heuristic UTD formulations and FDTD," *IEEE Transactions on Antennas and Propagation*, vol. 47, pp. 1702–1708, November 1999.

[91] Saleh, A. A. M. and Valenzuela, R. A., "A statistical model for indoor multipath propagation," *IEEE Journal on Selected Areas in Communications*, vol. SAC-5, pp. 128–137, February 1987.

[92] Sarkar, T. K., Ji, Z., Kim, K., Medouri, A., and Salazar-Palma, M., "A survey of various propagation models for mobile communication," *IEEE Antennas and Propagation Magazine*, vol. 45, pp. 51–82, June 2003.

[93] Sato, K., Manabe, T., Ihara, T., Saito, H., Ito, S., Tanaka, T., Sugai, K., Murakami, Y., Shibayama, M., Konishi, Y., and Kimura, T., "Measurements of reflection and transmission characteristics of interior structures of office buildings in the 60-GHz band," *IEEE Transactions on Antennas and Propagation*, vol. 45, pp. 1783–1792, December 1997.

[94] Sauleau, R., Thouroude, D., Coquet, P., and Daniel, J. P., "Theoretical reflection coefficient of metal grid reflectors at a dielectric interface," *International Journal of Infrared and Millimeter Waves*, vol. 20, no. 2, pp. 325–339, 1998.

[95] Seidel, S. Y. and Rappaport, T. S., "Site-specific propagation prediction for wireless in-building personal communication system design," *IEEE Transactions on Vehicular Technology*, vol. 43, pp. 879–891, November 1994.

[96] Semiconductor, O., "Designing with PECL (ECL at +5.0 V)." Application Note AND8090/D, Online: http://www.onsemi.com/pub/Collateral/AN1406-D.PDF, Sept. 1999.

[97] Semiconductor, O., "Interfacing with ECLinPS." Application Note AND8066/D, Online: http://www.onsemi.com/pub/Collateral/AND8066-D.PDF, May 2002.

[98] Semiconductor, O., "Termination of ECL logic devices." Application Note AND8020/D, Online: http://www.onsemi.com/pub/Collateral/AND8020-D.PDF, Aug. 2002.

[99] Senior, T. B. A. and Volakis, J. L., *Approximate Boundary Conditions in Electromagnetics*. IEE Electromagnetic Waves Series, UK: The Institution of Electrical Engineers, 1995.

[100] Shore, R. A. and Yaghjian, A. D., "Dual-surface integral equations in electromagnetic scattering," *IEEE Transactions on Antennas and Propagations*, vol. 53, pp. 1706–1709, May 2005.

[101] Smith, G. S., *An Introduction to Classical Electromagnetic Radiation*. New York: Cambridge University Press, 1997.

[102] Starkov, A. S., "Diffraction by dielectric wedge," in *Day on Diffraction, 2001*, pp. 256–266, 29-31 May 2001.

[103] Stavrou, S. and Sanders, S. R., "Review of constitutive parameters of building materials," in *Twelfth International Conference on Antennas and Propagation*, pp. 211– 215, 31 March-3 April 2003.

[104] Stratton, J. A., *Electromagnetic Theory*. McGraw-Hill Book Company, Inc, 1st ed., 1941.

[105] Suzuki, H., "A statistical model of urban radio propagation," *IEEE Transactions on Communications*, vol. 25, pp. 673–680, July 1977.

[106] Tenerelli, P. A. and Bostian, C. W., "Measurements of 28 GHz diffraction loss by building corners," in *The Ninth IEEE International Symposium on Personal, Indoor and Mobile Radio Communications*, vol. 3, pp. 1166–1169, Sept 8-11 1998.

[107] Tenerelli, P. A. J., "Diffraction by buildings at 28 GHz: measurements and modeling," master's thesis, Virginia Tech, June 1998. Online: http://scholar.lib.vt.edu/theses/available/etd-71098-185056/unrestricted/TENETD.PDF.

[108] Tiberio, R., Pelosi, G., and Manara, G., "A uniform GTD formulation for the diffraction by a wedge with impedance faces," *IEEE Transactions on Antennas and Propagation*, vol. 33, pp. 867–873, August 1985.

[109] Tiberio, R., Pelosi, G., Manara, G., and Pathak, P. H., "High-frequency scattering from a wedge with impedance faces illuminated by a line source, part I: diffraction," *IEEE Transactions on Antennas and Propagation*, vol. 37, pp. 212–218, February 1989.

[110] Tsang, K.-F., Chan, W.-S., Jing, D., Kang, K., Yuen, S.-Y., and Zhang, W.-X., "Radiosity method: a new propagation model for microcellular communication," in *IEEE Antennas and Propagation Society International Symposium*, 1998.

[111] Turin, G. L., Clapp, F. D., Johnston, T. L., Fine, S. B., and Lavry, D., "A statistical model of urban multipath propagation," *IEEE Transactions on Vehicular Technology*, vol. 21, pp. 1–9, February 1972.

[112] Twersky, V., "On scattering and reflection of electromagnetic waves by rough surfaces," *IRE Transactions on Antennas and Propagation*, vol. 5, pp. 81–90, January 1957.

[113] Valenzuela, G. R., "The effective reflection coefficients in forward scatter from a dielectric slightly rough surface," *Preceedings of the IEEE*, vol. 48, p. 1279, August 1970.

[114] Walfisch, J. and Bertoni, H. L., "A theoretical model of UHF propagation in urban urban environments," *IEEE Transactions on Antennas and Propagation*, vol. 36, pp. 1788–1796, December 1988.

[115] Wang, H. and Rappaport, T. S., "A parametric formulation of the UTD diffraction coefficient for real-time propagation prediction modeling," *IEEE Antennas and Wireless Propagation Letters*, vol. 4, pp. 253–257, 2005.

[116] Wang, Y., Afsar, M. N., and Grignon, R., "Complex permittivity and permeability of carbonyl iron powders at microwave frequencies," in *IEEE Antennas and Propagation Symposium*, vol. 4, pp. 619–622, 22-27 June 2003.

[117] Watson, G. N., "The diffraction of electric waves by the Earth," *Proceedings of the Royal Society of London*, vol. 95, pp. 83–99, October 1918.

[118] Woodworth, M. B. and Yaghjian, A. D., "Derivation, application conjugate gradient solution of the dual-surface integral equations for three-dimensional, multi-wavelength perfect conductors," in *PIER 5, Progress in Electromagnetics Research* (Sarkar, T., ed.), pp. 103–130, New York: Elsevier, 1991.

[119] Wu, M., Zhao, Z., He, H., and Yao, X., "Preparation and microwave characteristics of magnetic iron fibers," *Journal of Magnetism and Magnetic Materials*, vol. 217, pp. 89–92, July 2000.

[120] Xu, H., Rappaport, T. S., Boyle, R. J., and Schaffner, J. H., "Measurements and models for 38-GHz point-to-multipoint radiowave propagation," *IEEE Journal on Selected Areas in Communications*, vol. 18, pp. 310–321, March 2000.

[121] Yaghjian, A. D., "An overview of near-field antenna measurements," *IEEE Transactions on Antennas and Propagation*, vol. 34, pp. 30–45, January 1986.

[122] Zavadskii, V. and Sakharova, M., "Application of the special functionΨ_Φ in problems of wave diffraction in wedge-shaped regions," *Sov. Phys. Acoust.*, vol. 13, pp. 48–54, 1967.

VITA

Ryan J. Pirkl received the B.S., M.S., and Ph.D. degrees in electrical engineering from the Georgia Institute of Technology in 2005, 2007, and 2010, respectively. In 2004, he joined the Propagation Group where he studied and developed wireless channel measurement systems and techniques applicable to in situ characterization of radio wave propagation mechanisms. In 2008, Ryan spent three months in Auckland, New Zealand investigating indoor radio wave propagation with researchers from the Radio Systems Group at the University of Auckland. In 2010, he began working as a postdoctoral researcher at the National Institute of Standards and Technology in Boulder, Colorado where he will be developing and characterizing an environment emulator for wireless systems testing.